

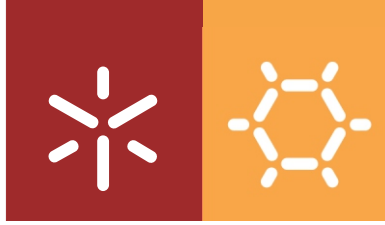


Gellan Gum-Based Hydrogels for Tissue Engineering Applications

Silvia Cristina Araújo Vieira

Universidade do Minho
Instituto de Investigação em Biomateriais,
Biodegradáveis e Biomiméticos





Universidade do Minho

Instituto de Investigação em Biomateriais,
Biodegradáveis e Biomiméticos

Sílvia Cristina Araújo Vieira

Gellan Gum-Based Hydrogels for Tissue Engineering Applications

Tese de Doutoramento
Doutoramento em Engenharia de Tecidos,
Medicina Regenerativa e Células Estaminais

Trabalho efetuado sob a orientação do
Doutor Joaquim Miguel Antunes Correia de Oliveira
e do
Professor Doutor Rui Luís Gonçalves dos Reis

DIREITOS DE AUTOR E CONDIÇÕES DE UTILIZAÇÃO DO TRABALHO POR TERCEIROS

Este é um trabalho académico que pode ser utilizado por terceiros desde que respeitadas as regras e boas práticas internacionalmente aceites, no que concerne aos direitos de autor e direitos conexos.

Assim, o presente trabalho pode ser utilizado nos termos previstos na licença abaixo indicada.

Caso o utilizador necessite de permissão para poder fazer um uso do trabalho em condições não previstas no licenciamento indicado, deverá contactar o autor, através do RepositóriUM da Universidade do Minho.

Licença concedida aos utilizadores deste trabalho



**Atribuição
CC BY**

<https://creativecommons.org/licenses/by/4.0/>

ACKNOWLEDGEMENTS

This thesis is the end of a big journey. A journey of knowledge. Scientific knowledge but also personal, in a great amount. Fortunately, I was never alone along the ride, and I was lucky enough to have with me the best examples that I could ask for. Firstly, I would like to acknowledge my supervisor, Dr. Miguel Oliveira. His support, and mentorship along these years are invaluable. He always trusted in me and on my work, even when I doubt that I could achieve the final line. But also, for never letting me settle inside the comfort zone. I learnt to like being outside it, and that is something that one does not learn from the books. This work is his work too.

I would also like to extend my gratitude to Professor Rui Reis, that allowed me to be part of 3B's Research Group as a Master student and later, as a PhD candidate. And now, looking back for all these years I cannot count the things that I have learnt with Professor Rui. But one thing I know, a researcher that only knows science, does not know Science at all.

During the last years I had the pleasure to work in distinct research groups, that always received me with great support. Hence, I would like to acknowledge Professor Africa González-Fernández, from University of Vigo, as well as her group; to the Nanotech4ALS consortium, for all the support and scientific gatherings; and to Professor Kristi Anseth and her research group, from University of Colorado Boulder.

My gratitude also extends to the funding agencies that supported this work, in particular to the Foundation for Science and Technology (FCT) for my PhD grant (SFRH/BD/102710/2014), to the IACOBUS Program, and to the Foundation D. Manuel II for the Award "Príncipe da Beira Biomedical Sciences".

This work would be much harder without the help of my friends, colleagues, technical staff and management team of 3B's Research Group. My special thanks to all of them. In particular to Sara, Alex, Ivo and Ricardo, for everything I learnt and keep learning from of you. Thank you for always being there.

Finally, I would like to thank my family, for all the support and patience. Álvaro, thank you for all the unconditional support along the last years. For always being there, celebrating with me the good moments, but also during the innumerable bad ones, and to teach me how simple the things can be. To my mom, dad and sister, I do not have enough words to express how grateful I am, but this work is dedicated to all of you. I am what I am because of you and I would not be here, writing these lines, without your help, support, and guidance. Thank you so much!

To my grandmother, that was always proud of my achievements, often even more than myself.

STATEMENT OF INTEGRITY

I hereby declare having conducted this academic work with integrity. I confirm that I have not used plagiarism or any form of undue use of information or falsification of results along the process leading to its elaboration.

I further declare that I have fully acknowledged the Code of Ethical Conduct of the University of Minho.

GELLAN GUM-BASED HYDROGELS FOR TISSUE ENGINEERING APPLICATIONS

ABSTRACT

The use of hydrogels as platforms for Tissue Engineering and Regenerative Medicine approaches has been growing in the past years. Their resemblance to the natural extracellular matrix, and facility to modify and tailor their final properties are some of the aspects that appeal researchers around the world to use this type of material. Different hydrogel sources have been exploited and processed using different methodologies, resulting in different structures that can be tailored for the intended application. Indeed, cell-material interactions can be adjusted by using distinct hydrogel designs, processing methods or sources. One of the natural materials that has been considered for Tissue Engineering and Regenerative Medicine strategies is gellan gum. This natural polymer has been used for different applications over the last years, on its natural form or after chemical modifications. Among such modifications, gellan gum methacrylation already showed promising results on Tissue Engineering. Nevertheless, the impact of the crosslinking and processing strategies used with the material are still not well established. This thesis aimed to highlight the versatility of this polymer, achieved by using different crosslinking strategies. Ionic crosslinking with calcium chloride, one of the most used methods to prepare gellan gum hydrogels, were firstly considered envisioning bone tissue engineering. Ionic crosslinking was also used to prepare traceable hydrogels, taking advantage of the affinity of methacrylated gellan gum to the divalent paramagnetic manganese ion. The ionic-responsive property of gellan gum allowed a minimally invasive administration of gellan gum in the vicinities of the central nervous system, as well as the desired traceability. At last, a different strategy was used to obtain hydrogels with immunoprotective capabilities, intended to be used on immunoisolation strategies. Polyelectrolyte complexation of gellan gum with poly-L-lysine yielded a semipermeable membrane, capable of blocking the passage of the immune cells towards the hydrogel core, where therapeutic cells are encapsulated. Altogether, the different approaches used on the scope of this thesis showed the versatility of methacrylated gellan gum and the importance of carefully chose the crosslinked methodology to prepare hydrogels, as they greatly influence final hydrogel behaviour.

Keywords: crosslinking, hydrogels, methacrylated gellan gum, tissue engineering and regenerative medicine.

HIDROGÉIS À BASE DE GOMA GELANA PARA APLICAÇÕES EM ENGENHARIA DE TECIDOS

RESUMO

O uso de hidrogéis como plataformas para a Engenharia de Tecidos e Medicina Regenerativa tem vindo a crescer nos últimos anos. A semelhança com a matriz extracelular natural, assim como a facilidade em modificar e adaptar as suas propriedades finais, são alguns dos fatores que levam à utilização deste tipo de material. Hidrogéis provenientes de diferentes fontes foram já explorados, e processados usando diferentes metodologias, resultando em diferentes estruturas que podem ser personalizadas para a aplicação pretendida. De facto, as interações entre células e materiais podem ser ajustadas usando hidrogéis preparados com diferentes métodos ou formas de processamento. Um dos materiais naturais considerados para as estratégias de Engenharia de Tecidos e Medicina Regenerativa é a goma gelana. Este polímero natural tem sido utilizado para diferentes aplicações ao longo dos últimos anos, na sua forma natural ou após modificações químicas. Entre essas modificações, a metacrilção da goma gelana já apresentou resultados promissores em Engenharia de Tecidos. No entanto, o impacto das estratégias de reticulação e processamento usadas no material, ainda não está bem estabelecido. Esta tese teve como objetivo destacar a versatilidade deste polímero, pelo uso de diferentes estratégias de reticulação. Inicialmente, foi considerada a reticulação iónica com cloreto de cálcio, um dos métodos mais utilizados para a preparação de hidrogéis de goma gelana, para aplicação em regeneração óssea. A reticulação iónica foi também usada para preparar hidrogéis rastreáveis, aproveitando a afinidade da goma de gelana metacrilada com o manganês, um ião divalente paramagnético. A reticulação da goma gelana na presença de iões permitiu uma administração minimamente invasiva do material nas proximidades do sistema nervoso central, bem como a rastreabilidade desejada. Finalmente, uma estratégia diferente foi usada para obter hidrogéis com capacidade imunoprotetora, destinados a ser usados como imunoproteção. Complexos de polieletrólitos formados pela interação da goma de gelana com poli-L-lisina originaram uma membrana semipermeável, capaz de bloquear a passagem das células do sistema imunitário em direção ao núcleo de hidrogel, onde as células com fins terapêuticos são encapsuladas. Em suma, as diferentes abordagens utilizadas no contexto desta tese mostraram a versatilidade da goma de gelana metacrilada e a importância de escolher cuidadosamente a metodologia de reticulação para preparar hidrogéis, pois estas têm grande influência no comportamento final do hidrogel.

Palavras-chave: goma gelana metacrilada, hidrogéis, reticulação, engenharia de tecidos e medicina regenerativa.

TABLE OF CONTENTS

ACKNOWLEDGEMENTS	III
STATEMENT OF INTEGRITY	IV
ABSTRACT	V
RESUMO	VI
TABLE OF CONTENTS	VII
LIST OF ABBREVIATIONS AND ACRONYMS	XIV
LIST OF FIGURES	XX
LIST OF SUPPLEMENTARY FIGURES	XXII
LIST OF SUPPLEMENTARY MOVIES	XXII
LIST OF SUPPLEMENTARY TABLES	XXII
LIST OF EQUATIONS	XXII
SHORT CURRICULUM VITAE	XXIII
LIST OF PUBLICATIONS	XXIV
INTRODUCTION TO THE THESIS STRUCTURE	XXIX
SECTION 1: GENERAL INTRODUCTION	1
CHAPTER I: NATURAL-BASED HYDROGELS - FROM PROCESSING TO APPLICATIONS	2
I.1 Introduction	3
I.2 Natural Polymers for Hydrogels: Structure and Function	3
<i>I.2.1 Polysaccharides</i>	7
<i>I.2.2 Proteins</i>	13
I.3 Processing Methods and Applications for TERM.....	16
<i>I.3.1 Lithography</i>	16
<i>I.3.2 Emulsion</i>	17
<i>I.3.3 Extrusion</i>	19
<i>I.3.4 Bioprinting</i>	20
<i>I.3.5 Microfluidics</i>	22
<i>I.3.6 Cryogelation</i>	23
I.4 Final Remarks and Future Directions.....	23
I.5 References	24
CHAPTER II: ENGINEERING HYDROGELS FOR MODULATION OF MATERIAL-CELL INTERACTIONS	43

II.1 Introduction	44
II.2 Hydrogel Preparation	45
II.3 Physical Crosslinking	46
<i>II.3.1 Ionic/Electrostatic Interactions</i>	46
<i>II.3.2 Thermal Induction</i>	48
II.4 Chemical Crosslinking.....	49
<i>II.4.1 Photopolymerization</i>	49
<i>II.4.2 "Click-chemistry"</i>	51
<i>II.4.3 Enzymatic Crosslinking</i>	54
II.5 Material-cell Interactions	55
<i>II.5.1 Hydrogel Stability</i>	55
<i>II.5.2 Mechanical Properties</i>	60
<i>II.5.3 Immune Response</i>	72
II.6 Concluding Remarks and Future Trends.....	74
II.7 References	76
SECTION 2: EXPERIMENTAL DESIGN	92
CHAPTER III: MATERIALS AND METHODS	93
III.1 Materials and Processing	94
<i>III.1.1 Methacrylated Gellan Gum</i>	94
<i>III.1.2 Hyaluronic Acid</i>	95
<i>III.1.3 Poly-L-lysine</i>	96
III.2 Physicochemical Characterization	97
<i>III.2.1 Weight Loss Ratio</i>	97
<i>III.2.2 Size Variation of Hydrogels</i>	97
<i>III.2.3 Scanning Electron Microscopy</i>	98
<i>III.2.4 Energy Dispersive Spectroscopy</i>	100
<i>III.2.5 X-ray Diffraction</i>	100
<i>III.2.6 Micro-Computed Tomography</i>	101
<i>III.2.7 Calcium Colorimetric Assay</i>	101
<i>III.2.8 Rheology</i>	101
<i>III.2.9 Injection Ability</i>	103
<i>III.2.10 Inductively Coupled Plasma-Optical Emission Spectrometry</i>	103
<i>III.2.11 X-ray Photoelectron Spectroscopy</i>	104
<i>III.2.12 Zeta Potential</i>	105
<i>III.2.13 Fourier Transform Infrared Spectroscopy</i>	107
<i>III.2.14 Atomic Force Microscopy</i>	108
III.3 <i>In vitro</i> Permeability Studies	109

III.3.1 Methylene Blue.....	109
III.3.2 Bovine Serum Albumin	110
III.3.3 Dexamethasone.....	110
III.3.4 Dextran-FITC.....	111
III.4 Bioactivity Study	111
III.5 Optical Microscopy.....	112
III.5.1 Brightfield Microscopy.....	112
III.5.2 Fluorescence Microscopy.....	113
III.6 Cell Culture Conditions	115
III.6.1 Growth and Harvesting of the Cells.....	116
III.6.2 Human-derived Adipose Stem Cells.....	116
III.6.3 Androgen-sensitive Human Prostate Adenocarcinoma Cells (LNCaP).....	117
III.6.4 Human Monocytic Cell Line (THP-1).....	117
III.6.5 Mouse Macrophage Cell Line (Raw 264.7).	117
III.6.6 Human Peripheral Blood Mononuclear Cells.....	117
III.7 Cell Viability and Morphology.....	118
III.7.1 Live/Dead	118
III.7.2 MEM Extract Test.....	119
III.7.3 DNA Quantification	120
III.7.4 Real-time Cell Proliferation	120
III.7.5 Cell Morphology.....	121
III.8 Immune Response.....	122
III.8.1 Complement Activation	122
III.8.2 Cytokine Release	123
III.9 <i>In vivo</i> Tests - Biocompatibility and Function.....	124
III.9.1 Mice Models	124
III.9.2 Histochemistry.....	125
III.10 Magnetic Resonance Imaging.....	126
III.11 References	130
SECTION 3: EXPERIMENTAL PART	135
CHAPTER IV: SELF-MINERALIZING CA-ENRICHED METHACRYLATED GELLAN GUM BEADS FOR BONE TISSUE ENGINEERING.....	136
IV.1 Graphical Abstract	137
IV.2 Introduction	137
IV.3 Materials and Methods.....	139
IV.3.1 Preparation of Methacrylated Gellan Gum (GG-MA) and CaCl ₂ Solutions	139
IV.3.2 Preparation of Ca-enriched GG-MA Beads.....	140

IV.3.3 Physicochemical Characterization of Ca-enriched GG-MA Beads.....	140
IV.3.4 In vitro Bioactivity Test.....	140
IV.3.5 Drug Release Studies.....	141
IV.3.6 In vitro Studies.....	142
IV.3.7 In vivo Subcutaneous Implantation.....	144
IV.3.8 Statistical Analysis.....	145
IV.4 Results.....	145
IV.4.1 Ca-enriched GG-MA Hydrogel Beads Characterization.....	145
IV.4.2 Drug Release Profile.....	148
IV.4.3 Cytocompatibility and Immunocompatibility.....	149
IV.4.4 In Vivo Bioactivity.....	152
IV.5 Discussion.....	153
IV.6 Conclusion.....	157
IV.7 Acknowledgments.....	158
IV.8 References.....	158

CHAPTER V: MN-BASED METHACRYLATED GELLAN GUM HYDROGELS FOR MRI-GUIDED CELL DELIVERY

AND IMAGING 164

V.1 Graphical Abstract.....	165
V.2 Introduction.....	165
V.3 Materials and Methods.....	168
V.3.1 Preparation of Methacrylated Gellan Gum (GG-MA), MnCl ₂ and aCSF Solutions.....	168
V.3.2 Preparation of Mn-based GG-MA Hydrogels.....	168
V.3.3 Rheological Studies.....	169
V.3.4 Injection Ability Test.....	169
V.3.5 Permeability Studies.....	169
V.3.6 Degradation Profile.....	170
V.3.7 Manganese Release Profile – Inductively Coupled Plasma-Optical Emission Spectroscopy.....	170
V.3.8 Human-derived Adipose Stem Cells (hASCs) Isolation and Culture.....	170
V.3.9 Cell Encapsulation.....	171
V.3.10 Live/Dead Staining.....	171
V.3.11 Animal Surgeries.....	172
V.3.12 Phantom Magnetic Resonance Imaging.....	172
V.3.13 In vivo Magnetic Resonance Imaging.....	172
V.3.14 Statistical Analysis.....	173
V.4 Results and Discussion.....	173
V.4.1 Preparation of Mn-based GG-MA Hydrogels.....	173
V.4.2 Injection Ability.....	176

<i>V.4.3 Hydrogel Permeability</i>	176
<i>V.4.4 Degradation Profile</i>	178
<i>V.4.5 Manganese Release Profile and Magnetic Resonance Imaging</i>	178
<i>V.4.6 Cell Viability: hASCs Encapsulation</i>	179
<i>V.4.7 In Vivo Magnetic Resonance Imaging</i>	180
V.5 Conclusion	182
V.6 Acknowledgements	182
V.7 Supporting Information	183
<i>V.7.1 Rheological Characterization: Phase Angle and Shear Viscosity</i>	183
<i>V.7.2 Biocompatibility: Injection with 18G Needle</i>	183
V.8 References	183

CHAPTER VI: METHACRYLATED GELLAN GUM AND HYALURONIC ACID HYDROGEL BLENDS FOR IMAGE-GUIDED NEUROSURGERIES..... 188

VI.1 Graphical Abstract	189
VI.2 Introduction	189
VI.3 Materials and Methods.....	191
<i>VI.3.1 Gellan Gum Methacrylation</i>	191
<i>VI.3.2 Artificial Cerebrospinal Fluid (aCSF)</i>	192
<i>VI.3.3 Methacrylated Gellan Gum Pre-gel Solutions Supplemented with MnCl₂ (MnGG-MA)</i>	192
<i>VI.3.4 Methacrylated Gellan Gum/Sodium Hyaluronate Blends (MnGG-MA/HA)</i>	192
<i>VI.3.5 Rheological Studies</i>	192
<i>VI.3.6 Injection Ability Test</i>	193
<i>VI.3.7 Permeability Studies</i>	193
<i>VI.3.8 Degradation Profile</i>	193
<i>VI.3.9 Manganese Release Profile – Inductively Coupled Plasma-Optical Emission Spectroscopy (ICP)</i>	194
<i>VI.3.10 Human-derived Adipose Stem Cells Isolation and Culture</i>	194
<i>VI.3.11 Cell Encapsulation</i>	194
<i>VI.3.12 Live/Dead Staining</i>	195
<i>VI.3.13 MnGG-MA/HA In Vivo Transplantation</i>	195
<i>VI.3.14 Magnetic Resonance Imaging - Phantom Imaging</i>	196
<i>VI.3.15 Magnetic Resonance Imaging – In Vivo Imaging</i>	196
<i>VI.3.16 Statistical Analysis</i>	196
VI.4 Results and Discussion	197
<i>VI.4.1 Preparation and Characterization of MnGG-MA/HA Hydrogel Blends</i>	197
<i>VI.4.2 MRI Imaging</i>	201
<i>VI.4.3 In Vivo Magnetic Resonance Imaging</i>	202
<i>VI.4.4 hASCs Encapsulation and Viability</i>	203

VI.5 Conclusion	205
VI.6 Conflict of Interest.....	205
VI.7 Acknowledgments.....	205
VI.8 References	206

CHAPTER VII: COMPOSITION COMPRISING POLYELECTROLYTE COMPLEXES, METHODS AND USES

THEREOF 209

VII.1 Technical Field.....	210
VII.2 Background	210
VII.3 General Description	212
VII.4 Brief Description of the Drawings.....	215
VII.5 Detailed Description	216
VII.6 Claims.....	223
<i>VII.6.1 Amended Claims (Pursuant to Rule 161(1) and 162 of the European Patent Convention)</i>	225
VII.7 Drawings	227

CHAPTER VIII: METHACRYLATED GELLAN GUM/POLY-L-LYSINE POLYELECTROLYTE COMPLEX BEADS FOR CELL-BASED THERAPIES 233

VIII.1 Graphical Abstract	234
VIII.2 Introduction	234
VIII.3 Materials and Methods.....	236
<i>VIII.3.1 Production of GG-MA/PLL Beads</i>	236
<i>VIII.3.2 Injection Ability Tests</i>	237
<i>VIII.3.3 Zeta Potential Measurements</i>	237
<i>VIII.3.4 Fourier-Transformed Infrared (FTIR) Spectroscopy</i>	237
<i>VIII.3.5 X-ray Photoelectron Spectroscopy (XPS) Measurements</i>	237
<i>VIII.3.6 Beads' Surface Morphology and Size</i>	238
<i>VIII.3.7 Size Variation and Weight Loss Profile</i>	238
<i>VIII.3.8 Mechanical Stability</i>	239
<i>VIII.3.9 Permeability Tests</i>	239
<i>VIII.3.10 Qualitative Determination of Total Complement Activation</i>	240
<i>VIII.3.11 Cytokine Release from Human Peripheral Blood Mononuclear Cells (hPBMCs)</i>	240
<i>VIII.3.12 In vivo Tests</i>	241
<i>VIII.3.13 In Vitro Tests: Biocompatibility, Cell Morphology, and Proliferation</i>	242
<i>VIII.3.14 Statistical Analysis</i>	245
VIII.4 Results and Discussion	245
<i>VIII.4.1 Preparation and Characterization of GG-MA/PLL PEC Beads</i>	245
<i>VIII.4.2 Permeability Studies</i>	251

<i>VIII.4.3 Immunoprotection</i>	254
<i>VIII.4.4 Subcutaneous Implantation of GG-MA/PLL PEC Beads</i>	257
<i>VIII.4.5 In vitro Assay Using hASC-laden GG-MA/PLL PEC Beads</i>	258
VIII.5 Conclusion.....	261
VIII.6 Acknowledgements	261
VIII.7 Supplementary Information	263
<i>VIII.7.1 PEC Formation Reaction</i>	263
<i>VIII.7.2 PEC Formation Conditions</i>	264
<i>VIII.7.3 Mechanical Stability</i>	265
<i>VIII.7.4 Release Analysis and Modeling</i>	266
<i>VIII.7.5 Complement System Activation</i>	267
<i>VIII.7.6 Surface Elemental Composition</i>	268
<i>VIII.7.7 Supplementary Movies</i>	268
VIII.8 References	268
SECTION 4: CONCLUDING REMARKS	273
CHAPTER IX: GENERAL CONCLUSIONS AND FUTURE PERSPECTIVES	274
IX.1 General Conclusions	274
IX.2 Future Perspectives	278
READER NOTES	281

LIST OF ABBREVIATIONS AND ACRONYMS

A

AB	Alamarblue® dye
aCSF	Artificial cerebrospinal fluid
AFM	Atomic force microscopy
ALS	Amyotrophic lateral sclerosis
ANOVA	Analysis of variance
APA	Alginate-poly-L-lysine-alginate
ASC	Adipose stem cell
ATCC	American type culture collection
ATP	Adenosine triphosphate
AzR	Alizarin red

B

BCIP	5-bromo-4-chloro-3-indolyl phosphate
BDNF	Brain-derived neurotrophic factor
BE	Binding energy
BMP	Bone morphogenetic proteins
BSA	Bovine serum albumin
BTE	Bone tissue engineering
BX	<i>M</i> -boroxole

C

CA	California
CAD-CAM	Computer-aided design and computer aided manufacturing
CAE	Constant analyzer energy
Calcein-AM	Calcein acetoxymethyl ester
CaP	Calcium phosphates
CBFa1	Osteoblast transcription factor, core-binding factor alpha 1
CC	Creative commons
CCD	Charge-coupled device
CEC	N-carboxyethyl chitosan
CGGGRGDS	Cysteine-glycine-glycine-glycine-arginine-glycine-aspartic acid-serine
CINBIO	Centro de Investigaci3n Biom3dicas
CNPC	Cortical neuron progenitor cells
CNS	Central nervous system
CS	Chondroitin sulfate
CSF	Cerebrospinal fluid

D

DA	Diels-alder
DAPI	Dapi
DBCO	Dibenzocyclooctyne
DDS	Drug delivery system
DGAV-DSPA	Direção Geral de Veterinária, Direção de Serviços de Proteção Animal (Portuguese Licensing Authority)
DMEM	Dulbecco's modified eagle medium
DNA	Deoxyribonucleic acid
DP	Dermal papilla
DPBS	Dulbecco's phosphate-buffered saline
DPSC	Dental pulp stromal cells
DS	Degree of substitution

E

ECM	Extracellular matrix
EDC	1-ethyl-3-(3-dimethylaminopropyl)carbodiimide hydrochloride
EDS	Energy-dispersive X-ray spectroscopy
EDTA	Ethylenediamine tetracetic acid
EO	Ethylene oxide gas
EP	European patent
EPC	Endothelial progenitor cells
ERC	European research council
ERDF	European regional development fund
EthD-1	Ethidium homodimer-1
EU	European union

F

FA	Flip angle
FAK	Focal adhesion kinases
FBS	Fetal bovine serum
FCT	Foundation for Science and Technology
FEDER	Fundo Europeu de Desenvolvimento Regional
FELASA	Federation for Laboratory Animal Science Associations
FITC	Fluorescein isothiocyanate
FOV	Field of view
FPBA	2-fluorophenylboronic acid
FTIR	Fourier Transform Infrared spectroscopy

G

G	α -L-guluronic acid monomers
---	-------------------------------------

G'	Storage modulus
G''	Loss modulus
G*	Complex modulus
GAG	Glycosaminoglycan
GalNAc	N-acetylgalactosamine
GelMA	Gelatin methacrylate
Gd	Gadolinium
GDNF	Glial cell-line derived neurotrophic factor
GG	Gellan gum
GG-LA	Low-acyl gellan gum
GG-MA	Methacrylated gellan gum
GlcA	Glucuronic acid
GMA	Glycidyl methacrylate
GMP	Good manufacturing practice
H	
HA	Hyaluronic acid
hASCs	Human-derived adipose stem cells
hPBMC	Human peripheral blood mononuclear cells
HRP	Horseradish peroxidase
Hyal	Hyaluronidase
I	
ICP-OES	Inductively coupled plasma-optical emission spectrometry
ICVS	Instituto de Investigação em Ciências da Vida e Saúde
IFN- γ	Interferon gamma
IGF-1	Insulin growth factor type-1
IgG	Immunoglobulin G
IL	Interleukin
ISO	International Organization for Standardization
K	
Kca	κ -carrageenan
<i>KE</i>	Kinetic energy of the emitted electrons
L	
LAP	Lithium acylphosphinate
LbL	Layer-by-layer
LCST	Lower critical solution temperature
LINC	Linker of nucleoskeleton and cytoskeleton
LMNA	Laminin A
LNCaP	Androgen-sensitive human prostate adenocarcinoma cells

LPS Lipopolysaccharide
LSCM Laser scanning confocal microscope
LVER Linear viscoelastic region

M

M β -D-mannuronic monomers
MAPK Mitogen activated protein kinases
MB Methylene blue
MDA-MB-231 Triple negative breast cancer line
MDA-MB-231Br Brain metastasizing variant of the triple negative breast cancer line MDA-MB-231
MEM Minimum essential alpha medium
MMP Matrix metalloproteinases
MO Missouri
MR Magnetic resonance
MRI Magnetic resonance imaging
MSC Mesenchymal stem cells
MSCGM MSC growth medium
MT Masson's trichrome
MW Molecular weight
MWCO Molecular weight cut-off
MyoD1 Muscle transcription factor
 μ -CT Micro-computed tomography

N

NaHA Sodium hyaluronate
NCL Nanotechnology characterization laboratory
NFAT Nuclear factor of activated T-cells
NGF Neural growth factor
NIH National Institutes of Health
NMR Nuclear magnetic resonance
NorHA Norbornene-modified HA
NRK Normal rat kidney epithelial cells
NS Not significant
NY New york

O

OSA Oxidized sodium alginate

P

PBS Phosphate buffered saline

PEC	Polyelectrolyte complexes
PEDdiPDA	Poly(ethylene glycol) di-photodegradable acrylate
PEG	Polyethylene glycol
PI	Propidium iodide
PLL	Poly-L-lysine
PMA	Phorbol12-myristate 13-acetate
PNIPAAm	Poly(<i>N</i> -isopropylacrylamide)
PVDF	Polyvinylidene fluoride

R

R&D	Research and development
RGD	Arginine-glycine-aspartic acid
RNA	Ribonucleic acid
ROI	Region of interest
ROS	Reactive oxygen species
RPMI	Roswell park memorial institute
RT	Room temperature
RTCA	Real-time cell analyzer
RUNX	Runt-related transcription factor2

S

SBF	Simulated body fluid
SD	Standard deviation
SDS-PAGE	Sodium dodecyl sulfate and polyacrylamide gel
SEM	Scanning electron microscopy
SPAAC	Azide-alkyne cycloaddition
SPM	Scanning probe microscope

T

TAZ	Transcriptional coactivator with PDZ-binding motif
TCP	Tricalcium phosphate
TCPS	Tissue culture polystyrene
TDSC	Tendon-derived stem cells
TE	Tissue engineering
TERM	Tissue engineering and regenerative medicine
TGF	Transforming growth factor
T _H 1	T helper 1 cell
T _H 2	T helper 2 cell
THP-1	Human monocyte cell line
TNF	Tumor necrosis factor
TRITC	Tetramethylrhodamine B isothiocyanate-phalloidin

U

UCSC	Umbilical cord derived stem cells
UCST	Upper critical solution temperature
UK	United Kingdom
UM	University of Minho
USA	United States of America
UV	Ultraviolet
UV-vis	Ultraviolet-visible

V

VEGF	Vascular endothelial growth factor
VS-HA	Vinyl sulfone modified HA

W

WBA	Wulff-type <i>o</i> -amino-methylphenylboronic acid
-----	---

X

XPS	X-ray photoelectron spectroscopy
XRD	X-ray diffraction

Y

YAP	Yes-associated protein
-----	------------------------

LIST OF FIGURES

Figure I-1. Schematic representation of the processing methods considered for this chapter and representative resulting structures.	18
Figure I-2. Comparison of bioprinter types regarding their components and characteristics.	20
Figure I-3. Material properties for bioprinting applications.	21
Figure II-1. Hydrogel classification categories.	44
Figure II-2. Schematic representation of the most widely used crosslinking strategies for hydrogel formation.	46
Figure II-3. Hydrogel crosslinking using ionic interactions.	47
Figure II-4. Electrostatic interaction between polyelectrolytes of opposite charge allows the formation of multilayered constructs.	48
Figure II-5. Thermo-responsive hydrogels.	49
Figure II-6. Photopolymerization strategies.	51
Figure II-7. Overview of the discussed chemical crosslinking chemistries.	53
Figure II-8. Enzymatic crosslink.	54
Figure II-9. Schematic overview of the material-cell interactions discussed in this review.	56
Figure II-10. Overview of the TRAFFIC system.	58
Figure II-11. Schematic representation of the mechanotransduction phenomena.	60
Figure II-12. MSCs response to substrate stiffness.	62
Figure II-13. Elastic versus viscoelastic matrices on mechanotransduction.	64
Figure II-14. Time of exposure to stiff microenvironments affects MSCs fate.	66
Figure II-15. Host immune response to hydrogels.	73
Figure III-1. Schematic representation of methacrylation reaction used to prepare GG-MA.	94
Figure III-2. Chemical structure of PLL.	96
Figure III-3. Schematic representation of the methodology used to access hydrogel's size variation.	98
Figure III-4. Schematic representation of a scanning electron microscope and signal generation.	99
Figure III-5. Illustration of an oscillatory experiment using a parallel plate geometry, and resulting stress and strain wave relationships, for a viscoelastic material.	102
Figure III-6. Setup used to measure the force needed to extrude hydrogels.	103
Figure III-7. Schematic representation of an XPS equipment.	104
Figure III-8. Principle of surface potential measurement.	106
Figure III-9. Schematic representation of transmission FTIR instrumentation.	107
Figure III-10. Schematic illustration of the AFM principle.	108
Figure III-11. Chemical structure of methylene blue.	109
Figure III-12. Crystal structure of bovine serum albumin.	110
Figure III-13. Chemical structure of dexamethasone 21-phosphate disodium salt.	110
Figure III-14. Chemical structure of dextran-FITC.	111
Figure III-15. Schematic representation of the filter set used in standard a fluorescence microscope.	114

Figure III-16. Schematic drawing of a laser scanning confocal microscope's objective.	115
Figure III-17. Schematic representation of the xCELLigence RTCA technology.....	121
Figure III-18. The distinct pathways of the complement system.	122
Figure IV-1. Ca-enriched GG-MA beads preparation and characterization.	146
Figure IV-2. <i>In vitro</i> bioactivity: SBF immersion.	147
Figure IV-3. <i>In vitro</i> bioactivity: μ CT imaging.	148
Figure IV-4. Drug Release Profile from Ca-enriched GG-MA Beads.	149
Figure IV-5. <i>In vitro</i> assays with Ca-enriched GG-MA beads.....	150
Figure IV-6. Relative C3b protein measured after Complement Activation assay.....	151
Figure IV-7. <i>In vivo</i> bioactivity of Ca-enriched GG-MA beads.	153
Figure V-1. Mn-based GG-MA hydrogels preparation and rheological characterization.....	175
Figure V-2. Release and degradation profiles of Mn-based GG-MA hydrogels.	177
Figure V-3. Cell encapsulation within Mn-based GG-MA hydrogel fibers.	180
Figure V-4. Magnetic resonance T1 weighted imaging of Mn-based GG-MA hydrogels.	181
Figure VI-1. Characterization of MnGG-MA/HA hydrogels.	198
Figure VI-2. Degradation profile of MnGG-MA/HA hydrogels.	200
Figure VI-3. Permeability of MnGG-MA/HA hydrogels.	201
Figure VI-4. Magnetic resonance T1 weighted imaging of MnGG-MA/HA hydrogels.	202
Figure VI-5. Cell encapsulation within MnGG-MA/HA hydrogel fibers.	204
Figure VII-1. Schematic representation of a FTIR spectra.....	227
Figure VII-2. Size comparison of capsules before and after immersion in distilled water, PBS and DMEM.....	227
Figure VII-3. Pictures of different formulations of GG/PLL capsules, before and after incubation with distilled water.	228
Figure VII-4. SEM images of GG/PLL capsules at different magnifications.	229
Figure VII-5. Live/dead assay on encapsulated androgen-sensitive human prostate adenocarcinoma (LNCaP) cells.	229
Figure VII-6. Schematic representation of GG-PLL spheres, and method of obtaining thereof.....	230
Figure VII-7. Characterization of an embodiment of GG microcapsules	230
Figure VII-8. Schematic representation of a controlled release of BSA-FITC or Methylene Blue from two different formulations.	231
Figure VII-9. Pictures confirming that live cells are found inside the PEC capsules of the present disclosure.....	232
Figure VIII-1. Preparation and characterization of GG-MA/PLL PEC beads.	247
Figure VIII-2. Surface morphology and stability of GG-MA/PLL PEC beads.	250
Figure VIII-3. Permeability of GG-MA/PLL PEC beads.	253
Figure VIII-4. Assessment of GG-MA/PLL PEC beads immunocompatibility (<i>in vitro</i>).	254
Figure VIII-5. <i>In vivo</i> biocompatibility of GG-MA/PLL PEC beads.	258
Figure VIII-6. <i>In vitro</i> assessment of GG-MA/PLL PEC beads effect on hASCs.	259
Figure VIII-7. <i>In vitro</i> assessment of the effect of GG-MA/PLL PEC leachable on hASCs.	260

LIST OF SUPPLEMENTARY FIGURES

Supplementary Figure V-1. Rheologic characterization of Mn-based hydrogels.	183
Supplementary Figure V-2. Cell encapsulation in GG-MA hydrogel supplemented with 0.1 mM.	183
Supplementary Figure VIII-1. Polyelectrolyte formation.	263
Supplementary Figure VIII-2. Polyelectrolyte complex optimization.	264
Supplementary Figure VIII-3. Mechanical stability of the GG-MA/PLL PEC beads.	265
Supplementary Figure VIII-4. Release analysis	266
Supplementary Figure VIII-5. Quantification of the complement system activation.	267

LIST OF SUPPLEMENTARY MOVIES

Supplementary Movie VIII-1. Formation of PEC beads.	268
Supplementary Movie VIII-2. Diffusion of Methylene Blue into a GG-MA/PLL PEC bead.	268

LIST OF TABLES

Table I-1. Examples of natural polysaccharides and their relevant properties for TERM applications.	4
Table I-2. Natural proteins and their relevant properties for TERM applications.	15
Table II-1. Recent strategies for immunoisolation.	59
Table II-2. Summary of the latest works addressing the effect of hydrogel mechanical properties in the mechanotransduction phenomena.	68
Table III-1. Properties of NovaMatrix® Sodium Hyaluronate Pharma Grade 150 (DuPont™).	96
Table III-2. Ion Concentration in Simulated Body Fluid (SBF)	112
Table III-3. Overview of materials and methods used per chapter.	128
Table IV-1. Cytokine release after incubation of hPBMCs with Ca-enriched GG-MA beads.	152
Table V-1. Composition of aCSF solution.	168
Table VIII-1. Cytokine release after incubation of hPBMCs with GG-MA/PLL PEC beads.	257

LIST OF SUPPLEMENTARY TABLES

Supplementary Table VIII-1. Surface elemental composition measured by XPS.	268
---	-----

LIST OF EQUATIONS

Equation III-1. Degree of substitution (DS).	95
Equation III-2. Weight loss ratio.	97
Equation III-3. Size variation.	98
Equation III-4. Bragg's law.	100
Equation III-5. Complex modulus.	102
Equation III-6. Phase difference (phase angle expressed as loss tangent).	102
Equation III-7. Volume of SBF used for testing the hydrogels.	112

SHORT CURRICULUM VITAE

Sílvia C. Araújo Vieira (MSc) is a PhD candidate at the 3B's Research Group, member of the Portuguese Government Associate Laboratory ICVS/3B's, University of Minho, Portugal. (<http://www.3bs.uminho.pt/users/silviavieira>; ORCID: 0000-0002- 6481-4500).

As background, Sílvia Vieira has a MSc on Bioengineering – Molecular Biotechnology, finished in 2014, by the Institute of Biomedical Sciences Abel Salazar and Faculty of Engineering, University of Porto. During her Master course, she had the opportunity to work in other Institutions, such as Institute for Molecular and Cell Biology (University of Porto, Portugal) and the Department of Physiology, Anatomy and Genetics (University of Oxford, United Kingdom).

She started her work at the 3B's Research Group in 2014, as MSc student. The developed work was focused on the field of biomaterials and nanotechnology for biomedical applications, namely for bone tissue engineering. During her master thesis, she acquired significant knowledge on gold nanoparticles, specifically gold nanorods, and their functionalization with gellan gum hydrogels, under the supervision of Dr. Miguel Oliveira and Dr. Pedro Granja.

After finishing her masters, she was awarded an individual FCT grant (SFRH/BD/102710/2014), and since 2015, Sílvia is enrolled in the PhD program Tissue Engineering, Regenerative Medicine and Stem Cells of University of Minho, developing her work at 3B's Research Group under supervision of Dr. Miguel Oliveira. Besides her work at 3B's, she is also collaborating with other Research Groups, including CINBIO from the University of Vigo, under supervision of Professor África González-Fernández; the Mossakowski Medical Research Centre, Polish Academy of Sciences, under supervision of Professor Barbara Lukomska; and the BioFrontiers Institute, University of Colorado Boulder, Colorado, where she worked under the supervision of Professor Kristi Anseth. In 2018, Sílvia Vieira was awarded with the Prize Príncipe da Beira for Biomedical Sciences.

She also presented several oral communications both in national and international conferences in the field of Tissue Engineering and had been acting as a referee of international peer-reviewed journals upon invitation.

LIST OF PUBLICATIONS

The work performed during the PhD period resulted in the publications listed below.

Papers in international scientific journals with referees:

“Methacrylated Gellan Gum/Poly-L-lysine Polyelectrolyte Complex Beads for Cell-Based Therapies”.
Vieira S., Silva Morais A., Garet E., Silva-Correia J., Reis R.L., González-Fernández A., Oliveira J.M.
(submitted).

“Mn-Based Methacrylated Gellan Gum Hydrogels for MRI-Guided Cell Delivery and Imaging”, **Vieira S.**,
Strymecka P., Stanaszek L., Silva-Correia J., Drela K., Fiedorowicz M., Malysz-Cymborska I., Janowski
M., Reis R. L., Lukomska B., Walczak P., Oliveira J. M. (submitted)

“Methacrylated Gellan Gum and Hyaluronic Acid Hydrogel Blends for Image-Guided Neuro interventions”,
Vieira S., Strymecka P., Stanaszek L., Silva-Correia J., Drela K., Fiedorowicz M., Malysz-Cymborska I.,
Rogujski P., Janowski M., Reis R. L., Lukomska B., Walczak P., Oliveira J. M. *Journal of Materials
Chemistry B*, 8, 5928-5937, DOI: 10.1039/d0tb00877j, 2020.

“Self-mineralizing Ca-enriched Methacrylated Gellan Gum Beads for Bone Tissue Engineering”. **Vieira S.**,
Silva Morais A., Garet E., Silva-Correia J., Reis R.L., González-Fernández A., Oliveira J.M., *Acta
Biomaterialia*, 93, 74-85, DOI: 10.1016/j.actbio.2019.01.053, 2019.

"*In Vivo* Performance of Hierarchical HRP-Crosslinked Silk Fibroin/ β -TCP Scaffolds for Osteochondral
Tissue Regeneration". Ribeiro V. P., Pina S., Canadas R. F., Morais A., Vilela C., **Vieira S.**, Cengiz I. F.,
Reis R. L., and Oliveira J. M., *Regenerative Medicine Frontiers*, 1:e190007,
DOI: 10.20900/rmf20190007, 2019.

“Indirect printing of hierarchical patient-specific scaffolds for meniscus tissue engineering”. Costa J.; Silva-
Correia J., Pina S., Morais A., **Vieira S.**, Espregueira Mendes J.; Pereira H., Reis R.L., Oliveira J. M., *Bio-
design and Manufacturing*, 2, 225-241, DOI: 10.1007/s42242-019-00050-x, 2019.

“Thermal annealed silk fibroin membranes for periodontal guided tissue regeneration”. Geão C., Costa-
Pinto A. R., Cunha-Reis C., Ribeiro V.P., **Vieira S.**, Oliveira J.M., Reis R.L., Oliveira A.L., *Journal of
Materials Science: Materials in Medicine*, 30:27, DOI: 10.1007/s10856-019-6225-y, 2019.

"Tuning Enzymatically-crosslinked Silk fibroin Hydrogel Properties for the Development of a Colorectal
cancer Extravasation 3D Model on a Chip", Carvalho M. R., Maia F. R., **Vieira S.**, Reis R. L., and Oliveira
J. M., *Global Challenges*, vol. 2, issue 5-6, pp. 1700100, DOI: 10.1002/gch2.201700100, 2018.

Reviews in international scientific journals with referees:

"Engineering Hydrogels for Modulation of Material-Cell Interactions", **Vieira S.**, Reis R. L., and Oliveira J. M. (*submitted*)

"Advanced Biomaterials and Processing Methods for Liver Regeneration: State-of-the-Art and Future Trends". da Silva Morais A., **Vieira S.**, Zhao X., Mao Z., Gao C., Oliveira J. M., and Reis R. L., *Advanced Healthcare Materials*, pp. 1901435, DOI: 10.1002/adhm.201901435, 2020.

"Hydrogel-based Scaffolds to Support Intrathecal Stem Cell Transplantation as a Gateway to the Spinal Cord: Clinical Needs, Biomaterials, and Imaging Technologies", Oliveira, J. M., Carvalho, L., Silva-Correia, J., **Vieira S.**, Majchrzak M., Lukomska B., Stanaszek L., Strymecka P., Malysz-Cymborska I., Golubczyk D., Kalkowski L., Reis R. L., Janowski M., Walczak P., *npj Regenerative Medicine*, 3:8, DOI: 10.1038/s41536-018-0046-3, 2018.

"The Potential of Hyaluronic acid in Immunoprotection and Immunomodulation: Chemistry, Processing and Function", Zamboni F., **Vieira S.**, Reis R. L., Oliveira J. M., and Collins M. N., *Progress in Materials Science*, 97, 97-122. DOI: 10.1016/j.pmatsci.2018.04.003, 2018.

Book Chapters:

"Natural-Based Hydrogels: From Processing to Applications", **Vieira S.**, Morais A., Silva-Correia J., Oliveira J. M., and Reis R. L., in *Encyclopedia of Polymer Science and Technology*, (Ed.), DOI: 10.1002/0471440264.pst652, 2017.

"Natural-Origin Materials for Tissue Engineering and Regenerative Medicine", Silva S. S., Fernandes E. M., Pina S., Silva-Correia J., **Vieira S.**, Oliveira J. M., and Reis R. L., in *Comprehensive Biomaterials II*, DOI: 10.1016/B978-0-12-803581-8.10134-1, 2017.

"Nanoparticles-Based Systems for Osteochondral Tissue Engineering", Oliveira I., **Vieira S.**, Oliveira J. M., Reis R. L., in Oliveira J., Pina S., Reis R., San Roman J. (eds) *Osteochondral Tissue Engineering. Advances in Experimental Medicine and Biology*, vol 1059, DOI: 10.1007/978-3-319-76735-2_9, 2018.

Patents:

"Hydrogel Comprising Manganese, Methods and Uses Thereof". Oliveira J. M., **Vieira S.**, Oliveira E., Silva-Correia J., Reis R. L., Walczak P., Malysz-Cymborska I., Golubczyk D., Kalkowski L., Majchrzak M., Janowski M., Strymecka P., Stanaszek L., Lukomska B., Svendsen T., Asdahl L. C., and Sætrang H. E. M.. Published as WO/2019/123423 and EP3501553 (A1).

“Composition Comprising Polyelectrolyte Complexes, Methods and Uses Thereof”. **Vieira S.**, Silva-Correia J., Oliveira J.M., Reis R.L.. Published as WO/2017/089974, EP3380078 (A1) and US20180344652 (B2).

Oral Communications:

“Gellan gum-based Capsules for Cell Therapies”. **Vieira S.**, Silva Morais A., Garet E., González-Fernández A., Reis, R. L. , and Oliveira J. M., *CHEM2NATURE 2018* Conference, Porto, Portugal, 2018.

“Gellan Gum: a Multifunctional Tool to Modulate Cell Microenvironment” **Vieira S.**, Silva Morais A., Reis R. L., Oliveira J.M. Rapid Fire at *TERMIS-AM*, Charlotte NC, 2017. *Tissue Engineering Part A*, Dec 2017, DOI:10.1089/ten.tea.2017.29003.abstracts.

“Traceable Hydrogels for Cell and Drug Delivery”. **Vieira S.**, Gonçalves C., Silva-Correia J., Reis R. L., Oliveira J. M., *TERM STEM 2016* Conference, Guimarães, Portugal, 2016.

“Advanced Functional Materials for Islet Cell Encapsulation”. **Vieira S.**, Reis R.L., Oliveira J. M., *5th ICVS/3B's Meeting*, Braga, Portugal, 2015.

"Indirect printed patient-specific scaffolds with a bioactive bottom layer for meniscus regeneration." Costa J. B., Silva-Correia J., Pina S., da Silva Morais A., **Vieira S.**, Pereira H., Espregueira-Mendes J., Reis R. L., and Oliveira J. M., *3rd Workshop BAMOS*, 6th November, Braga, Portugal, 2019.

"*In vivo* Performance of HRP-silk fibroin/ZnSr doped β -TCP Scaffolds for Osteochondral Tissue Regeneration" Ribeiro V. P., Pina S., Canadas R. F., Araujo A., Morais A., Vilela C., **Vieira S.**, Cengiz I. F., Reis R. L., and Oliveira J. M., *15th Bath Biomechanics Symposium*, 2019.

Poster Presentations:

“Methacrylated Gellan Gum Poly-L-Lysine complexes as semipermeable matrix for cell-based therapies”. **Vieira S.**, Silva Morais A., Garet E., Silva-Correia J., Reis, R. L., González-Fernández A., and Oliveira J. M., *1st Discoveries Forum on Regenerative and Precision Medicine*, Porto, Portugal, 2019.

“Manganese-based Methacrylated Gellan Gum Hydrogels as Injectable System for Image-guided Cell Delivery”. **Vieira S.**, Strymecka P., Stanaszek L., Silva-Correia J., Lukomska B., Reis R. L., Walczak P., Oliveira J.M., *TERMIS EU 2019*, Rhodes, Greece, 2019.

"Gellan Gum-Poly-L-Lysine Complexes: A New Biomaterial Platform for Cell Encapsulation". **Vieira S.**, Garet E., Silva Morais A., Reis, R. L., González-Fernández A., and Oliveira J. M., *SFB Annual Meeting 2018*, Hilton Atlanta, Atlanta, United States, 2018.

"Self-mineralizing Methacrylated Gellan Gum Hydrogels". **Vieira S.**, Silva Morais A., Silva-Correia J., Reis, R. L., and Oliveira, J. M., *CHEM2NATURE Final Conference*, Porto, Portugal, 2018.

"Gellan gum-based Capsules for Cell Therapies". **Vieira S.**, Silva Morais A., Silva-Correia J., Reis, R. L., and Oliveira, J. M., *TERM STEM 2017*, Fundação Dr. António Cupertino de Miranda, Porto, Portugal, 2017.

"Gellan Gum-Poly-L-Lysine Complexes for Cell Encapsulation". **Vieira S.**, Silva Morais, A., Reis, R. L., Oliveira J.M., *SFB Annual Meeting 2017*, Minneapolis Convention Center, Minneapolis, United States, 2017.

"Hierarchical HRP-crosslinked silk fibroin/ZnSr- β -TCP scaffolds for osteochondral tissue engineering: *In vivo* assessment of biological performance". Ribeiro V. P., Pina S., Canadas R. F., da Silva Morais A., Vilela C., **Vieira S.**, Cengiz I. F., Reis R. L., and Oliveira J. M., *FoReCaST 2nd Workshop*, Porto, Portugal, 2019.

"Indirect Printed Patient Specific Scaffolds with a Bioactive Bottom Layer for Meniscus". Costa J. B., Silva-Correia J., Pina S., da Silva Morais A., **Vieira S.**, Pereira H., Espregueira-Mendes J., Reis R. L., and Oliveira J. M., *FoReCaST 2nd Workshop*, Porto, Portugal, 2019.

"Hierarchical bilayered silk fibroin scaffolds containing ZnSr- β -TCP particles for osteochondral tissue regeneration". Ribeiro V. P., Cengiz I. F., Canadas R. F., Costa J. B., **Vieira S.**, da Silva Morais A., Vilela C., García-Fernández L., Fernández-Gutierrez M., San-Román J., Oliveira J. M., and Reis R. L., *CHEM2NATURE Final Conference*, Porto, Portugal, 2018.

Awards:

- Príncipe da Beira Award for Biomedical Sciences, 2017;
- Promotion of cooperation between Galiza and Northern region of Portugal - IACOBUS Travel Grant – 2017;

- IACOBUS paper with “Self-mineralizing Ca-enriched Methacrylated Gellan Gum Beads for Bone Tissue Engineering”. Vieira S., Silva Morais A., Garet E., Silva-Correia J., Reis R.L., González-Fernández A., Oliveira J.M., Acta Biomaterialia, doi: 10.1016/j.actbio.2019.01.053;
- FCT individual PhD scholarship.

Training and Certificates:

- Laboratory Animal Science Course – FELASA (Federation for Laboratory Animal Science Associations) Category C;
- Radiologic Protection (2019).

INTRODUCTION TO THE THESIS STRUCTURE

The present thesis is divided into four main Sections that comprise ten Chapters. Except for Chapter III, and Chapter VII, each chapter is based on manuscripts that are either published or submitted in international peer-reviewed publications. Chapter VII refers to a filed international patent application, that was the basis of two granted patents at the European Patent Office and United States Patent and Trademark Office.

Following this structure, the reader will first start with a general introduction to hydrogels (Section 1), which is divided in two chapters (Chapter I and Chapter II). Section 2 is focused on the experimental design, with Chapter III bringing together the materials and methods used in the present work. Section 3, the main body of the thesis, compiles five distinct original scientific works, divided in five different chapters. In this section, each individual chapter is organized like a scientific manuscript, respecting the different subsections that typically exist in a scientific paper. A list of relevant references is also provided as a subsection within each chapter. The last section, Section 4, is an overall conclusion of the present work, as well as starting point for future studies, based on the findings described along the present thesis.

Briefly, this thesis can be outlined as follows:

Section 1: General Introduction

Chapter I: “Natural-Based Hydrogels - From Processing to Applications”. This first chapter provides an overview on the natural polymers commonly used for Tissue Engineering approaches, as well as the processing methods that can be applied to prepare hydrogels from such polymers.

Chapter II: “Engineering Hydrogels for Modulation of Material-Cell Interactions”. After the overview provided in Chapter I, the reader will find a deeper insight on hydrogels in Chapter II, with focus on cell-material interactions.

Section 2: Experimental Design

Chapter III: This chapter compiles the materials and methods used to perform the experimental work developed under the scope of this thesis.

Section 3: Experimental Part

Chapter IV: “Self-mineralizing Ca-enriched Methacrylated Gellan Gum Beads for Bone Tissue Engineering”. The first chapter of the experimental part of the present thesis explores the application of gellan gum as a calcium reservoir, with application in bone tissue engineering strategies.

Chapter V: “Mn-Based Methacrylated Gellan Gum Hydrogels for MRI-Guided Cell Delivery and Imaging”.

In this chapter the gellan gum properties are explored to prepare injectable hydrogels suitable for cell encapsulation and real time tracking, via magnetic resonance imaging.

Chapter VI: “Methacrylated Gellan Gum and Hyaluronic Acid Hydrogel Blends for Image-Guided Neuro interventions”. As follow-up of the previous chapter, Chapter VI studies the impact of the introduction of hyaluronic acid in gellan gum hydrogels, envisioning *in loco* cell delivery.

Chapter VII: “Composition Comprising Polyelectrolyte Complexes, Methods and Uses Thereof”. This chapter comprises the description, as filled, of an international patent application, relating to the preparation of polyelectrolyte complex hydrogels.

Chapter VIII: “Methacrylated Gellan Gum/Poly-L-lysine Polyelectrolyte Complex Beads for Cell-Based Therapies”. The last chapter of this section explores the patented technology of previous Chapter VII, envisioning cell encapsulation and immunoprotection.

Section 4: Concluding Remarks

Chapter IX: General Conclusions and Future Perspectives. The final chapter of this thesis summarizes the general conclusions of the present work and sets the ground for future work on the hydrogels' field, in particular regarding to gellan gum-based strategies.

“The noblest pleasure is the joy of understanding.”

Leonardo da Vinci

SECTION 1: General Introduction

Chapter I: Natural-Based Hydrogels - From Processing to Applications*

ABSTRACT

Natural-based hydrogels have been widely used for Tissue Engineering and Regenerative Medicine (TERM) as a platform to better mimic the native extracellular matrix of different tissues. Polysaccharides and proteins of natural origin have been functionalized, tuned, and processed using different methods to produce different scaffolds and medical devices. Herein, the recent reports dealing with the application of natural-based hydrogels in TERM strategies are overviewed. Moreover, different methodologies used to process the polymeric hydrogels are also described as well as the most relevant strategies used within the scope of TERM.

* This chapter is based on the following publication:

"Natural-Based Hydrogels: From Processing to Applications", Vieira S., Morais A., Silva-Correia J., Oliveira J. M., and Reis R. L., in *Encyclopedia of Polymer Science and Technology*, (Ed.), DOI: 10.1002/0471440264.pst652, 2017.

I.1 Introduction

Hydrogels are water swollen three-dimensional networks, formed by hydrophilic homopolymers or copolymers, that display numerous interesting properties for Tissue Engineering and Regenerative Medicine (TERM) [1]. The low interfacial tension between the hydrogels and the environmental fluids results in low protein adsorption rate and cell adhesion, making them highly biocompatible. Moreover, the soft and pliable nature of the gel reduces the mechanical irritation on the surrounding area, and provides a high degree of permeability to nutrients and metabolites [2].

Hydrogels formed from natural polymers display a structure close to the extracellular matrix (ECM) of human tissues, rendering these structures usually cell-friendly and more appealing from the medical point-of-view [3]. However, they can undergo batch-to-batch variability, which may affect the reproducibility of results. On the other hand, synthetic polymers have more controllable properties but often require the use of toxic solvents that can affect cell viability. Through the following sections, the reader will find information regarding the most used natural polymers on the scope of hydrogels development for application in TERM. For a better comprehension, the chapter is divided in two sections: (i) fundamentals on the natural polymers used to produce hydrogels, and (ii) hydrogels processing techniques.

I.2 Natural Polymers for Hydrogels: Structure and Function

Natural hydrogels have been broadly applied on TERM, mostly due to their inherent biocompatibility, low toxicity and susceptibility to enzymatic degradation [4, 5]. They are mainly produced from natural fibrous proteins or polysaccharides, resembling the ECM structure. As result, natural hydrogels display a structure close to the ECM of human tissues, able to provide chemical and biological cues that support cell responses.

In the next section the most common used hydrogels for TERM are discussed, as summarized in Table I-1.

Table I-1. Examples of natural polysaccharides and their relevant properties for TERM applications.

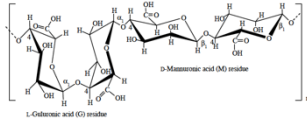
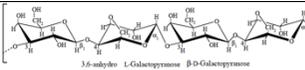
Polymer	Repeating unit	Source	Gelation method	Relevant properties of resulting hydrogel	Chemical modification Functionalization	Commercial Products	Processing Methods	Applications
Alginate		Brown seaweed and bacteria (Azotobacter and Pseudomonas).	Ionotropic	Mild gelation conditions with divalent ions; Suitable for <i>in situ</i> injectable applications.	Gamma irradiation and oxidation for size control [6]; Conjugation of cellular adhesion motifs (e.g. RGD peptide) [7].	NOVATACH™ (FMC, R&D); PRONOVA™ (FMC, R&D). Cartipatch® (Clinical studies [8])	Emulsion [9-11]; Extrusion [12, 13]; Bioprinting [14, 15]; Microfluidics [16]; Cryogelation [17-20].	Cartilage [21], bone [22, 23], cardiac [24] and intervertebral disk [25] TE; cell encapsulation [26]; drug reservoir [27].
Agarose		Red algae (Rhodophyceae).	Thermal	Thermally reversible gels with thermal hysteresis; Low protein adhesion; Transparency allows photo-modification	Conjugation with cellular adhesive motifs (e.g. RGD peptide, laminin derivatives) [28]; Addition of photosensitive motifs [29].	Cartipatch® (Clinical studies [8])	Photolithography [29]; Emulsion [30, 31]; Bioprinting [32]; Cryogelation [33, 34].	Cell encapsulation [1, 2, 35]; cartilage TE [36]; nerve regeneration [29].

Table I-1. Continued.

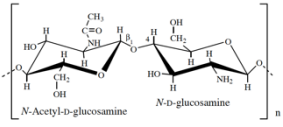
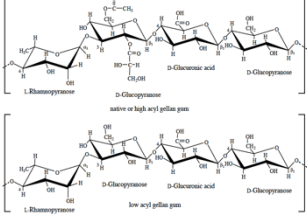
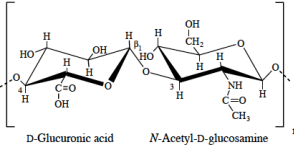
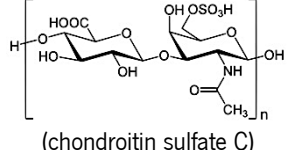
<p>Chitosan</p>	 <p>The diagram shows the repeating unit of chitosan, a linear polysaccharide. It consists of two pyranose rings linked by a beta-1,4-glycosidic bond. The left ring is N-Acetyl-D-glucosamine, with an acetyl group (-COCH₃) attached to the nitrogen at the C2 position. The right ring is N-D-glucosamine, with a free amino group (-NH₂) at the C2 position. The entire unit is enclosed in brackets with a subscript 'n'.</p>	<p>Animal (deacetylation of chitin from crustacean shells and insect exoskeletons).</p>	<p>Ionotropic</p>	<p>Cationic nature with nitrogen in its composition; Soluble in dilute acids; Chemical and physical crosslinking.</p>	<p>Addition of chemical crosslinkers (e.g. genipin) or photosensibile motifs by covalent bounds [37].</p>	<p>Reaxon® Nerve Guide (Medovent GmbH, clinic)</p>	<p>Photolithography [38]; Emulsion [39-42]; Microfluidic [43]; Cryogelation [44-47].</p>	<p>Injectable hydrogels [48]; cell and drug carrier [49, 50].</p>
<p>Gellan Gum</p>	 <p>The diagram shows two repeating units of gellan gum. The top structure is labeled 'native or high acyl gellan gum' and features a complex chain of four pyranose rings: L-thamnosamine, D-glucopyranose, D-glucosonic acid, and D-glucopyranose. The bottom structure is labeled 'low acyl gellan gum' and features a simpler chain of three pyranose rings: L-thamnosamine, D-glucopyranose, and D-glucopyranose. Both structures are enclosed in brackets with a subscript 'n'.</p>	<p>Bacteria (Sphingomonas elodea).</p>	<p>Thermal Ionotropic</p>	<p>Thermo-responsive polymer; Gelation in presence of divalent ions; Non-angiogenic when methacrylated;</p>	<p>Methacrylation [51]; Conjugation of cellular adhesion motifs (e.g. RGD peptide) [52, 53]. EDC crosslinking [54].</p>	<p>Mimsys G® (Irisbiosciences, R&D)</p>	<p>Photolithography [38]; Emulsion [55, 56]; Bioprinting [52].</p>	<p>Cartilage [51, 57-59], intervertebral disc [60], neural [52] and skin [54] TE; dental care [61]; gene delivery [62, 63].</p>

Table I-1. Continued.

<p>Hyaluronic Acid</p>	 <p>The diagram shows the repeating unit of Hyaluronic Acid, a disaccharide chain. It consists of a D-Glucuronic acid unit linked to an N-Acetyl-D-glucosamine unit. The D-Glucuronic acid unit is a six-membered ring with a carboxylic acid group at C5 and hydroxyl groups at C2, C3, and C6. The N-Acetyl-D-glucosamine unit is also a six-membered ring with an acetamido group at C2 and a hydroxyl group at C6. The units are linked via a beta-1,3-glycosidic bond between the C3 of the glucuronic acid and the C1 of the glucosamine. The entire unit is enclosed in brackets with a subscript 'n'.</p>	<p>Animal (skin, umbilical cord, synovial fluid and vitreous humor); microbial (recombinant production).</p>	<p>Thermal</p>	<p>Inherent biocompatibility; Biodegradable; Bioactivity and non-immunogenic nature; High viscoelasticity and space filling properties; Hydrophilic.</p>	<p>Methacrylate groups [64, 65]; EDC crosslinking [66, 67]; Crosslinking with derivatives of divinyl sulfone [68].</p>	<p>Synvisc-one® (Sanofi, clinic); Corgel® BioHydrogel (Lifecore, R&D).</p>	<p>Photolithography [69]; Emulsion [70, 71]; Bioprinting [72]; Cryogelation [73, 74].</p>	<p>Wound healing and cell adhesion barrier [75-77]; nerve [78-80], cartilage [81-84], bone [64, 85] and cardiac regeneration [86].</p>
<p>Chondroitin sulfate</p>	 <p>The diagram shows the repeating unit of Chondroitin sulfate, a disaccharide chain. It consists of a D-Galactose unit linked to a 2-Sulfamethyl-L-glucosamine unit. The D-Galactose unit is a six-membered ring with a carboxylic acid group at C5 and hydroxyl groups at C2, C3, and C6. The 2-Sulfamethyl-L-glucosamine unit is also a six-membered ring with a sulfamethyl group at C2 and a hydroxyl group at C6. The units are linked via a beta-1,3-glycosidic bond between the C3 of the galactose and the C1 of the glucosamine. The entire unit is enclosed in brackets with a subscript 'n'.</p> <p>(chondroitin sulfate C)</p>	<p>Animal (skin, cartilage, tendons and heart valves).</p>	<p>Photo after chemical modification</p>	<p>Biocompatible; Non-immunogenic; Enzymatically degraded by chondroitinase; Provides resistance to cartilage tissue.</p>	<p>Methacrylation [87]</p>	<p>Integra® Flowable Wound Matrix (Integra LifeScience, clinic).</p>	<p>Cryogelation [46]</p>	<p>Cartilage repair [88, 89]; Treatment of atherosclerosis [48]; Bioadhesive for biomaterial adhesion to tissues [90].</p>

I.2.1 Polysaccharides

I.2.1.1 Alginate

Alginate is an anionic polysaccharide, composed by a linear block copolymer of β -D-mannuronic (M) and α -L-guluronic acid (G) monomers, which can form homopolymeric (G/G and M/M) or heteropolymeric (G/M or M/G) structures (Table I-1). These moieties are present in variable ratios and sequences, depending on the source of alginate [91]. It is commonly extracted from brown seaweed [92] and two kinds of bacteria, *Azotobacter* and *Pseudomonas* [93].

The hardening process of alginate hydrogels occurs via ionic crosslinking, by addition of divalent ions (e.g. Ca^{2+} , Sr^{2+} or Ba^{2+}) to the sol phase. Although it was assumed that cations are more prone to bind to the G blocks, recent studies suggest that M/G blocks are also actively involved in the crosslinking process [1, 94]. The mechanical properties of alginate hydrogels are strongly influenced by the ratio of G and M blocks. Due to diaxial linking between residues, G blocks are stiffer than M or M/G blocks [95]. As a result, alginates rich in G blocks origins stronger gels in tension and compression tests [96]. The G/M ratio can also affect the pore size distribution of the hydrogel, since lower G/M ratios origin smaller pores. After gelation, the mechanical properties of the hydrogels, such viscosity and stiffness, mostly rely on polymer concentration and molecular weight distribution [97]. Gelling conditions also influence the hydrogel structure. For instance, it is known that Ca^{2+} ions diffuse slowly at low temperatures, resulting in a more ordered crosslinked polymer [96].

Likewise, G/M ratio influences the dissolution of alginate gels. The process occurs through the exchange of crosslinking ions with monovalent cations present in the surrounding environment. Although dissolution of the gel occurs, the polymer chains cannot be degraded by the biological activity of the host [1], since mammals do not have the enzyme that can degrade alginate. Despite enzymatic degradation is not feasible, some methods were developed to promote degradation. The application of gamma irradiation allows the control of the molecular weight distribution, by breaking the high molecular weight chains of alginate into smaller ones [6]. Partial oxidation of alginate with sodium periodate turns the chains more prone to degradation via hydrolysis, without changing its capacity to form gels [98, 99]. As a result, the polymer can be cleaned faster *in vivo* [100]. One of the drawbacks of alginate is that cells cannot adhere to it, since this polymer does not provide cell adhesion motifs. Cellular adhesion molecules, such as laminin [7], fibronectin or RGD (arginine-glycine-aspartic acid) peptides [101, 102], may be added conjugated with alginate in order to improve cell adhesion.

Due to their biocompatibility, non-immunogenicity and hydrophilic nature, alginate hydrogels are used for several TE purposes [103], including cartilage [21], bone [22, 23], cardiac [24], and intervertebral disk regeneration [25]. Within these areas of application, the hydrogels can be used for different purposes, which can vary from cell encapsulation [26] to encapsulation of therapeutic molecules for drug delivery purposes [27], and surgical dressings [104].

1.2.1.2 Agarose

Agarose is a neutral polysaccharide composed by two monomers, β -D-galactopyranosyl and 3,6-anhydro- α -L galactopyranosyl (Table I-1). This polymer is commonly extracted from the cell wall of a group of red algae (*Rhodophyceae*). It is a thermo-responsive polymer, exhibiting temperature-sensitive water solubility. As a result, agarose needs to be heated, in order to be miscible in water, and then cooled down below the gelling temperature. At this point, agarose structure changes from a random-coil configuration to a double helix [105], and the solution undergoes a sol-gel transition, forming a hydrogel. The gelling temperature can be tuned in function of agarose concentration, molecular weight and structure [1, 2]. The molecular weight of agarose also affects the critical concentration for gel formation, the elasticity of the polymer network and the strain at failure [106]. The sol-gel transition is reversible, with a significant difference between gelling and melting points (thermal hysteresis), mainly attributed to occurrence of helices aggregation [106].

Agarose does not provide cell adhesion motifs. As a result, it is necessary to conjugate the polymer with cell adhesion epitopes in order to allow the interaction between cells and the material [28]. The addition of photo-sensible motifs, as S-2-nitrobenzyl-cysteine, is used to allow a photo-modification of agarose hydrogels [29]. This approach is only possible because agarose hydrogels are optical transparent.

Agarose gels are generally well accepted by the human body once implanted, which makes this polymer a suitable material for cell encapsulation [1, 2, 35]. However, agarose is only degraded by some bacteria and not by mammals. Such fact difficult the application of agarose hydrogels on TE applications, since it requires the continuous degradation of scaffold materials for further substitution by new tissue. Nevertheless, some research groups are studying these hydrogels as a TE tool, namely for cartilage repair [8, 36], and nerve regeneration [29].

1.2.1.3 Chitosan

Chitosan is a linear polysaccharide, composed by β -(1-4)-linked D-glucosamine and N-acetyl-D-glucosamine units (Table I-1). It is obtained by partial deacetylation of chitin, a structural polymer of the

exoskeleton of crustaceans and insects. Most of the commercially available chitin is obtained from crabs and shrimp shells [37], which is then deacetylated using an alkaline treatment. When 60% of deacetylation (or more) is achieved, the polymer is named chitosan [107].

The gelation methods for chitosan can involve either physical associations or chemical crosslinking. When the network formation is driven only by physical interactions (non-covalent nature), the gelation can be reversed. Additionally, these gels are highly influenced by several parameters including pH, temperature and concentration. Thence, physical hydrogels are generally mechanically weak and present a short lifetime in physiological media, which can be advantageous for short-term drug release applications [37]. Physical gels also have a tunable gel swelling behavior, achieved by means of varying the nature and the concentration of each component and consequently, the number of interactions.

To obtain more robust chitosan hydrogels, one should consider the use of irreversible chemical crosslinkers that bind the polymeric chains via covalent bounds. Those bounds can be formed through the addition of small molecules (e.g. glutaraldehyde, genipin), secondary polymerizations or by attaching photo- or enzyme-sensitive molecules on chitosan, which then crosslink after exposure to UV or enzymes action [37].

Chitosan is a very distinct polysaccharide owing to: (i) its cationic nature, (ii) the presence of nitrogen in its molecular structure, (iii) biodegradability, and (iv) possibility of sterilization [37]. In acidic solutions, chitosan is soluble and positively charged. However, due to presence of intermolecular hydrogen bounds, chitosan is insoluble in water at neutral pH. These properties make chitosan a suitable hydrogel material for several biomedical applications, including injectable systems [48], drug delivery [49], and cell encapsulation [50].

1.2.1.4 Gellan Gum

Gellan gum (GG) is a biodegradable anionic heteropolysaccharide secreted by the bacteria *Sphingomonas elodea* [108]. Its molecular structure is based in one repeating unit consisting of 1,4- α -L-rahmnose, 1,3- β -D-glucose, 1,4- β -D-glucuronic acid and 1,4- β -D-glucose (Table I-1) [109-111]. The high acyl form, the native one, has two types of acyl substituents: acetyl and L-glyceryl [112]. They are located in the same glucose residue but while L-glyceryl is present, on average, once per repeat, acetyl appears once per two repeating units [113]. Low acyl GG is obtained through alkaline hydrolysis of native GG, where both of the acyl residues are removed [108].

GG is a thermo-responsive polymer. Therefore, at high temperatures, GG has a disordered coiled conformation. But as the temperature decreases, polymer chains start to fold into a double helix structure, acquiring a “gel-like” structure [112]. Nevertheless, in order to obtain stable hydrogels is necessary the presence of mono or divalent ions [114, 115].

The gel characteristics are highly influenced by the presence of acyl groups [116], particularly the L-glyceryl due to its dimensions and frequency in the polymer [113]. In high-acyl GG, the acyl residues are located on the periphery of the helix, obstructing the polymer chain association. Thus, packing is less effective, and the resulting gels are soft, elastic and non-brittle. In contrast, low-acyl GG produces firm, non-elastic and brittle gels since ions can easily link polymer chains and form a branched network. The number of acyl groups also affects the GG degradation kinetics. When placed in culture medium at 37 °C with 5% CO₂, the hydrogels made from high acyl GG degraded faster as compared to hydrogels of low-acyl GG [117]. Other gel properties like gelling temperature, gel strength and rate of gel formation depend on several factors of the prepared solution, such as pH value [118], type and concentration of ions on the hardening bath [119], and presence of sugars [120].

Several strategies have been developed for GG functionalization of GG [121, 122], to improve its physicochemical and biological functions, including mechanical properties [54], gelation time, solubility in water [51] and cell adhesion ability [52, 53]. Most of these strategies use the free carboxylic group to chemically modify GG. For instance, the addition of methacrylates makes the hydrogel photo-crosslinkable, improves its stability and turns the polymer soluble in water at 37 °C [51].

As a product, GG is approved for food, non-food, cosmetic and pharmaceutical use in numerous countries, including the United States and the European Union [123]. Applications of GG hydrogels and its derivatives for TE, namely for cartilage [51, 57-59], intervertebral disc [60], neural [52], and skin [54] TE applications, dental care [61], and gene delivery [62, 63] are also being studied [121].

1.2.1.5 Glycosaminoglycans

Glycosaminoglycans (GAGs) are long linear polysaccharides produced by animal cells. Their structure comprises repeating hexosamine-uronic or hexosamine-galactose disaccharides sulfated in variable degrees [124]. It is possible to distinguish two types of GAGs (i) non-sulfated GAGs, as hyaluronic acid (HA), and (ii) sulfated GAGs, like heparin and heparan sulfate, chondroitin sulfate (CS) and keratan sulfate. GAGs have a high structural heterogeneity caused by alterations in chain length, composition, and further modification by additional sulfation. GAGs chains, except HA ones, are usually covalently linked to a

protein core, forming proteoglycans monomers. Some of these monomers can further associate with a molecule of HA to form proteoglycan aggregates named hyalactins [125].

Due to their polyanionic nature, GAGs bind to divalent cations (e.g. Ca^{2+} and Na^{2+}) when in aqueous solution. This results in a high hydrodynamic volume and low compressibility that creates a size-selective barrier, where only small molecules can pass through.

GAGs are involved in many biological processes like function of several cytokines, chemokines, enzymes, growth factors, and adhesion molecules, which regulates processes like adhesion, migration, proliferation, and differentiation of different cell types [126].

Hyaluronic Acid

HA is a high molecular weight non-sulfated linear GAG, composed by repeating disaccharide units of D-glucuronic acid and N-acetylglucosamine, linked together via alternating β -1,4 and β -1,3 glycosidic bonds (Table I-1) [127]. The carboxylic groups present in glucuronic acid units render HA polyanionic at physiological pH. Furthermore, one of the faces of HA molecule is hydrophobic due to clusters of hydrogen atoms [128].

HA is present in all mammals and inside the organism appears in salt form as hyaluronate. It can be found in the ECM of many soft connective tissues (e.g. skin, umbilical cord, synovial fluid and vitreous humor), acting as a space filler, lubricant, and osmotic buffer in the native ECM [129, 130]. However, for biomedical purposes it is extracted from rooster comb, human umbilical cord or via bacterial fermentation, for large quantities [131, 132].

When in physiological solutions, HA expands, due to mutual repulsions between carboxyl groups, water is entrapped within the structure thus forming a hydrated network. At higher concentrations, HA chains form a porous meshwork with increased mutual repulsion between molecules that causes a swelling pressure. If an external pressure is applied, the meshwork will contract. But when the pressure is removed, the meshwork goes back to its original conformation [128]. It can acquire a new conformation if new restrictions are applied to counterweight the swelling pressure. This characteristic is responsible for the resilience and malleability of tissues [128]. HA is degraded by hyaluronidases (hyase) or reactive oxygen species into small oligosaccharides. Afterwards, these oligosaccharides are further degraded by D-glucuronidase and N-acetyl-hexosaminidase [133].

Before being used as hydrogel, HA needs to be chemically modified, since native HA is susceptible to degradation and has inferior mechanical properties [127]. HA can be crosslinked using, for instance, methacrylate groups [64, 65], 1-ethyl-3-(3-dimethylaminopropyl) carbodiimide hydrochloride (EDC) [66, 67] or divinyl sulfone derivatives [68]. The resulting hydrogels are less susceptible to enzymatic degradation and present more robust mechanical properties when compared to native HA. Also, HA do not favor cell adhesion, so only the incorporation of adhesion motifs allows the creation of a hydrogel that supports cell attachment and proliferation [134].

As a biomaterial, HA has been used for the fabrication of bioartificial matrices due to its inherent biocompatibility, biodegradability, and bioactivity along with non-immunogenic nature [127]. The high viscoelasticity and space filling properties makes HA a very attractive tool for several applications such as ophthalmic surgery, osteoarthritis treatment and cosmetic applications. Also, the hydrophilic nature of HA is a great advantage for applications that require minimal cellular adhesion, such as tissue adhesion barriers and wound healing [75-77]. HA hydrogels are also being studied for nerve [78-80], cartilage [81-84], bone [64, 85] or cardiac [86] regeneration.

Chondroitin Sulfate

CS is a sulfated GAG that consists of repetitive N-acetylgalactosamine (GalNAc) – glucuronic acid (GlcA) disaccharide units (Table I-1). The sulfation pattern is tissue-specific, but mainly occurs in the hydroxyl residues at position 4 and/or 6 of N-acetylgalactosamine or, less frequently, at position 2/3 of the glucuronic acid [124]. CS has been classified into four major types, depending on the sulfated locations: CS-A (GlcA-GalNAc-4-SO₄), CS-C (GlcA-GalNAc-6-SO₄), CS-D (GlcA-2-SO₄-GalNAc-6-SO₄) and CS-E (GlcA-GalNAc-4,6-diSO₄). The presence of sulfate groups on CS influences its mechanical properties. For instance, much of the resistance of cartilage to compression results from the electrostatic repulsion provided by those groups [48].

CS is found in many tissues like skin, cartilage, tendons and heart valves. It is a biocompatible, non-immunogenic and pliable polymer, very attractive for TE. Chemical modification of CS with methacrylate groups allows photopolymerization of CS hydrogels [87]. The properties of the hydrogel prepared by this method are dependent on the degree of methacrylate substitution as well as on the macromere concentration before polymerization. The resulting gels have a high swelling pressure, allowing the intake of water without compromising the mechanical properties of the hydrogel [135]. The degradation of CS

once inside the body is related to the action of chondroitinase, an enzyme produced by mammalian cells and specifically targets CS degradation.

CS has been used on cartilage repair [89, 136], for the treatment of atherosclerosis [48] or as a bioadhesive for biomaterial adhesion to tissues [90]. Although it is known that CS regulates the expression of the chondrocyte phenotype, the application of pure CS has a negative effect on chondrocyte bioactivity [88]. By using blends of CS with other polymers, such as collagen or synthetic polymers, the incorporation of this polymer has shown benefits for cartilage repair [137].

I.2.2 Proteins

I.2.2.1 Collagen

Collagen is the most abundant protein in the body and also the major insoluble protein of the ECM and connective tissue. Although approximately 16 different types of collagen are described, 80 to 90% of human body collagen comprises types I, II and III [138]. The structure of these collagen molecules is based on three polypeptide chains, entangled to form a rope structure with three strands. As a structural protein its main function is to provide mechanical integrity to different tissues and organs like tendons or bone.

Due to its abundance, collagen type I can be extracted from different tissues, mostly from bovine or porcine origin, like skin and ligaments, via enzymatic [139] or acidic treatments [140]. Marine sources for collagen extraction (as marine sponges, fish skins, and scales) are also being exploited as a sustainable alternative source [141-143]. Acid-solubilized collagen self-assembles to form a hydrogel when neutralized and heated. In such conditions, collagen aggregates in fibrils with the same cross-striated pattern of native collagen [144].

Its abundance, ubiquity and biocompatibility renders collagen type I fibers very popular for biomedical applications [145]. Collagen can be used in an unmodified form or coupled with chemical crosslinkers like glutaraldehyde, genipin or water-soluble carbodiimides [146, 147]. In mammals, unmodified collagen is easily biodegraded on the corresponding amino acids by collagenases and metalloproteases. On the other hand, crosslinked collagen has a slower degradation rate [148].

As referred, collagen is abundant on ECM of many tissues. It naturally contains cell adhesive motifs, like RGD, important for cell-matrix interactions. Collagen hydrogels have been used for cartilage repair [149-151], vocal cord regeneration [152, 153], spinal cord repair [154], and skin repair [155, 156] (Table

I-2). Due to physicochemical and mechanical properties of the hydrogel and its susceptibility to substantial shrinkage during cell culture, their potential applications in hard tissue engineering are hindered [157].

1.2.2.2 Silk Fibroin

Silks proteins are spun into fibers by silk producing arthropods, like spiders and silkworms. Silkworm silk [158], such as the derived from *Bombyx mori*, is usually preferred over the other natural sources of silk since it is commonly available and has a greater yield of fiber [159]. Two different proteins compose the silk fiber: a central filament of fibroin (70-80%), a structural protein; and sericin (20-30%), a water-soluble glue-like protein that wraps fibroin. Because silk-based biomaterials are produced with sericin-free silk, silkworm cocoons need to be boiled in an alkaline solution in order to remove sericin.

Fibroin from *B. mori* is composed by a heavy (MW 350 kDa) and a light (MW 25 kDa) chain, linked by disulfide bounds. When fibroin is spun by the silkworm, its primary structure, the amino acid sequence (Gly-Ser-Gly-Ala-Gly-Ala) $_n$, is arranged in β -sheet secondary structures, with interactions between the methyl and hydrogen groups of opposing sheets. This structure, named silk II, is stabilized by hydrogen bonds and van der Waals forces and is not soluble in water. To obtain a water-soluble material - silk I – silk II must be treated with concentrated solutions of chaotropic salts, such as lithium bromide (LiBr), as a way to break the strong hydrogen bonds. The salt is then removed by dialysis against distilled water and afterwards against polyethylene glycol, to increase protein concentration [160]. This silk solution is called “regenerated silk” and can be used to produce silk hydrogels.

Table I-2. Natural proteins and their relevant properties for TERM applications.

Polymer	Source	Gelation Method	Relevant properties of the hydrogels	Chemical Modification/Functionalization	Commercial Products	Processing Methods	Applications
Collagen	Animal (skin and ligaments, connective tissue). Marine Sources (marine sponges, fish skins, and scales)	Thermal/pH variation	Degraded by mammals by collagenases and metalloproteases; Naturally contains cell adhesive motifs; Possible shrinkage during cell culture.	Addition of motifs that allow chemical crosslinking (e.g. genipin) [147].	CaReS-1S® (Arthro-Kinetics, clinic); Integra® Flowable Wound Matrix (Integra LifeScience, clinic).	Emulsion [41, 161]; Bioprinting [32, 162]; Cryogelation [163-165].	Cartilage repair [149-151], vocal cord regeneration [152, 153] spinal cord repair [154] and skin repair [155, 156].
Silk fibroin	Animal (arthropods as <i>Bombyx mori</i>)	Mechanical stress, pH variation, enzymatically mediated.	Slow degradability; Good mechanical properties.	ECM molecules [166]; NeutrAvidin/biotin [167].	Pre-clinical [168]	Cryogelation [169-171]	Nervous system repair [172]; cartilage [173, 174] and bone [169, 175] TE.

Hydrogels are prepared through sol-gel transition of regenerated silk in the presence of acids, dehydrating agents, ions, enzymes, sonication or lyophilization. The sol-gel transition process is affected by different factors including mechanical stresses, protein concentration, temperature, pH and salt concentration in solution [176]. These hydrogels can be degraded by several serine proteases (eg.: proteinase K, protease XIV and collagenase) and matrix metalloproteinases (MMPs) [177]. The degradation rate is dependent on the β -sheet content and organization of the hydrogel. Silk fibroin hydrogels can be improved by their functionalization. For instance, it is possible to turn silk structures target-specific [167], using the biotin-avidin system; or more prone to cell adhesion [166], by addition of ECM molecules to the hydrogel.

Silk fibroin has been increasingly studied for biomedical purposes. Such interest is mostly due to its biocompatibility, slow degradability and mechanical properties. Silk fibroin hydrogels have been showing a great potential in TE approaches of different tissues, like nervous system [172], cartilage [173, 174], and bone [169, 175] (Table I-2). The hydrogels can be applied as injectable [178, 179] or non-injectable delivery systems; or cell encapsulation approaches [166], due to its gelation in mild conditions.

I.3 Processing Methods and Applications for TERM

The natural based hydrogels produced from the polymers described above can be processed under different ways to produce a wide range of structures, for numerous applications. Through this section, the reader will find a succinct description of the most interesting processing methods applied on TERM (depicted in Figure I-1) as well as their main applications.

I.3.1 Lithography

Lithography (in Greek: 'lithos' means stone; 'graphein' means to write), invented by Alois Senefelder in 1776, is a planographic printing procedure initially based on the use of a plate or stone with a smooth surface [180]. Nowadays, lithographic processing approaches, wherein hydrogel colloids modeling is highly controlled and reproducible, have arisen as an interesting alternative to current colloidal hydrogel synthesis procedures [181]. During the last years, several lithographic techniques have been established, among which lithography through controlled chemical design, photolithography, soft-lithography, stereolithography, scanning probe microscope (SPM) lithography as well as nanoimprint lithography [182]. Photolithography, or photopatterning, process is based on the exposure of a photo-crosslinkable polymer sensitive surface to UV light through the geometric contours of a mask [183]. This overcomes one of the limitations of hydrogels based on the general lack of spatial and temporal heterogeneity [184].

Photolithographic protocols have been applied for several biomedical applications since the development of different natural-based photo-crosslinkable hydrogels [38, 69, 185-189] used either to create 2D scaffold or 3D networks for cell growth or encapsulation [190-192]. The uniform encapsulation, low heat production as well as good temporal and spatial control of kinetics represent some of the benefits of photolithography systems [193]. As result, this technique has been widely used in TE to develop 3D scaffolds for culturing several cell types, *i.e.* hepatocytes [194], endothelial cells, fibroblasts, cardiac stem cells, C2C12 myoblasts [195, 196], hippocampal neurons [197], and mouse embryonic stem cells [198]. However, the technique has been shown some drawbacks [95, 199] and it is more suitable for synthetic polymers [200]. Although photolithography is useful and powerful; it is in fact not always the best appropriate technique for biological experiments. Therefore, soft lithography, applied to fabricate microstructures by using elastomeric molds [201], is used to solve most of the biological problems that request the application of microfabrication [202-204]. This method provides tools to create, with precise spatial control, cellular or acellular microscale hydrogels. Indeed, this process has demonstrated some limitations when using different chemically or ionically crosslinked hydrogel substrates, such as alginate or chitosan [205]. But it could be a suitable approach to create 3D systems to evaluate cellular interactions or for tissue engineering applications.

I.3.2 Emulsion

Emulsification is a widely used technique for fabricating micro- and nanoscale hydrogel particles/spheres. The emulsification process is achieved by agitation of a multi-phase mixture to obtain small droplets of hydrogel precursors within a hydrophobic medium, such as oil or organic solvent [95, 199]. The hydrogel precursor droplets, which are formed as result of mixing, can be crosslinked using different crosslinking mechanisms (e.g. temperature, pH and UV exposure) to produce spherical micro or nano-gels. By using emulsification technique, the size of the hydrogel droplets can be controlled by varying a number of experimental factors such as: i) mechanical agitation intensity, ii) viscosity of the hydrogel precursor, and iii) use of surfactants that can regulate the surface tension between the different phases, and also prevent aggregation of the resulting particles [183, 199]. The main advantage of emulsification is that it allows to generate micro- or nano-gels in a relatively simple and easy manner [199]. However, there are some limitations associated to this technique. Although the size of the originated particles is controlled by the process conditions, typically emulsification originates a wide particle size distribution when compared to other processing methods. Furthermore, the shape of the fabricated gels is generally limited to spheres. This process has been used to develop microgels from a wide range of natural and synthetic materials

including agarose [30, 31], alginate [9-11], chitosan [39, 41, 42], collagen [41, 161], hyaluronic acid [70, 71], gellan gum [55, 56] and gelatin [206, 207]. Microspheres made by emulsification have been applied as drug delivery systems, vehicles for cell encapsulation in *in vitro* culturing or as building blocks to assemble modular scaffolds [208] in a variety of tissue engineering applications. Also, spherical microgels obtained by emulsification are used for immunoisolation, *i.e.* to protect transplanted cells from a host immune reaction, while allowing exchange of oxygen/nutrients and cell metabolites between the hydrogel microenvironment and surrounding area [95]. Other applications being investigated for emulsified microgels are cartilage and bone regeneration [41, 209-211], vocal fold regeneration [70, 212] and mucoadhesive (nasal) delivery [40].



Figure I-1. Schematic representation of the processing methods considered for this chapter and representative resulting structures. Scanning electron microscopy (SEM) images for lithography (reprinted with permission from [205]. Copyright 2006 American Chemical Society) and cryogels (reprinted with permission from [164] Copyright 2015 Elsevier); optical microscope images for emulsion (reprinted with permission from [30] Copyright 2007 Elsevier), extrusion (reprinted with permission from [213] Copyright 2013 Wiley-VCH Verlag GmbH & Co. KGaA) and microfluidics (reprinted with permission from [214] Copyright 2013 Springer Nature); photograph of bioprinted structures (reprinted with permission from [14] Copyright 2015 IOP Publishing).

I.3.3 Extrusion

Spherical-based hydrogels are rather interesting for cell encapsulation. Their large surface area to volume ratio confers an advantage to the mass transport phenomena that occurs between the hydrogel borders [2]. Extrusion methods are commonly used to encapsulate cells within these spherical hydrogels. These methods can be divided into four techniques [1]: (i) dripping; (ii) coaxial air flow; (iii) vibrational break-up, and (iv) bioelectrospray.

The first is considered the easiest method to encapsulate cells. Briefly, it consists on the extrusion of a cell-laden hydrogel precursor, through a capillary, into a suitable hardening bath, using a liquid-air system [12]. A drop is formed on the tip of the tube until it reaches a critical mass. At this point, the drop detaches from the tip due to the influence of gravitational force. The final dimensions of the beads are commonly above 1 mm, and are strongly related with several parameters including the surface tension, the size of the tip, and the distance between the tip and the hardening bath [12].

Coaxial air-flow method is used when smaller beads are needed. In this technique the extruding droplet falls before reach the critical mass due to the action of compressed air throughout the tip of the extrusion tube [215]. The bead size can then be controlled by the gas flow, with higher flows resulting in smaller beads.

The vibrational encapsulator can also be used to obtain particles with lower size. This technique is based on the laminar jet break-up that occurs as a result of the presence of vibration in the extrusion nozzle, making mono-dispersed beads, with a diameter around 300 μm at a high production rate [13, 216].

At last, bioelectrospray is also used as a way to produce beads with small size. It is based on the application of an electrostatic potential between the hardening bath and the needle tip, generating an electrostatic stress on the liquid surface. When the surface tension is overtaken by this electrostatic stress, the excess of surface charge is expelled leading to the formation of a jet of drops [1].

As mentioned before, extrusion methods are widely used for cell encapsulation purposes. Islet cell encapsulation research, for instance, is highly based on these techniques [213, 217, 218]. Other areas of application include bone regeneration [219] and stem cell preservation and storage [220]. The encapsulation of embryonic stem cells in gel particles has also been used to develop more controllable environments for cell differentiation [221].

I.3.4 Bioprinting

Printing technology evolved from a two-dimensional (2D) perspective to three-dimensional (3D) approaches. It is also called additive manufacturing because it implies the formation of 3D structures using a bottom-up approach, with layer-by-layer deposition of materials. The advances in the field have allowed the application of this principle for TERM strategies, making possible the printing of cells and biocompatible materials into 3D structures. The rationale behind this application is to use these additive processes to obtain tissues and organs suitable for transplantation, surpassing the need of donors. For that, biological materials, living cells and biochemicals – the bioinks - are positioned in a controlled manner, using the layer-by layer approach, forming 3D tissue/organs [222].

Along the years, several different technologies have been developed and tuned for bioprinting. The most common methods are: (i) inkjet, (ii) micro-extrusion, and (iii) laser-assisted bioprinting. Each one of these methods has its drawbacks/limitations as listed in Figure I-2, that should be considered according with the biomaterial to be used, cell viability to be achieved and desired resolution.

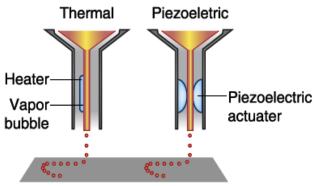
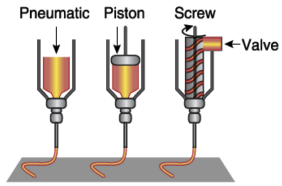
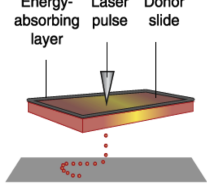
	Inkjet	Microextrusion	Laser assisted
Schematic representation			
Material viscosities	3.5 – 12 mPa/s	30 mPa/s to > 6x10 ⁷ mPa/s	1-300 mPa/s
Gelation method	Chemical Photo-crosslinking	Chemical Photo-crosslinking Shear thinning Temperature	Chemical Photo-crosslinking
Preparation time	Low	Low to medium	Medium to high
Print speed	Fast (1-10 000 droplets/s)	Slow (10-50 μm/s)	Medium-fast (200-1 600 mm/s)
Resolution	<1 pl to >300 pl, 50 μm wide	5 μm to millimeters wide	Microscale resolution
Cell viability	>85%	40-80%	>95%
Cell density	Low, <10 ⁶ cells/ml	High, cell spheroids	Medium, 10 ⁸ cells/ml
Printer cost	Low	Medium	High

Figure I-2. Comparison of bioprinter types regarding their components and characteristics. Adapted from [222] with permission from Macmillan Publishers Ltd: Nature Biotechnology, Copyright 2014.

Another key aspect to be considered when using a bioprinting approach is the material to be used. This can be very challenging, considering all the requirements that the materials should meet. As depicted in Figure I-3, the final performance of the construct depends on several properties of the biomaterial. Besides the requirements needed for any biomaterial used on TERM, as biocompatibility, suitable degradation rate and mechanical properties, they must have a proper viscosity, gelation methods/time and rheological properties, compatible with the bioprinter technology.



Figure I-3. Material properties for bioprinting applications.

One of the great advantages of bioprinting is the possibility to create customized structures in an automatic and precise way, using computer-aided design and computer aided manufacturing (CAD-CAM) [223]. Therefore, it is possible to produce customized and patient-specific structures, using a 3D reconstruction of their organs as template for the bioprinting process.

Although bioprinting is at its infancy, and with room for new technical approaches [14, 224], a considerable number of researchers started to use these techniques in their fields of expertise. For instance, Lozano *et al.* [52] used GG modified with the RGD peptide to produce brain-like structures with neural cells encapsulated within it. Strategies for bone [15, 32, 225, 226], cartilage [227-230] and osteochondral [72] regeneration; cancer research [231]; cardiovascular regeneration [232-234]; neural tissue regeneration [235]; skin [162]; and liver microtissues fabrication [236-238] are also being attempted.

I.3.5 Microfluidics

Microfluidics technology has been progressively used to several biological and tissue engineering applications. These microfluidics systems, which aimed to process and manipulate single or multi-phase flows within microchannels [239], have been applied in the fabrication of highly complex and dynamic functional microengineered constructs (e.g. microgels and microfibers) with high perfusion capacity and highly controllable, reproducible, and optimizable [240]. Usually, cells, in combination with the selected polymeric hydrogel precursor (synthetic or natural), are allowed to flow by means of those microchannels, which allow controlling the architecture of the hydrogel. Then, these cell-loaded microgels can be processed layer-by-layer on each other, recreating the 3D complexity of *ex vivo* tissues [241]. Furthermore, the microfluidics technology has also been used to create microgels in different shapes (*i.e.* spheres, disks, hemispheres, core-shell structures, Janus-like particles and fibers) [240]. Actually, microfluidic systems have been used for single cell analysis [242, 243], drug screening [244-246] and engineering tissue-like structures [16, 247].

Address the absence of a large blood vessels system to supply nutrients and oxygen to the surrounding tissues is one key challenge of the tissue engineering approach. Microfluidic hydrogels have demonstrated potential to create functional tissues with improved vascularization while allowing the control of cell behavior through microchannels delivery of chemical signals [248]. Different techniques can be used to engineer microgels [249-252]. For example, polyethylene glycol (PEG) and agarose hydrogels have been fabricated embedded with microchannels by a simple molding method, presenting enhanced mechanical stability [253]. Moreover, microfluidic cell-encapsulating agarose hydrogels and multilayered cell-collagen constructs have been engineered by soft lithography [254] and bioprinting [255] approaches respectively. Recently, the development of microfluidics-based devices, termed Organs-on-chips, aiming to mimic organ tissue *in vitro* have attracted great deal of attention [256]. For instance, microfluidic-based devices have been settled, based on natural polymers [257], for specific application in different organs among which the kidney (collagen) [258], liver (chitosan) [43], lung [259] and heart [247]. Because vascularization is critical for the persistence of engineered tissues *in vitro* and *in vivo*, several studies are focused on developing microfluidic models for angiogenesis in order to increase regenerate vascularized tissue constructs *in vitro* [240, 260-262]. Nevertheless, further development of hierarchically linked vascular complexes need to be established, knowing that one of the most important challenge is the *in vivo* integration of microfluidic networks in the host vascular network.

I.3.6 Cryogelation

The polymer cryogels, which the name is composed of two parts – 'cryo' from the Greek κρυος (cryos) meaning cold or ice, and 'gel' meaning a colloid semisoft material [263], represent an embryonic class of biomaterials that has recently started drawing interest as potential tissue scaffolds for *in vitro* cell culture and regenerative medicine. These macro-porous hydrogels presented an inherent interconnected open macro-porous structure [264]. The cryogels preparation process, called cryogelation, is a simple and easily reproducible method of introducing pores into hydrogels. During this procedure, the crosslinking reactions arise at a temperature below the freezing point of the solvent, generating an apparently frozen structure based on solvent crystals and unfrozen liquid microchannels. The formed crystals generate a highly interconnected porous structure corresponding to the pores after melting [265-267]. The physical properties and characterization of the cryogels in terms of porosity, mechanical strength, stability and non-specific interactions, have been well defined and demonstrated that these cryo-structures presented high flexibility, fast alterable conversion in 3D microstructures in response to external factors, and outstanding swell ability in aqueous media. That results in adequate cellular migration, ingrowth, and can be further used as a regenerative model in tissue engineering [268-270]. Actually, natural polymers such as agarose [33, 34], alginate [17-20], chitosan [44, 45, 47], hyaluronic acid [73, 74], chondroitin sulfate [46], silk fibroin [169, 170], and collagen [163, 164] have been used alone or in combination to form stable physical cryogels. The potential application of these cryo-structures in regenerative medicine has been suggested for brain [271, 272], liver [171, 273], bone [165, 274], and cartilage [46, 275-277] tissue engineering and has delivery systems [46, 278].

I.4 Final Remarks and Future Directions

Several polymeric materials show great promise when processed as hydrogels in a wide range of TERM applications. The relevance of natural-based hydrogels became clearer when appropriate blending/chemical modifications, and wide range of processing methods, are carried out to overcome the biofunctional and architectural limitations of native polymers that are used to produce the hydrogels. These include poor mechanical strength, biodegradation rate, porosity, permeability to solutes and nutrients, a reduced temperature window for viable cell encapsulation/homogenous cell dispersion and poor biological performance (e.g. poor cell adhesion and bioadhesive properties). Among all natural-origin hydrogels that have been reported, it is now evident that the recently reported gellan gum and enzymatically crosslinked silk fibroin hydrogels show great promise due to their rapid gelation, injection

ability, stimuli-responsiveness, biodegradability, and excellent compatibility *in vitro* and *in vivo*. In particular, their application for the encapsulation of cells and drug delivery when using automated and reproducible processing methods (e.g. rapid prototyping) will allow new ways to be opened for the personalized treatment of metabolic and musculoskeletal diseases, and cancer, in a near future.

I.5 References

1. Gasperini, L., J.F. Mano, and R.L. Reis, *Natural polymers for the microencapsulation of cells*. Journal of The Royal Society Interface, 2014. **11**: p. 20140817-20140817.
2. Uludag, H., P. De Vos, and P.A. Tresco, *Technology of mammalian cell encapsulation*. Advanced Drug Delivery Reviews, 2000. **42**(1-2): p. 29-64.
3. Santos, E., et al., *Biomaterials in cell microencapsulation*. Advances in Experimental Medicine and Biology, 2010. **670**: p. 5-21.
4. Hunt, J.a., et al., *Hydrogels for tissue engineering and regenerative medicine*. Journal of Materials Chemistry B, 2014. **2**(33): p. 5319-5319.
5. Mano, J.F., et al., *Natural origin biodegradable systems in tissue engineering and regenerative medicine: present status and some moving trends*. Journal of the Royal Society, Interface, 2007. **4**: p. 999-1030.
6. Lee, D.W., et al., *Effect of γ -Irradiation on Degradation of Alginate*. Journal of Agricultural and Food Chemistry, 2003. **51**(16): p. 4819-4823.
7. Dhoot, N.O., et al., *Peptide-modified alginate surfaces as a growth permissive substrate for neurite outgrowth*. Journal of Biomedical Materials Research Part A, 2004. **71A**(2): p. 191-200.
8. Clavé, A., et al., *Third-generation autologous chondrocyte implantation versus mosaicplasty for knee cartilage injury: 2-year randomized trial*. Journal of Orthopaedic Research, 2016. **34**(4): p. 658-665.
9. Zekorn, T., et al., *Alginate coating of islets of Langerhans: in vitro studies on a new method for microencapsulation for immuno-isolated transplantation*. Acta Diabetologica, 1992. **29**(1): p. 41-45.
10. Poncelet, D., *Production of Alginate Beads by Emulsification/Internal Gelation*. Annals of the New York Academy of Sciences, 2001. **944**(1): p. 74-82.
11. Chan, L.W., H.Y. Lee, and P.W.S. Heng, *Production of alginate microspheres by internal gelation using an emulsification method*. International Journal of Pharmaceutics, 2002. **242**(1): p. 259-262.
12. Lee, B.B., P. Ravindra, and E.S. Chan, *Size and Shape of Calcium Alginate Beads Produced by Extrusion Dripping*. Chemical Engineering & Technology, 2013. **36**(10): p. 1627-1642.

13. Mazzitelli, S., et al., *Production and Characterization of Alginate Microcapsules Produced by a Vibrational Encapsulation Device*. Journal of Biomaterials Applications, 2008. **23**(2): p. 123-145.
14. Tabriz, A.G., et al., *Three-dimensional bioprinting of complex cell laden alginate hydrogel structures*. Biofabrication, 2015. **7**(4): p. 045012-045012.
15. Leite, Á.J., et al., *Bioplotting of a bioactive alginate dialdehyde-gelatin composite hydrogel containing bioactive glass nanoparticles*. Biofabrication, 2016. **8**(3): p. 035005-035005.
16. Leng, L., et al., *Mosaic hydrogels: One-step formation of multiscale soft materials*. Advanced Materials, 2012. **24**(27): p. 3650-3658.
17. Singh, D., et al., *Engineering three-dimensional macroporous hydroxyethyl methacrylate-alginate-gelatin cryogel for growth and proliferation of lung epithelial cells*. Journal of Biomaterials Science, Polymer Edition, 2013. **24**(11): p. 1343-1359.
18. Bencherif, S.a., et al., *Injectable preformed scaffolds with shape-memory properties*. Proceedings of the National Academy of Sciences of the United States of America, 2012. **109**(48): p. 19590-5.
19. Katsen-Globa, A., et al., *Towards ready-to-use 3-D scaffolds for regenerative medicine: Adhesion-based cryopreservation of human mesenchymal stem cells attached and spread within alginate-gelatin cryogel scaffolds*. Journal of Materials Science: Materials in Medicine, 2014. **25**(3): p. 857-871.
20. Tripathi, A. and A. Kumar, *Multi-Featured Macroporous Agarose-Alginate Cryogel: Synthesis and Characterization for Bioengineering Applications*. Macromolecular Bioscience, 2011. **11**(1): p. 22-35.
21. Pleumeekers, M.M., et al., *The in vitro and in vivo capacity of culture-expanded human cells from several sources encapsulated in alginate to form cartilage*. European Cells and Materials, 2014. **27**: p. 264-280.
22. Krishnan, L., et al., *Hydrogel-based Delivery of rhBMP-2 Improves Healing of Large Bone Defects Compared With Autograft*. Clinical Orthopaedics and Related Research®, 2015. **473**(9): p. 2885-2897.
23. Simmons, C.A., et al., *Dual growth factor delivery and controlled scaffold degradation enhance in vivo bone formation by transplanted bone marrow stromal cells*. Bone, 2004. **35**(2): p. 562-9.
24. Ruvinov, E. and S. Cohen, *Alginate biomaterial for the treatment of myocardial infarction: Progress, translational strategies, and clinical outlook*. Advanced Drug Delivery Reviews, 2016. **96**: p. 54-76.
25. Naqvi, S.M. and C.T. Buckley, *Differential Response of Encapsulated Nucleus Pulposus and Bone Marrow Stem Cells in Isolation and Coculture in Alginate and Chitosan Hydrogels*. Tissue Engineering Part A, 2015. **21**(1-2): p. 288-299.

26. Balyura, M., et al., *Transplantation of bovine adrenocortical cells encapsulated in alginate*. Proceedings of the National Academy of Sciences, 2015. **112**(8): p. 2527-2532.
27. Ma, Y. and A.G.A. Coombes, *Designing colon-specific delivery systems for anticancer drug-loaded nanoparticles: An evaluation of alginate carriers*. Journal of Biomedical Materials Research Part A, 2014. **102**(9): p. 3167-3176.
28. Connelly, J.T., et al., *Fibronectin- and collagen-mimetic ligands regulate bone marrow stromal cell chondrogenesis in three-dimensional hydrogels*. European Cells and Materials, 2011. **22**: p. 168-77.
29. Luo, Y. and M.S. Shoichet, *A photolabile hydrogel for guided three-dimensional cell growth and migration*. Nature Materials, 2004. **3**(4): p. 249-253.
30. Zhou, Q.-Z., et al., *Preparation of uniform-sized agarose beads by microporous membrane emulsification technique*. Journal of Colloid and Interface Science, 2007. **311**(1): p. 118-127.
31. Mu, Y., A. Lyddiatt, and A.W. Pacek, *Manufacture by water/oil emulsification of porous agarose beads: Effect of processing conditions on mean particle size, size distribution and mechanical properties*. Chemical Engineering and Processing: Process Intensification, 2005. **44**(10): p. 1157-1166.
32. Duarte Campos, D.F., et al., *Bioprinting Organotypic Hydrogels with Improved Mesenchymal Stem Cell Remodeling and Mineralization Properties for Bone Tissue Engineering*. Advanced Healthcare Materials, 2016. **5**(11): p. 1336-1345.
33. Evtyugin, V.G., et al., *Sorption of microorganisms by wide-porous agarose cryogels containing grafted aliphatic chains of different length*. Microbiology, 2009. **78**(5): p. 603-608.
34. Eichhorn, T., et al., *Macroporous composite cryogels with embedded polystyrene divinylbenzene microparticles for the adsorption of toxic metabolites from blood*. Journal of Chemistry, 2013. **2013**: p. 1-8.
35. Luan, N.M. and H. Iwata, *Xenotransplantation of islets enclosed in agarose microcapsule carrying soluble complement receptor 1*. Biomaterials, 2012. **33**(32): p. 8075-8081.
36. Mesallati, T., C.T. Buckley, and D.J. Kelly, *Engineering cartilaginous grafts using chondrocyte-laden hydrogels supported by a superficial layer of stem cells*. Journal of Tissue Engineering and Regenerative Medicine, 2017. **11**(5): p. 1343-1353.
37. Bhattarai, N., J. Gunn, and M. Zhang, *Chitosan-based hydrogels for controlled, localized drug delivery*. Advanced Drug Delivery Reviews, 2010. **62**(1): p. 83-99.
38. Coutinho, D.F., et al., *Microfabricated photocrosslinkable polyelectrolyte-complex of chitosan and methacrylated gellan gum*. Journal of Materials Chemistry, 2012. **22**: p. 17262.
39. Klinkesorn, U., *The Role of Chitosan in Emulsion Formation and Stabilization*. Food Reviews International, 2013. **29**(4): p. 371-393.

40. Patil, S.B. and K.K. Sawant, *Chitosan microspheres as a delivery system for nasal insufflation*. Colloids and Surfaces B: Biointerfaces, 2011. **84**(2): p. 384-389.
41. Wang, L., R.R. Rao, and J.P. Stegemann, *Delivery of Mesenchymal Stem Cells in Chitosan/Collagen Microbeads for Orthopedic Tissue Repair*. Cells Tissues Organs, 2013. **197**(5): p. 333-343.
42. Wang, L.-Y., G.-H. Ma, and Z.-G. Su, *Preparation of uniform sized chitosan microspheres by membrane emulsification technique and application as a carrier of protein drug*. Journal of Controlled Release, 2005. **106**(1): p. 62-75.
43. Lee, K.H., et al., *Microfluidic synthesis of pure chitosan microfibers for bio-artificial liver chip*. Lab on a Chip, 2010. **10**(10): p. 1328-1334.
44. Berillo, D., B. Mattiasson, and H. Kirsebom, *Cryogelation of chitosan using noble-metal ions: In situ formation of nanoparticles*. Biomacromolecules, 2014. **15**(6): p. 2246-2255.
45. Bhat, S. and A. Kumar, *Cell proliferation on three-dimensional chitosan-agarose-gelatin cryogel scaffolds for tissue engineering applications*. Journal of Bioscience and Bioengineering, 2012. **114**(6): p. 663-670.
46. Dwivedi, P., et al., *Study of Different Delivery Modes of Chondroitin Sulfate Using Microspheres and Cryogel Scaffold for Application in Cartilage Tissue Engineering*. International Journal of Polymeric Materials and Polymeric Biomaterials, 2014. **63**(16): p. 859-872.
47. Hedström, M., et al., *Monolithic macroporous albumin/chitosan cryogel structure: A new matrix for enzyme immobilization*. Analytical and Bioanalytical Chemistry, 2008. **390**(3): p. 907-912.
48. Li, Y., J. Rodrigues, and H. Tomás, *Injectable and biodegradable hydrogels: gelation, biodegradation and biomedical applications*. Chemical Society Reviews, 2012. **41**(6): p. 2193-2221.
49. Bernkop-Schnürch, A. and S. Dünnhaupt, *Chitosan-based drug delivery systems*. European Journal of Pharmaceutics and Biopharmaceutics, 2012. **81**(3): p. 463-9.
50. Custódio, C.A., et al., *Cell selective chitosan microparticles as injectable cell carriers for tissue regeneration*. Biomaterials, 2015. **43**: p. 23-31.
51. Silva-Correia, J., et al., *Gellan gum-based hydrogels for intervertebral disc tissue-engineering applications*. Journal of Tissue Engineering and Regenerative Medicine, 2011. **5**(6): p. e97-107.
52. Lozano, R., et al., *3D printing of layered brain-like structures using peptide modified gellan gum substrates*. Biomaterials, 2015. **67**: p. 264-273.
53. Ferris, C.J.J., et al., *Peptide modification of purified gellan gum*. Journal of Materials Chemistry B, 2015. **3**(6): p. 1106-1115.
54. Lee, M.-W., H.-J. Chen, and S.-W. Tsao, *Preparation, characterization and biological properties of Gellan gum films with 1-ethyl-3-(3-dimethylaminopropyl)carbodiimide cross-linker*. Carbohydrate Polymers, 2010. **82**(3): p. 920-926.

55. Hafezi, F., et al., *Transplantation of nano-bioglass/gelatin scaffold in a non-autogenous setting for bone regeneration in a rabbit ulna*. Journal of Materials Science: Materials in Medicine, 2012. **23**(11): p. 2783-92.
56. Moslemy, P., S.R. Guiot, and R.J. Neufeld, *Production of size-controlled gellan gum microbeads encapsulating gasoline-degrading bacteria*. Enzyme and Microbial Technology, 2002. **30**(1): p. 10-18.
57. Oliveira, J.T., et al., *Gellan gum: a new biomaterial for cartilage tissue engineering applications*. Journal of Biomedical Materials Research. Part A, 2009. **93**(3): p. 852-63.
58. Oliveira, J.T., et al., *Performance of new gellan gum hydrogels combined with human articular chondrocytes for cartilage regeneration when subcutaneously implanted in nude mice*. Journal of Tissue Engineering and Regenerative Medicine, 2009. **3**(7): p. 493-500.
59. Silva-Correia, J., et al., *Angiogenic potential of gellan-gum-based hydrogels for application in nucleus pulposus regeneration: in vivo study*. Tissue Engineering. Part A, 2012. **18**(11-12): p. 1203-12.
60. Pina, S., J.M. Oliveira, and R.L. Reis, *Natural-Based Nanocomposites for Bone Tissue Engineering and Regenerative Medicine: A Review*. Advanced Materials, 2015. **27**(7): p. 1143-1169.
61. Chang, S.J., et al., *In vitro properties of gellan gum sponge as the dental filling to maintain alveolar space*. Carbohydrate Polymers, 2012. **88**(2): p. 684-689.
62. Goyal, R., et al., *Gellan gum-PEI nanocomposites as efficient gene delivery agents*. Journal of Biomedical Nanotechnology, 2011. **7**(1): p. 38-9.
63. Goyal, R., et al., *Gellan gum blended PEI nanocomposites as gene delivery agents: evidences from in vitro and in vivo studies*. European Journal of Pharmaceutics and Biopharmaceutics, 2011. **79**(1): p. 3-14.
64. Bae, M.S., et al., *Photo-cured hyaluronic acid-based hydrogels containing growth and differentiation factor 5 (GDF-5) for bone tissue regeneration*. Bone, 2014. **59**: p. 189-98.
65. Kim, D.H., et al., *Phenotypic stability, matrix elaboration and functional maturation of nucleus pulposus cells encapsulated in photocrosslinkable hyaluronic acid hydrogels*. Acta Biomaterialia, 2015. **12**: p. 21-9.
66. Collins, M.N. and C. Birkinshaw, *Hyaluronic acid based scaffolds for tissue engineering—a review*. Carbohydrate Polymers, 2013. **92**(2): p. 1262-79.
67. Collins, M.N. and C. Birkinshaw, *Investigation of the swelling behavior of crosslinked hyaluronic acid films and hydrogels produced using homogeneous reactions*. Journal of Applied Polymer Science, 2008. **109**(2): p. 923-931.
68. Hahn, S.K., et al., *Anti-inflammatory drug delivery from hyaluronic acid hydrogels*. Journal of Biomaterials Science Polymer Edition, 2004. **15**(9): p. 1111-1119.

69. Gramlich, W.M., I.L. Kim, and J.A. Burdick, *Synthesis and orthogonal photopatterning of hyaluronic acid hydrogels with thiol-norbornene chemistry*. *Biomaterials*, 2013. **34**(38): p. 9803-11.
70. Jia, X., et al., *Hyaluronic Acid-Based Microgels and Microgel Networks for Vocal Fold Regeneration*. *Biomacromolecules*, 2006. **7**(12): p. 3336-3344.
71. Lim, S.T., et al., *Preparation and evaluation of the in vitro drug release properties and mucoadhesion of novel microspheres of hyaluronic acid and chitosan*. *Journal of Controlled Release*, 2000. **66**(2): p. 281-292.
72. Shim, J.-H., et al., *Three-dimensional bioprinting of multilayered constructs containing human mesenchymal stromal cells for osteochondral tissue regeneration in the rabbit knee joint*. *Biofabrication*, 2016. **8**(1): p. 014102-014102.
73. Owen, S.C., et al., *Hyaluronic acid click hydrogels emulate the extracellular matrix*. *Langmuir*, 2013. **29**(24): p. 7393-7400.
74. Ström, A., A. Larsson, and O. Okay, *Preparation and physical properties of hyaluronic acid-based cryogels*. *Journal of Applied Polymer Science*, 2015. **132**(29): p. n/a-n/a.
75. Kim, Y.-M., et al., *Adipose-derived stem cell-containing hyaluronic acid/alginate hydrogel improves vocal fold wound healing*. *The Laryngoscope*, 2014. **124**(3): p. E64-E72.
76. Li, L., et al., *Biodegradable and injectable in situ cross-linking chitosan-hyaluronic acid based hydrogels for postoperative adhesion prevention*. *Biomaterials*, 2014. **35**(12): p. 3903-17.
77. Na, S.Y., et al., *Hyaluronic acid/mildly crosslinked alginate hydrogel as an injectable tissue adhesion barrier*. *Journal of Materials Science: Materials in Medicine*, 2012. **23**(9): p. 2303-2313.
78. Schizas, N., et al., *Hyaluronic acid-based hydrogel enhances neuronal survival in spinal cord slice cultures from postnatal mice*. *Journal of Biomaterials Applications*, 2014. **28**(6): p. 825-836.
79. Führmann, T., et al., *Click-crosslinked injectable hyaluronic acid hydrogel is safe and biocompatible in the intrathecal space for ultimate use in regenerative strategies of the injured spinal cord*. *Methods*, 2015. **84**: p. 60-69.
80. Moshayedi, P. and S.T. Carmichael, *Hyaluronan, neural stem cells and tissue reconstruction after acute ischemic stroke*. *Biomatter*, 2013. **3**(1): p. e23863-e23863.
81. Ha, C.W., et al., *Cartilage Repair Using Composites of Human Umbilical Cord Blood-Derived Mesenchymal Stem Cells and Hyaluronic Acid Hydrogel in a Minipig Model*. *Stem Cells Translational Medicine*, 2015. **4**(9): p. 1044-1051.
82. Yu, Y., et al., *Use of Recombinant Human Stromal Cell-Derived Factor 1 α -Loaded Fibrin/Hyaluronic Acid Hydrogel Networks to Achieve Functional Repair of Full-Thickness Bovine Articular Cartilage Via Homing of Chondrogenic Progenitor Cells*. *Arthritis & Rheumatology*, 2015. **67**(5): p. 1274-1285.

83. Toh, W.S., et al., *Modulation of mesenchymal stem cell chondrogenesis in a tunable hyaluronic acid hydrogel microenvironment*. *Biomaterials*, 2012. **33**(15): p. 3835-3845.
84. Kim, I.L., R.L. Mauck, and J.A. Burdick, *Hydrogel design for cartilage tissue engineering: A case study with hyaluronic acid*. *Biomaterials*, 2011. **32**(34): p. 8771-8782.
85. Hulsart-Billström, G., et al., *Bisphosphonate-Linked Hyaluronic Acid Hydrogel Sequesters and Enzymatically Releases Active Bone Morphogenetic Protein-2 for Induction of Osteogenic Differentiation*. *Biomacromolecules*, 2013. **14**(9): p. 3055-3063.
86. Abdalla, S., et al., *Hyaluronic acid-based hydrogel induces neovascularization and improves cardiac function in a rat model of myocardial infarction*. *Interactive Cardiovascular and Thoracic Surgery*, 2013. **17**(5): p. 767-772.
87. Karumbaiah, L., et al., *Chondroitin Sulfate Glycosaminoglycan Hydrogels Create Endogenous Niches for Neural Stem Cells*. *Bioconjugate Chemistry*, 2015. **26**(12): p. 2336-2349.
88. Bryant, S.J., J.A. Arthur, and K.S. Anseth, *Incorporation of tissue-specific molecules alters chondrocyte metabolism and gene expression in photocrosslinked hydrogels*. *Acta Biomaterialia*, 2005. **1**(2): p. 243-252.
89. Varghese, S., et al., *Chondroitin sulfate based niches for chondrogenic differentiation of mesenchymal stem cells*. *Matrix Biology*, 2008. **27**(1): p. 12-21.
90. Wang, D.-A., et al., *Multifunctional chondroitin sulphate for cartilage tissue–biomaterial integration*. *Nature Materials*, 2007. **6**(5): p. 385-392.
91. de Vos, P., et al., *Polymers in cell encapsulation from an enveloped cell perspective*. *Advanced Drug Delivery Reviews*, 2014. **67-68**: p. 15-34.
92. Draget, K.I., O. Smidsrød, and G. Skjåk-Bræk, *Alginates from Algae*, E.J. Vandamme, S. De Baets, and A. Steinbüchel, Editors. 2005, Wiley-VCH Verlag GmbH & Co. KGaA: Weinheim, Germany.
93. Sabra, W., A.P. Zeng, and W.D. Deckwer, *Bacterial alginate: physiology, product quality and process aspects*. *Applied Microbiology and Biotechnology*, 2001. **56**(3-4): p. 315-25.
94. Donati, I., et al., *New hypothesis on the role of alternating sequences in calcium-alginate gels*. *Biomacromolecules*, 2005. **6**(2): p. 1031-1040.
95. Slaughter, B.V., et al., *Hydrogels in Regenerative Medicine*. *Advanced Materials*, 2009. **21**(32-33): p. 3307-3329.
96. Drury, J.L., R.G. Dennis, and D.J. Mooney, *The tensile properties of alginate hydrogels*. *Biomaterials*, 2004. **25**(16): p. 3187-99.
97. West, E., et al., *Physical properties of alginate hydrogels and their effects on in vitro follicle development*. *Biomaterials*, 2007. **28**(30): p. 4439-4448.

98. Bouhadir, K.H., et al., *Degradation of partially oxidized alginate and its potential application for tissue engineering*. Biotechnology Progress, 2001. **17**(5): p. 945-50.
99. Priddy, L.B., et al., *Oxidized alginate hydrogels for bone morphogenetic protein-2 delivery in long bone defects*. Acta Biomaterialia, 2014. **10**(10): p. 4390-9.
100. Kong, H.J., et al., *Controlling Rigidity and Degradation of Alginate Hydrogels via Molecular Weight Distribution*. Biomacromolecules, 2004. **5**(5): p. 1720-1727.
101. Taketa, H., et al., *Peptide-modified Substrate for Modulating Gland Tissue Growth and Morphology In Vitro*. Scientific Reports, 2015. **5**: p. 11468-11468.
102. Rowley, J.A., G. Madlambayan, and D.J. Mooney, *Alginate hydrogels as synthetic extracellular matrix materials*. Biomaterials, 1999. **20**(1): p. 45-53.
103. Bidarra, S.J., C.C. Barrias, and P.L. Granja, *Injectable alginate hydrogels for cell delivery in tissue engineering*. Acta Biomaterialia, 2014. **10**(4): p. 1646-62.
104. Poor, A.E., et al., *Control of Multi-Drug-Resistant Pathogens with Non-Thermal-Plasma-Treated Alginate Wound Dressing*. Surgical Infections, 2014. **15**(3): p. 233-243.
105. Lahaye, M. and C. Rochas, *Chemical structure and physico-chemical properties of agar*. Hydrobiologia, 1991. **221**(1): p. 137-148.
106. Normand, V., et al., *New Insight into Agarose Gel Mechanical Properties*. Biomacromolecules, 2000. **1**(4): p. 730-738.
107. Croisier, F. and C. Jérôme, *Chitosan-based biomaterials for tissue engineering*. European Polymer Journal, 2013. **49**(4): p. 780-792.
108. Kang, K.S., et al., *Agar-like polysaccharide produced by a pseudomonas species: production and basic properties*. Applied and Environmental Microbiology, 1982. **43**(5): p. 1086-91.
109. Jansson, P.-E., B. Lindberg, and P.A. Sandford, *Structural studies of gellan gum, an extracellular polysaccharide elaborated by Pseudomonas elodea*. 1983. p. 135-139.
110. Milas, M., X. Shi, and M. Rinaudo, *On the physicochemical properties of gellan gum*. Biopolymers, 1990. **30**: p. 451-464.
111. O'Neill, M.A., R.R. Selvendran, and V.J. Morris, *Structure of the acidic extracellular gelling polysaccharide produced by Pseudomonas elodea*. 1983. p. 123-133.
112. Chandrasekaran, R., A. Radha, and V.G. Thailambal, *Roles of potassium ions, acetyl and L-glyceryl groups in native gellan double helix: An X-ray study*. Carbohydrate Research, 1992. **224**: p. 1-17.
113. Kuo, M.-S., A.J. Mort, and A. Dell, *Identification and location of l-glycerate, an unusual acyl substituent in gellan gum*. Carbohydrate Research, 1986. **156**(0): p. 173-187.

114. Shimazaki, T., et al., *Influence of Ca²⁺-ion upon viscoelastic properties of gellan gum aqueous solutions*. Polymer Gels and Networks, 1995. **3**(3): p. 295-309.
115. Tang, J., M.A. Tung, and Y. Zeng, *Gelling properties of gellan solutions containing monovalent and divalent cations*. Journal of Food Science, 1997. **62**: p. 688-&.
116. Morris, E.R., K. Nishinari, and M. Rinaudo, *Gelation of gellan – A review*. Food Hydrocolloids, 2012. **28**: p. 373-411.
117. Lee, H., et al., *Optimizing gelling parameters of gellan gum for fibrocartilage tissue engineering*. Journal of Biomedical Materials Research Part B: Applied Biomaterials, 2011. **98B**(2): p. 238-245.
118. Picone, C.S.F. and R.L. Cunha, *Influence of pH on formation and properties of gellan gels*. Carbohydrate Polymers, 2011. **84**: p. 662-668.
119. Dai, L., X. Liu, and Z. Tong, *Critical behavior at sol–gel transition in gellan gum aqueous solutions with KCl and CaCl₂ of different concentrations*. Carbohydrate Polymers, 2010. **81**(2): p. 207-212.
120. Evageliou, V., et al., *Compression of gellan gels. Part II: Effect of sugars*. Food Hydrocolloids, 2010. **24**(4): p. 392-397.
121. Stevens, L.R., et al., *Tissue engineering with gellan gum*. Biomaterials Science, 2016. **4**(9): p. 1276-1290.
122. Bacelar, A.H., et al., *Recent progress in gellan gum hydrogels provided by functionalization strategies*. Journal of Materials Chemistry B, 2016. **4**(37): p. 6164-6174.
123. Dhar, S., et al., *Natural Gum Reduced/Stabilized Gold Nanoparticles for Drug Delivery Formulations*. Chemistry – A European Journal, 2008. **14**(33): p. 10244-10250.
124. Salbach, J., et al., *Regenerative potential of glycosaminoglycans for skin and bone*. Journal of Molecular Medicine, 2012. **90**(6): p. 625-635.
125. Yamaguchi, Y., *Lecticans: organizers of the brain extracellular matrix*. Cellular and molecular life sciences : CMLS, 2000. **57**(2): p. 276-289.
126. Gandhi, N.S. and R.L. Mancera, *The Structure of Glycosaminoglycans and their Interactions with Proteins*. Chemical Biology & Drug Design, 2008. **72**(6): p. 455-482.
127. Xu, X., et al., *Hyaluronic acid-based hydrogels: from a natural polysaccharide to complex networks*. Soft Matter, 2012. **8**(12): p. 3280-3280.
128. Toole, B.P., *Hyaluronan: from extracellular glue to pericellular cue*. Nature Reviews Cancer, 2004. **4**(7): p. 528-539.
129. Laurent, T.C., U.B.G. Laurent, and J.R.E. Fraser, *The structure and function of hyaluronan: An overview*. Immunology and Cell Biology, 1996. **74**(2): p. A1-A7.

130. Clegg, T.E., D. Caborn, and C. Mauffrey, *Viscosupplementation with hyaluronic acid in the treatment for cartilage lesions: a review of current evidence and future directions*. European Journal of Orthopaedic Surgery & Traumatology, 2013. **23**(2): p. 119-124.
131. Shiedlin, A., et al., *Evaluation of Hyaluronan from Different Sources: Streptococcus z ooepidemicus , Rooster Comb, Bovine Vitreous, and Human Umbilical Cord*. Biomacromolecules, 2004. **5**(6): p. 2122-2127.
132. Kogan, G., et al., *Hyaluronic acid: a natural biopolymer with a broad range of biomedical and industrial applications*. Biotechnology Letters, 2006. **29**(1): p. 17-25.
133. Rodén, L., et al., *Enzymic pathways of hyaluronan catabolism*. Ciba Foundation Symposium, 1989. **143**: p. 60-76; discussion 76-86, 281-285.
134. Park, Y.D., N. Tirelli, and J.A. Hubbell, *Photopolymerized hyaluronic acid-based hydrogels and interpenetrating networks*. Biomaterials, 2003. **24**(6): p. 893-900.
135. Nicodemus, G.D. and S.J. Bryant, *Cell Encapsulation in Biodegradable Hydrogels for Tissue Engineering Applications*. Tissue Engineering Part B: Reviews, 2008. **14**(2): p. 149-165.
136. Bryant, S.J., et al., *Synthesis and Characterization of Photopolymerized Multifunctional Hydrogels: Water-Soluble Poly(Vinyl Alcohol) and Chondroitin Sulfate Macromers for Chondrocyte Encapsulation*. Macromolecules, 2004. **37**(18): p. 6726-6733.
137. Balakrishnan, B. and R. Banerjee, *Biopolymer-Based Hydrogels for Cartilage Tissue Engineering*. Chemical Reviews, 2011. **111**(8): p. 4453-4474.
138. Lodish, H., et al., *Collagen: The Fibrous Proteins of the Matrix*, in *Molecular Cell Biology*. 2000, W. H. Freeman: New York, NY.
139. Wang, W., et al., *Enzymatic Extraction and Characteristics of Collagen Fibers from Cattle Skin*, T.-C. Zhang, et al., Editors. 2014, Springer Berlin Heidelberg. p. 1441-1448.
140. Rajan, N., et al., *Preparation of ready-to-use, storable and reconstituted type I collagen from rat tail tendon for tissue engineering applications*. Nature Protocols, 2007. **1**(6): p. 2753-2758.
141. Fernandes-Silva, S., et al., *Porous Hydrogels From Shark Skin Collagen Crosslinked Under Dense Carbon Dioxide Atmosphere*. Macromolecular Bioscience, 2013. **13**(11): p. 1621-1631.
142. Barros, A.A., et al., *Water and Carbon Dioxide: Green Solvents for the Extraction of Collagen/Gelatin from Marine Sponges*. ACS Sustainable Chemistry & Engineering, 2015. **3**(2): p. 254-260.
143. Silva, J.C., et al., *Extraction of Collagen/Gelatin from the Marine Demosponge Chondrosia reniformis (Nardo, 1847) Using Water Acidified with Carbon Dioxide – Process Optimization*. Industrial & Engineering Chemistry Research, 2016. **55**(25): p. 6922-6930.
144. Schmitt, F.O., C.E. Hall, and M.A. Jakus, *Electron microscope investigations of the structure of collagen*. Journal of Cellular and Comparative Physiology, 1942. **20**(1): p. 11-33.

145. Glowacki, J. and S. Mizuno, *Collagen scaffolds for tissue engineering*. Biopolymers, 2008. **89**(5): p. 338-344.
146. Nam, K., et al., *Preparation of a collagen/polymer hybrid gel for tissue membranes. Part II: in vitro and in vivo biological properties of the collagen gels*. Acta Biomaterialia, 2010. **6**(2): p. 409-17.
147. Chan, K.L.S., et al., *Crosslinking of collagen scaffolds promotes blood and lymphatic vascular stability*. Journal of Biomedical Materials Research. Part A, 2014. **102**(9): p. 3186-95.
148. Damink, L., *In vitro degradation of dermal sheep collagen cross-linked using a water-soluble carbodiimide*. Biomaterials, 1996. **17**(7): p. 679-684.
149. Zheng, L., et al., *In Vivo Cartilage Engineering with Collagen Hydrogel and Allogeneous Chondrocytes After Diffusion Chamber Implantation in Immunocompetent Host*. Tissue Engineering Part A, 2009. **15**(8): p. 2145-2153.
150. Yuan, T., et al., *Collagen hydrogel as an immunomodulatory scaffold in cartilage tissue engineering*. Journal of Biomedical Materials Research Part B: Applied Biomaterials, 2014. **102**(2): p. 337-344.
151. Zhang, L., et al., *An in vitro study of collagen hydrogel to induce the chondrogenic differentiation of mesenchymal stem cells*. Journal of Biomedical Materials Research Part A, 2012. **100A**(10): p. 2717-2725.
152. Park, H., et al., *Three-Dimensional Hydrogel Model Using Adipose-Derived Stem Cells for Vocal Fold Augmentation*. Tissue Engineering Part A, 2010. **16**(2): p. 535-543.
153. Hahn, M.S., et al., *Collagen composite hydrogels for vocal fold lamina propria restoration*. Biomaterials, 2006. **27**(7): p. 1104-1109.
154. Iwata, A., et al., *Long-term survival and outgrowth of mechanically engineered nervous tissue constructs implanted into spinal cord lesions*. Tissue Engineering, 2006. **12**(1): p. 101-110.
155. Helary, C., M. Zarka, and M.M. Giraud-Guille, *Fibroblasts within concentrated collagen hydrogels favour chronic skin wound healing*. Journal of Tissue Engineering and Regenerative Medicine, 2012. **6**(3): p. 225-237.
156. Wong, V.W., et al., *Engineered Pullulan–Collagen Composite Dermal Hydrogels Improve Early Cutaneous Wound Healing*. Tissue Engineering Part A, 2011. **17**(5-6): p. 631-644.
157. El-Fiqi, A., et al., *Collagen hydrogels incorporated with surface-aminated mesoporous nanobioactive glass: Improvement of physicochemical stability and mechanical properties is effective for hard tissue engineering*. Acta Biomaterialia, 2013. **9**(12): p. 9508-9521.
158. Fang, G., et al., *Exploration of the tight structural-mechanical relationship in mulberry and non-mulberry silkworm silks*. Journal of Materials Chemistry B, 2016. **4**(24): p. 4337-4347.
159. Kundu, B., et al., *Silk fibroin biomaterials for tissue regenerations*. Advanced Drug Delivery Reviews, 2013. **65**(4): p. 457-470.

160. Rockwood, D.N., et al., *Materials fabrication from Bombyx mori silk fibroin*. Nature Protocols, 2011. **6**(10): p. 1612-1631.
161. Santana, R.C., et al., *Emulsifying properties of collagen fibers: Effect of pH, protein concentration and homogenization pressure*. Food Hydrocolloids, 2011. **25**(4): p. 604-612.
162. Koch, L., et al., *Skin tissue generation by laser cell printing*. Biotechnology and Bioengineering, 2012. **109**(7): p. 1855-1863.
163. Lin, W., et al., *Collagen cryogel cross-linked by dialdehyde starch*. Macromolecular Materials and Engineering, 2010. **295**(2): p. 100-107.
164. Tan, H., et al., *Collagen cryogel cross-linked by naturally derived dialdehyde carboxymethyl cellulose*. Carbohydrate Polymers, 2015. **129**: p. 17-24.
165. Rodrigues, S.C., et al., *Preparation and characterization of collagen-nanohydroxyapatite biocomposite scaffolds by cryogelation method for bone tissue engineering applications*. Journal of Biomedical Materials Research - Part A, 2013. **101 A**(4): p. 1080-1094.
166. Davis, N.E., et al., *Enhanced function of pancreatic islets co-encapsulated with ECM proteins and mesenchymal stromal cells in a silk hydrogel*. Biomaterials, 2012. **33**(28): p. 6691-7.
167. Wang, X. and D.L. Kaplan, *Functionalization of Silk Fibroin with NeutrAvidin and Biotin*. Macromolecular Bioscience, 2011. **11**(1): p. 100-110.
168. Yan, L.P., et al., *Tumor Growth Suppression Induced by Biomimetic Silk Fibroin Hydrogels*. Scientific Reports, 2016. **6**: p. 31037.
169. Ak, F., et al., *Macroporous silk fibroin cryogels*. Biomacromolecules, 2013. **14**(3): p. 719-727.
170. Bhardwaj, N., S. Chakraborty, and S.C. Kundu, *Freeze-gelled silk fibroin protein scaffolds for potential applications in soft tissue engineering*. International Journal of Biological Macromolecules, 2011. **49**(3): p. 260-267.
171. Kundu, B. and S.C. Kundu, *Bio-inspired fabrication of fibroin cryogels from the muga silkworm Antheraea assamensis for liver tissue engineering*. Biomedical Materials (Bristol, England), 2013. **8**(5): p. 055003-055003.
172. Hopkins, A.M., et al., *Silk Hydrogels as Soft Substrates for Neural Tissue Engineering*. Advanced Functional Materials, 2013. **23**(41): p. 5140-5149.
173. Silva, S.S., et al., *Novel genipin-cross-linked chitosan/silk fibroin sponges for cartilage engineering strategies*. Biomacromolecules, 2008. **9**(10): p. 2764-2774.
174. Yodmuang, S., et al., *Silk microfiber-reinforced silk hydrogel composites for functional cartilage tissue repair*. Acta Biomaterialia, 2015. **11**: p. 27-36.
175. Jin, Y., et al., *Bio-inspired mineralization of hydroxyapatite in 3D silk fibroin hydrogel for bone tissue engineering*. Colloids and Surfaces. B, Biointerfaces, 2015. **134**: p. 339-345.

176. Matsumoto, A., et al., *Mechanisms of silk fibroin sol-gel transitions*. Journal of Physical Chemistry B, 2006. **110**(43): p. 21630-21638.
177. Brown, J., et al., *Impact of silk biomaterial structure on proteolysis*. Acta Biomaterialia, 2015. **11**: p. 212-21.
178. Yan, L.P., et al., *Injectable Silk Fibroin Hydrogels with Ionic Strength and pH Response for Tissue Engineering and Regenerative Medicine Applications*. Journal of Tissue Engineering and Regenerative Medicine, 2013. **7**: p. 6-52.
179. Yan, L.-P., et al., *Tumor Growth Suppression Induced by Biomimetic Silk Fibroin Hydrogels*. Scientific Reports, 2016. **6**: p. 31037-31037.
180. Subramani, K., *Fabrication of Hydrogel Micropatterns by Soft Photolithography*. Second ed. 2010: Elsevier Inc. 261-276.
181. Helgeson, M.E., S.C. Chapin, and P.S. Doyle, *Hydrogel microparticles from lithographic processes: Novel materials for fundamental and applied colloid science*. Current Opinion in Colloid and Interface Science, 2011. **16**(2): p. 106-117.
182. Krishna, M.G. and P. Kumar, *Non-Lithographic Techniques for Nanostructuring of Thin Films and Bulk Surfaces*. Second ed. 2010: Elsevier Inc. 93-130.
183. El-Sherbiny, I. and M. Yacoub, *Hydrogel scaffolds for tissue engineering: Progress and challenges*. Global cardiology science & practice, 2013. **2013**(3): p. 316-42.
184. Wade, R.J. and J.a. Burdick, *Engineering ECM signals into biomaterials*. Materials Today, 2012. **15**(10): p. 454-459.
185. Alsop, A.T., et al., *Photopatterning of vascular endothelial growth factor within collagen-glycosaminoglycan scaffolds can induce a spatially confined response in human umbilical vein endothelial cells*. Acta Biomaterialia, 2014. **10**(11): p. 4715-4722.
186. Li, Y., et al., *Non-Covalent Photo-Patterning of Gelatin Matrices Using Caged Collagen Mimetic Peptides*. Macromolecular Bioscience, 2015. **15**: p. 52-62.
187. Liu, J., et al., *Hydrogels for Engineering of Perfusable Vascular Networks*. International Journal of Molecular Sciences, 2015. **16**(7): p. 15997-16016.
188. Martin, T.A., et al., *The generation of biomolecular patterns in highly porous collagen-GAG scaffolds using direct photolithography*. Biomaterials, 2011. **32**(16): p. 3949-3957.
189. Mosiewicz, K.a., et al., *In situ cell manipulation through enzymatic hydrogel photopatterning*. Nature Materials, 2013. **12**(11): p. 1072-8.
190. Zorlutuna, P., et al., *Microfabricated Biomaterials for Engineering 3D Tissues*. Advanced Materials, 2012. **24**(14): p. 1782-1804.

191. Liu, J., et al., *A microfluidic photolithography for controlled encapsulation of single cells inside hydrogel microstructures*. Science China Chemistry, 2012. **55**(4): p. 494-501.
192. Linnenberger, A., et al., *Three dimensional live cell lithography*. Optics Express, 2013. **21**(8): p. 10269-77.
193. Mironi-Harpaz, I., et al., *Photopolymerization of cell-encapsulating hydrogels: Crosslinking efficiency versus cytotoxicity*. Acta Biomaterialia, 2012. **8**(5): p. 1838-1848.
194. Liu Tsang, V., et al., *Fabrication of 3D hepatic tissues by additive photopatterning of cellular hydrogels*. FASEB journal : official publication of the Federation of American Societies for Experimental Biology, 2007. **21**(3): p. 790-801.
195. Macadangdang, J., et al., *Capillary force lithography for cardiac tissue engineering*. Journal of Visualized Experiments, 2014(88): p. 1-8.
196. Aubin, H., et al., *Directed 3D cell alignment and elongation in microengineered hydrogels*. Biomaterials, 2010. **31**(27): p. 6941-6951.
197. Zorlutuna, P., et al., *Stereolithography-based hydrogel microenvironments to examine cellular interactions*. Advanced Functional Materials, 2011. **21**(19): p. 3642-3651.
198. Bajaj, P., et al., *Patterned Three-Dimensional Encapsulation of Embryonic Stem Cells using Dielectrophoresis and Stereolithography*. Advanced Healthcare Materials, 2013. **2**(3): p. 450-458.
199. Khademhosseini, A. and R. Langer, *Microengineered hydrogels for tissue engineering*. Biomaterials, 2007. **28**(34): p. 5087-92.
200. Bajaj, P., et al., *3D Biofabrication Strategies for Tissue Engineering and Regenerative Medicine*. Annual Review of Biomedical Engineering, 2014. **16**(May): p. 247-76.
201. Jeon, H., C.G. Simon, and G. Kim, *A mini-review: Cell response to microscale, nanoscale, and hierarchical patterning of surface structure*. Journal of Biomedical Materials Research - Part B Applied Biomaterials, 2014: p. 1580-1594.
202. Whitesides, G.M., et al., *Soft Lithography in Biology and Biochemistry*. Annual Review of Biomedical Engineering, 2001. **3**: p. 335-73.
203. Jiang, X. and G.M. Whitesides, *Engineering Microtools in Polymers to Study Cell Biology*. Engineering in Life Sciences, 2003. **3**(12): p. 475-480.
204. Chen, C.S., X. Jiang, and G.M. Whitesides, *Microengineering the Environment of Mammalian Cells in Culture*. MRS Bulletin, 2005. **30**(03): p. 194-201.
205. Franzesi, G.T., et al., *A controlled-release strategy for the generation of cross-linked hydrogel microstructures*. Journal of the American Chemical Society, 2006. **128**(47): p. 15064-15065.
206. Iwamoto, S., et al., *Preparation of gelatin microbeads with a narrow size distribution using microchannel emulsification*. AAPS PharmSciTech, 2002. **3**(3): p. 72-76.

207. Kong, Y.-q., et al., *Preparation of gelatin microparticles using water-in-water (w/w) emulsification technique*. Journal of Food Engineering, 2011. **103**(1): p. 9-13.
208. Elbert, D.L., *Liquid–liquid two-phase systems for the production of porous hydrogels and hydrogel microspheres for biomedical applications: A tutorial review*. Acta Biomaterialia, 2011. **7**(1): p. 31-56.
209. Andreas, K., et al., *Biodegradable insulin-loaded PLGA microspheres fabricated by three different emulsification techniques: Investigation for cartilage tissue engineering*. Acta Biomaterialia, 2011. **7**(4): p. 1485-1495.
210. Ortega-Oller, I., et al., *Bone Regeneration from PLGA Micro-Nanoparticles*. BioMed Research International, 2015. **2015**: p. 1-18.
211. Miao, G., et al., *Investigation of emulsified, acid and acid-alkali catalyzed mesoporous bioactive glass microspheres for bone regeneration and drug delivery*. Materials Science and Engineering: C, 2013. **33**(7): p. 4236-4243.
212. Kolachala, V.L., et al., *Slow-release nanoparticle-encapsulated delivery system for laryngeal injection*. The Laryngoscope, 2010: p. NA-NA.
213. Ma, M., et al., *Core–Shell Hydrogel Microcapsules for Improved Islets Encapsulation*. Advanced Healthcare Materials, 2013. **2**(5): p. 667-672.
214. Onoe, H., et al., *Metre-long cell-laden microfibres exhibit tissue morphologies and functions*. Nature Materials, 2013. **12**(6): p. 584-590.
215. Rabanel, J.-M., et al., *Progress technology in microencapsulation methods for cell therapy*. Biotechnology Progress, 2009. **25**(4): p. 946-963.
216. Penolazzi, L., et al., *Encapsulation of Mesenchymal Stem Cells from Wharton's Jelly in Alginate Microbeads*. Tissue Engineering Part C: Methods, 2010. **16**(1): p. 141-155.
217. Chen, T., et al., *Alginate Encapsulant Incorporating CXCL12 Supports Long-Term Allo- and Xenoislet Transplantation Without Systemic Immune Suppression*. American Journal of Transplantation, 2015. **15**(3): p. 618-627.
218. Vegas, A.J., et al., *Long-term glycemic control using polymer-encapsulated human stem cell-derived beta cells in immune-competent mice*. Nature Medicine, 2016.
219. Correia, C.R., et al., *Semipermeable Capsules Wrapping a Multifunctional and Self-regulated Co-culture Microenvironment for Osteogenic Differentiation*. Scientific Reports, 2016. **6**: p. 21883-21883.
220. Swioklo, S., A. Constantinescu, and C.J. Connon, *Alginate-Encapsulation for the Improved Hypothermic Preservation of Human Adipose-Derived Stem Cells*. Stem Cells Translational Medicine, 2016. **5**(3): p. 339-349.

221. Magyar, J.P., et al., *Mass Production of Embryoid Bodies in Microbeads*. Annals of the New York Academy of Sciences, 2001. **944**(1): p. 135-143.
222. Murphy, S.V. and A. Atala, *3D bioprinting of tissues and organs*. Nature Biotechnology, 2014. **32**(8): p. 773-785.
223. Cengiz, I.F., et al., *Building the basis for patient-specific meniscal scaffolds: From human knee MRI to fabrication of 3D printed scaffolds*. Bioprinting, 2016. **1-2**: p. 1-10.
224. He, Y., et al., *Research on the printability of hydrogels in 3D bioprinting*. Scientific Reports, 2016. **6**: p. 29977-29977.
225. Zehnder, T., et al., *Evaluation of an alginate–gelatine crosslinked hydrogel for bioplotting*. Biofabrication, 2015. **7**(2): p. 025001-025001.
226. Neufurth, M., et al., *Engineering a morphogenetically active hydrogel for bioprinting of bioartificial tissue derived from human osteoblast-like SaOS-2 cells*. Biomaterials, 2014. **35**(31): p. 8810-8819.
227. Xu, T., et al., *Hybrid printing of mechanically and biologically improved constructs for cartilage tissue engineering applications*. Biofabrication, 2013. **5**(1): p. 015001-015001.
228. Izadifar, Z., et al., *Analyzing Biological Performance of 3D-Printed, Cell-Impregnated Hybrid Constructs for Cartilage Tissue Engineering*. Tissue Engineering Part C: Methods, 2016. **22**(3): p. 173-188.
229. Markstedt, K., et al., *3D Bioprinting Human Chondrocytes with Nanocellulose–Alginate Bioink for Cartilage Tissue Engineering Applications*. Biomacromolecules, 2015. **16**(5): p. 1489-1496.
230. Costantini, M., et al., *3D bioprinting of BM-MSCs-loaded ECM biomimetic hydrogels for in vitro neocartilage formation*. Biofabrication, 2016. **8**(3): p. 035002-035002.
231. Ivanovska, J., et al., *Biofabrication of 3D Alginate-Based Hydrogel for Cancer Research: Comparison of Cell Spreading, Viability, and Adhesion Characteristics of Colorectal HCT116 Tumor Cells*. Tissue Engineering Part C: Methods, 2016. **22**(7): p. 708-715.
232. Duan, B., et al., *3D bioprinting of heterogeneous aortic valve conduits with alginate/gelatin hydrogels*. Journal of Biomedical Materials Research Part A, 2013. **101**(5): p. 1255-64.
233. Kang, L.H., et al., *Optimizing Photo-Encapsulation Viability of Heart Valve Cell Types in 3D Printable Composite Hydrogels*. Annals of Biomedical Engineering, 2016.
234. Duan, B., *State-of-the-Art Review of 3D Bioprinting for Cardiovascular Tissue Engineering*. Annals of Biomedical Engineering, 2017. **45**(1): p. 195-209.
235. Hsieh, F.-Y. and S.-h. Hsu, *3D bioprinting: A new insight into the therapeutic strategy of neural tissue regeneration*. Organogenesis, 2015. **11**(4): p. 153-158.

236. Knowlton, S. and S. Tasoglu, *A Bioprinted Liver-on-a-Chip for Drug Screening Applications*. Trends in Biotechnology, 2016.
237. Ma, X., et al., *Deterministically patterned biomimetic human iPSC-derived hepatic model via rapid 3D bioprinting*. Proceedings of the National Academy of Sciences, 2016. **113**(8): p. 2206-2211.
238. Faulkner-Jones, A., et al., *Bioprinting of human pluripotent stem cells and their directed differentiation into hepatocyte-like cells for the generation of mini-livers in 3D*. Biofabrication, 2015. **7**(4): p. 044102-044102.
239. Whitesides, G.M., *The origins and the future of microfluidics*. Nature, 2006. **442**(7101): p. 368-373.
240. Annabi, N., et al., *25th anniversary article: Rational design and applications of hydrogels in regenerative medicine*. Advanced Materials, 2014. **26**(1): p. 85-123.
241. Nichol, J.W. and A. Khademhosseini, *Modular tissue engineering: engineering biological tissues from the bottom up*. Soft Matters, 2010. **5**(7): p. 1312-1319.
242. Qasaimeh, M.a., T. Gervais, and D. Juncker, *Microfluidic quadrupole and floating concentration gradient*. Nature Communications, 2011. **2**(May): p. 464-464.
243. Cha, C., et al., *Microfluidics-assisted fabrication of gelatin-silica core-shell microgels for injectable tissue constructs*. Biomacromolecules, 2014. **15**(1): p. 283-290.
244. An, D., K. Kim, and J. Kim, *Microfluidic System Based High Throughput Drug Screening System for Curcumin/TRAIL Combinational Chemotherapy in Human Prostate Cancer PC3 Cells*. Biomolecules & Therapeutics, 2014. **22**(4): p. 355-62.
245. Du, G.S., et al., *Cell-based drug combination screening with a microfluidic droplet array system*. Analytical Chemistry, 2013. **85**(14): p. 6740-6747.
246. Moraes, C., *The Discovery Channel: microfluidics and microengineered systems in drug screening*. Integrative Biology, 2015. **7**(3): p. 285-288.
247. Annabi, N., et al., *Hydrogel-coated microfluidic channels for cardiomyocyte culture*. Lab on a Chip, 2013. **13**(18): p. 3569-3569.
248. Chung, B.G., et al., *Microfluidic fabrication of microengineered hydrogels and their application in tissue engineering*. Lab on a Chip, 2012. **12**(1): p. 45-45.
249. Agarwal, A.K., et al., *Autonomously-triggered microfluidic cooling using thermo-responsive hydrogels*. Lab on a Chip, 2007. **7**(3): p. 310-315.
250. Golden, A.P. and J. Tien, *Fabrication of microfluidic hydrogels using molded gelatin as a sacrificial element*. Lab on a Chip, 2007. **7**(6): p. 720-725.
251. Cuchiara, M.P., et al., *Multilayer microfluidic PEGDA hydrogels*. Biomaterials, 2010. **31**(21): p. 5491-5497.

252. Hatch, A., G. Hansmann, and S.K. Murthy, *Engineered Alginate Hydrogels for Effective Microfluidic Capture and Release of Endothelial Progenitor Cells from Whole Blood*. *Langmuir*, 2011. **27**(7): p. 4257-4264.
253. Huang, G., et al., *Cell-encapsulating microfluidic hydrogels with enhanced mechanical stability*. *Soft Matter*, 2012. **8**(41): p. 10687-10687.
254. Ling, Y., et al., *A cell-laden microfluidic hydrogel*. *Lab on a Chip*, 2007. **7**(6): p. 756-762.
255. Lee, W., et al., *On-demand three-dimensional freeform fabrication of multi-layered hydrogel scaffold with fluidic channels*. *Biotechnology and Bioengineering*, 2010. **105**(6): p. 1178-1186.
256. Bhatia, S.N. and D.E. Ingber, *Microfluidic organs-on-chips*. *Nature Biotechnology*, 2014. **32**(8): p. 760-772.
257. He, J., et al., *Layer-by-layer micromolding of natural biopolymer scaffolds with intrinsic microfluidic networks*. *Biofabrication*, 2013. **5**(2): p. 025002-025002.
258. Huang, H.-C., et al., *Enhancement of renal epithelial cell functions through microfluidic-based coculture with adipose-derived stem cells*. *Tissue Engineering. Part A*, 2013. **19**(17-18): p. 2024-34.
259. Potkay, J.a., *The promise of microfluidic artificial lungs*. *Lab on a Chip*, 2014. **14**(21): p. 4122-4138.
260. Dai, X.Z., et al., *A novel in vitro angiogenesis model based on a microfluidic device*. *Chinese Science Bulletin*, 2011. **56**(31): p. 3301-3309.
261. Smith, Q. and S. Gerecht, *Going with the flow: microfluidic platforms in vascular tissue engineering*. *Current Opinion in Chemical Engineering*, 2014. **3**: p. 42-50.
262. Young, E.W.K., *Advances in Microfluidic Cell Culture Systems for Studying Angiogenesis*. *Journal of Laboratory Automation*, 2013. **18**(6): p. 427-436.
263. Lozinsky, V.I., et al., *Polymeric cryogels as promising materials of biotechnological interest*. *Trends in Biotechnology*, 2003. **21**(10): p. 445-451.
264. Plieva, F.M., et al., *Pore structure in supermacroporous polyacrylamide based cryogels*. *Soft Matter*, 2005. **1**(4): p. 303-303.
265. Lozinsky, V.I. and O. Okay, *Basic Principles of Cryotropic Gelation*, in *Polymeric Cryogels*. 2014. p. 49-101.
266. Okay, O. and V.I. Lozinsky, *Synthesis and Structure–Property Relationships of Cryogels*, in *Polymeric Cryogels*. 2014. p. 103-157.
267. Plieva, F.M., H. Kirsebom, and B. Mattiasson, *Preparation of macroporous cryostructured gel monoliths, their characterization and main applications*. *Journal of Separation Science*, 2011. **34**(16-17): p. 2164-2172.

268. Ertürk, G. and B. Mattiasson, *Cryogels-versatile tools in bioseparation*. Journal of Chromatography A, 2014. **1357**: p. 24-35.
269. Gun'ko, V.M., I.N. Savina, and S.V. Mikhailovsky, *Cryogels: Morphological, structural and adsorption characterisation*. Advances in Colloid and Interface Science, 2013. **187-188**: p. 1-46.
270. Henderson, T.M.a., et al., *Cryogels for biomedical applications*. Journal of Materials Chemistry B, 2013. **1**(21): p. 2682-2682.
271. Sarnowska, A., et al., *Encapsulation of mesenchymal stem cells by bioscaffolds protects cell survival and attenuates neuroinflammatory reaction in injured brain tissue after transplantation*. Cell Transplantation, 2013. **22**(SUPPL.1).
272. Jurga, M., et al., *The performance of laminin-containing cryogel scaffolds in neural tissue regeneration*. Biomaterials, 2011. **32**(13): p. 3423-3434.
273. Shteyer, E., et al., *Reduced liver cell death using an alginate scaffold bandage: A novel approach for liver reconstruction after extended partial hepatectomy*. Acta Biomaterialia, 2014. **10**(7): p. 3209-3216.
274. Mishra, R., et al., *Biocomposite cryogels as tissue-engineered biomaterials for regeneration of critical-sized cranial bone defects*. Tissue Engineering - Part A, 2014. **20**(3-4): p. 751-762.
275. Kuo, C.-Y., et al., *Incorporation of chitosan in biomimetic gelatin/chondroitin-6-sulfate/hyaluronan cryogel for cartilage tissue engineering*. Carbohydrate Polymers, 2015. **117**: p. 722-730.
276. Bhat, S., A. Tripathi, and A. Kumar, *Supermacroporous chitosan-agarose-gelatin cryogels: in vitro characterization and in vivo assessment for cartilage tissue engineering*. Journal of the Royal Society, Interface, 2011. **8**(57): p. 540-554.
277. Gupta, A., et al., *Evaluation of three-dimensional chitosan-agarose-gelatin cryogel scaffold for the repair of subchondral cartilage defects: an in vivo study in a rabbit model*. Tissue Engineering Part A, 2014: p. 140521043257004-140521043257004.
278. Bagri, L.P., J. Bajpai, and a.K. Bajpai, *Evaluation of starch based cryogels as potential biomaterials for controlled release of antibiotic drugs*. Bulletin of Materials Science, 2011. **34**(7): p. 1739-1748.

Chapter II: Engineering Hydrogels for Modulation of Material-Cell Interactions*

ABSTRACT

Hydrogels are a recurrent platform for Tissue Engineering strategies. Their versatility and the variety of available methods for tuning their properties highly contribute to hydrogels' success. As a result, the design of advanced hydrogels has been thoroughly studied, in the quest for better solutions not only for drugs- and cell-based therapies but also for more fundamental studies. The wide variety of sources, crosslinking strategies, and functionalization methods, and mostly the resemblance of hydrogels to the natural extracellular matrix, make this 3D hydrated structures an excellent tool for TE approaches. The state-of-the-art information regarding hydrogel design, processing methods, and the influence of different hydrogel formulations on the final cell-biomaterial interactions are overviewed herein.

* This chapter is based on the following publication:

"Engineering Hydrogels for Modulation of Material-Cell Interactions", Vieira S., Reis R. L., and Oliveira J. M. (*submitted*)

II.1 Introduction

Since their introduction in the 1960s, hydrogels have been studied for a plethora of applications [1, 2]. Tissue Engineering field is one of the research areas in which hydrogel development and application retrieve fascinating results [3-6], either from simple hydrogel networks or when using the more advanced stimuli-responsive hydrogels [7]. These three-dimensional networks are mainly formed by hydrophilic polymers that can be of natural or synthetic nature, or even a mixture of both, with a rather significant amount of possible combinations. Such a volume of options translated into a wide range of hydrogel formulations already described, and a lot more would undoubtedly be uncovered, considering the potential of these structures. As a result, hydrogels have been classified according to several factors, as illustrated in Figure II-1. These include the source of the polymeric network, the ionic charge of the resulting gel, as well as the crosslinking and preparation methods used to obtain the 3D structure. Additionally, the hydrogels can be classified according to their behavior after preparation, particularly regarding their response to chemical, biochemical and/or physical stimuli, and degradability.

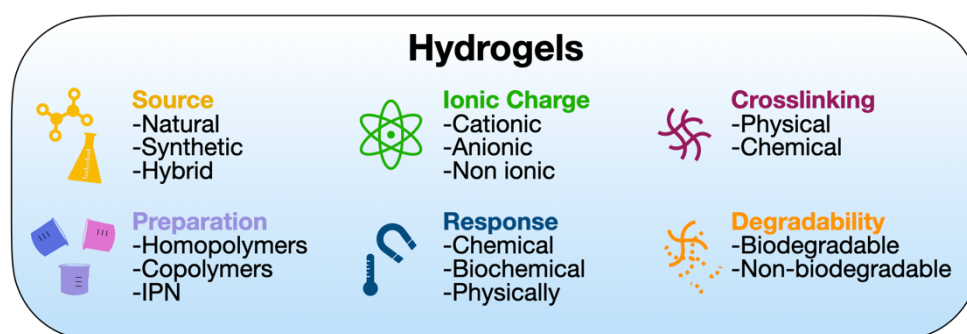


Figure II-1. Hydrogel classification categories. Hydrogels can be categorized according with their polymer source, preparation method, final ionic charge, responsive behaviors, type of crosslinking and degradability.

The variety of possible hydrogel formulations turned these biomaterials a highly interesting tool for tissue regeneration. Besides the type of polymer, or mixture used, other levels of complexity and/or functionality can be obtained. Most of the hydrogel precursors can be further functionalized, using different types of chemistries to add specific biological ligands or responsive motifs [8, 9]. As a result, hydrogel applications have been growing in the last few years, from cell delivery approaches to more fundamental studies, as cell-material interactions or mechanobiology.

It is well known that the external environment profoundly influences cell behavior. That is valid not only when cells are embedded by their natural ECM, but also when biomaterials are present. This interaction

occurs in a multiscale level, meaning that hydrogel designing must consider both bulk and microscale properties of the final hydrogel. In this review, we aim to highlight the most recent hydrogel engineering developments and how these biomaterials can influence and tune cell behavior.

II.2 Hydrogel Preparation

Most of the polymers used as hydrogel precursors are highly soluble on water, mostly due to the abundant presence of hydrophilic groups as $-NH_2$, $-COOH$, $-OH$, or $-SO_3H$. To form the 3D network, it is necessary to propitiate the conditions to occur a sol-gel transition, forming a gel non-flowing phase. Although the constituent polymers show a high affinity to water, their dissolution can be prevented by the crosslink between their monomers, using chemical or physical approaches, as schematically represented in Figure II-2. Physically crosslinked hydrogels are obtained by taking advantage of reversible intermolecular interactions. Those can be of different natures, being the ionic/electrostatic, and hydrophobic interactions the most common, and therefore will be discussed below. Besides those, hydrogen bonding [10-12], metal coordination [13, 14], or host-guest interactions [15, 16] can also be used as physical approaches for hydrogel crosslinking. As physical hydrogels are highly dependent on the polymer's intrinsic properties, it is harder to fine-tune the final hydrogel assets. In this regard, chemical hydrogels allow superior control on the mechanical properties and degradation profile, as well as spatiotemporal resolution [17]. The crosslink occurs due to the formation of covalent bonds amongst the polymeric backbone, which are stronger than those observed in physically crosslinked gels. Chemical crosslinks include photopolymerization, enzymatic crosslink, and "click" chemistry [17].

More than allowing the formation of a three-dimensional network, the crosslinking strategies can play an important role in the final mechanical and biochemical properties of the hydrogel [18]. Also, when cell and/or drug entrapment is envisaged, it must be assured that the whole process uses mild conditions that are compatible with the therapeutic agents used. Indeed, it is preferred to prepare hydrogels using conditions similar to the physiological ones, although some crosslinking strategies cannot meet these criteria. In such cases, care must be taken to minimize the time that cells are exposed to the harmful agent. While chemical crosslinking offers superior control and flexibility over the hydrogel formation process, physical crosslinking does not need external chemical agents, being therefore considered a safer approach for biomedical applications [19]. These mechanisms can also be combined in order to obtain improved hydrogels [20-22]. Regardless, the tradeoff between safety and efficacy must be considered when designing hydrogels to achieve a successful and functional formulation.

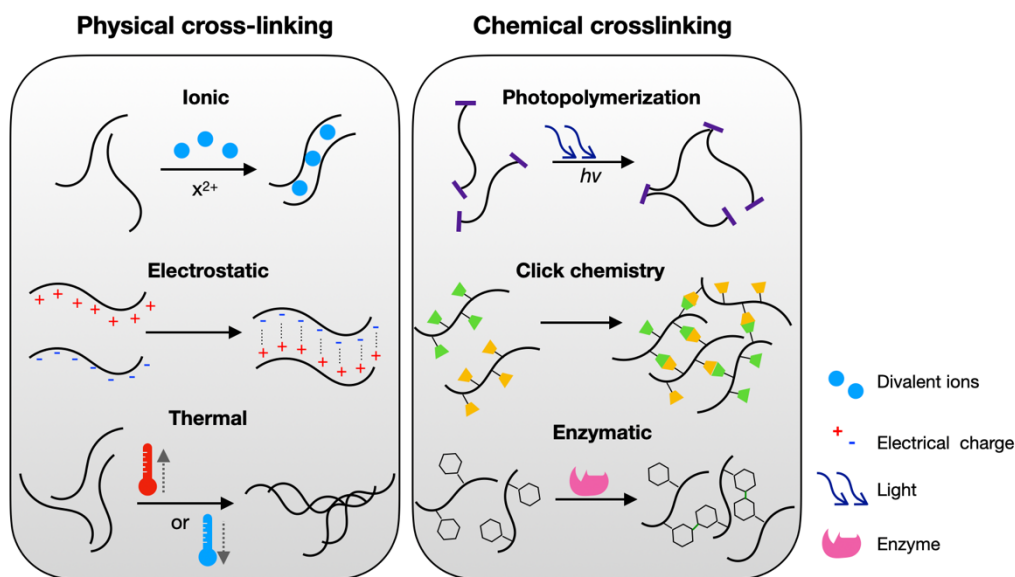


Figure II-2. Schematic representation of the most widely used crosslinking strategies for hydrogel formation. These include physical crosslinking methods, as ionic crosslink, electrostatic interaction and thermal-induced crosslink; and chemical crosslinking, including photopolymerization, click chemistry reactions and enzyme-catalyzed crosslink.

II.3 Physical Crosslinking

II.3.1 Ionic/Electrostatic Interactions

Ionic/electrostatic interaction is routinely used to obtain physically crosslinked natural-based hydrogels. Most of the natural polymers are charged at neutral pH, either due to the presence of carboxylic (alginate, gellan gum or hyaluronic acid) or amine (gelatin and chitosan) groups on their backbone [23]. When these polymers interact with molecules of different charge, the charged groups become shielded, decreasing water-polymer interactions, which leads to the formation of an insoluble complex. For example, alginate has a high affinity to alkaline earth cations, as Ba^{2+} , Sr^{2+} , or Ca^{2+} [24]. The affinity of alginate molecules to these ions is not equal, with Ba^{2+} showing the greatest one, meaning that distinct hydrogel properties can be obtained only by changing the ionic crosslinker [25, 26]. Upon interaction, the ionic components are enclosed in an egg-box structure formed between two chains of different alginate molecules, thus leading to hydrogel gelation (Figure II-3).

Gellan gum (GG) is another example of natural-derived polymers that also form stable gels in the presence of divalent ions. Although GG has a thermo-responsive behavior, which is discussed below, stable GG hydrogels are only obtained when ions are present as crosslinkers [27]. Similar to alginate, the gelation process is affected by the chemical nature of the ions used as crosslinkers. Monovalent cations, as Na^{2+}

or K^+ , induce a mild GG gelation via screening effect. On the other hand, divalent cations such as Ca^{2+} or Mg^{2+} , lead to GG aggregation through the abovementioned screening effect, but also due to the bonding of two carboxylate groups present on its glucuronic acid groups [28, 29].

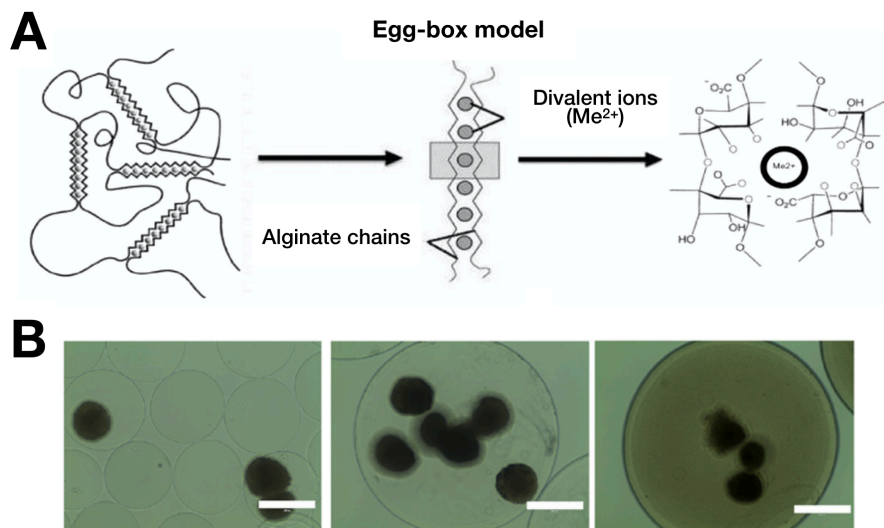


Figure II-3. Hydrogel crosslinking using ionic interactions. A - Drawing of the egg-box model for alginate crosslinking. Divalent ions, typically Ca^{2+} , are enclosed within the alginate polymeric chains, forming an “egg-box”-like structure. Adapted with permission from [25]. B - Representative bright-field images of alginate spheres containing stem cell-derived β -cells as a therapy approach for Type 1 Diabetes Mellitus (scale bars: 400 μm). Retrieved with permission from [30].

The electrostatic interaction can also occur between two polyelectrolytes of different charge, forming a polyelectrolyte complex (PEC) hydrogel. In this regard, alginate and chitosan are often used to prepare hydrogels via this technique, considering its inherent opposed charged nature (Figure II-4). Polyelectrolyte complexation can be used to prepare stable structures with different geometries, including macromolecular complexes [31-34], multilayered polyelectrolyte constructs [35, 36], polyelectrolyte complex fibers [37], and bulk hydrogels [38]. Although the interaction is mainly driven by electrostatic bonds, it can also include inter-macromolecular interactions as hydrogen bonding, van der Waals forces, hydrophobic, and dipole interactions [39].

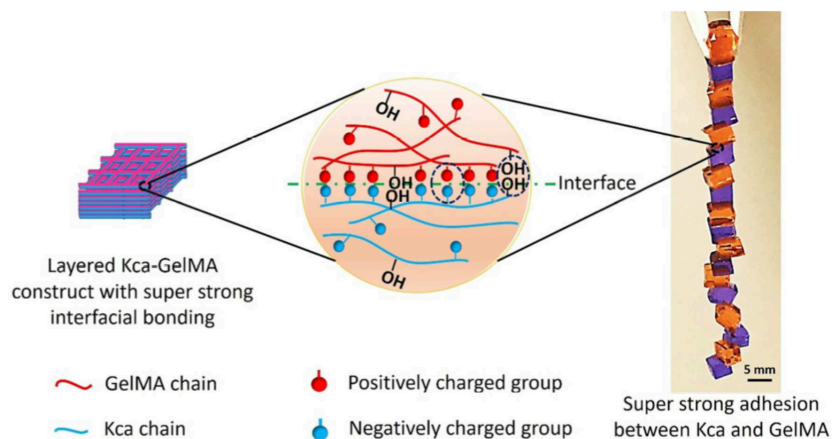


Figure II-4. Electrostatic interaction between polyelectrolytes of opposite charge allows the formation of **multilayered constructs**. The drawing shows the interaction between κ -carrageenan (Kca) and gelatin methacrylate (GelMA), that permits the 3D printing of polymeric layers due to the strong interface bonding. Retrieved from [36] with permission.

II.3.2 Thermal Induction

Thermally driven gelation is another common approach to prepare hydrogels, as many polymers of natural and synthetic nature are sensitive to temperature. The physical entanglement of the polymeric network occurs due to hydrophobic interactions, as a result of increasing or decreasing temperature [40]. However, thermo-responsive polymers can only be used for cell encapsulation if the sol-gel transition occurs near-physiological values. Therefore, polymers with transition temperatures near 37 °C are preferred for such approaches. Particularly, minimally invasive procedures that rely on injectable formulations into the body, take particular advantage of hydrogels with thermal driven gelation [41-43].

If a polymer forms a gel when heated, the temperature where the sol-gel transition occurs is the lower critical solution temperature (LCST). Below this temperature, the polymeric network is soluble in water, and no gel is formed. The synthetic polymer poly(*N*-isopropylacrylamide) (PNIPAAm) is a typical example of this kind of polymers [44], and has been applied for different TE approaches [45-48]. The sol-gel transition of PNIPAAm occurs around 32 °C [49], although LCST can be modified by copolymerization of PNIPAAm with other polymers, widening its range of applications [50-52]. On the other hand, for polymers that gel upon cooling, the crosslink occurs below the upper critical solution temperature (UCST), as the polymer starts to pack in physically rigid polymeric backbones. This is the case for most natural thermo-responsive polymers, such as gelatin or gellan gum (Figure II-5). Both polymers crosslink due to a network re-organization from a random coil to helix, but their UCSTs are considerably different. The sol-gel transition of gelatin occurs around 25 °C, meaning that it dissolves at body temperature.

Thus, gelatin is often combined with other polymers, or chemically crosslinked, to increase its UCST [53]. However, other works take advantage of this low transition temperature to obtain hydrogels using room temperature conditions. That is particularly useful in bioprinting, as the thermal gelation of gelatin prevents a premature loss of structures' shape [54, 55]. GG, by its turn, has a UCST far above physiologic conditions, limiting its dissolution at room temperature, as well as the preparation of hydrogels with encapsulated bioactive agents [56]. As an alternative, methacrylated GG (GG-MA) is water-soluble at room temperature [57] and can be used as a substitute of low acyl GG when high temperatures cannot be employed.

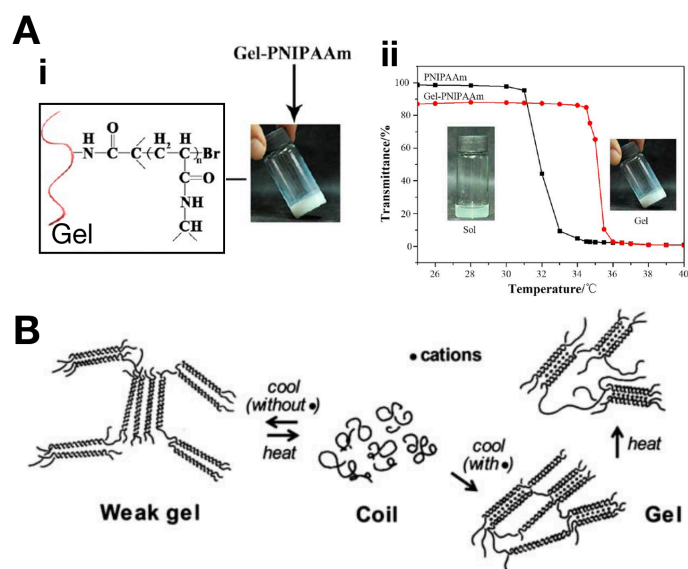


Figure II-5. Thermo-responsive hydrogels. A – Gelatin-PNIPAAm hydrogel (i) schematic representation of the polymer precursor and (ii) phase transition analysis of the Gel–PNIPAAm aqueous solution using UV–vis spectrophotometry at 350 nm. The increase of the gelation temperature to near physiological conditions allowed the use of this hydrogel as an injectable carrier for stem cells for the treatment of a bone cranial defect. Adapted from [58]. B - Schematic representation of GG crosslink process, according with Robinson *et al.* [59]. GG is thermo-sensitive, forming a weak gel upon cooling. A strong gel is only formed in presence of cations, that stabilize the GG double-helices. Retrieved from [60].

II.4 Chemical Crosslinking

II.4.1 Photopolymerization

Photo-activated hydrogels have been widely used in the field of tissue engineering (TE), mostly to rapidly prepare cell-laden hydrogels [61]. This approach often requires chemical modification of the backbone polymer to include functional photo-responsive groups, as (meth)acrylates. Also, it is necessary the presence of a photoinitiator to start the reaction [57, 62]. Different molecules are available as

cytocompatible radical photoinitiators. The majority of them are UV light-sensitive, as 2-hydroxy-4-(2-hydroxyethoxy)-2-methylpropiophenone (Irgacure 2959) [63, 64]. However, the putative DNA damage caused by UV light [65] has driven biomedical photochemistry to the use of visible light-sensitive photoinitiators, including lithium acylphosphinate (LAP) [66, 67], riboflavin [68], or ruthenium [69, 70]. Lim *et al.* [71] recently showed that the photo-crosslinking of cell-laden hydrogels using ruthenium/sodium persulfate induces less adverse effects on human articular chondrocytes compared to hydrogels prepared with LAP or Irgacure 2959.

Regardless of the photoinitiator nature, polymerization is triggered when these molecules are exposed to light, forming free radicals that, in turn, can react with the modified polymer. As a result, new covalent, intermolecular bonds are formed, and the crosslink occurs. The polymerization process can proceed following two different pathways, depending on the functional groups available at the backbone polymers. The most common polymerization method is the free radical chain-growth polymerization, where the formed radicals interact with the vinyl bonds of the (meth)acrylates groups [18]. Although it is possible to obtain hydrogels with tunable mechanical properties and degradation rates, the polymerization rate is inhibited by the presence of oxygen [72]. When oxygen is present, free radicals can interact with it, forming peroxy radicals that do not contribute to the reaction.

On the other hand, free radical step-growth reactions occur by the interaction of thiols with acrylates/enes, which are insensitive to the presence of oxygen [73, 74]. Additionally, the thiol-acrylate reaction involves a supplementary propagation step, since the acrylate groups can also react with the carbon-based radicals. This mixed-mode polymerization can be easily adjusted by changing the thiol:acrylate ratios, resulting in tunable hydrogel properties [73]. Considering the advantages of this system over the conventional free radical polymerization, different polymers were already modified to contain thiol and acrylate/ene groups. As a result, thiol-acrylate and thiol-ene chemistries have been widely and successfully used to prepare biocompatible hydrogels from different polymers, including polyethylene glycol (PEG) [75-77], hyaluronic acid (HA) [78, 79], gelatin [80, 81], and alginate [82]. One promising application of these photo-reactions is the biofabrication field [83]. As an alternative to the free-radical chain-growth crosslinking strategies, the step-growth polymerization of thiol-ene results in a more homogenous network that can be easily tailored and modified by the addition of any thiol-containing biomolecules, as schematically represented in Figure II-6. A notable example of this application is the modular thiol-ene alginate bioink recently developed by Ooi *et al.* [82]. Using this method, the authors

previous modification of the backbone polymers, it has gathered a great deal of attention over the past years [85]. That is highly related to the selectivity, efficiency, and thermo-reversibility associated with these reactions. Also, DA reactions do not require the addition of any catalyst, which poses as an additional advantage for this system [86]. As said, DA chemistry requires a polymeric functionalization, which typically includes the addition of furan and maleimide groups [87]. For example, HA has been modified with furan for further crosslinking with dimaleimide PEG [88]. The reaction leads to the formation of a tunable hydrogel, where mechanical and degradation properties can be controlled by the furan to maleimide molar ratio. Although promising, the resulting gels are only compatible with 2D culture systems, as the crosslink involves a sub-physiologic pH of 5.5. To tackle this issue, furan-HA can be substituted by the electron-rich hyaluronan-methylfuran [89], as it accelerates the DA reaction at physiologic pH (Figure II-7A). Using such conditions, cells can be successfully encapsulated into the hydrogel's matrix while taking advantage of DA reaction properties.

By its turn, Michael-type reactions occur via the addition of a nucleophile Michael donor, and an electrophilic carbon-carbon double bond conjugated with a carbonyl group that behaves as a Michael acceptor (Figure II-7B). Examples of Michael donors are thiols and amines, but thiol-based molecules are usually preferred, considering the higher nucleophilicity and selectivity at physiological pH and temperature. On the other hand, Michael acceptors are more variable amongst the hydrogel preparations reported in the literature, including acrylates, acrylamides, vinyl sulfones, and maleimides [90]. This reaction is compatible with aqueous environments, room temperature, and physiological pH, making it suitable for biomedical hydrogel applications, including cell encapsulation and injectable formulations [89, 91]. As an example, thiolated gelatin was already used in combination with different PEG-modified molecules (PEG-maleimide, PEG-acrylate, and PEG-vinyl sulfone) to prepare bioinks [92]. Interestingly, the gelation time could be tailored by changing the Michael acceptor of the system, with PEG maleimide conferring the fastest gelation (<30 s) while PEG-vinyl sulfone the slower (>10 min). Hydrogels made from modified PEG [93, 94], chitosan [95], and HA [96] are some examples of the applicability of this reaction in TE.

II.4.3 Enzymatic Crosslinking

The use of enzymes to chemically crosslink hydrogels has gathered a great deal of attention, as these molecules can be considered as “green-catalysts” of hydrogel formation. One of the main advantages of enzyme-based systems is the substrate specificity that reduces the occurrence of toxic side reactions. The possibility to control hydrogel formation kinetics, the relatively fast gelation, and the resulting strong covalent bonding also contribute to the increasing interest in this strategy [102]. As a result, different enzyme-mediated methods have been developed until now, using different types of enzymes and often using Nature as inspiration.

Transglutaminases, which are part of the transferase’s family, are widely used in the TE setting. These thiol enzymes catalyze the formation of covalent bonds between the γ -carboxamide group of glutamines and a free lysine amine group. The gelation occurs in 5 to 20 min, and the resulting bonds are greatly resistant to proteolysis, making it possible to obtain stable networks [103]. A remarkable example of transglutaminase-catalyzed reactions is the formation of fibrin clots from soluble fibrin, the “biological glue” formed during blood coagulation. The enzymatic activity of transglutaminases has already been quite explored, mostly for the crosslink of various peptides, such as collagen or gelatin [104-106], or modified polymers carrying the transglutaminase substrates [107, 108].

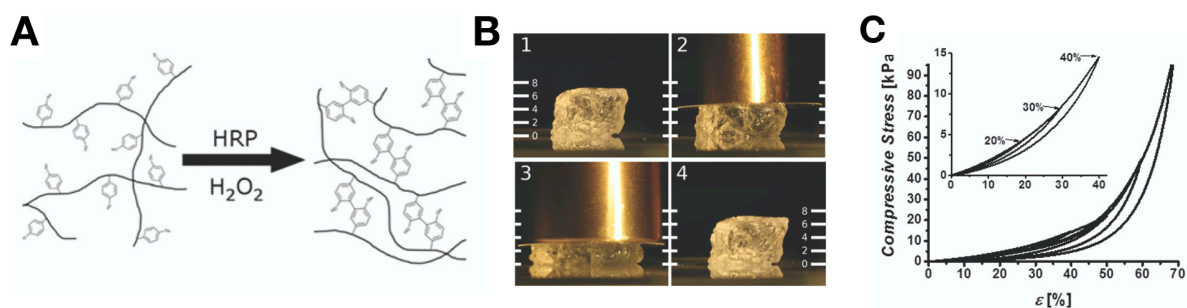


Figure II-8. Enzymatic crosslink. A – Molecules rich in phenolic groups can be crosslinked using HRP enzyme, in the presence of H₂O₂. B – Silk hydrogels obtained by HRP-mediated crosslink show an elastic behavior and superior mechanical properties. After \approx 50 % compression, under 50 g (2) and 100 g (3) brass weights, the hydrogel shows complete recovery (4). Scale is in millimeters. C – Cyclic compression curves of hydrogels showing excellent recovery below 70 % strain, and complete recovery below 40 % strain (inset). Adapted from [109].

Horseshadish peroxidase (HRP) is the most used oxidative enzyme in TE, when crosslinking is envisaged. As an oxidative enzyme, HRP catalyzes the oxidation of aromatic proton donors (such as phenols, anilines, or amines), resulting in the coupling of the formed reactive species, using H₂O₂ as a cofactor. The specificity of HRP makes it only interact with polymers that have hydroxyphenyl groups, such as

polymers containing tyramine, tyrosine or 4-hydroxyphenyl acetic acid. While some polymers naturally present the groups mentioned above, others need to be functionalized for further HRP-mediated crosslink. That includes gelatin [110, 111], PEG [112, 113], HA [114-116], alginate [117, 118], among others. A typical example of HRP-mediated crosslink is the hydrogels prepared from silk fibroin (SF) [109, 119], obtained by the chemical crosslink between two tyrosine residues (Figure II-8). The resulting hydrogels are elastic, with tunable mechanical properties [109], paving the way for a wide range of applications from fundamental studies [120] to biofabrication [121]. Moreover, this chemical crosslink can be combined with the SF physical crosslink, caused a conformation change from random coil to β -sheet. Such “dual crosslink” greatly enhances the hydrogel’s mechanical properties, particularly its compressive modulus, which can be as high as 3 MPa [122].

II.5 Material-cell Interactions

As mentioned before, hydrogels can be prepared from different sources, with different properties, and further modified using several different approaches. Consequently, hydrogels can display different assets that must be tailored for the final desired application. The following section discusses these macroscale properties and how they fit into different TE strategies, as schematically represented in Figure II-9.

II.5.1 Hydrogel Stability

The growing interest in stem-cell based therapies led to an increased effort to improve the final stem cell fate. In this regard, hydrogels are considered an ideal tool to help cell survival and correct placement. They can be used as carriers, improving cell function and viability, while providing protection from the hostile environment found in diseased or wounded tissues [123]. Typically, encapsulated cells are delivered by injection, using minimally invasive techniques. Shear-thinning materials, compatible with reversible crosslinking strategies, are thence preferred for this kind of approach [124]. Being shear-thinning, hydrogels exhibit a liquid-like behavior under the shear stress created by the injection procedure, thus allowing cell delivery. After injection, the reversible nature of the crosslink leads to the recovery of the hydrogel mechanical properties, assuring a homogeneous encapsulation that prevents leakage of its cargo to the surrounding media. Besides being essential for the initial cell retention in the desired place, hydrogel fate must be compliant with the final purpose of the cell-based strategy. While degradation is necessary in some cases, other approaches require stable hydrogels capable of protecting transplanted cells for long periods.

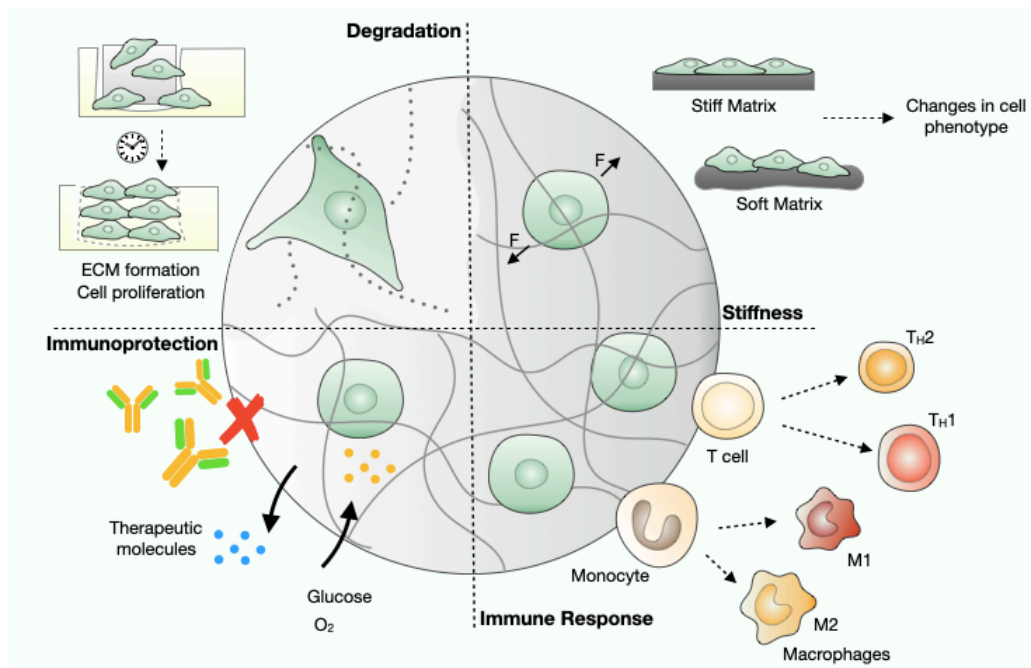


Figure II-9. Schematic overview of the material-cell interactions discussed in this review. Degradable hydrogels are preferred for cell delivery approaches, where cell proliferation and migration are intended, leading to *in situ* ECM formation. However, the hydrogel can act as an immunoprotective device, displaying a semi-permeable behavior, where only small molecules enter in the hydrogel space, a strategy suitable for cell encapsulation purposes. Upon interaction with the host, the hydrogels elicit an immune response that can be tailored to favor a pro-regenerative phenotype. At last, the mechanical properties of the hydrogel are also important as they greatly influence cell fate and function.

TE strategies often rely on the implantation of exogenous therapeutic cells to regenerate the damaged tissues [125-127]. To be successful, these approaches trust on cell proliferation and migration from the hydrogel to the surrounding environment, as well as *de novo* ECM synthesis, combined with a sustained degradation of the biomaterial. At last, the tissue is repaired, due to *de novo* ECM synthesis combined with the therapeutic effect of encapsulated cells. Therefore, it is rather important that the hydrogel degrades at a suitable rate, compatible with sustained cell migration or new ECM formation. Such timing poses a particular challenge in the field and can be tackled by modifying the crosslinking strategy or the polymers used to prepare the hydrogels.

Hydrogels prepared from biodegradable materials [125], or modified polymers containing degradable groups [128, 129], are often used due to their inherent degradability. In such cases, the primary degradation mechanism is enzymatic degradation and/or hydrolytic degradation. Hydrogels designed to be degraded via enzymatic degradation take advantage of the enzymatic pool existent in the body, particularly proteases as matrix metalloproteinases (MMPs). Although some polymers are naturally

degraded by such enzymes, as gelatin [130], others need to be modified to include enzyme-labile motifs [131]. The typical example of modified hydrogels for proteolytical degradation purposes is PEG-based hydrogels [132-135], but others, including natural polymers, have already been modified for the same end. GG, as an example, was modified to include divinyl sulfone groups, able to react with dithiol peptide crosslinkers sensitive to MMP-1 [136]. The resulting gels showed a bioresponsive behavior, with promising results for vascularization as endothelial cells could polarize on these matrices, but not on unmodified hydrogels. Alginate [137-139] and HA [140, 141] are examples of other polymers modified to promote cell-mediated degradation.

On the other hand, immunoisolation strategies require full protection of the biological material from the host immune system. This technology has been largely developed as a treatment for Type 1 Diabetes Mellitus, where only insulin-producing cells are transplanted into the host [142]. The rationale implies the transplantation of therapeutic relevant cells in the absence of immunosuppression. Therefore, the biomaterial of choice must be stable for long periods, avoiding the interaction between the host immune cells and the transplanted material. However, the material-tissue interface must be semipermeable, allowing the free diffusion of small nutrients and therapeutic molecules between encapsulated cells and the surrounding environment. In this regard, microencapsulation using alginate has been the most studied strategy, with several works reporting the feasibility of this material as an immunoprotective matrix [143, 144]. Interestingly, it was already shown that alginate immunoprotective properties depend not only on the alginate type, but also on the ion used to perform the ionic crosslink. Microcapsules prepared with barium are typically more stable and biocompatible than those prepared with calcium, meaning that barium should be preferred for this type of application [145].

Amongst the latest works on immunoisolation, the work of Vegas *et al.* [30] has shown how alginate modification can improve the immunoisolation capacity of the hydrogel matrix. By functionalizing the alginate with specific peptides, it was possible to engineer microcapsules capable of mitigating the foreign-body response in mice models. Without any immunosuppression, the authors could maintain and correct the glycemic values for a period of up to 174 days, the moment when the implants were retrieved. Although the work published by Vegas *et al.* is undoubtedly a significant step towards a clinical application, other strategies and materials have been reported during the last years for immunoprotection purposes, as summarized in Table II-1 [146-156].

An *et al.* [148] engineered an interesting approach for immunoisolation of islets cells, the TRAFFIC system (Figure II-10). Instead of spherical microcapsules, the authors prepared alginate threads, using nylon sutures as templates and spider silk as inspiration. The aim was to modify the thread with a nanoporous polymeric coating to mimic the capillary-enabled water collection and retention observed in certain spiders. The nanoporous coating served as a CaCl_2 reservoir that later was used to crosslink a thin alginate layer around the whole thread. The resulting threads were more mechanically robust than bare alginate fibers and easily handled, including laparoscopic implantation and retrieval. It was also verified that the device provides immunoprotection to encapsulated islets up to 1 month, similar to neat alginate fibers. Overall, the possibility to easily implant and retrieve the system, allied with the immunoprotection feature, paves the way for future clinic applications of this strategy.

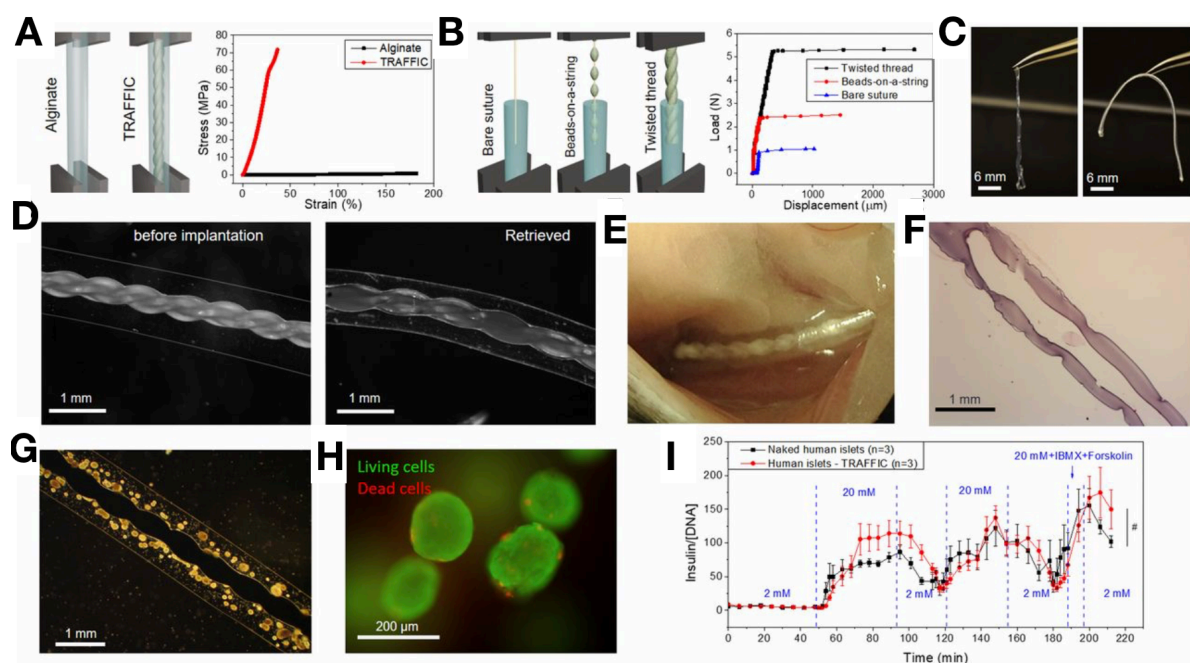


Figure II-10. Overview of the TRAFFIC system. A – Schematic representation and plot of the strain-stress measurement, comparing bare alginate fibers and TRAFFIC; B – Schematic representation and results of the load-displacement measurement, comparing bare alginate fibers with bead-on-a-string configuration and the twisted thread (TRAFFIC); C - Handling of neat alginate fiber (right) and a TRAFFIC device (left); D - Microscopic images comparing the structure of TRAFFIC before and after 7-month implantation in mice; E - TRAFFIC device inside the intraperitoneal cavity of a mouse; F - Hematoxylin and eosin staining of retrieved; G - Human islet cells encapsulated in the alginate layer; H - Live (green)/dead (red) staining of encapsulated human islets; I - Results of a dynamic perfusion test for glucose stimulated insulin secretion comparing naked islets with encapsulated ones. $n = 3$, mean \pm SEM (standard error mean), # $P > 0.05$. Retrieved with permission from [148].

Table II-1. Recent strategies for immunoisolation.

Hydrogel	Crosslink	Structure	Cell-type	Main Conclusions	Ref.
Thiolated HA/thiolated gelatin	Michael addition	Bulk hydrogel	Canine and rat islets	Semi-permeable matrix due to thermodynamically favorable interactions between hydrogel and dextran. Allogeneic transplant of islets into rats reversed diabetes up to 18 months.	[149]
Alginate	Ionic crosslink	Bulk hydrogel	Rat and human islets	Suture threads coated with alginate. The threads improve mechanical strength allowing a facile retrieve of the construct.	[148]
Alginate	Ionic crosslink	Microcapsules	Human and murine islets	Comparison between free and microencapsulated islets. Small microcapsules caused only a slightly delayed insulin response compared to unencapsulated islets. Larger capsules decreased the total amount of insulin released.	[150]
Alginate and methacrylated chitosan	Ionic and photo-crosslink	Microcapsules	Porcine islets	Good islet viability and function after 1 month of <i>in vitro</i> culturing. Improved biocompatibility over APA capsules.	[151]
PEG	Photo-crosslink	Bulk hydrogels	Mouse embryonic fibroblasts	Comparative study to assess the effect of functional end groups of multi-arm PEG on hydrogel stability and host immune response. PEG-vinyl sulfone evidenced an attenuated immune response,	[152]
PEG	Michael addition	Bulk hydrogels	Rat islets	Long term stability <i>in vitro</i> and <i>in vivo</i> . Functionalization of PEG with RGD improved insulin responsiveness. Addition of a vasculogenic, degradable hydrogel layer enhanced islet viability <i>in vivo</i> .	[153]
PEG vinyl sulfone	Michael addition and photo-crosslink	Core-shell hydrogel	Mice ovaries	Proteolytically degradable hydrogel core and non-degradable shell. Ovaries encapsulated within the core, in conductive environment for tissue development. Non-degradable shell protected the tissue from immune response.	[154, 155]
PEG diacrylate (575 and 3500 Da)	Photo-crosslink	Ultra-thin coating	Jurkat	Films with 100-200 nm thickness. 10 and 20 kDa molecules are blocked, but 4 kDa move freely.	[156]

II.5.2 Mechanical Properties

The importance of ECM on cell fate has already been established, and it is now known that matrix mechanical properties significantly affect how cells proliferate, migrate, and even maintain their normal phenotype [157]. In this regard, the mechanical properties of hydrogels must be considered when designing hydrogels for TE, to recapitulate the correct mechanical information.

Cells can sense and interact with their external mechanical environment via integrin-mediated focal adhesion signaling [158]. The mechanical resistance of the ECM to cell-generated forces dictates the stability of the focal adhesion complexes, which likely activate mechanoresponsive signaling pathways. Such information, which is converted into a biochemical signal through mechanotransduction, ends up changing the gene expression of resident cells by different pathways, as schematically represented in Figure II-11 [159].

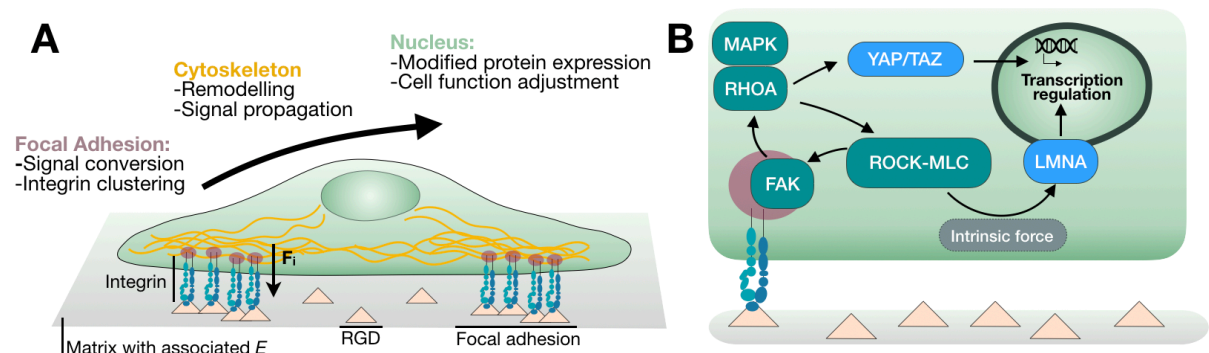


Figure II-11. Schematic representation of the mechanotransduction phenomena. A – Cell-material interaction via focal adhesions starts a signaling cascade that travels through the cytoplasm to the nucleus. B – Overview of the signaling cascade triggered by cell mechanosensing.

These include the FAK-RhoA-Rho kinase cascade [160], a pathway that starts with the phosphorylation and activation of RhoA and Mitogen Activated Protein Kinases (MAPK) by focal adhesion kinases (FAK). As a result, mechanosensitive transcription factors are translocated into the cell nucleus, altering the gene expression as a response to the mechanical environment. For example, YAP (Yes-associated protein) and TAZ (transcriptional coactivator with PDZ-binding motif) are emerging as universal control systems on mechanosensing, in 2D and 3D conditions, as well as in a wide range of elastic and viscoelastic stimuli [161]. As mediators of mechanical cues, the translocation of YAP/TAZ into the nuclei occurs when cells are in contact with stiff substrates [161]. This translocation is independent of the Hippo/LATS cascade but depends on the aforementioned FAK-RhoA-Rho kinase cascade [162].

The mechanical signals can also be directly transmitted to the nucleus. Lamina proteins, as laminin A (LMNA), physically connect the nucleus with the cytoskeleton through the LINC (“linker of nucleoskeleton and cytoskeleton”) complex [163]. The mechanical signals can then reach the nuclear structure, thus affecting chromatin structure and gene expression [164].

Regarding hydrogel design, the mechanical properties are often studied considering the biomaterial elasticity and its stiffness. To that end, hydrogels with different stiffnesses are typically obtained by systematically changing the polymer concentration or crosslinking density [165-169]. Such combinations resulted in hydrogels with elastic modulus (E) ranging from Pa to MPa [170], that can be used as platforms in order to improve TE strategies [171] but also to study the mechanotransduction phenomena [172]. Table II-2 summarizes the latest studies on this subject [165-169, 171-201].

Pelham *et al.* [173] demonstrated that substrate flexibility affected cell morphology and locomotion, and recent works have been strengthening their results by showing the impact of substrate stiffness on mesenchymal stem cells (MSC) migration [176]. The latest data suggests that most of cell behavior is influenced by mechanotransduction, including migration, proliferation, differentiation, and even the immunomodulatory effect [159, 198, 202-204]. Although, it was the seminal work of Engler *et al.* [174] that clearly demonstrated the importance of matrix stiffness on stem cell differentiation (Figure II-12). Polyacrylamide gels with defined stiffnesses were obtained by varying the concentration of the crosslinker (bis-acrylamide) and used as a platform to study the differentiation of MSCs. They found that lineage specification of MSCs can be directed by matrix stiffness and that matrices with tissue-like stiffness induced stem cells to differentiate into the analogous specific cell lineages. It was observed that soft substrates with a brain-like stiffness ($0.1 < E < 1$ kPa) induced neurogenesis, while stiff substrates with an elastic modulus of 25-40 kPa promote osteogenesis. These results shed light on the idea of stem cell pre-commitment into a specific lineage using biomaterials to overcome an inhospitable *in vivo* environment.

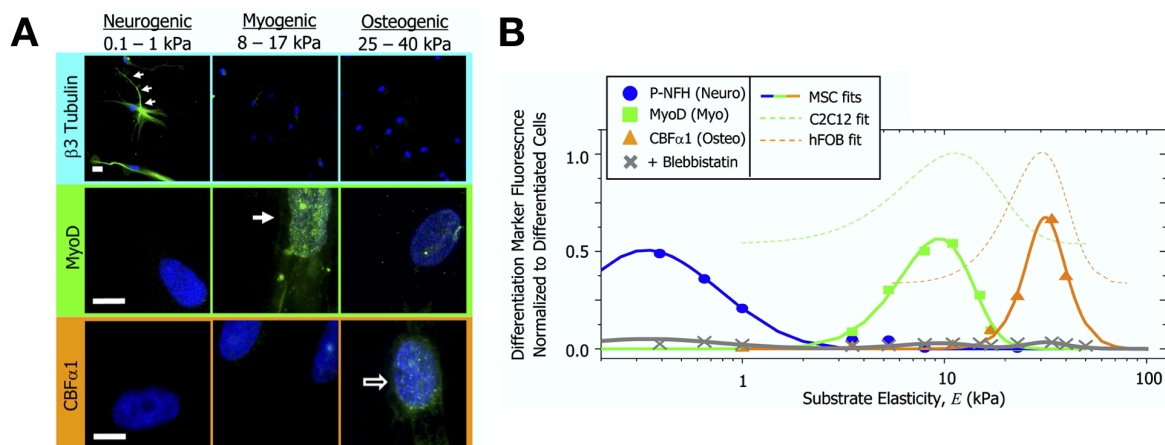


Figure II-12. MSCs response to substrate stiffness. A – Fluorescence microscopy images showing the expression of a neuronal cytoskeletal marker ($\beta 3$ tubulin), a muscle transcription factor (MyoD1) and an osteoblast transcription factor (CBFa1, core-binding factor alpha 1) in substrates of different stiffness. $\beta 3$ tubulin is expressed in cells cultured on soft matrices but not on intermediate or stiff substrates. By its turn, MyoD1 is upregulated only in MSCs cultured on matrices with intermediate stiffness. At last, the presence of CBFa1 is noticed expressed only on stiff gels. Scale bar is 5 μm . B – Lineage specification, assessed by the fluorescent intensity of differentiation markers, is maximum when cells are cultured in matrices with a stiffness typical of each tissue type. Blebbistatin blocks all marker expression in MSCs. Adapted with permission from [174].

Undoubtedly, Engler's work had a great impact on Mechanobiology, and a great deal of attention has been given to this matter since then. However, it has been noticed that time-dependent mechanical properties can also impact the cell-matrix interaction. Therefore, a lot of work has been developed recently in order to engineer viscoelastic hydrogels, that better recapitulate the ECM properties, and allow to study the influence of time-dependent deformations on mechanotransduction. Contrarily to what occurs in pure elastic substrates, in hydrogels that exhibit stress relaxation properties, the resistance to cell-induced forces decreases over time, changing the way the cell perceives its surroundings (Figure II-13A).

Chaudhuri *et al.* [179, 205] successfully designed a set of hydrogels with similar initial elastic modulus but a wide range of stress relaxation rates, using the same concentration of the backbone polymer. Their results showed that the relaxation times greatly influence the behavior of encapsulated MSCs, as hydrogels with faster relaxation times enhanced cell spreading, proliferation, and osteogenic differentiation. The authors claimed that such effect was transduced via integrin-based adhesions, local clustering of Arg-Gly-Asp ligands (RGD), actomyosin contractility, and YAP translocation into the nucleus. For this study, the authors used RGD-modified alginate of different molecular weight, as well as PEG spacers, to modulate the relaxation times, as shown in Figure II-13B. Other strategies can also be used

to tune the viscoelasticity and relaxation times of hydrogels, always taking advantage of physically associative or reversible covalent chemical bonds. For instance, boronate-based hydrogels allow the formation of synthetic matrices with different viscoelasticity, which is proven to be useful as a platform for studying the mechanotransduction phenomena [185, 186]. The faster association and dissociation dynamics of boronates, as compared to other reversible bonds, permit the study of events triggered by short relaxation times. Moreover, by changing the boronic acid derivatives, it is possible to finely tune the relaxation dynamics (Figure II-13C). As an example, the use of 2-fluorophenylboronic acid (FPBA), 1-hydroxy-1,3-dihydrobenzo[*c*][1,2]oxaborole (*m*-boroxole, BX), or a Wulff-type *o*-amino-methylphenylboronic acid (WBA), considerably changed the relaxation time of the resulting hydrogels. That can be attributed to the different binding constants, as the strongest bonds (using FPBA) had the slowest relaxation as opposed to the weakest WBA-based bonds, which showed a faster relaxation time [185].

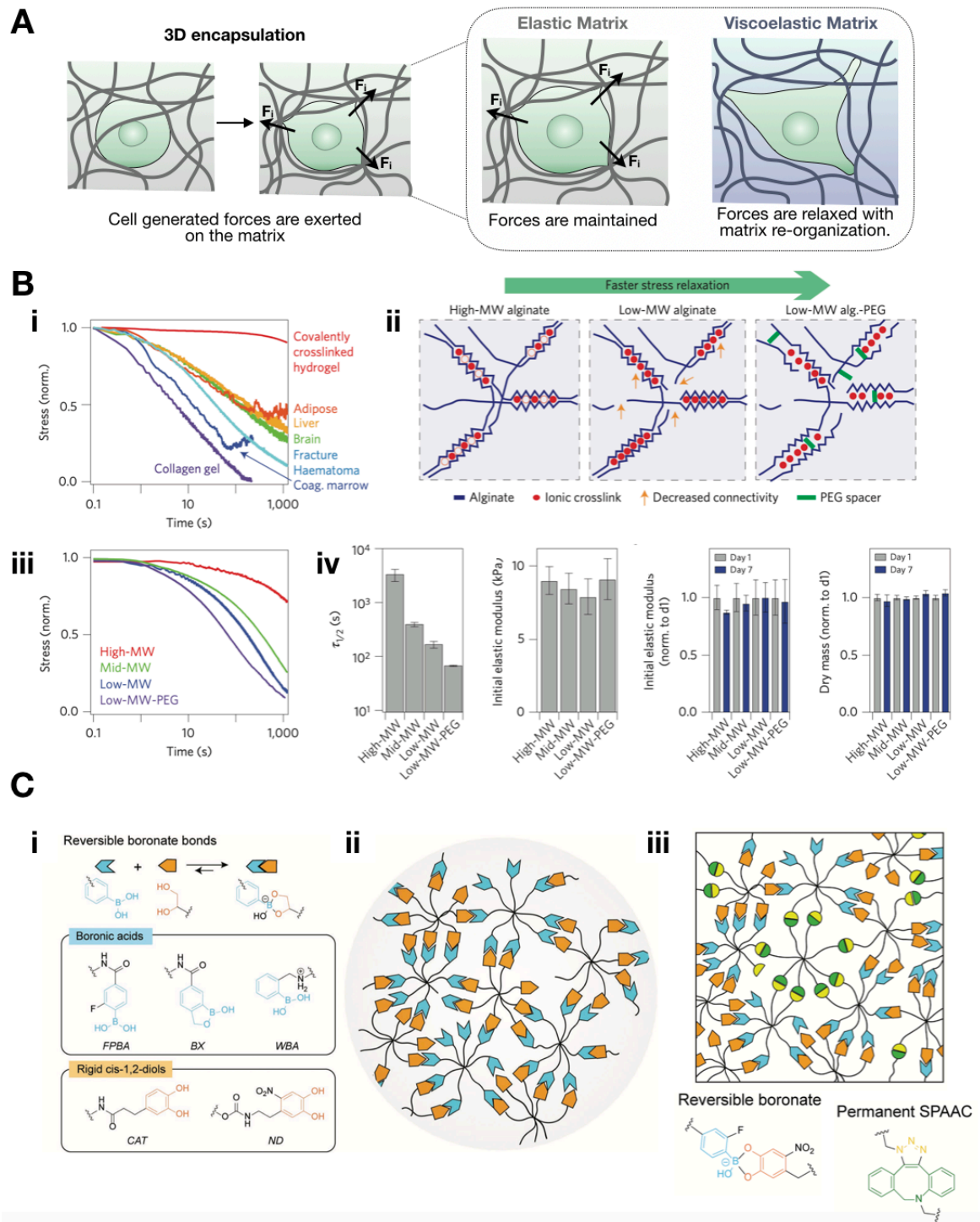


Figure II-13. Elastic versus viscoelastic matrices on mechanotransduction. A – Schematic representation of the cell rearrangement on elastic and viscoelastic matrices. B – Viscoelastic alginate hydrogel prepared with different polymer molecular weights and PEG spacers. Since the stress relaxation properties are independent of initial elastic modulus and matrix degradation, it is possible to mimic the viscoelastic behaviors of living tissues. (i) stress relaxation tests using various rat tissues, an initial fracture hematoma (human), a collagen gel and a polyacrylamide crosslinked gel. (ii) schematic representation of the approach used to increase the rate of stress relaxation. (iii) stress relaxation tests using the different alginate hydrogel formulations, showing

a decrease on stress relaxation time by lowering the molecular weight and introduction of PEG spacers. (iv) Plotted values of the time needed for the stress relax to half of its original value ($\tau_{1/2}$); the initial elastic modulus measurements; Elastic modulus of the gels after 1 and 7 days in cell culture conditions, normalized by the value at day 1; dry mass of alginate hydrogels after 1 day or 7 days in culture normalized by the value at day 1. Data are shown as mean \pm SD. Retrieved from [179]. C – Adaptable fast relaxing boronate-based hydrogels. (i) Reaction scheme illustrating the reversible formation of boronates and chemical structures of the different boronic acid derivatives used to modify the material relaxation time. (ii) Schematic drawing of the polymeric network based on 8-arm PEG functionalized with boronates and cis-1,2-diols. (iii) Representation of the hydrogel network with permanent azide-alkyne cycloaddition (SPAAC) bounds and reversible boronate bonds. These hydrogels are better suitable for cell culturing due to their superior stability. Adapted with permission from [185].

Another relevant consideration that must be highlighted when considering matrix stiffness is its impact on MSCs differentiation capacity. Taking advantage of the photoinduced softening of modified PEG hydrogels, it was possible to study the “mechanical memory” of MSCs, as depicted in Figure II-14 [177, 178]. Surprisingly, chromatin organization and histone acylation states induced by the rigid matrix can be reversed if cells are cultured only for 1 day prior to softening; after a longer culture period, like 10 days, those changes became irreversible. This mechanical dosing gives more insight on the deleterious effect of long term MSCs expansion, a step typically crucial to obtain therapeutic relevant cell number and is typically performed using rigid plastic flasks [177].

Although the bibliography discussed until now focuses mainly on MSCs, the effect of the mechanical properties on cell function has been shown to be valid to other cell types as myoblasts [183], vascular progenitor cells [206], dental pulp stromal cells [189], podocytes [199], to name a few. Also, it is important to stress that the mechanotransduction phenomena cannot be pictured only from the stiffness point of view. Besides the previously mentioned time-dependent properties, *i.e.*, viscoelasticity, also the cell-ligand density [196], presence of different ECM proteins [197], and cell volume/density [194], play an important role on the final cell response and must be taken into account [181].

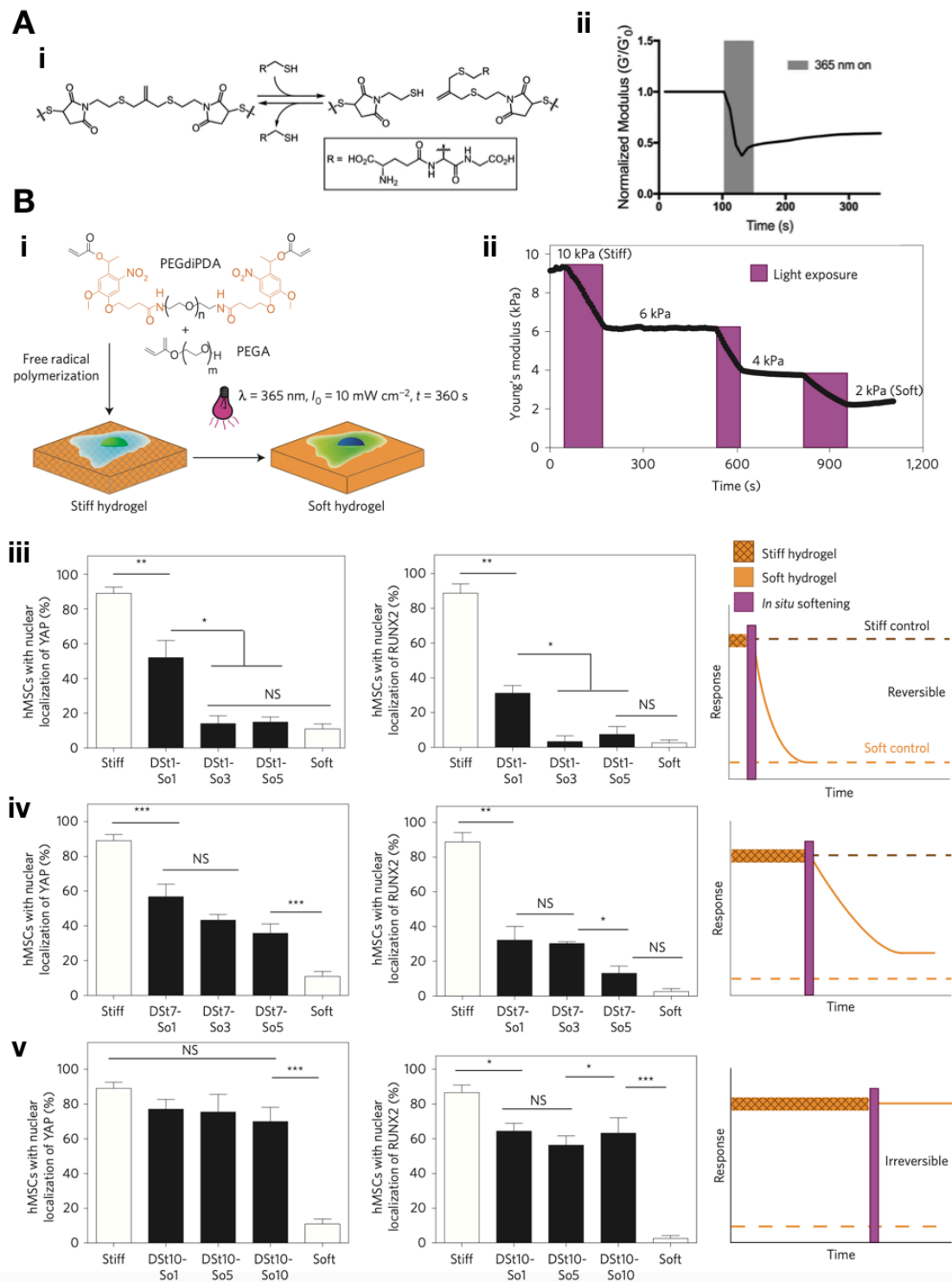


Figure II-14. Time of exposure to stiff microenvironments affects MSCs fate. A – Photo-responsive hydrogels with stiff-to-soft transition. (i) Mechanism that leads to the change of mechanical properties, where crosslink fragmentation is achieved through radical-mediated addition of glutathione to the allyl sulfide crosslinker. (ii) Normalized modulus of a hydrogel before and after light exposure (365 nm) in the presence of LAP. B – Photodegradable hydrogels with phototunable substrate modulus to study the reversibility of mechanical dosing. (i) hydrogels were prepared via free-radical polymerization of PEGdiPDA, a photodegradable

crosslinker, and monoacrylated PEG. Stiff to soft transition occurs upon light exposure at 365 nm, in presence of LAP. (ii) Changes on the young modulus with light exposure times, wherein different light doses can be used to tune the final mechanical properties. (iii) Cell culture on a stiff hydrogel for 1 day does not affect the YAP and RUNX2 (Runt-related transcription factor2) response to *in situ* softening, with MSCs demonstrating a transient and fully reversible activation of YAP and RUNX2. (iv) After 7 days of culture on stiff hydrogels, YAP and RUNX2 response to *in situ* softening and MSCs demonstrated a partially reversible activation of YAP and RUNX2. (v) However, of mechanical dosing on stiff hydrogels induced an irreversible activation of YAP and RUNX2, as YAP and RUNX2 persisted at active levels significantly above basal levels for soft hydrogels. Data presented as mean±SEM (standard error mean). NS, not significant; *, $p < 0.05$; **, $p < 0.01$; ***, $p < 0.001$. Adapted with permission from [177, 178].

Table II-2. Summary of the latest works addressing the effect of hydrogel mechanical properties in the mechanotransduction phenomena.

HYDROGEL	E (KPA)	PROPERTIES	CELL TYPE	MAIN EFFECT	MAIN CONCLUSIONS	REF
Polyacrylamide coated with type 1 collagen	0.015-0.07	2D Elastic	3T3 (fibroblasts) NRK (epithelial)	Cell adhesion	Stiffer substrates promote cell adhesion, by phosphotyrosine action on cell adhesion sites. Flexible substrates promote highly dynamic adhesion points.	[173]
Polyacrylamide coated with type 1 collagen	0.1-40	2D Elastic	MSCs	Cell differentiation	Soft matrices that mimic brain are neurogenic, stiffer matrices that mimic muscle are myogenic, and comparatively rigid matrices that mimic collagenous bone induce osteogenic differentiation	[174]
RGD-modified alginate	2.5-110	3D Elastic	MSCs	Cell adhesion	Cell-traction needed to sense and bind to cell adhesion motifs. RGD clustering was maximized in matrices of intermediate rigidity.	[175]
Polyacrylamide coated with fibronectin	1-160	2D Elastic	MSCs	Cell migration	MSC durotaxis is dependent on the stiffness gradient and not only stiffness	[172, 176]
Photodegradable PEG	2-30	2D Elastic	MSCs	DNA modification	MSCs retain mechanical information from past physical environments. Mechanical dosing for long periods causes constitutive alterations.	[177, 178]
RGD-modified alginate	9-17	3D Viscoelastic	MSCs	Cell migration, proliferation and differentiation	Faster relaxation times enhances cell spreading, proliferation and osteogenic differentiation of MSC.	[179]
Self-assembling peptides	1.5-9	3D Viscoelastic	MSCs	Hydrogel design	System provides control over matrix stiffness and binding sites.	[180]
RGD-modified alginate	3-30	3D Elastic	MSC and CNPCs	Transcriptome alterations	Cells encapsulated in hydrogels with different stiffness, stress relaxation and adhesion ligand density. RNA-seq analysis used to study the effect of each parameter on cells' transcriptome.	[165, 181]
Gelatin	2-24	2D Elastic	TDSC	Cell differentiation	Tenogenic, chondrogenic, and osteogenic lineages were inhibited on stiff hydrogels, due to fak and erk1/2 phosphorylation.	[182]
PEG DBCO	9-30	3D Elastic	C2C12	Cell differentiation; disease model	Mimicking of physiologic stiffening associated with muscle disease and aging. Stiffen matrices hamper spreading, with yap being concentrated in the cytoplasm.	[183]

Table II-2. Continued.

Dextran	6-109	3D Elastic	EPCs	Cell differentiation	Matrix stiffness regulates differentiation of EPCs during vasculogenesis. Stiffer gels induced higher vascularization, using the Ras/Mek signalling pathway.	[167]
Matrigel/alginate	0.09-0.93	3D Elastic	A549 (lung adenocarcinoma)	Cell migration and proliferation	Stiffer conditions enhanced cell proliferation and invasiveness.	[184]
PEG-diacrylate	10-60	2D Elastic	DP	ECM mimicking	Softer hydrogels are better to mimic the native environment of DP cells.	[168]
RGD-modified methacrylated ha	0.2-4.5	2D Elastic	MDA-MB-231Br	Cell adhesion, spreading, proliferation and migration.	Cell adhesion, spreading, proliferation, and migration significantly increased with the hydrogel stiffness. Response is mediated by focal adhesion kinase-phosphoinositide-3 kinase pathway.	[169]
PEG boronate	27-60	2D and 3D Viscoelastic	MSCs	Hydrogel design	Cytocompatible fast relaxing hydrogels, that maintain structural and mechanical properties under cell culturing conditions.	[185, 186]
HA/collagen	0.008-1.5	3D Viscoelastic	MSCs	ECM mimicking	Hydrogel captures the viscoelasticity and fibrillarity of ECM in tissues.	[187]
Polyacrylamide coated with fibronectin	3-35	2D Elastic	ASCs	Hydrogel design	High-throughput system allows to study 54 different extracellular matrix types of defined stiffness, shape, and area.	[188]
Polyacrylamide with hydroxyapatite microparticles	3-75	2D Elastic	DPSCs	Cell differentiation	Cells are affected by the mechanical properties of the hydrogel. Relatively stiff substrates (>75 kpa) may be needed for significant mineralization.	[189]
Polyacrylamide	16-19	2D Viscoelastic	3T3 (fibroblasts)	Hydrogel design	Method to prepare soft viscoelastic solids, with viscoelastic properties that can be tuned to closely mimic soft tissues.	[190]
Adamantane norbornene-modified HA/β-cyclodextrin-modified HA; polyacrylamide	0.1-10	2D Viscoelastic	MSCs and 3T3 (fibroblasts)	Hydrogel design	Mathematical modulation of dynamics of focal adhesions.	[191]
Polyacrylamide containing azobenzene	2-8	2D Elastic	MSCs	Hydrogel design	New platform to study mechano-signaling in cells responding to dynamic changes in stiffness.	[192]

Table II-2. Continued.

Collagen-coated methacrylated HA	0.150-3	2D Elastic	Mammary epithelial cells	Cell signaling pathways	Stiffness-dependent responses are modulated by TGF β and YAP signaling.	[193]
Fibronectin coated methacrylated HA	5-23	3D Elastic	MSCs	Hydrogel design (stiffness vs. volume)	3D microniches with varying stiffness and volume. Focal adhesion formation, stress fiber organization, and YAP/TAZ activity is not only regulated by substrate stiffness and is sensitive to cell volume.	[194]
Fibronectin-conjugated polyacrylamide	0.15-10	2D Elastic	ASCs	Vascularization	Soft substrates enhance ROS expression and the production of pro-angiogenic factors.	[166]
RGD - modified alginate	1-20	3D Viscoelastic	MSCs	Cell migration	Cells seeded on stiffer matrices expressed low laminin a/c and decreased nuclear stiffness. Nuclear deformation is then used to help cell migration.	[195]
Functionalized polyacrylamide	3-38	2D Elastic	Embryonic cells	Hydrogel design (stiffness vs. Biochemical cues)	Modification with different cell ligands to study the impact of biochemical cues on mechanotransduction. In intermediate concentration of biochemical cues, stem cell mechanotransduction depends on substrate stiffness. For low or very high concentrations biochemical cues override the effect of substrate stiffness. Regardless of substrate stiffness, low ligand concentration results in low nuclear YAP while high ligand concentration leads to high nuclear YAP.	[196, 197]
RGD-modified alginate	1-15	3D Elastic	MSCs, ASCs and UCSCs	Hydrogel optimization for cell differentiation	Platform allowed to establish the optimal combination of parameters for maximal differentiation, which varied with lineage and cell type.	[171]
Polyacrylamide	0.5-200	2D Elastic	MSCs	Cell paracrine function	Model to explore the effects of substrate stiffness on the paracrine function. Soft substrates elicit a higher production of immunomodulatory and trophic factors.	[198]
Hydrolyzed polyacrylamide	0.6–44	2D Elastic	Podocytes	Cell culture and ECM mimicking	Podocytes cultured on hydrogel with stiffness near the elasticity of the glomerular basement membrane (0.9 to 9.9 kPa) provides the best conditions for podocytes, with a normal regulation of podocin.	[199]

Table II-2. Continued.

Anthracene-functionalized PEG	10-50	2D Elastic	C2C12 and cardiac fibroblasts	Cell signaling pathways	Dynamic stiffening gels induce NFAT translocation into the nucleus of cardiac fibroblasts, which not happens when using static hydrogels.	[200]
Hydrazone crosslinked PEG	60	3D Viscoelastic	Chondrocytes	ECM mimicking	Viscoelastic hydrogel with different percentages of alkyl-hydrazone and benzyl-hydrazone. The incorporation of adaptable alkyl-hydrazone bonds improves neotissue formation.	[201]

NRK - Normal rat kidney epithelial cells; CNPCs - cortical neuron progenitor cells; TDSC - tendon-derived stem cells; DBCO – dibenzocyclooctyne; C2C12 - mouse myoblast cell line; EPCs - endothelial progenitor cells; DP - dermal papilla; MDA-MB-231Br - brain metastasizing variant of the triple negative breast cancer line MDA-MB-231; ROS - reactive oxygen species; DPSCs – dental pulp stromal cells; TGF β - transforming growth factor UCSCs – umbilical cord derived stem cells; NFAT - Nuclear factor of activated T-cells

II.5.3 Immune Response

Host immune responses often lead to an engraftment impairment or even rejection upon hydrogel *in vivo* implantation. Because of that, the immune system was for long considered a foe of TE strategies, and a substantial amount of work was developed to inhibit such unwanted immune response [207]. Nevertheless, the interplay between the immune system and biomaterials is more intricated than initially thought. In fact, some of the immune system effectors generate a positive outcome on tissue healing and regeneration. As a result, the immune system is now considered a regulator between tissue regeneration and rejection [208]. More than suppress its action, researchers are now focused on modulating the immune response to have a balanced spatiotemporal expression of the different immune effectors, yielding a successful *in vivo* implantation.

The paradigm shift occurred using Nature as a great source of inspiration. Recently, it was found that macrophages play a key role in the regeneration of salamander limbs after injury [209]. Later, the role of these cells on neonatal heart regeneration was unveiled, strengthening the importance of macrophages in the regeneration context [210]. This pivotal role arises mostly from the plasticity of these cells, which can be polarized in two different states, depending on the stimuli received. As part of the innate immune response, macrophages are immediately triggered after body exposure to a biomaterial. Macrophages phenotype can be broadly classified as M1 or M2, where M1 macrophages are linked with a pro-inflammatory function and M2 with anti-inflammatory and wound-healing action [211]. Upon activation, macrophages can stimulate T cells from the body's adaptive immune system, orchestrating a mutually dependent immune response that dictates the final biomaterial's immune environment. M1 macrophages boost T_H1 cells, which in turn stimulate the differentiation of more M1 macrophages, starting a feedback process that promotes a pro-inflammatory phenotype. On the other hand, M2 macrophages stimulate T_H2 cells which mediate a response towards tissue regeneration and wound healing (Figure II-15A) [212].

Thus, more than suppress the immune response, biomaterials should be designed to adjust the M1:M2 ratio, and consequently the T_H1/T_H2 response, towards the later. For that, it is important to consider several aspects of the biomaterial of choice, starting with the biomaterial type. As an example, the response triggered by HA is highly dependent on its molecular weight [213]. While high molecular weight HA typically exerts an anti-inflammatory effect, low molecular weight HA fragments are known to promote a T_H1 , pro-inflammatory response [214, 215]. Biomaterials containing methacrylic acid motifs can also bias macrophage into a regenerative pro-phenotype. Recently, PEG-hydrogels functionalized with

methacrylic acid showed promising results in a skeletal muscle implant, where they increased the expression of IL-10, TNF α , and M2 macrophage markers [216].

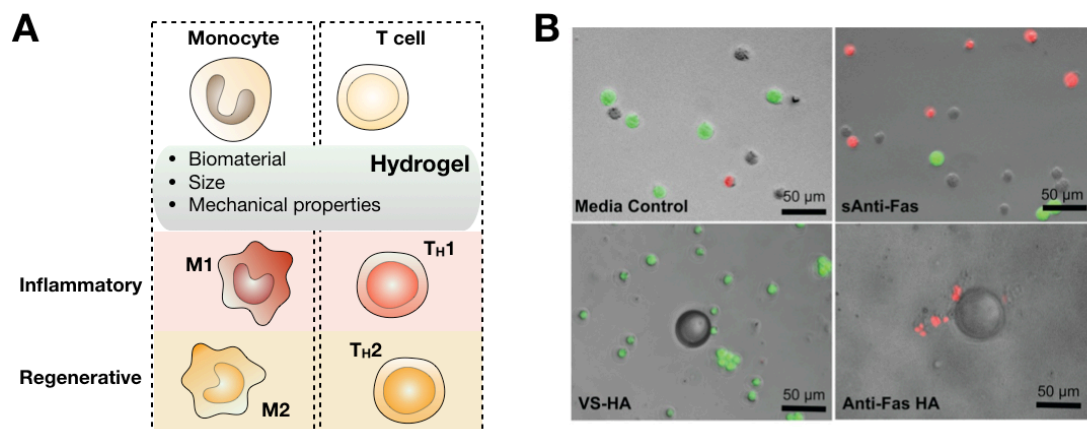


Figure II-15. Host immune response to hydrogels. A – Monocyte and T cell polarization is highly influenced by hydrogel properties, such as the biomaterial source, hydrogel size and mechanical properties. Monocytes can differentiate in M1 or M2 macrophages, and T cells polarize into T helper 1 (T_H1) or T helper 2 (T_H2). The final host immune response, inflammatory or pro-regenerative, will highly depend on the ratio of each of the differentiated/polarized cells. While M1 and T_H1 cells are typical of an inflammatory response, M2 and T_H2 are effectors of a pro-regenerative response. B – Hydrogels can be further modified to modulate the immune response. The presence of hyaluronic microsphere hydrogels modified with anti-Fas molecules (Anti-Fas HA) decreased T cell viability, as compared to a media control. Besides HA is known by its immunomodulatory properties, vinyl sulfone modified HA (VS-HA) hydrogels did not elicit the same toxic effect on T cells. Soluble anti-Fas (sAnti-Fas), was also able to decrease cell viability but in a lesser extent. Representative merged bright field and fluorescent images for T cells cultured for 48h. Adapted with permission from [217].

Dendritic cells also have a preeminent role in the immune response, via antigen-presentation to naïve T cells [218]. Similarly to macrophages, dendritic cells' activation is correlated with the nature of the biomaterial [218] as well as its source [219]. Park *et al.* studied the effect of different biomaterials on dendritic cell maturation. Their study revealed that high molecular weight HA inhibited dendritic cells maturation, contrarily to chitosan or poly(lactic-co-glycolic acid) [220]. Considering the tight relationship between dendritic cell's activation and T_H1-response, it is highly expected that materials capable of activating dendritic cells would elicit a strong inflammatory reaction [218].

The last paragraphs considered the biomaterial *per se* and how its inherent properties might interfere with the host immune system. Nevertheless, it is virtually possible to combine any molecule of interest to modulate the immune system towards a regenerative response [221]. As an example, HA hydrogels have been functionalized with anti-Fas molecules to improve the survival of neural stem cells [217].

Despite the natural anti-inflammatory properties of HA, the presence of anti-Fas elicit T cell death upon contact with the hydrogel, decreasing its viability to 65% as compared to control media (Figure II-15B). Addition of zwitterionic elements, as phosphorylcholine, can also be used to prevent the immune response [222, 223]. The strong electrostatic interactions between zwitterions and water molecules hinders the water displacement needed for protein binding on the material surface, thus affecting the material recognition by the immune system. Besides the source of the backbone polymer and final hydrogel size [224], the material mechanical properties [222] can also affect the final immune response.

II.6 Concluding Remarks and Future Trends

Hydrogel development opened up a new era for many scientific fields, including Tissue Engineering and Regenerative Medicine. These hydrated three-dimensional structures allow to better mimic the natural extracellular matrix conditions of different tissues, meaning that hydrogels are a suitable choice for recreating the *in vivo* cell microenvironment. Thence, hydrogels are a great alternative for the unrealistic two-dimensional culture conditions found on plastic surfaces, conferring a more realistic scenario.

And if it is true that several methods are available to prepare and modify hydrogel's properties, it is also important to stress how these changes and preparation methods can affect the final cell-material interaction. Changes in parameters such as polymer source or crosslink strategies, can lead to drastic changes in the final hydrogel outcome. Indeed, the possibility to dictate cell fate by tailoring the physical and chemical properties of the biomaterial has raised a great deal of interest. Undoubtedly, the crosslinking method plays an important role when envisioning tissue engineering applications. Often, it must comply with physiological parameters as well as with cell's delicate nature, which are not compatible with some of the developed methods. Rapid crosslinking periods using cell-friendly materials are typically desired and can be achieved using physical and chemical approaches. Moreover, the combination of both methods may endow hydrogels with further stability and functionality. Mainly, crosslinking methods that rely on dynamically reversible bounds are of great interest for the development of self-healing hydrogels. Indeed, the higher durability and stability of self-healing hydrogels, capable of shape recovery upon damage, are rather interesting features, and in the future, self-healing gels will probably change the current Tissue Engineering paradigm.

On the other side, the impact of this delicate and complex relationship between cells and microenvironment must be seriously considered. It is then necessary to think carefully about the design of a hydrogel, making sure that the gel meets the criteria of the intended applications. Besides studying

the cyto- and biocompatibility of the produced hydrogels, the study of the long-term hydrogel functionality it is of utmost importance. For example, a highly biodegradable hydrogel cannot be applied in immunoprotective approaches, and vice-versa, even if the hydrogel has shown great biocompatibility on previous studies. Regarding degradable hydrogels, most of their uses rely on a time-dependent degradation process that must be similar to the regeneration timeframe. Therefore, the field is focused on improving the network kinetics to fine-tune the degradation process, while avoiding the formation of deleterious hydrogel by-products.

On the other hand, the design of immunoprotective hydrogels is now focused on the development of new materials and/or chemistries that may better modulate the host immune response. Certainly, the last few years were prolific on the development of new, improved strategies with extraordinary results. Nevertheless, together with nutrient and oxygen diffusion, the adverse immune response is still the main bottleneck for the translation of this promising technology from the bench to the bedside, and therefore the efforts to improve this strategy will continue.

Considering the close material-cell relationship, the latest studies show that this impact starts as soon as cells contact with the biomaterial and sense the mechanical properties of their environment. Such contact can be irreversible and modify the cellular behavior to a great extent, and therefore it must be entirely understood to avoid unwanted cell responses. However, one can also use material's mechanical properties to easily instruct stem cells into defined cell lines, or secretory function, which are advantageous when designing tissue engineering solutions.

Regardless, hydrogel development is a bubbling field, and the new advances and designs brought new challenges. The possibility to engineer hydrogels that specifically respond to environmental cues paved the way for more targeted and active solutions. It is now possible to design dynamic materials, capable of responding to microenvironmental cues, as a native extracellular matrix (ECM). Such an exciting opportunity has driven several researchers to pursue of new and improved hydrogels that can dynamically change over time, as a response to an external stimulus or to the environment of the host diseased tissue. Certainly, dynamic hydrogels that can undergo temporal and spatial changes hold great potential for future Tissue Engineering applications. Therefore, it is highly expected an increase in the number of works related to new chemistries and engineering methods to precisely control the hydrogel fate and, consequently, cell responses.

II.7 References

1. Calo, E. and V.V. Khutoryanskiy, *Biomedical applications of hydrogels: A review of patents and commercial products*. European Polymer Journal, 2015. **65**: p. 252-267.
2. Ahadian, S., H. Savoji, and A. Khademhosseini, *Recent Advances in Hydrogels for Tissue Engineering*. Chemical Engineering Progress, 2018. **114**(5): p. 56-63.
3. Slaughter, B.V., et al., *Hydrogels in Regenerative Medicine*. Advanced Materials, 2009. **21**(32-33): p. 3307-3329.
4. Peppas, N.A., et al., *Hydrogels in biology and medicine: From molecular principles to bionanotechnology*. Advanced Materials, 2006. **18**(11): p. 1345-1360.
5. Annabi, N., et al., *25th anniversary article: Rational design and applications of hydrogels in regenerative medicine*. Advanced Materials, 2014. **26**(1): p. 85-123.
6. Khademhosseini, A. and R. Langer, *Microengineered hydrogels for tissue engineering*. Biomaterials, 2007. **28**(34): p. 5087-92.
7. Hoffman, A.S., *Stimuli-responsive polymers: biomedical applications and challenges for clinical translation*. Advanced Drug Delivery Reviews, 2013. **65**(1): p. 10-6.
8. Huang, G., et al., *Functional and Biomimetic Materials for Engineering of the Three-Dimensional Cell Microenvironment*. Chemical Reviews, 2017. **117**(20): p. 12764-12850.
9. Rosales, A.M. and K.S. Anseth, *The design of reversible hydrogels to capture extracellular matrix dynamics*. Nature Reviews Materials, 2016. **1**.
10. Guo, M., et al., *Tough stimuli-responsive supramolecular hydrogels with hydrogen-bonding network junctions*. Journal of the American Chemical Society, 2014. **136**(19): p. 6969-77.
11. Teng, L., et al., *Weak Hydrogen Bonds Lead to Self-Healable and Bioadhesive Hybrid Polymeric Hydrogels with Mineralization-Active Functions*. Biomacromolecules, 2018. **19**(6): p. 1939-1949.
12. Liu, B., et al., *Hydrogen bonds autonomously powered gelatin methacrylate hydrogels with super-elasticity, self-heal and underwater self-adhesion for sutureless skin and stomach surgery and E-skin*. Biomaterials, 2018. **171**: p. 83-96.
13. Ding, H.Y., et al., *Tough supramolecular hydrogels with excellent self-recovery behavior mediated by metal-coordination interaction*. Polymer, 2019. **171**: p. 201-210.
14. Yi, X., et al., *Tunable Mechanical, Antibacterial, and Cytocompatible Hydrogels Based on a Functionalized Dual Network of Metal Coordination Bonds and Covalent Crosslinking*. ACS Applied Materials and Interfaces, 2018. **10**(7): p. 6190-6198.
15. Rowland, M.J., et al., *An adherent tissue-inspired hydrogel delivery vehicle utilised in primary human glioma models*. Biomaterials, 2018. **179**: p. 199-208.

16. Wang, Z., et al., *A Rapidly Self-Healing Host-Guest Supramolecular Hydrogel with High Mechanical Strength and Excellent Biocompatibility*. *Angewandte Chemie International Edition*, 2018. **57**(29): p. 9008-9012.
17. Echalié, C., et al., *Chemical cross-linking methods for cell encapsulation in hydrogels*. *Materials Today Communications*, 2019. **20**.
18. Hu, W., et al., *Advances in crosslinking strategies of biomedical hydrogels*. *Biomaterials Science*, 2019. **7**(3): p. 843-855.
19. Hennink, W.E. and C.F. van Nostrum, *Novel crosslinking methods to design hydrogels*. *Advanced Drug Delivery Reviews*, 2002. **54**(1): p. 13-36.
20. Ghanian, M.H., H. Mirzadeh, and H. Baharvand, *In Situ Forming, Cytocompatible, and Self-Recoverable Tough Hydrogels Based on Dual Ionic and Click Cross-Linked Alginate*. *Biomacromolecules*, 2018. **19**(5): p. 1646-1662.
21. Ye, B.H., et al., *An in-situ formable and fibrils-reinforced polysaccharide composite hydrogel by self-crosslinking with dual healing ability*. *Composites Science and Technology*, 2018. **156**: p. 238-246.
22. Chen, T., et al., *Ultratough, Self-Healing, and Tissue-Adhesive Hydrogel for Wound Dressing*. *ACS Applied Materials and Interfaces*, 2018. **10**(39): p. 33523-33531.
23. Silva, S.S., et al., *2.11 Polymers of Biological Origin*, in *Comprehensive Biomaterials II*, P. Ducheyne, Editor. 2017, Elsevier: Oxford. p. 228-252.
24. Montanucci, P., et al., *Insights in Behavior of Variably Formulated Alginate-Based Microcapsules for Cell Transplantation*. *BioMed Research International*, 2015. **2015**: p. 965804.
25. Dodero, A., et al., *Alginate-based hydrogels prepared via ionic gelation: An experimental design approach to predict the crosslinking degree*. *European Polymer Journal*, 2019. **118**: p. 586-594.
26. Morch, Y.A., et al., *Effect of Ca²⁺, Ba²⁺, and Sr²⁺ on alginate microbeads*. *Biomacromolecules*, 2006. **7**(5): p. 1471-1480.
27. Miyoshi, E., T. Takaya, and K. Nishinari, *Effects of salts on the gel-sol transition of gellan gum by differential scanning calorimetry and thermal scanning rheology*. *Thermochimica Acta*, 1995. **267**: p. 269-287.
28. Chandrasekaran, R., *Interactions of Ordered Water and Cations in the Gel-Forming Polysaccharide Gellan Gum*. *Water Relationships in Foods*, 1991: p. 773-784.
29. Morris, E.R., K. Nishinari, and M. Rinaudo, *Gelation of gellan - A review*. *Food Hydrocolloids*, 2012. **28**(2): p. 373-411.
30. Vegas, A.J., et al., *Long-term glycemic control using polymer-encapsulated human stem cell-derived beta cells in immune-competent mice*. *Nature Medicine*, 2016. **22**(4): p. 446-446.

31. Facchi, D.P., et al., *Polyelectrolyte complexes based on alginate/tanfloc: Optimization, characterization and medical application*. International Journal of Biological Macromolecules, 2017. **103**: p. 129-138.
32. Oliveira, M.B., H.X.S. Bastos, and J.F. Mano, *Sequentially Moldable and Bondable Four-Dimensional Hydrogels Compatible with Cell Encapsulation*. Biomacromolecules, 2018. **19**(7): p. 2742-2749.
33. Alsharabasy, A.M., S.A. Moghannem, and W.N. El-Mazny, *Physical preparation of alginate/chitosan polyelectrolyte complexes for biomedical applications*. Journal of Biomaterials Applications, 2016. **30**(7): p. 1071-9.
34. Lv, X., et al., *Influence of chitosan oligosaccharide on the gelling and wound healing properties of injectable hydrogels based on carboxymethyl chitosan/alginate polyelectrolyte complexes*. Carbohydrate Polymers, 2019. **205**: p. 312-321.
35. Costa, R.R. and J.F. Mano, *Polyelectrolyte multilayered assemblies in biomedical technologies*. Chemical Society Reviews, 2014. **43**(10): p. 3453-79.
36. Li, H., et al., *Three-Dimensional Bioprinting of Oppositely Charged Hydrogels with Super Strong Interface Bonding*. ACS Applied Materials and Interfaces, 2018. **10**(13): p. 11164-11174.
37. Raghothaman, D., et al., *Cell type dependent morphological adaptation in polyelectrolyte hydrogels governs chondrogenic fate*. Biomedical Materials (Bristol, England), 2016. **11**(2): p. 025013.
38. Murakawa, K., et al., *Polyelectrolyte complexation via viscoelastic phase separation results in tough and self-recovering porous hydrogels*. Journal of Materials Chemistry B, 2019. **7**(35): p. 5296-5305.
39. Meka, V.S., et al., *A comprehensive review on polyelectrolyte complexes*. Drug Discovery Today, 2017. **22**(11): p. 1697-1706.
40. Sponchioni, M., U. Capasso Palmiero, and D. Moscatelli, *Thermo-responsive polymers: Applications of smart materials in drug delivery and tissue engineering*. Materials Science & Engineering. C: Materials for Biological Applications, 2019. **102**: p. 589-605.
41. Li, Z., et al., *Differentiation of cardiosphere-derived cells into a mature cardiac lineage using biodegradable poly(N-isopropylacrylamide) hydrogels*. Biomaterials, 2011. **32**(12): p. 3220-32.
42. Wang, L., et al., *Construction of Injectable Self-Healing Macroporous Hydrogels via a Template-Free Method for Tissue Engineering and Drug Delivery*. ACS Applied Materials and Interfaces, 2018. **10**(43): p. 36721-36732.
43. Ohya, Y., *Temperature-responsive biodegradable injectable polymer systems with conveniently controllable properties*. Polymer Journal, 2019. **51**(10): p. 997-1005.
44. Klouda, L., *Thermoresponsive hydrogels in biomedical applications: A seven-year update*. European Journal of Pharmaceutics and Biopharmaceutics, 2015. **97**(Pt B): p. 338-49.

45. Mellati, A., et al., *Microengineered 3D cell-laden thermoresponsive hydrogels for mimicking cell morphology and orientation in cartilage tissue engineering*. Biotechnology and Bioengineering, 2017. **114**(1): p. 217-231.
46. Wiltsey, C., et al., *Characterization of injectable hydrogels based on poly(N-isopropylacrylamide)-g-chondroitin sulfate with adhesive properties for nucleus pulposus tissue engineering*. Journal of Materials Science: Materials in Medicine, 2013. **24**(4): p. 837-47.
47. Pentlavalli, S., et al., *Simple Radical Polymerization of Poly(Alginate-Graft-N-Isopropylacrylamide) Injectable Thermoresponsive Hydrogel with the Potential for Localized and Sustained Delivery of Stem Cells and Bioactive Molecules*. Macromolecular Bioscience, 2017. **17**(11).
48. Klouda, L., et al., *Thermoresponsive, in situ cross-linkable hydrogels based on N-isopropylacrylamide: fabrication, characterization and mesenchymal stem cell encapsulation*. Acta Biomaterialia, 2011. **7**(4): p. 1460-7.
49. Schild, H.G., *Poly (N-Isopropylacrylamide) - Experiment, Theory and Application*. Progress in Polymer Science, 1992. **17**(2): p. 163-249.
50. Tang, S., et al., *Development of Novel N-isopropylacrylamide (NIPAAm) Based Hydrogels with Varying Content of Chrysin Multiacrylate*. Gels, 2017. **3**(4).
51. Rodkate, N. and M. Rutnakornpituk, *Multi-responsive magnetic microsphere of poly(N-isopropylacrylamide)/carboxymethylchitosan hydrogel for drug controlled release*. Carbohydrate Polymers, 2016. **151**: p. 251-259.
52. Fathi, M., et al., *Dual thermo-and pH-sensitive injectable hydrogels of chitosan/(poly(N-isopropylacrylamide-co-itaconic acid)) for doxorubicin delivery in breast cancer*. International Journal of Biological Macromolecules, 2019. **128**: p. 957-964.
53. Cheng, Y.H., S.H. Yang, and F.H. Lin, *Thermosensitive chitosan-gelatin-glycerol phosphate hydrogel as a controlled release system of ferulic acid for nucleus pulposus regeneration*. Biomaterials, 2011. **32**(29): p. 6953-61.
54. Zhang, T., et al., *Mechanical characterization of bioprinted in vitro soft tissue models*. Biofabrication, 2013. **5**(4): p. 045010.
55. Duan, B., et al., *3D bioprinting of heterogeneous aortic valve conduits with alginate/gelatin hydrogels*. Journal of Biomedical Materials Research Part A, 2013. **101**(5): p. 1255-64.
56. Bacelar, A.H., et al., *Recent progress in gellan gum hydrogels provided by functionalization strategies*. Journal of Materials Chemistry B, 2016. **4**(37): p. 6164-6174.
57. Silva-Correia, J., et al., *Gellan gum-based hydrogels for intervertebral disc tissue-engineering applications*. Journal of Tissue Engineering and Regenerative Medicine, 2011. **5**: p. e97-107.
58. Ren, Z.W., et al., *Effective Bone Regeneration Using Thermosensitive Poly(N-Isopropylacrylamide) Grafted Gelatin as Injectable Carrier for Bone Mesenchymal Stem Cells*. ACS Applied Materials and Interfaces, 2015. **7**(34): p. 19006-19015.

59. Robinson, G., C.E. Manning, and E.R. Morris, *Conformation and Physical Properties of the Bacterial Polysaccharides Gellan, Welan, and Rhamsan*, in *Food Polymers, Gels and Colloids*, E. Dickinson, Editor. 1991, Woodhead Publishing. p. 22-33.
60. Ferris, C.J., et al., *Modified gellan gum hydrogels for tissue engineering applications*. *Soft Matter*, 2013. **9**(14): p. 3705-3711.
61. Zhong, J., et al., *Hydrogel matrix to support stem cell survival after brain transplantation in stroke*. *Neurorehabilitation and Neural Repair*, 2010. **24**(7): p. 636-44.
62. Klotz, B.J., et al., *Gelatin-Methacryloyl Hydrogels: Towards Biofabrication-Based Tissue Repair*. *Trends in Biotechnology*, 2016. **34**(5): p. 394-407.
63. Brown, G.C.J., et al., *Covalent Incorporation of Heparin Improves Chondrogenesis in Photocurable Gelatin-Methacryloyl Hydrogels*. *Macromolecular Bioscience*, 2017. **17**(12).
64. Poldervaart, M.T., et al., *3D bioprinting of methacrylated hyaluronic acid (MeHA) hydrogel with intrinsic osteogenicity*. *PLoS ONE*, 2017. **12**(6): p. e0177628.
65. Williams, C.G., et al., *Variable cytocompatibility of six cell lines with photoinitiators used for polymerizing hydrogels and cell encapsulation*. *Biomaterials*, 2005. **26**(11): p. 1211-8.
66. Brown, T.E., et al., *Photopolymerized dynamic hydrogels with tunable viscoelastic properties through thioester exchange*. *Biomaterials*, 2018. **178**: p. 496-503.
67. Rao, V.V., et al., *Rescuing mesenchymal stem cell regenerative properties on hydrogel substrates post serial expansion*. *Bioengineering & Translational Medicine*, 2019. **4**(1): p. 51-60.
68. Applegate, M.B., et al., *Photocrosslinking of Silk Fibroin Using Riboflavin for Ocular Prostheses*. *Advanced Materials*, 2016. **28**(12): p. 2417-20.
69. Whittaker, J.L., et al., *Facile and rapid ruthenium mediated photo-crosslinking of Bombyx mori silk fibroin*. *Journal of Materials Chemistry B*, 2014. **2**(37): p. 6259-6270.
70. Dickerson, M.B., et al., *3D Printing of Regenerated Silk Fibroin and Antibody-Containing Microstructures via Multiphoton Lithography*. *ACS Biomaterials Science & Engineering*, 2017. **3**(9): p. 2064-2075.
71. Lim, K.S., et al., *Visible Light Cross-Linking of Gelatin Hydrogels Offers an Enhanced Cell Microenvironment with Improved Light Penetration Depth*. *Macromolecular Bioscience*, 2019. **19**(6): p. e1900098.
72. Aromaa, M.K. and P.K. Vallittu, *Delayed post-curing stage and oxygen inhibition of free-radical polymerization of dimethacrylate resin*. *Dental Materials*, 2018. **34**(9): p. 1247-1252.
73. Rydholm, A.E., C.N. Bowman, and K.S. Anseth, *Degradable thiol-acrylate photopolymers: polymerization and degradation behavior of an in situ forming biomaterial*. *Biomaterials*, 2005. **26**(22): p. 4495-506.

74. McCall, J.D. and K.S. Anseth, *Thiol-ene photopolymerizations provide a facile method to encapsulate proteins and maintain their bioactivity*. *Biomacromolecules*, 2012. **13**(8): p. 2410-7.
75. Lin, C.C., C.S. Ki, and H. Shih, *Thiol-norbornene photo-click hydrogels for tissue engineering applications*. *Journal of Applied Polymer Science*, 2015. **132**(8).
76. Fairbanks, B.D., et al., *A Versatile Synthetic Extracellular Matrix Mimic via Thiol-Norbornene Photopolymerization*. *Advanced Materials*, 2009. **21**(48): p. 5005-5010.
77. Fiedler, C.I., et al., *Enhanced mechanical properties of photo-clickable thiol-ene PEG hydrogels through repeated photopolymerization of in-swollen macromer*. *Soft Matter*, 2016. **12**(44): p. 9095-9104.
78. Gramlich, W.M., I.L. Kim, and J.A. Burdick, *Synthesis and orthogonal photopatterning of hyaluronic acid hydrogels with thiol-norbornene chemistry*. *Biomaterials*, 2013. **34**(38): p. 9803-11.
79. Acosta-Velez, G.F., et al., *Photocurable Bioink for the Inkjet 3D Pharming of Hydrophilic Drugs*. *Bioengineering (Basel)*, 2017. **4**(1).
80. Munoz, Z., H. Shih, and C.C. Lin, *Gelatin hydrogels formed by orthogonal thiol-norbornene photochemistry for cell encapsulation*. *Biomaterials Science*, 2014. **2**(8): p. 1063-1072.
81. Bertlein, S., et al., *Thiol-Ene Clickable Gelatin: A Platform Bioink for Multiple 3D Biofabrication Technologies*. *Advanced Materials*, 2017. **29**(44).
82. Ooi, H.W., et al., *Thiol-Ene Alginate Hydrogels as Versatile Bioinks for Bioprinting*. *Biomacromolecules*, 2018. **19**(8): p. 3390-3400.
83. Grigoryan, B., et al., *Multivascular networks and functional intravascular topologies within biocompatible hydrogels*. *Science*, 2019. **364**(6439): p. 458-464.
84. Xu, Z.H. and K.M. Bratlie, *Click Chemistry and Material Selection for in Situ Fabrication of Hydrogels in Tissue Engineering Applications*. *ACS Biomaterials Science & Engineering*, 2018. **4**(7): p. 2276-2291.
85. Gregoritz, M. and F.P. Brandl, *The Diels-Alder reaction: A powerful tool for the design of drug delivery systems and biomaterials*. *European Journal of Pharmaceutics and Biopharmaceutics*, 2015. **97**(Pt B): p. 438-53.
86. Gandini, A., *The furan/maleimide Diels-Alder reaction: A versatile click-unclick tool in macromolecular synthesis*. *Progress in Polymer Science*, 2013. **38**(1): p. 1-29.
87. Stewart, S.A., et al., *Cross-Linked Hydrogels Formed through Diels-Alder Coupling of Furan- and Maleimide-Modified Poly(methyl vinyl ether-alt-maleic acid)*. *Langmuir*, 2016. **32**(7): p. 1863-1870.
88. Nimmo, C.M., S.C. Owen, and M.S. Shoichet, *Diels-Alder Click cross-linked hyaluronic acid hydrogels for tissue engineering*. *Biomacromolecules*, 2011. **12**(3): p. 824-30.

89. Smith, L.J., et al., *Diels-Alder Click-Cross-Linked Hydrogels with Increased Reactivity Enable 3D Cell Encapsulation*. *Biomacromolecules*, 2018. **19**(3): p. 926-935.
90. Azagarsamy, M.A. and K.S. Anseth, *Bioorthogonal Click Chemistry: An Indispensable Tool to Create Multifaceted Cell Culture Scaffolds*. *ACS Macro Letters*, 2013. **2**(1): p. 5-9.
91. Lee, J.H., *Injectable hydrogels delivering therapeutic agents for disease treatment and tissue engineering*. *Biomaterials Research*, 2018. **22**: p. 27.
92. Rutz, A.L., et al., *Employing PEG crosslinkers to optimize cell viability in gel phase bioinks and tailor post printing mechanical properties*. *Acta Biomaterialia*, 2019. **99**: p. 121-132.
93. Qayyum, A.S., et al., *Design of electrohydrodynamic sprayed polyethylene glycol hydrogel microspheres for cell encapsulation*. *Biofabrication*, 2017. **9**(2): p. 025019.
94. Kim, J., et al., *Characterization of the crosslinking kinetics of multi-arm poly(ethylene glycol) hydrogels formed via Michael-type addition*. *Soft Matter*, 2016. **12**(7): p. 2076-85.
95. Teng, D.-y., et al., *Synthesis and characterization of in situ cross-linked hydrogel based on self-assembly of thiol-modified chitosan with PEG diacrylate using Michael type addition*. *Polymer*, 2010. **51**(3): p. 639-646.
96. Walimbe, T., et al., *Incorporation of types I and III collagen in tunable hyaluronan hydrogels for vocal fold tissue engineering*. *Acta Biomaterialia*, 2019. **87**: p. 97-107.
97. Wei, Z., et al., *Self-healing polysaccharide-based hydrogels as injectable carriers for neural stem cells*. *Scientific Reports*, 2016. **6**: p. 37841.
98. Pandit, A.H., N. Mazumdar, and S. Ahmad, *Periodate oxidized hyaluronic acid-based hydrogel scaffolds for tissue engineering applications*. *International Journal of Biological Macromolecules*, 2019. **137**: p. 853-869.
99. Kim, D.Y., et al., *Injectable hydrogels prepared from partially oxidized hyaluronate and glycol chitosan for chondrocyte encapsulation*. *Carbohydrate Polymers*, 2017. **157**: p. 1281-1287.
100. Zhang, Z., et al., *Rapid-Forming and Self-Healing Agarose-Based Hydrogels for Tissue Adhesives and Potential Wound Dressings*. *Biomacromolecules*, 2018. **19**(3): p. 980-988.
101. Hozumi, T., et al., *Injectable Hydrogel with Slow Degradability Composed of Gelatin and Hyaluronic Acid Cross-Linked by Schiff's Base Formation*. *Biomacromolecules*, 2018. **19**(2): p. 288-297.
102. Guebitz, G.M. and G.S. Nyanhongo, *Enzymes as Green Catalysts and Interactive Biomolecules in Wound Dressing Hydrogels*. *Trends in Biotechnology*, 2018. **36**(10): p. 1040-1053.
103. Rachel, N.M. and J.N. Pelletier, *Biotechnological applications of transglutaminases*. *Biomolecules*, 2013. **3**(4): p. 870-88.

104. Zhao, L., et al., *A novel smart injectable hydrogel prepared by microbial transglutaminase and human-like collagen: Its characterization and biocompatibility*. Materials Science & Engineering. C: Materials for Biological Applications, 2016. **68**: p. 317-326.
105. Liu, S.H., et al., *A Facile Strategy for Fabricating Tissue Engineering Scaffolds with Sophisticated Prevascularized Networks for Bulk Tissue Regeneration*. Macromolecular Materials and Engineering, 2019. **304**(5).
106. Araujo-Custodio, S., et al., *Injectable and Magnetic Responsive Hydrogels with Bioinspired Ordered Structures*. ACS Biomaterials Science & Engineering, 2019. **5**(3): p. 1392-1404.
107. Ranga, A., et al., *Hyaluronic Acid Hydrogels Formed in Situ by Transglutaminase-Catalyzed Reaction*. Biomacromolecules, 2016. **17**(5): p. 1553-60.
108. Cavalli, E., et al., *Characterization of polydactyl chondrocytes and their use in cartilage engineering*. Scientific Reports, 2019. **9**(1): p. 4275.
109. Partlow, B.P., et al., *Highly tunable elastomeric silk biomaterials*. Advanced Functional Materials, 2014. **24**(29): p. 4615-4624.
110. Kim, G., et al., *Tonsil-derived mesenchymal stem cell-embedded in situ crosslinkable gelatin hydrogel therapy recovers postmenopausal osteoporosis through bone regeneration*. PLoS ONE, 2018. **13**(7): p. e0200111.
111. Liu, Y., S. Sakai, and M. Taya, *Impact of the composition of alginate and gelatin derivatives in bioconjugated hydrogels on the fabrication of cell sheets and spherical tissues with living cell sheaths*. Acta Biomaterialia, 2013. **9**(5): p. 6616-23.
112. Sun Han Chang, R., et al., *Rheological Analysis of the Gelation Kinetics of an Enzyme Cross-linked PEG Hydrogel*. Biomacromolecules, 2019. **20**(6): p. 2198-2206.
113. Ren, K.X., et al., *Enzymatically crosslinked hydrogels based on linear poly(ethylene glycol) polymer: performance and mechanism*. Polymer Chemistry, 2017. **8**(45): p. 7017-7024.
114. Khanmohammadi, M., S. Sakai, and M. Taya, *Characterization of encapsulated cells within hyaluronic acid and alginate microcapsules produced via horseradish peroxidase-catalyzed crosslinking*. Journal of Biomaterials Science, Polymer Edition, 2019. **30**(4): p. 295-307.
115. Raia, N.R., et al., *Enzymatically crosslinked silk-hyaluronic acid hydrogels*. Biomaterials, 2017. **131**: p. 58-67.
116. Jooybar, E., et al., *An injectable platelet lysate-hyaluronic acid hydrogel supports cellular activities and induces chondrogenesis of encapsulated mesenchymal stem cells*. Acta Biomaterialia, 2019. **83**: p. 233-244.
117. Ashida, T., S. Sakai, and M. Taya, *Propagation of human iPS cells in alginate-based microcapsules prepared using reactions catalyzed by horseradish peroxidase and catalase*. Artificial Cells, Nanomedicine, and Biotechnology, 2016. **44**(6): p. 1406-9.

118. Sakai, S., et al., *Horseradish peroxidase/catalase-mediated cell-laden alginate-based hydrogel tube production in two-phase coaxial flow of aqueous solutions for filament-like tissues fabrication*. *Biofabrication*, 2013. **5**(1): p. 015012.
119. Ribeiro, V.P., et al., *Rapidly responsive silk fibroin hydrogels as an artificial matrix for the programmed tumor cells death*. *PLoS ONE*, 2018. **13**(4): p. e0194441.
120. Yan, L.P., et al., *Tumor Growth Suppression Induced by Biomimetic Silk Fibroin Hydrogels*. *Scientific Reports*, 2016. **6**: p. 31037.
121. Costa, J.B., et al., *Fast Setting Silk Fibroin Bioink for Bioprinting of Patient-Specific Memory-Shape Implants*. *Advanced Healthcare Materials*, 2017. **6**(22).
122. Su, D., et al., *Enhancing Mechanical Properties of Silk Fibroin Hydrogel through Restricting the Growth of beta-Sheet Domains*. *ACS Applied Materials and Interfaces*, 2017. **9**(20): p. 17489-17498.
123. Burdick, J.A., R.L. Mauck, and S. Gerecht, *To Serve and Protect: Hydrogels to Improve Stem Cell-Based Therapies*. *Cell Stem Cell*, 2016. **18**(1): p. 13-5.
124. Uman, S., A. Dhand, and J.A. Burdick, *Recent advances in shear-thinning and self-healing hydrogels for biomedical applications*. *Journal of Applied Polymer Science*, 2019.
125. Guo, B., et al., *Degradable conductive self-healing hydrogels based on dextran-graft-tetraaniline and N-carboxyethyl chitosan as injectable carriers for myoblast cell therapy and muscle regeneration*. *Acta Biomaterialia*, 2019. **84**: p. 180-193.
126. Spencer, A., et al., *Bioprinting of a cell-laden conductive hydrogel composite*. *ACS Applied Materials and Interfaces*, 2019.
127. Yao, M., et al., *A dual-enzymatically cross-linked injectable gelatin hydrogel loaded with BMSC improves neurological function recovery of traumatic brain injury in rats*. *Biomaterials Science*, 2019.
128. Lueckgen, A., et al., *Enzymatically-degradable alginate hydrogels promote cell spreading and in vivo tissue infiltration*. *Biomaterials*, 2019. **217**: p. 119294.
129. Han, W.M., et al., *Co-delivery of Wnt7a and muscle stem cells using synthetic bioadhesive hydrogel enhances murine muscle regeneration and cell migration during engraftment*. *Acta Biomaterialia*, 2019. **94**: p. 243-252.
130. Le Thi, P., et al., *In situ forming gelatin hydrogels by dual-enzymatic cross-linking for enhanced tissue adhesiveness*. *Journal of Materials Chemistry B*, 2017. **5**(4): p. 757-764.
131. Fonseca, K.B., P.L. Granja, and C.C. Barrias, *Engineering proteolytically-degradable artificial extracellular matrices*. *Progress in Polymer Science*, 2014. **39**(12): p. 2010-2029.

132. Kraehenbuehl, T.P., et al., *Three-dimensional extracellular matrix-directed cardioprogenitor differentiation: systematic modulation of a synthetic cell-responsive PEG-hydrogel*. Biomaterials, 2008. **29**(18): p. 2757-66.
133. Lutolf, M.P., et al., *Synthetic matrix metalloproteinase-sensitive hydrogels for the conduction of tissue regeneration: engineering cell-invasion characteristics*. Proceedings of the National Academy of Sciences of the United States of America, 2003. **100**(9): p. 5413-8.
134. Vigen, M., J. Ceccarelli, and A.J. Putnam, *Protease-sensitive PEG hydrogels regulate vascularization in vitro and in vivo*. Macromolecular Bioscience, 2014. **14**(10): p. 1368-79.
135. Stevens, K.R., et al., *Degradable hydrogels derived from PEG-diacrylamide for hepatic tissue engineering*. Journal of Biomedical Materials Research Part A, 2015. **103**(10): p. 3331-8.
136. da Silva, L.P., et al., *Gellan Gum Hydrogels with Enzyme-Sensitive Biodegradation and Endothelial Cell Biorecognition Sites*. Advanced Healthcare Materials, 2018. **7**(5).
137. Fonseca, K.B., et al., *Molecularly designed alginate hydrogels susceptible to local proteolysis as three-dimensional cellular microenvironments*. Acta Biomaterialia, 2011. **7**(4): p. 1674-82.
138. Fonseca, K.B., et al., *Injectable MMP-sensitive alginate hydrogels as hMSC delivery systems*. Biomacromolecules, 2014. **15**(1): p. 380-90.
139. Sun, J., et al., *The development of cell-initiated degradable hydrogel based on methacrylated alginate applicable to multiple microfabrication technologies*. Journal of Materials Chemistry B, 2017. **5**(40): p. 8060-8069.
140. Jha, A.K., et al., *Matrix metalloproteinase-13 mediated degradation of hyaluronic acid-based matrices orchestrates stem cell engraftment through vascular integration*. Biomaterials, 2016. **89**: p. 136-47.
141. Ren, Y., et al., *A collagen mimetic peptide-modified hyaluronic acid hydrogel system with enzymatically mediated degradation for mesenchymal stem cell differentiation*. Materials Science and Engineering: C, 2020. **108**: p. 110276.
142. de Vos, P. and P. Marchetti, *Encapsulation of pancreatic islets for transplantation in diabetes: the untouchable islets*. Trends in Molecular Medicine, 2002. **8**(8): p. 363-6.
143. Canibano-Hernandez, A., et al., *Hyaluronic acid enhances cell survival of encapsulated insulin-producing cells in alginate-based microcapsules*. International Journal of Pharmaceutics, 2019. **557**: p. 192-198.
144. Gimi, B. and K.V. Nemani, *Advances in alginate gel microencapsulation of therapeutic cells*. Critical Reviews in Biomedical Engineering, 2013. **41**(6): p. 469-81.
145. Duvivier-Kali, V.F., et al., *Complete protection of islets against allo rejection and autoimmunity by a simple barium-alginate membrane*. Diabetes, 2001. **50**(8): p. 1698-1705.

146. Oliveira, M.B., J. Hatami, and J.F. Mano, *Coating Strategies Using Layer-by-layer Deposition for Cell Encapsulation*. Chemistry, an Asian Journal, 2016. **11**(12): p. 1753-64.
147. Hu, S. and P. de Vos, *Polymeric Approaches to Reduce Tissue Responses Against Devices Applied for Islet-Cell Encapsulation*. Frontiers in Bioengineering and Biotechnology, 2019. **7**: p. 134.
148. An, D., et al., *Designing a retrievable and scalable cell encapsulation device for potential treatment of type 1 diabetes*. Proceedings of the National Academy of Sciences of the United States of America, 2018. **115**(2): p. E263-E272.
149. Harrington, S., et al., *Hyaluronic Acid/Collagen Hydrogel as an Alternative to Alginate for Long-Term Immunoprotected Islet Transplantation*. Tissue Engineering Part A, 2017.
150. Buchwald, P., et al., *Glucose-stimulated insulin release: Parallel perfusion studies of free and hydrogel encapsulated human pancreatic islets*. Biotechnology and Bioengineering, 2018. **115**(1): p. 232-245.
151. Hillberg, A.L., et al., *Encapsulation of porcine pancreatic islets within an immunoprotective capsule comprising methacrylated glycol chitosan and alginate*. Journal of Biomedical Materials Research, Part B: Applied Biomaterials, 2015. **103**(3): p. 503-18.
152. Day, J.R., et al., *The impact of functional groups of poly(ethylene glycol) macromers on the physical properties of photo-polymerized hydrogels and the local inflammatory response in the host*. Acta Biomaterialia, 2018. **67**: p. 42-52.
153. Weaver, J.D., et al., *Design of a vascularized synthetic poly(ethylene glycol) macroencapsulation device for islet transplantation*. Biomaterials, 2018. **172**: p. 54-65.
154. Day, J.R., et al., *Encapsulation of ovarian allograft precludes immune rejection and promotes restoration of endocrine function in immune-competent ovariectomized mice*. Scientific Reports, 2019. **9**(1): p. 16614.
155. Day, J.R., et al., *Immunoisolating poly(ethylene glycol) based capsules support ovarian tissue survival to restore endocrine function*. Journal of Biomedical Materials Research Part A, 2018. **106**(5): p. 1381-1389.
156. Lilly, J.L., et al., *Characterization of molecular transport in ultrathin hydrogel coatings for cellular immunoprotection*. Biomacromolecules, 2015. **16**(2): p. 541-9.
157. Stowers, R.S., et al., *Matrix stiffness induces a tumorigenic phenotype in mammary epithelium through changes in chromatin accessibility*. Nature Biomedical Engineering, 2019.
158. Schwartz, M.A. and D.W. DeSimone, *Cell adhesion receptors in mechanotransduction*. Current Opinion in Cell Biology, 2008. **20**(5): p. 551-6.
159. Wolfenson, H., B. Yang, and M.P. Sheetz, *Steps in Mechanotransduction Pathways that Control Cell Morphology*. Annual Review of Physiology, 2019. **81**: p. 585-605.

160. Burridge, K., E. Monaghan-Benson, and D.M. Graham, *Mechanotransduction: from the cell surface to the nucleus via RhoA*. Philosophical Transactions of the Royal Society, B: Biological Sciences, 2019. **374**(1779): p. 20180229.
161. Brusatin, G., et al., *Biomaterials and engineered microenvironments to control YAP/TAZ-dependent cell behaviour*. Nature Materials, 2018. **17**(12): p. 1063-1075.
162. Dupont, S., et al., *Role of YAP/TAZ in mechanotransduction*. Nature, 2011. **474**(7350): p. 179-83.
163. Crisp, M., et al., *Coupling of the nucleus and cytoplasm: role of the LINC complex*. Journal of Cell Biology, 2006. **172**(1): p. 41-53.
164. Cho, S., J. Irianto, and D.E. Discher, *Mechanosensing by the nucleus: From pathways to scaling relationships*. Journal of Cell Biology, 2017. **216**(2): p. 305-315.
165. Darnell, M., L. Gu, and D. Mooney, *RNA-seq reveals diverse effects of substrate stiffness on mesenchymal stem cells*. Biomaterials, 2018. **181**: p. 182-188.
166. Yang, H., et al., *Materials Stiffness-Dependent Redox Metabolic Reprogramming of Mesenchymal Stem Cells for Secretome-Based Therapeutic Angiogenesis*. Advanced Healthcare Materials, 2019. **8**(20): p. e1900929.
167. Xue, C., et al., *Matrix stiffness regulates arteriovenous differentiation of endothelial progenitor cells during vasculogenesis in nude mice*. Cell Proliferation, 2019. **52**(2): p. e12557.
168. Tan, J.J.Y., et al., *Impact of substrate stiffness on dermal papilla aggregates in microgels*. Biomaterials Science, 2018. **6**(6): p. 1347-1357.
169. Narkhede, A.A., et al., *The influence of matrix stiffness on the behavior of brain metastatic breast cancer cells in a biomimetic hyaluronic acid hydrogel platform*. Journal of Biomedical Materials Research Part A, 2018. **106**(7): p. 1832-1841.
170. Vining, K.H. and D.J. Mooney, *Mechanical forces direct stem cell behaviour in development and regeneration*. Nature Reviews Molecular Cell Biology, 2017. **18**(12): p. 728-742.
171. Hung, B.P., et al., *Defining hydrogel properties to instruct lineage- and cell-specific mesenchymal differentiation*. Biomaterials, 2019. **189**: p. 1-10.
172. Hadden, W.J., et al., *Stem cell migration and mechanotransduction on linear stiffness gradient hydrogels*. Proceedings of the National Academy of Sciences of the United States of America, 2017. **114**(22): p. 5647-5652.
173. Pelham, R.J., Jr. and Y. Wang, *Cell locomotion and focal adhesions are regulated by substrate flexibility*. Proceedings of the National Academy of Sciences of the United States of America, 1997. **94**(25): p. 13661-5.
174. Engler, A.J., et al., *Matrix elasticity directs stem cell lineage specification*. Cell, 2006. **126**(4): p. 677-89.

175. Huebsch, N., et al., *Harnessing traction-mediated manipulation of the cell/matrix interface to control stem-cell fate*. Nature Materials, 2010. **9**(6): p. 518-26.
176. Vincent, L.G., et al., *Mesenchymal stem cell durotaxis depends on substrate stiffness gradient strength*. Biotechnology Journal, 2013. **8**(4): p. 472-84.
177. Yang, C., et al., *Mechanical memory and dosing influence stem cell fate*. Nature Materials, 2014. **13**(6): p. 645-52.
178. Killaars, A.R., et al., *Extended Exposure to Stiff Microenvironments Leads to Persistent Chromatin Remodeling in Human Mesenchymal Stem Cells*. Advanced Science, 2019. **6**(3): p. 1801483.
179. Chaudhuri, O., et al., *Hydrogels with tunable stress relaxation regulate stem cell fate and activity*. Nature Materials, 2016. **15**(3): p. 326-34.
180. Hoglebe, N.J., et al., *Independent control of matrix adhesiveness and stiffness within a 3D self-assembling peptide hydrogel*. Acta Biomaterialia, 2018. **70**: p. 110-119.
181. Darnell, M., et al., *Material microenvironmental properties couple to induce distinct transcriptional programs in mammalian stem cells*. Proceedings of the National Academy of Sciences of the United States of America, 2018. **115**(36): p. E8368-E8377.
182. Liu, C., et al., *Matrix stiffness regulates the differentiation of tendon-derived stem cells through FAK-ERK1/2 activation*. Experimental Cell Research, 2018. **373**(1-2): p. 62-70.
183. Brown, T.E., et al., *Secondary Photocrosslinking of Click Hydrogels To Probe Myoblast Mechanotransduction in Three Dimensions*. Journal of the American Chemical Society, 2018. **140**(37): p. 11585-11588.
184. Alonso-Nocelo, M., et al., *Matrix stiffness and tumor-associated macrophages modulate epithelial to mesenchymal transition of human adenocarcinoma cells*. Biofabrication, 2018. **10**(3): p. 035004.
185. Tang, S., et al., *Adaptable Fast Relaxing Boronate-Based Hydrogels for Probing Cell-Matrix Interactions*. Advanced Science, 2018. **5**(9): p. 1800638.
186. Marozas, I.A., K.S. Anseth, and J.J. Cooper-White, *Adaptable boronate ester hydrogels with tunable viscoelastic spectra to probe timescale dependent mechanotransduction*. Biomaterials, 2019. **223**: p. 119430.
187. Lou, J., et al., *Stress relaxing hyaluronic acid-collagen hydrogels promote cell spreading, fiber remodeling, and focal adhesion formation in 3D cell culture*. Biomaterials, 2018. **154**: p. 213-222.
188. Major, L.G. and Y.S. Choi, *Developing a high-throughput platform to direct adipogenic and osteogenic differentiation in adipose-derived stem cells*. Journal of Tissue Engineering and Regenerative Medicine, 2018. **12**(10): p. 2021-2028.

189. Datko Williams, L., et al., *Effects of substrate stiffness on dental pulp stromal cells in culture*. Journal of Biomedical Materials Research Part A, 2018. **106**(7): p. 1789-1797.
190. Charrier, E.E., et al., *Control of cell morphology and differentiation by substrates with independently tunable elasticity and viscous dissipation*. Nature Communications, 2018. **9**(1): p. 449.
191. Gong, Z., et al., *Matching material and cellular timescales maximizes cell spreading on viscoelastic substrates*. Proceedings of the National Academy of Sciences of the United States of America, 2018. **115**(12): p. E2686-E2695.
192. Lee, I.N., et al., *Photoresponsive Hydrogels with Photoswitchable Mechanical Properties Allow Time-Resolved Analysis of Cellular Responses to Matrix Stiffening*. ACS Applied Materials and Interfaces, 2018. **10**(9): p. 7765-7776.
193. Ondeck, M.G., et al., *Dynamically stiffened matrix promotes malignant transformation of mammary epithelial cells via collective mechanical signaling*. Proceedings of the National Academy of Sciences of the United States of America, 2019. **116**(9): p. 3502-3507.
194. Bao, M., et al., *Cellular Volume and Matrix Stiffness Direct Stem Cell Behavior in a 3D Microniche*. ACS Applied Materials and Interfaces, 2019. **11**(2): p. 1754-1759.
195. Lin, C., et al., *Matrix promote mesenchymal stromal cell migration with improved deformation via nuclear stiffness decrease*. Biomaterials, 2019. **217**: p. 119300.
196. Lee, S., et al., *Hydrogels with enhanced protein conjugation efficiency reveal stiffness-induced YAP localization in stem cells depends on biochemical cues*. Biomaterials, 2019. **202**: p. 26-34.
197. Stanton, A.E., X. Tong, and F. Yang, *Extracellular matrix type modulates mechanotransduction of stem cells*. Acta Biomaterialia, 2019. **96**: p. 310-320.
198. Ji, Y., et al., *Substrate stiffness affects the immunosuppressive and trophic function of hMSCs via modulating cytoskeletal polymerization and tension*. Biomaterials Science, 2019.
199. Abdallah, M., et al., *Influence of Hydrolyzed Polyacrylamide Hydrogel Stiffness on Podocyte Morphology, Phenotype, and Mechanical Properties*. ACS Applied Materials and Interfaces, 2019. **11**(36): p. 32623-32632.
200. Gunay, K.A., et al., *PEG-Anthracene Hydrogels as an On-Demand Stiffening Matrix To Study Mechanobiology*. Angewandte Chemie International Edition, 2019. **58**(29): p. 9912-9916.
201. Richardson, B.M., et al., *Hydrazone covalent adaptable networks modulate extracellular matrix deposition for cartilage tissue engineering*. Acta Biomaterialia, 2019. **83**: p. 71-82.
202. Panciera, T., et al., *Mechanobiology of YAP and TAZ in physiology and disease*. Nature Reviews Molecular Cell Biology, 2017. **18**(12): p. 758-770.
203. Prager-Khoutorsky, M., et al., *Fibroblast polarization is a matrix-rigidity-dependent process controlled by focal adhesion mechanosensing*. Nature Cell Biology, 2011. **13**(12): p. 1457-65.

204. Mammoto, A., T. Mammoto, and D.E. Ingber, *Mechanosensitive mechanisms in transcriptional regulation*. Journal of Cell Science, 2012. **125**(Pt 13): p. 3061-73.
205. Chaudhuri, O., et al., *Substrate stress relaxation regulates cell spreading*. Nature Communications, 2015. **6**: p. 6364.
206. Wong, L., et al., *Substrate stiffness directs diverging vascular fates*. Acta Biomaterialia, 2019. **96**: p. 321-329.
207. Mitrousis, N., A. Fokina, and M.S. Shoichet, *Biomaterials for cell transplantation*. Nature Reviews Materials, 2018. **3**(11): p. 441-456.
208. Crupi, A., et al., *Inflammation in tissue engineering: The Janus between engraftment and rejection*. European Journal of Immunology, 2015. **45**(12): p. 3222-3236.
209. Godwin, J.W., A.R. Pinto, and N.A. Rosenthal, *Macrophages are required for adult salamander limb regeneration*. Proceedings of the National Academy of Sciences of the United States of America, 2013. **110**(23): p. 9415-20.
210. Aurora, A.B., et al., *Macrophages are required for neonatal heart regeneration*. Journal of Clinical Investigation, 2014. **124**(3): p. 1382-92.
211. Morris, A.H., D.K. Stamer, and T.R. Kyriakides, *The host response to naturally-derived extracellular matrix biomaterials*. Seminars in Immunology, 2017. **29**: p. 72-91.
212. Sadtler, K., et al., *Design, clinical translation and immunological response of biomaterials in regenerative medicine*. Nature Reviews Materials, 2016. **1**(7).
213. Zamboni, F., et al., *The potential of hyaluronic acid in immunoprotection and immunomodulation: Chemistry, processing and function*. Progress in Materials Science, 2018. **97**: p. 97-122.
214. Rayahin, J.E., et al., *High and low molecular weight hyaluronic acid differentially influence macrophage activation*. ACS Biomaterials Science & Engineering, 2015. **1**(7): p. 481-493.
215. Cyphert, J.M., C.S. Trempus, and S. Garantziotis, *Size Matters: Molecular Weight Specificity of Hyaluronan Effects in Cell Biology*. International Journal of Cell Biology, 2015. **2015**: p. 563818.
216. Carleton, M.M. and M.V. Sefton, *Injectable and degradable methacrylic acid hydrogel alters macrophage response in skeletal muscle*. Biomaterials, 2019. **223**: p. 119477.
217. Shendi, D., D.R. Albrecht, and A. Jain, *Anti-Fas conjugated hyaluronic acid microsphere gels for neural stem cell delivery*. Journal of Biomedical Materials Research Part A, 2017. **105**(2): p. 608-618.
218. Zhu, F.J., et al., *Role of dendritic cells in the host response to biomaterials and their signaling pathways*. Acta Biomaterialia, 2019. **94**: p. 132-144.

219. Molzer, C., et al., *Activation of dendritic cells by crosslinked collagen hydrogels (artificial corneas) varies with their composition*. Journal of Tissue Engineering and Regenerative Medicine, 2019. **13**(9): p. 1528-1543.
220. Park, J. and J.E. Babensee, *Differential functional effects of biomaterials on dendritic cell maturation*. Acta Biomaterialia, 2012. **8**(10): p. 3606-17.
221. Rowley, A.T., et al., *Extracellular Matrix-Based Strategies for Immunomodulatory Biomaterials Engineering*. Advanced Healthcare Materials, 2019. **8**(8).
222. Jansen, L.E., et al., *Zwitterionic PEG-PC Hydrogels Modulate the Foreign Body Response in a Modulus-Dependent Manner*. Biomacromolecules, 2018. **19**(7): p. 2880-2888.
223. Jain, P., et al., *Zwitterionic Hydrogels Based on a Degradable Disulfide Carboxybetaine Cross-Linker*. Langmuir, 2019. **35**(5): p. 1864-1871.
224. Veisoh, O., et al., *Size- and shape-dependent foreign body immune response to materials implanted in rodents and non-human primates*. Nature Materials, 2015. **14**(6): p. 643-651.

Section 2: Experimental Design

Chapter III: Materials and Methods

ABSTRACT

This chapter compiles all the relevant information regarding the materials and methods used in the experimental work developed under the scope of this thesis. Gellan gum hydrogels were prepared using different approaches and further characterized with distinct relevant techniques, which are described herein. For a rapid overview of all the techniques explored, a summary table is provided at the end of the present chapter.

III.1 Materials and Processing

III.1.1 Methacrylated Gellan Gum

As mentioned in previous Chapter 1, low acyl gellan gum (GG) is insoluble in water at room temperature. Thence, before being used as cell encapsulation matrix, GG solutions must be heated up to 50 °C, and then cooled using controlled conditions to avoid the thermal gelation of the material before cell incorporation. Also, the stability of physically crosslinked GG hydrogels is often compromised when implanted *in vivo* [1]. These drawbacks can be surpassed via chemical modification of the carboxylic group of GG by the addition of a methacrylate group [2], as shown in previous works regarding the development of injectable hydrogels for intervertebral disc regeneration. Indeed, low acyl GG can be chemically modified by the addition of methacrylate groups, as shown in Figure III-1, leading to an improved water solubility and processability at physiological temperature [2]. The obtained methacrylated gellan gum (GG-MA) hydrogels are then compatible with cell encapsulation. The mechanical properties of the resulting hydrogels, as well as their stability, are typically improved as compared to unmodified GG hydrogels [2]. Additionally, GG-MA based hydrogels did not elicit a significant inflammatory reaction after *in vivo* subcutaneous implantation in Lewis rats up to 18 days [3].

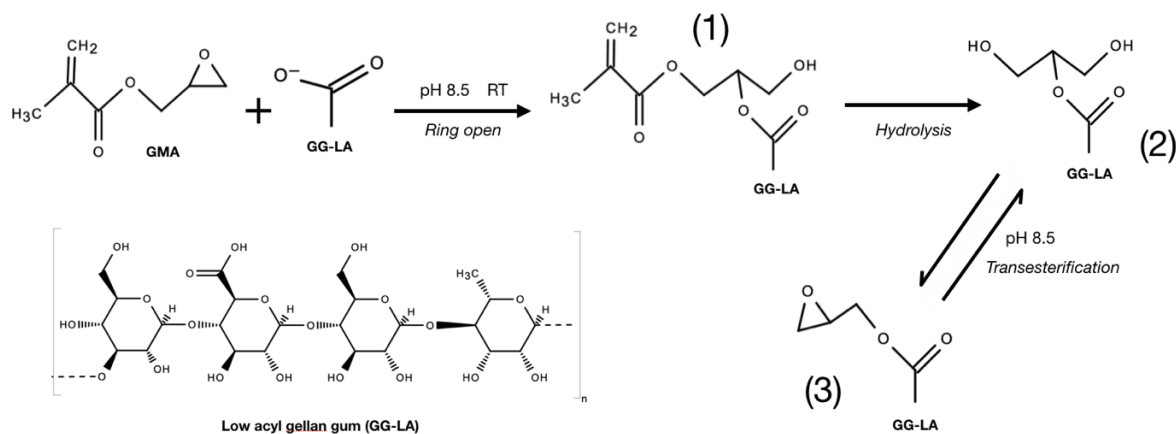


Figure III-1. Schematic representation of methacrylation reaction used to prepare GG-MA. Glycidyl methacrylate (GMA) is reacted with low-acyl gellan gum (GG-LA) under pH-controlled conditions (pH 8.5): (1) ring-opening product; (2) methacrylate hydrolysis mid-product; and (3) reversible trans-esterification product. Adapted from [2].

Methacrylated gellan gum (GG-MA) was obtained following the protocol from Silva-Correia *et al.* [2]. Concisely, glycidyl methacrylate (GMA, 97%, Sigma-Aldrich) was added to a low-acyl gellan gum solution (Gelzan™ CM Gelrite®, Sigma-Aldrich). This mixture was vigorously stirred overnight at room

temperature, with a constant control of pH at 8.5. After, cold acetone was used to precipitate the reaction products, which were further purified by dialysis (cellulose membrane, molecular weight cut-off 12 kDa, Sigma-Aldrich) against distilled water. At last, GG-MA was frozen at -80 °C and freeze-dried. The dry material was stored protected from light and in a dry place until further use.

The degree of substitution (DS, fraction of modified carboxyl groups per repeating unit) of the obtained GG-MA was assessed by proton nuclear magnetic resonance (¹H NMR) spectroscopy. This method relies on the magnetic properties of ¹H protons, giving an indication on the number of protons present in the analyzed compound. Since the obtained resonance signals are affected by the surrounding environment of each proton, ¹H NMR is a very attractive analysis technique to confirm polymer modification [4].

¹H NMR spectra were recorded with a 400 MHz Bruker Avance II spectrometer at 70 °C, on lyophilized materials dissolved in D₂O at a concentration of 10 mg.mL⁻¹. Chemical shifts were referred to the methyl group of rhamnose as an internal standard (δ 1.45 ppm [5]), and the DS was determined using Equation III-1 [1]. I_{DB} corresponds to the integration of the double bond proton peak of the methacrylate groups; I_{CH_3rham} to the integration of the methyl protons of the internal standard; n_{HDB} and n_{HCH_3rham} correspond to the number of protons in the double bond and the methyl group of rhamnose, respectively; and $n_{COOH_{monomer}}$ corresponds to the number of reactive -COO sites in the GG structure.

Equation III-1. Degree of substitution (DS).

$$DS = \frac{\frac{I_{DB}}{n_{HDB}}}{\frac{I_{CH_3rham}}{n_{HCH_3rham}}} \cdot n_{OH_{monomer}}$$

III.1.2 Hyaluronic Acid

Hyaluronic acid (HA) is a natural anionic glycosaminoglycan (GAG), commonly found in the extracellular matrix (ECM) of most animal tissues. As showed in Table I-1, this polymer comprises alternating units of glucuronic acid and *N*-acetylglucosamine [6-8]. HA is biodegradable, biocompatible, nonthrombogenic and nonimmunogenic [9-11], and is involved in several cellular processes, including angiogenesis, inflammation, cell adhesion and migration [12-14]. Therefore, HA has been used in the design of different tissue engineering constructs [9, 15-17].

Chapter VI addresses the use of HA in combination with GG-MA for cell encapsulation purposes. The developed hydrogels were prepared using ultra-pure sodium hyaluronate (NaHA) gently provided by DuPont™ (NovaMatrix® Sodium Hyaluronate Pharma Grade 150). According to the manufacturer, this product is prepared using sodium hyaluronate fermented from *Streptococcus zooepidemicus*, and further purified to high levels of purity. The properties of the resulting material are listed in Table III-1.

Table III-1. Properties of NovaMatrix® Sodium Hyaluronate Pharma Grade 150 (DuPont™).

Intrinsic Viscosity (m ³ .Kg ⁻¹)	2.1-2.8
Approximate Molecular Weight (kDa)	1200-1900
Endotoxins (EU.g ⁻¹)	≤ 40

III.1.3 Poly-L-lysine

Poly-L-lysine (PLL) is a cationic lysine homopolymer (Figure III-2), routinely used to coat tissue culture plastics as a way to increase cell adhesion to this material. PLL is also quite used to improve the durability and tune permeability of bulk anionic polymeric beads [18]. At pH 7, PLL contains a positively charged amino group, that easily interacts with negatively charged molecules, including proteins and cells' membrane elements. However, when PLL is used envisioning tissue engineering constructs, it is often necessary to mask this polymer, since PLL is known to be immunogenic [19].

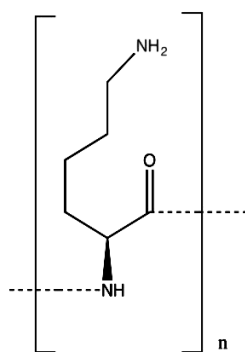


Figure III-2. Chemical structure of PLL.

In this work, PLL (Mw 150,000-300,000, Sigma-Aldrich) was used in Chapter VII and Chapter VIII to obtain semipermeable polyelectrolyte complexes, wherein the presence of PLL would modulate the permeability of bulk GG-MA.

III.2 Physicochemical Characterization

III.2.1 Weight Loss Ratio

Degradation kinetics is an important parameter to follow while designing hydrogels for tissue engineering applications [20]. As discussed in Chapter II, different applications require distinct degradation behaviors that can be tuned by means of using different hydrogel formulations.

In the present work, hydrogel degradation was evaluated by studying its weight loss ratio profile upon incubation in a suitable buffer solution. In Chapter V and Chapter VI, hydrogels were incubated in artificial cerebrospinal fluid (aCSF), as this solution is more suitable for mimicking the target environment; in Chapter VII and Chapter VIII, hydrogels were incubated in phosphate buffered saline (PBS). To better mimic a physiologic-like scenario, weight loss ratio was also assessed when in presence of enzymes. For that, PBS and aCSF were further supplemented with relevant enzymes, and incubation was performed at 37 °C. The weight loss ratio was calculated considering the weight of as-prepared hydrogels as initial weight (m_i). Then, hydrogels were incubated at 37 °C in the different incubation solutions. After specific time points, hydrogels were gently removed from the solutions, and the final mass of the samples was determined (m_f). Equation III-2 was applied to calculate the weight loss ratio at each time point.

Equation III-2. Weight loss ratio.

$$\text{Weight loss ratio (\%)} = \left(\frac{m_i - m_f}{m_i} \right) \times 100$$

III.2.2 Size Variation of Hydrogels

Another approach to quantify hydrogel stability under different conditions is to monitor its size along time (Figure III-3). On the hereby reported work, size variation was followed for the polyelectrolyte hydrogels prepared on Chapter VII and Chapter VIII. Hydrogel samples were incubated in PBS solutions with different pH (pH 4, pH 7.4 and pH 10) and cell culture media (α -MEM, Gibco®, Life Technologies), supplemented with 10 vol.% of heat-inactivated fetal bovine serum (FBS, Gibco®, Life Technologies, reference A3160802, EU approved) and 1 vol.% antibiotic-antimycotic solution (penicillin 100 units.mL⁻¹ and streptomycin 100 mg.mL⁻¹, Gibco®, Life Technologies) to evaluate size variations along time.

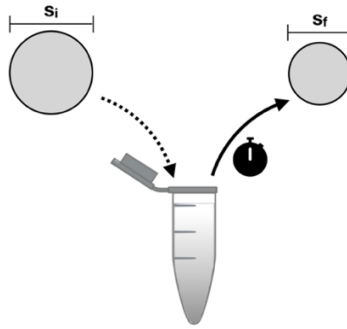


Figure III-3. Schematic representation of the methodology used to access hydrogel's size variation. Hydrogels with initial size s_i were incubated in PBS for a determined period. At distinct timepoints, hydrogels were retrieved and the final size (s_f) measured.

Optical images were obtained at defined timepoints, using brightfield microscopy, and beads' diameter measured using ImageJ software (version: 2.0.0-rc-69/1.52p). Considering that the size obtained at day 0 is the initial size (s_i) and that each time point a new size value was obtained (s_f), size variation was then obtained by applying Equation III-3.

Equation III-3. Size variation.

$$\text{Size variation (\%)} = \frac{s_f - s_i}{s_i} \times 100$$

III.2.3 Scanning Electron Microscopy

Scanning electron microscopy (SEM) was used to evaluate the surface of the developed materials at submicron resolutions [21], particularly samples' morphology and geometry. SEM micrographs can be obtained after the interaction between a material's surface and a focused electron beam. Briefly, while the electron beam is swept along the samples' surface, the escape of the incident electrons results in the emission of secondary electrons from the analyzed surface (Figure III-4). The dislocated electrons are collected and counted by a detector and are then converted into photons, rendering a final digital image. The depth resolution in secondary electron imaging can be as low as 1-10 nm [21].

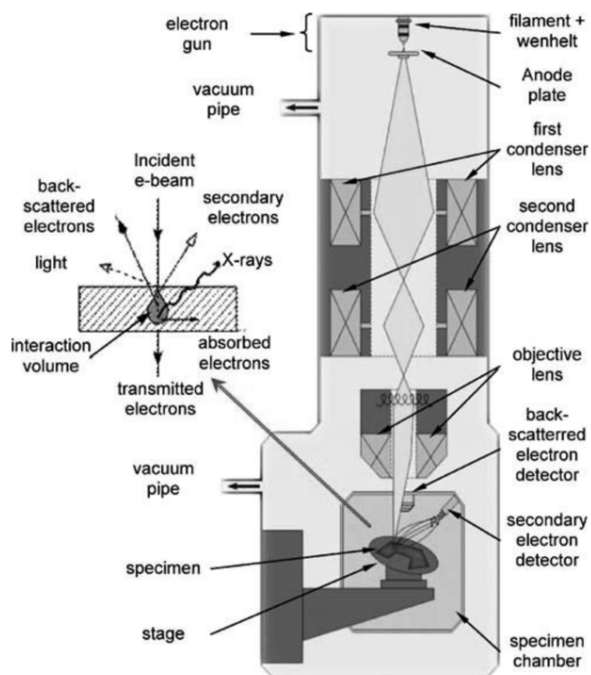


Figure III-4. Schematic representation of a scanning electron microscope and signal generation. The incident electron beam (e-beam) enters the sample, colliding with sample atoms. Upon reaching the sample, some electrons are back scattered and exit the sample. The secondary electrons generated close to the sample's surface can also escape from the sample, converted to photons, and counted by a photomultiplier tube. Retrieved from [22].

Herein, SEM was used in Chapter IV, Chapter VII and Chapter VIII. All samples were analyzed in its dry state. For that, the hydrogels were quickly frozen within liquid nitrogen, followed by sublimation under high vacuum to remove the dispersed solvent (LyoAlfa 10/15, Telstar). Flash freezing was preferred to avoid the formation of big ice crystals that may interfere with the final structure.

The use of dry material allowed to perform the electron microscopy technique at high-vacuum conditions, that prevents the electrons from being absorbed and scattered by molecules in the natural atmosphere [23]. Prior to SEM visualization, samples were fixed by mutual conductive adhesive tape and coated with a thin layer of gold using a sputter coater (EM ACE600, Leica). These steps help on the prevention of a “charging” phenomenon that may introduce errors on the analysis. Further electron beam damage of the samples, and artificial changes arising from the coating process, were considered non-relevant. To avoid damaging beam effects (burning effect), the hydrogels were visualized using a FEI Nova NanoSEM 200 operating at 15 kV accelerating voltage.

III.2.4 Energy Dispersive Spectroscopy

Scanning electron microscopes can also be used to further characterize samples regarding its qualitative and quantitative elemental composition. This method, energy-dispersive X-ray spectroscopy (EDS), takes advantage of the emitted X-rays from a sample upon interaction with the focused electron beam [21]. EDS relies on the measurement of the energy and intensity of these X-rays to identify the surface elemental composition of a sample.

In this work, EDS (QUANTAX200 Bruker, Germany) was used to study biomineralization of the hydrogels developed in Chapter IV. Prior to SEM analysis, samples were placed inside the SEM chamber without the gold pre-coating, as the presence of a coating layer might disturb the analysis.

III.2.5 X-ray Diffraction

X-ray diffraction (XRD) takes advantage of the interaction of X-rays with matter, to reveal detailed information about the crystallographic structure of samples [24]. When X-rays penetrate a material they are attenuated, absorbed, and scattered. For XRD, the most important effect is the Rayleigh (or coherent) scattering, which consists in an elastic scattering of X-ray photons due to its interaction with atoms in a periodic lattice [25]. In XRD experiments, samples are bombarded by an X-ray beam, and the intensity of the scattered X-rays is measured as a function of their scattering angle. The lattice spacing of a crystal can then be derived using the Bragg's law (Equation III-4).

Equation III-4. Bragg's law.

$$n\lambda = 2d \sin \theta$$

where n is the order of reflection, λ is the wavelength of x-rays, d is the characteristic spacing between the crystal planes of a given specimen, and θ is the angle between the incident beam and the normal to the reflecting lattice plane. Therefore, it is possible to determine the interplanar spacing d of crystallographic phases by measuring the scattering angles θ [26]. While amorphous samples produce broad peaks, covering the scattering angles, crystalline materials produce sharp peaks at specific angles. The recorded diffraction pattern can be compared with standard line patterns available in the literature, making possible the identification of unknown substances.

In this thesis, XRD was used in Chapter IV to study the crystalline structure of samples before and after bioactive studies, particularly the crystallinity of the developed apatite shell after incubation in simulated

body fluid (SBF). For that, a D8 Advance diffractometer (Bruker) using a Cu -K α radiation source was operated at 40kV, and 40mA (data were collected between $2\theta=5^\circ$ and 80°).

III.2.6 Micro-Computed Tomography

Micro-computed tomography (μ -CT) is a non-destructive imaging technique that allows a three dimensional visualization of the internal microstructure of objects, using X-rays [27]. For that, samples are placed in a rotative stage and illuminated by a micro-focused X-ray. At each rotation angle, a gray-scale magnified projection image is acquired at the μ -CT detector. The obtained images are then used to obtain a stack of virtual cross-section slices of the imaged object, considering the angular views acquired while the object rotates. The stack can be further processed, using a suitable imaging software, allowing surface rendering, volume rendering, or image segmentation to create realistic visual models of the object.

In the present work, μ -CT imaging was used to follow the apatite formation on the surface of the hydrogels developed in Chapter IV. The hydrogel *per se* has a low contrast, making its imaging a challenging approach. Regardless, the developed apatite layer is easily distinguishable in μ -CT images, due to its radiopacity. Acquisition was performed using a μ -CT (Skyscan 1772, Bruker, Germany), operated at 50 kV and image pixel size of 5 μ m. ImageJ software (version: 2.0.0-rc-69/1.52p) was used to re-construct the subsequent 3D images. At least, five samples were used per condition and per time point.

III.2.7 Calcium Colorimetric Assay

On Chapter IV, hydrogels were prepared using a CaCl₂ bath solution to promote an ionic crosslink of the polymeric matrix. Although the bath concentration is known, the final amount of calcium that is present inside the hydrogel matrix needed to be further quantified. Therefore, the calcium content was quantified after hydrogel samples production, using a Calcium Colorimetric Assay Kit (Roche), following the manufacturer's instructions. As prepared samples, making up a final GG-MA volume of 100 μ L, were mechanically destroyed in 1 mL of Milli-Q water. Then, 5 mL of this solution was mixed with 5 mL of 6 M HCl for 30 minutes, followed by the addition of proper volumes of the commercial reagents provided in the kit. Milli-Q water was used as "blank" control.

III.2.8 Rheology

The viscoelastic properties of the hydrogels developed under Chapter V and Chapter VI were quantified using oscillatory shear rheometry, specifically small amplitude oscillatory tests, as depicted in Figure III-5 [28]. The viscoelastic properties can be acquired under shear flow conditions, upon action of an external

shear force (F) over a unit area (A), taking the form of a shear stress (σ , Pa). In response, the upper layer of the fluid moves a given distance x , but the bottom remains stationary, thus creating a displacement gradient across the sample, termed shear strain (γ). In fluids, the shear strain continues to increase while the shear stress exists, creating a velocity gradient along the fluid – shear rate ($\dot{\gamma}$, s^{-1}) – which is the rate of change of strain with time.

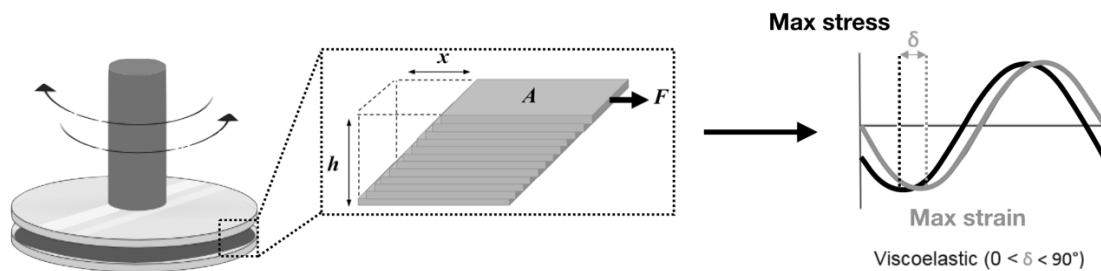


Figure III-5. Illustration of an oscillatory experiment using a parallel plate geometry, and resulting stress and strain wave relationships, for a viscoelastic material.

To perform the oscillatory tests, samples were loaded between two parallel plates separated by a known gap (h), where the upper plate oscillated at a given strain amplitude and frequency. The ratio of the applied strain to the measured stress determines the complex modulus (G^*) which is a quantitative measure of material stiffness (Equation III-5). The complex modulus can be represented as a sum of the elastic contribution (G' , storage modulus) and the viscous contribution (G'' , loss modulus). In viscoelastic materials, the response is time-delayed compared to the established oscillation. Therefore, the phase difference between stress and strain, the phase angle (δ), allowed the determination of the elastic (G') and viscous (G'') contributions, according to Equation III-6 [28].

Equation III-5. Complex modulus.

$$G^* = \frac{\sigma_{max}}{\gamma_{max}} = G' + iG''$$

Equation III-6. Phase difference (phase angle expressed as loss tangent).

$$\tan \delta = \frac{G''}{G'}$$

In the present work, the rheological analyses were performed using a Kinexus Pro+ rheometer (Malvern Instruments, UK), using the acquisition software rSpace. The measuring system was equipped with stainless steel (316 grade) parallel plates: the upper measurement geometry plate, with 8 mm of

diameter, and the 20 mm lower pedestal with roughened finish (to prevent sample slippage and resulting errors on the experiments). First, the Linear Viscoelastic Region was determined, and then single-frequency oscillation experiments were performed at 0.1 Hz for 30 minutes. Shear viscosity and shear stress were determined by rotational experiments, using an upper measurement geometry cone (40 mm diameter and 4° angle). All experiments were performed at 37 °C, and plots are the average of at least 3 experiments.

III.2.9 Injection Ability

Chapter V and Chapter VI refer to the design of injectable hydrogels for minimally invasive therapies. To be successful, the hydrogels must be compatible with a facile administration, which is only achieved when the forces needed to extrude the hydrogel are feasible for the applicant.

In this regard, the force needed to extrude the different hydrogels was measured using an in-house injection equipment (Paralab), as showed in Figure III-6. The pre-gel solutions were used to fill a 10 μL Hamilton syringe coupled with a 31 G needle. The material was extruded, by means of applying a force on the syringe piston, using a constant extrusion rate ($10 \mu\text{L}\cdot\text{min}^{-1}$). Thus, the load needed to extrude the material through the 31 G needle was measured and recorded using an appropriate software.

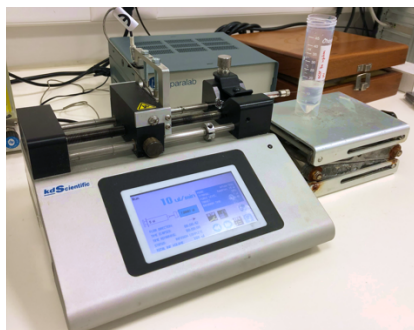


Figure III-6. Setup used to measure the force needed to extrude hydrogels. A syringe is mounted in a syringe pump, that simulates the use of the syringe. The force needed to extrude the hydrogel precursor is monitored and recorded using a suitable software.

III.2.10 Inductively Coupled Plasma-Optical Emission Spectrometry

Inductively coupled plasma-optical emission spectrometry (ICP-OES) was used to determine trace elements release from the hydrogels [29], prepared on the scope of Chapter V and Chapter VI. In this technique, liquid samples are injected into the instrument and converted to an aerosol by a nebulizer. Then, the aerosol is directed into a radiofrequency-induced argon plasma (40.86 MHz). When the sample mist reaches the plasma, it is dried, vaporized, and energized. As result, the component elements of the

sample, *i.e.* the sample's atoms, are excited. Both the atomic and ionic excited state species then return to low energy positions, leading to the emission of photons. The wavelength of the emitted photons is used to identify the elements from which they originated, while the total number of photons is directly proportional to the concentration of the originating element in the sample [30].

Thus, the release of manganese ions (Mn^{2+}) was quantified using ICP-OES (ICP; JY2000 2, Jobin Yvon, Horiba). Before analysis, all samples were dissolved in nitric acid, filtered using a 0.22 μm filter, and finally injected into the instrument. Manganese ($\lambda_{em}=259.37$ nm) concentrations were obtained by comparison with standard solutions, with a detection limit of 5 ppb.

III.2.11 X-ray Photoelectron Spectroscopy

Surface elemental composition of hydrogels prepared in Chapter VIII was studied using X-ray photoelectron spectroscopy (XPS, Axis Supra, Kratos, United Kingdom). Dehydrated samples were placed in an ultrahigh vacuum chamber to maximize the number of photoelectrons that reach the analyzer. Also, a co-axial electron neutralizer was used to minimize surface charging, which performed the neutralization by itself. As depicted in Figure III-7, once inside the chamber, samples were irradiated by a focused X-ray beam, produced by a monochromatic Al (K) X-ray source operating at 1486.6 eV, leading to a photoemission of core-level electrons of atoms present in the sample. Photoelectrons were collected from a take-off angle of 90° relative to the sample surface. Constant analyzer energy mode (CAE) with 160 eV pass energy was used for survey spectra while high-resolution spectra were recorded at 40 eV pass energy. Charge referencing was performed by setting lower binding energy C 1s photo peak at 285.0 eV.

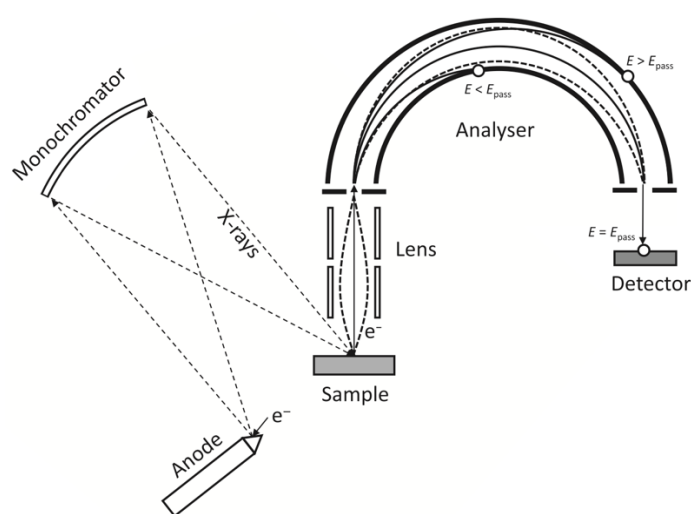


Figure III-7. Schematic representation of an XPS equipment. Retrieved from [31].

Surface elemental composition was then determined using the ESCApe™ software (Kratos, United Kingdom). Briefly, this software processes the data and converts the kinetic energy of the emitted electrons (KE) to binding energy (BE) using a relationship based on the photoelectric effect. As result, an XPS spectrum is retrieved, showing the BE (eV) on the x-axis and intensity of the peaks on the y-axis (arbitrary units – a.u.). The identification of the elements present in the samples is achieved considering that the binding energies of the core-level electrons are characteristic for each element. Thus, the detection of the emitted electrons, and their characteristic kinetic energies, allows a proper identification of the elements, and also provides information about their chemical and electronic state. The peak intensities in the energy spectrum are proportional to the number of atoms in the sample [32].

III.2.12 Zeta Potential

The work reported in Chapter VIII relates to the preparation and characterization of polyelectrolyte complexes. This includes the characterization of the polymeric materials used to prepare those complexes, particularly their electrical charge.

Briefly, for the assessment of this physical property it is assumed that, in a solution, each particle is surrounded by a liquid layer of oppositely charged ions. This layer, also called electrochemical double layer (Figure III-8), can be divided in two distinct parts: (i) inner region, or Stern layer, where the oppositely charged ions are strongly bond; and (ii) a diffuse region, that includes ions of different polarities, thus less firmly associated. The slipping plane, *i.e.* a theoretical boundary inside which the ions act as a single entity, is located within this diffuse layer and is used to measure the zeta potential [33]. Therefore, the zeta potential establishes the electrical potential difference between the dispersion media and the stationary layer of fluid surrounding the dispersed particles.

The existence of electrical charges on particles' surface allows its interaction with applied electrical fields. Such interactions result in particle movement, that is highly dependent on the way in which the movement is induced. As example, electrophoresis relates to a movement of a charged particle relative to the surrounding liquid under the influence of an applied electric field. Charged particles suspended in the electrolyte are thus attracted towards the electrode of opposite charge. After reaching an equilibrium, the particles move with a constant velocity that is dependent on the strength of the electric field, the dielectric constant of the medium, the viscosity of the medium and, at last, the zeta potential. Thence, although the zeta potential is not directly measured, it can be calculated using established theoretical models, particularly the one developed by Marjan von Smoluchowski.

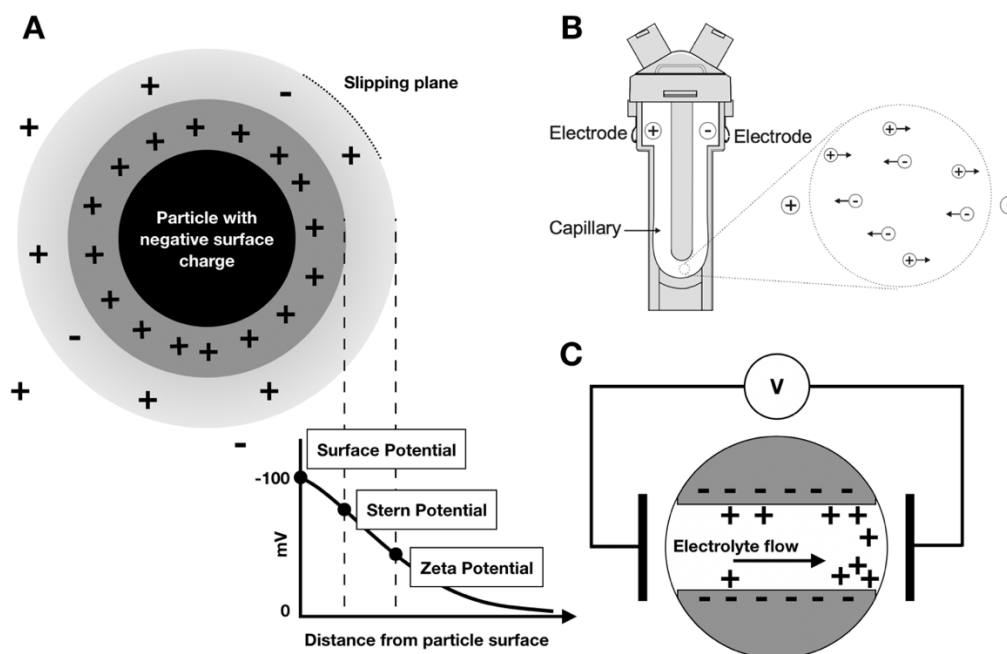


Figure III-8. Principle of surface potential measurement. A – Schematic representation of zeta potential. As distance increases from the particle surface, the zeta potential decreases exponentially, approaching to zero; B – Capillary cell used for the zeta potential measurement. Electric potential is applied at the electrodes, causing the movement of particles towards the electrode of opposite charge; C – Schematic representation of the streaming potential measurement, where an electrolyte flow in a capillary channel leading to its charge separation. Adapted from [33, 34].

On the other hand, streaming potential relates to the electric field that results from the movement of a liquid phase relative to a stationary solid phase. Upon the relative movement of the liquid, occurs a movement of the ions from the electrochemical double-layer to a position along the solid surface. The resulting charge separation origins a streaming potential, that can be used to calculate the surface zeta potential.

In this regard, the zeta potential of polymeric solutions was measured using a Zetasizer (Malvern Instruments, NanoZS) [35]. Each sample was equilibrated for 120 seconds at 25 °C prior reading, and the surface charge was calculated using the Smoluchowski model with an $F(Ka)$ value of 1.50. The surface zeta potential of resulting hydrogels was measured using a SurPASS Electrokinetic Analyzer (Anton Paar GmbH), combined with a cylindrical cell. The measurements were carried out in 0.01 M KCl electrolyte solution, and pH variation was controlled by adding 0.05 M HCl or 0.05 M NaCl.

III.2.13 Fourier Transform Infrared Spectroscopy

Fourier Transform Infrared spectroscopy (FTIR) relies on the absorbance of infrared radiation by sample molecules. Molecules only absorb radiation when light frequency match their specific vibration. Thence, FTIR method starts with the acquisition of the infrared radiation that passes through a sample, resulting in an interferogram (transmittance mode), as schematically represented in Figure III-9. Fourier transformations are then used to decompose the obtained interferograms in spectrograms. The obtained spectrograms depict the changes in infrared radiation intensity (y-axis, arbitrary units) as a function of the infrared frequency (x-axis, wavenumber). To avoid the overlap of bands of interest with the dominant band assigned to the OH group, it is advisable to analyze samples in their dry state.

In this work, FTIR was employed to perform a qualitative analysis of the polyelectrolyte complexes obtained in Chapters VII and VIII. Infrared spectra were recorded using the FTIR Spectrometer IR-Prestige-21 (Shimadzu) controlled by IRsolution software. All samples were dried, and then combined with potassium bromide (KBr, Sigma-Aldrich), an alkali halide that does not show any absorption in the infrared spectrum [36]. Semi-transparent discs were then produced through a press machine. Discs without sample were used to obtain the background spectrogram. Spectra were taken in the wavelength range of 4500-400 cm^{-1} , with an average of 32 scans and a resolution of 2 cm^{-1} .

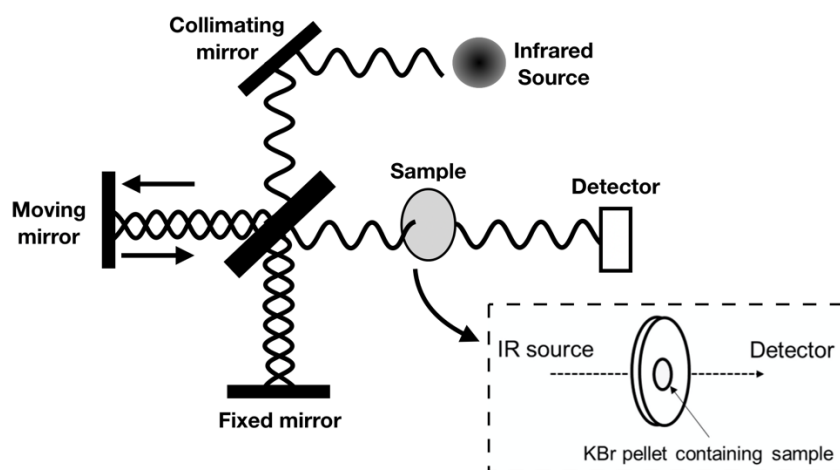


Figure III-9. Schematic representation of transmission FTIR instrumentation. The infrared beam is guided through the interferometer until reaching the sample, and finally the detector. The presence of a moving mirror varies the length of one optical path relative to the other, creating an interferogram. The Fourier transform is latter applied to convert the interferogram into an absorbance spectrum. Adapted from [37, 38].

III.2.14 Atomic Force Microscopy

Atomic force microscopy (AFM) is a high-resolution type of scanning microscopy, useful to obtain the topographical details of a sample at submicron resolutions. The method consists on a sharp tip fixed at the end of a flexible cantilever that systematically moves across the samples' surface (Figure III-10). When the tip approaches the surface, van der Waals, and electrostatic repulsion/attraction forces occur between an atom of the tip and an atom of the surface of the material. These interaction lead to a deflection of the cantilever, that is continuously monitored using a laser beam on the cantilever. As result, a three-dimensional topographical map is generated based on the measured deflections [39].

Herein, the surface topography of the polyelectrolyte complexes developed on Chapter VIII was imaged by tapping AFM, using an environmental setup. The AFM measurements were executed using a Nanowizard III (JPK Instruments) at room temperature in QI™ mode. Samples were attached to glass microscopy slides using a glue supplied by JPK Instruments, and then immersed in PBS. A silicon nitride cantilever with a silicon tip (MSNL-10, Bruker AFM Probes, Bruker) was used to scan the surface of samples on $10 \times 10 \mu\text{m}^2$ areas. AFM data was then analyzed using the JPK Data Processing software.

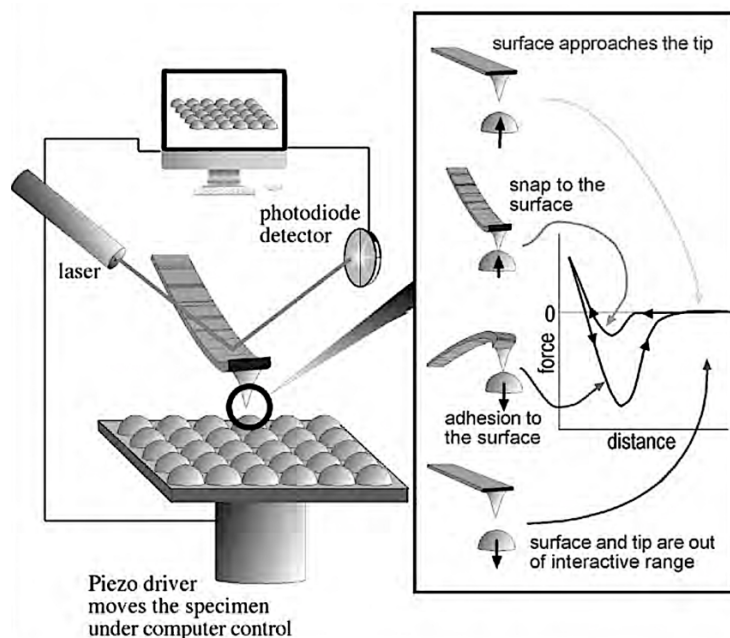


Figure III-10. Schematic illustration of the AFM principle. Retrieved from [32].

III.3 *In vitro* Permeability Studies

Hydrogel's permeability was assessed for the different formulations developed on the scope of the present thesis. In Chapter IV, the study of hydrogel permeability aimed to ascertain the possibility of using the hydrogels as drug delivery depots, for bone tissue engineering approaches. In Chapter V and Chapter VI, permeability was evaluated on the scope of cell-based therapies, where the hydrogels must allow the diffusion of therapeutic molecules of interest secreted by encapsulated cells. At last, in Chapter VII and Chapter VIII, permeability was quantified to study the feasibility of using the developed hydrogels as semi-permeable matrices for cell immunoprotection.

The aforementioned permeability studies were accomplished by monitoring the release of selected model molecules, whose properties are described below. For that, the model molecules were incorporated in distinct hydrogels, and their release from the hydrogel matrix to the external environment quantified using suitable techniques. As a result, different cumulative release profiles were obtained for each one of the molecules tested. Chapter VIII also evaluates the diffusion of model molecules from the surrounding environment to the hydrogel interior. For that, hydrogels were immersed into solutions containing the different model molecules. Diffusion was recorded using a standard camera coupled to a magnifying glass (for methylene blue) or by fluorescence confocal microscopy.

III.3.1 Methylene Blue

Methylene blue (MB, 0.32 kDa, Sigma-Aldrich), represented in Figure III-11, was used as a model for small molecules. Its molecular weight is on the same order of magnitude of small nutrients such as glucose (0.18 kDa), therefore mimicking the diffusion of those nutrients through the hydrogel matrix in Chapter VII and Chapter VIII. MB was loaded in hydrogels and its concentration in the supernatant was quantified along time by means of absorbance reading at 665 nm, in a microplate reader (Gen 5 2.01, Synergy HT, BioTek).

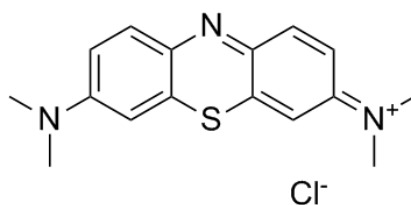


Figure III-11. Chemical structure of methylene blue.

III.3.2 Bovine Serum Albumin

Bovine serum albumin (BSA), represented in Figure III-12, was used in Chapter VII and Chapter VIII as a model of glomerular proteins. The release studies were performed using BSA coupled with fluorescein isothiocyanate conjugate (BSA-FITC, 66 kDa Sigma-Aldrich) to allow a straightforward quantification via fluorescence detection. The fluorescence emission of the retrieved supernatant was measured at an excitation wavelength of 485/20 nm and at an emission wavelength of 528/20 nm, in a microplate reader (Gen 5 2.01, Synergy HT, BioTek).

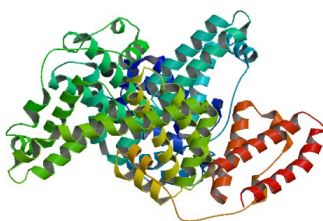


Figure III-12. Crystal structure of bovine serum albumin. Retrieved with permission from [40].

III.3.3 Dexamethasone

Dexamethasone 21-phosphate disodium salt (Dexa 21P, 0.516 kDa, Sigma-Aldrich), was loaded into the hydrogels beads developed in Chapter IV, to assess the feasibility of using this system as a platform for drug delivery. Dexamethasone is a glucocorticoid with a known positive effect on osteogenic differentiation [41], and therefore a good model for bone tissue engineering approaches. Bearing this in mind, Dexa 21P (Figure III-13) was encapsulated within the developed hydrogels, and its release was quantified by UV-vis spectroscopy at 243 nm (Synergy HT, BioTek).

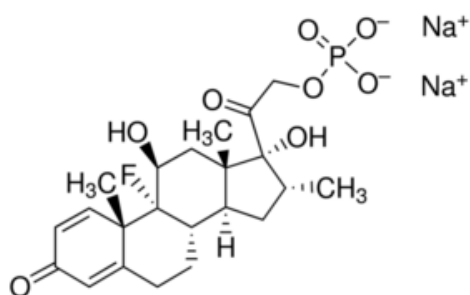


Figure III-13. Chemical structure of dexamethasone 21-phosphate disodium salt.

III.3.4 Dextran-FITC

Fluorescein isothiocyanate–dextran (dextran-FITC, Sigma-Aldrich) with different molecular weights (4, 20 and 70 kDa), were used to study the diffusion of similar molecules of different molecular weight in the hydrogels developed in Chapter IV, Chapter VII, and Chapter VIII. In Chapter V and Chapter VI, 70 kDa dextran-FITC was used as a model molecule for large molecules. In all experiments, dextran-FITC (Figure III-14) was loaded into the formulations tested, and the release was followed by quantifying the fluorescence emission of the resulting supernatant, using an excitation wavelength of 485/20 nm and an emission wavelength of 528/20 nm, in a microplate reader (Gen 5 2.01, Synergy HT, BioTek).

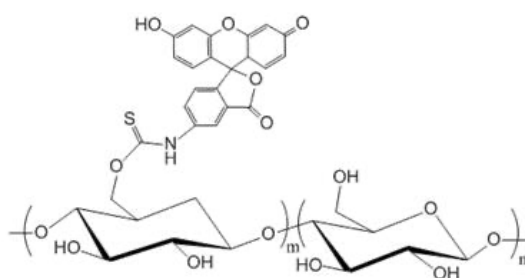


Figure III-14. Chemical structure of dextran-FITC.

III.4 Bioactivity Study

Bioactivity studies were conducted in Chapter IV, as the main goal of this work was to develop hydrogels suitable for bone tissue engineering. It is known from the state of art that the formation of a bone-like apatite layer on biomaterial's surface, under physiological conditions, is an essential requirement for establishing a bond between the material and bone [42]. In this regard, *in vivo* bioactivity can be anticipated using *in vitro* approaches such as immersing the material to be tested in simulated physiological fluids. For example, bioactivity can be studied upon immersion of the materials in simulated body fluid (SBF) [43]. As showed in Table III-2, the composition of SBF is designed to reproduce the ion concentrations found in human blood plasma. Upon immersion and incubation, bioactive materials promote the deposition of ions as a mineral phase, whose structure is similar to apatite.

In the work herein reported, the capability to form an apatite layer *in vitro* was assessed by immersion of the samples into SBF. The preparation of SBF followed the corrected protocol published by Kokubo and Takadama [42], with ion concentrations as shown in Table III-2. After being prepared, samples were rinsed in distilled water, immersed in the SBF solution, and incubated at 37 °C, with mechanical shaking. The volume of SBF used was obtained through the Equation III-7, where V_s is the volume of SBF (mL),

and S_a is the apparent surface area of the specimen (mm^2). At each timepoint, beads were collected, gently rinsed with distilled water, and lyophilized for further characterization.

Table III-2. Ion Concentration in Simulated Body Fluid (SBF)[44].

Solution	Concentration (mM)							
	Na ⁺	K ⁺	Mg ²⁺	Ca ²⁺	C ⁻	HCO ₃ ⁻	HPO ₄ ³⁻	SO ₄ ²⁻
Human blood plasma	142.0	5.0	1.5	2.5	103.0	27.0	1.0	0.5
SBF	142.0	5.0	1.5	2.5	147.8	4.2	1.0	0.5

Equation III-7. Volume of SBF used for testing the hydrogels.

$$V_s = \frac{S_a}{10}$$

III.5 Optical Microscopy

Optical imaging comprises systems that use the interaction of matter with light at different wavelengths, as infrared (300 GHz-430 THz, 700 nm-1 mm), visible (430-790 THz, 380-700 nm) and ultraviolet light (790 THz – 30 PHz, 10-300 nm) [45]. Different light sources, with distinct wavelength and intensity, can be used to interact with the samples. After this interaction (typically diffraction, refraction, scattering and/or absorption), light is collected using optical or electro-optical sensors, and analyzed.

Optical microscopy was used to evaluate hydrogels, from their overall stability to more complex biologic analyses, such as the biologic responses at the cell-biomaterial interface, or cell viability upon cell encapsulation [21]. An upright configuration was used to inspect the developed hydrogels. The sample was placed on a platform and then observed from above by an objective lens. Depending on the assay, samples were observed as a whole or sliced, mounted between a microscope slide and a coverslip. Additionally, an inverted microscope was used for routinely observation of live cells in culture, where samples were viewed through objective lenses positioned underneath the specimen platform.

III.5.1 Brightfield Microscopy

Brightfield microscopy was used to image hydrogels in Chapter VII and Chapter VIII, to follow their size and morphological changes upon incubation in different solutions. Also, in Chapter IV and Chapter VIII brightfield microscopy was used to image thin tissue sections after histologic staining. Sample

illumination occurs via transmitted white light that is emitted from below, passes through the samples and is then observed from an eyepiece located above the sample holder.

III.5.2 Fluorescence Microscopy

Fluorescence microscopy imaging is one of the most used techniques for *in vitro* imaging of tissue engineering constructs, as it offers improved spatial resolution and superior image depths. Briefly, it involves the absorption of light with a determined wavelength by a fluorophore (excitation). This light is then emitted from the fluorophore with a higher wavelength (emission), and detected by dedicated cameras, as schematically represented in Figure III-15 [46]. Nowadays, the available fluorescent labeling techniques and markers support the detection and monitoring of several intracellular events, cellular interactions, as well as tissue/construct integrity and structure. For instance, it is possible to routinely check cell viability, cell morphology or cell differentiation within a tissue-engineered construct.

As said, fluorescence microscopy relies on the use irradiation of high energy light into samples that show fluorescent behavior, or that were previously stained with fluorescent dyes, or fluorophores [21]. First, samples are marked with specific fluorophores, such as described below, and placed on the mechanical stage of the microscope. Then, excitation light, from a mercury arc lamp, passes through a filter that selects the wavelengths required to excite the fluorophores present on the sample. After passing the filter, excitation light hits a dichroic mirror, reflects towards the objective and finally illuminates the sample. Consequently, the fluorophore is excited and emits part of the energy as light in a longer, and less energetic wavelength. This emission light travels back to the objective, and across the dichroic mirror, that permits this longer wavelength emission light to pass, reaching the emission filter. This filter selects the emission wavelengths, rendering a clean and composed signal only of light from the excited fluorophore. At last, the emitted light is detected via a CCD (charge-coupled device) cameras, processed by computer algorithms, and the final image is obtained [21].

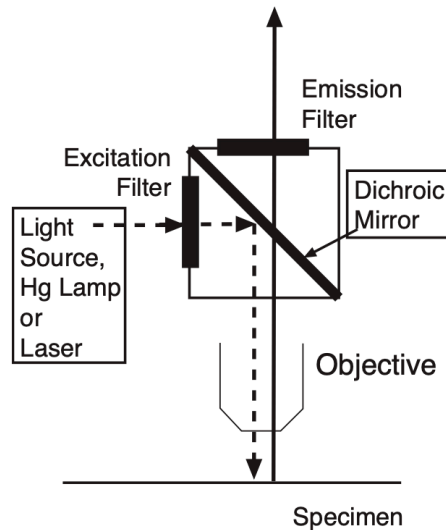


Figure III-15. Schematic representation of the filter set used in standard a fluorescence microscope. Dashed lines represent shorter wavelength excitation light, and solid lines longer wavelength emission light. Retrieved from [21].

In this thesis, fluorescent microscopy was used on the scope of the work of Chapter V, Chapter VI, Chapter VII, and Chapter VIII, to image cells after appropriate staining.

III.5.2.1 Confocal Microscopy

Confocal microscopy is also a fluorescence-based imaging technique, but it uses a laser beam as the light source, and a pinhole to assure the collection of light only from a singular focal plane (Figure III-16). The projection of out-of-focus light onto the image plane of the camera is then reduced, leading to an improvement in the resolution and contrast of images. This results in a clearer image, with superior spatial resolution, as compared to common fluorescence microscopy. Additionally, confocal microscopy is also advantageous to obtain 3D volumetric images, since the specimen can be scanned in depth with high spatial resolution. The high spatial resolution can also be used to obtain the three-dimensional structure of biomaterials, as far as they have intrinsic fluorescence or are previously labelled for that purpose [47].

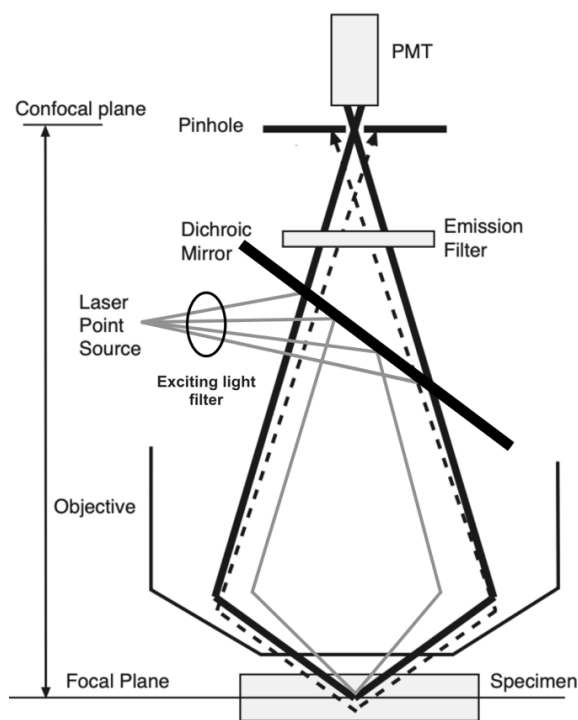


Figure III-16. Schematic drawing of a laser scanning confocal microscope's objective. The sample is illuminated by a laser that is reflected into the objective via a dichroic mirror. Fluorescence emitted from the focal plane is captured by the objective, passes through the dichroic mirror, emission filters, and arrives precisely at the opening of the pinhole aperture. Fluorescence from an out-of-focus plane is rejected. Adapted with permission from [21].

In the present work, confocal microscopy was performed using an inverted laser scanning confocal microscope (LSCM), for cell-laden hydrogels developed in Chapter VIII, and to study the permeability of the same hydrogels. The LSCM used has an inverted configuration, where objectives are placed below the sample stage. Thence, before being imaged, hydrogels were moved into a μ -dish plates (Ibidi® GmbH, Germany) that allowed hydrogel visualization from the bottom. Cell-laden hydrogels were covered by a drop of PBS during image acquisition, to avoid dehydration. Hydrogels analyzed for permeability evaluation were immersed in the PBS solution used along the assay.

III.6 Cell Culture Conditions

The *in vitro* evaluation of cells' response to biomaterials is fundamental to anticipate possible adverse reactions triggered by the presence of a biomaterial in a living organ. In this work, biocompatibility was studied *in vitro* using adipose-derived stem cells and androgen-sensitive human prostate adenocarcinoma cells (LNCaP). Immunocompatibility was also tackled in Chapter IV and Chapter VIII, where hydrogels were in contact with macrophage cell lines, human blood plasma and blood-derived cells.

III.6.1 Growth and Harvesting of the Cells

All the cell types were cultured in tissue culture flasks (75 or 150 cm²), filled with a suitable volume of cell culture media, and incubated at 37 °C in 95% relative humidity, and 5% CO₂. Cell culture media was changed every 2-3 days.

When cells reached near 90 % of confluence, the flasks were gently washed with sterile phosphate buffered saline (PBS), and attachment-dependent cells were detached by enzymatic action of a TrypLE™ Express Enzyme (Gibco®, Life Technologies) solution. This solution contains highly purified recombinant cell-dissociation enzymes and is a valuable alternative to porcine trypsin. After 5 min at 37 °C in a humidified air atmosphere and 5% CO₂, the TrypLE™ solution was diluted with cell culture medium and transferred to a new sterile falcon tube. Cells were then centrifuged (1200 rpm, at 25 °C for 5 min), and the resulting pellet collected and resuspended for further cell expansion or specific assays.

Before activation, THP1 cells do not attach to tissue culture flasks. Thence, the use of TrypLE™ solution is not needed. Cell passage occurs by removing half of the cell suspension followed by dilution of the reminiscent volume with fresh cell culture media.

III.6.2 Human-derived Adipose Stem Cells

Human-derived adipose stem cells (hASCs) were retrieved from the knee fat pad of healthy male and female donors with ages between 18 and 57 years, after informed consent, under established cooperative agreements between Hospital da Senhora da Oliveira (Guimarães, Portugal) and 3B's Research Group. All the samples were processed within 24 hours after tissue collection, and hASCs were enzymatically isolated, as previously described [48], with slight modifications. Briefly, fat tissue was minced into small pieces and digested with 0.075% collagenase type II (C6885, Sigma-Aldrich) dissolved in MEM cell culture media (Minimum Essential alpha Medium, α -MEM, Gibco®, Life Technologies), supplemented with 10 vol.% of heat-inactivated fetal bovine serum (FBS, Gibco®, Life Technologies, reference A3160802, EU approved) and 1 vol.% antibiotic-antimycotic solution (penicillin 100 units.mL⁻¹ and streptomycin 100 mg.mL⁻¹, Gibco®, Life Technologies). Tissue digestion took place overnight in a water bath at 37 °C, with shaking. Next, the resulting solution was passed through a 100 μ m cell strainer (Falcon) and centrifuged at 800 *g* for 10 minutes. The resulting pellet was collected and centrifuged again at 300 *g* for more 10 minutes. The pellet was then resuspended in culture media and expanded in tissue culture flasks. Cells were cultured until confluence at 37 °C, in a 5% CO₂ incubator, by changing the culture medium every 2-3 days.

III.6.3 Androgen-sensitive Human Prostate Adenocarcinoma Cells (LNCaP)

LNCaP cell line was gently provided by the Instituto Português de Oncologia do Porto. Cells were seeded in a 75 cm² culture flask (Sarstedt, Nümbrecht, Germany), using the Roswell Park Memorial Institute (RPMI) 1640 medium supplemented with 10 vol.% heat-inactivated FBS and 1 vol.% antibiotic-antimycotic solution (penicillin 100 units.mL⁻¹ and streptomycin 100 mg.mL⁻¹, Gibco®, Life Technologies). Cells were sub-cultured every 2-3 days and maintained in growth in an incubator with humidified air containing 5% CO₂ and at 37 °C.

III.6.4 Human Monocytic Cell Line (THP-1)

THP-1 monocytic cell line was obtained from ATCC (American Type Culture Collection, Middlesex, UK). Cells were seeded in a 75 cm² culture flask (Sarstedt, Nümbrecht, Germany), using RPMI 1640 medium supplemented with 10 vol.% heat-inactivated FBS and 2 vol.% Penicillin-Streptomycin (Gibco, Life Technologies). Cells were sub-cultured every 2-3 days and maintained in growth in an incubator with humidified air containing 5% CO₂ and at 37 °C. To activate THP-1 cells differentiation into macrophages, cells were treated with phorbol 12-myristate 13-acetate (PMA, Sigma-Aldrich) at 64 nM in culture media for 48 hours. Afterwards, the medium was replaced by fresh medium.

III.6.5 Mouse Macrophage Cell Line (Raw 264.7).

Mouse Macrophage Cell Line (Raw 264.7) was obtained from ATCC (American Type Culture Collection, Middlesex, UK). Cells were seeded in a 75 cm² culture flask (Sarstedt, Nümbrecht, Germany), using RPMI 1640 medium supplemented with 10 vol.% heat-inactivated FBS and 2 vol.% Penicillin-Streptomycin (Gibco, Life Technologies). Cells were sub-cultured every 2-3 days and maintained in growth in an incubator with humidified air containing 5% CO₂ and at 37 °C.

III.6.6 Human Peripheral Blood Mononuclear Cells

Human peripheral blood mononuclear cells (hPBMCs) were isolated from blood samples collected from three different healthy human donors, using a Ficoll-Paque PLUS™ (GE Healthcare) density gradient. For that, blood samples were supplemented with ethylenediamine tetraacetic acid (EDTA) to avoid coagulation, and further diluted using equal volume of PBS. The obtained mixture was added to Ficoll in a 7:3 ratio (diluted blood:Ficoll). This mix was centrifuged at 180 g for 30 minutes, at 20 °C. After centrifugation, hPBMCs were located at the interface between Ficoll and plasma. Cells were harvested from the interface, with the help of a Pasteur pipette, and washed twice with complete medium, by

centrifugation at 100 *g* for 5 minutes at 20 °C. At last, cells were seeded in a 96-well plate, using a cell density of 1×10^5 cells per well.

III.7 Cell Viability and Morphology

III.7.1 Live/Dead

Cell viability was evaluated in Chapter V, Chapter VI, Chapter VII, and Chapter VIII through a Live/Dead assay. This assay relied on the use of two fluorophores to distinctly stain live and dead (or unviable) cells. The rationale of this method relies on the different capability of the fluorophores to cross the cell membrane. Viable cells were detected upon staining with calcein acetoxymethyl ester (calcein-AM, excitation/emission maxima 488 nm/520 nm), which is not fluorescent *per se*. However, intracellular esterases present in the cytoplasm of living cells can cleave the acetoxymethyl ester function, resulting in free calcein. Then, the resulting calcein is free to bind with intracellular calcium, emitting a green fluorescence after proper light excitation. On the other hand, propidium iodide (PI, excitation/emission maxima of 493 nm/636 nm), or ethidium homodimer-1 (EthD-1, excitation/emission maxima 528 nm/617 nm), are non-permeant dyes, weakly fluorescent until bound to the DNA. These fluorochromes cannot enter into the cytoplasm of viable cells, but easily pass through damaged membranes, typical of unviable cells. Once inside the cytoplasm, both PI and EthD-1 can bind to the DNA and emit a red fluorescent signal.

Live/dead fluorescence assays were performed right after encapsulation, and at each timepoint. Calcein-AM and Propidium Iodide (PI) dyes (1 mg.mL^{-1} , Molecular Probes, Invitrogen, USA) were used to perform the Live/Dead assay in Chapter VII and Chapter VII. At each timepoint, the culture medium was removed, and 1 mL of PBS containing 2 μL of Calcein-AM and 1 μL of PI was added to each well. Samples were then incubated 10 minutes at 37 °C, protected from light. Thence, samples were washed three times with PBS and immediately visualized in the dark using a Fluorescence Microscope (Axioimage RZ1M, Zeiss, Germany) in Z-stack mode, using the AxioVision software. Percentage of live cells in each bead was then calculated using ImageJ software (version: 2.0.0-rc-69/1.52p).

In Chapter V and Chapter VI, live/dead fluorescence assays were performed at each time culture period, using the LIVE/DEAD Viability/Cytotoxicity Kit for mammalian cells (ThermoFisher Scientific). Calcein-AM stained the live cells and ethidium homodimer-1 (EthD-1) stained dead cells. At each timepoint, the culture medium was removed, and 150 μL of Calcein and EthD-1 diluted in PBS (0.5 μL of Calcein-AM and 2 μL of EthD-1 per 1 mL PBS) were added to each well. Samples were then incubated 20 minutes

at room temperature (RT), protected from light, and visualized in the dark using the fluorescence microscope Cell Observer SD (Carl Zeiss, Germany) in Z-stack mode. The percentage of live cells was then calculated using ImageJ software (version 2.0.0-rc-69/1.52p).

III.7.2 MEM Extract Test

The putative cytotoxic effect of hydrogel's leachable was assessed using a MEM extract test, based on the ISO 10993-5:2009 guidelines [49], with slight modifications. Hydrogels were incubated in 20 mL of complete culture α -MEM medium, for 24 hours at 37 °C under continuous agitation. Sterile tissue culture polystyrene (TCPS) coverslip and latex rubber extracts were used as positive and negative controls, respectively. After one day of culture, cell culture media was replaced by 1 mL of extraction fluid and cells incubated for more three days. Metabolic activity of cells was followed by Alamar Blue assay.

III.7.2.1 Alamar Blue

Alamar Blue bioassay is a generally used tool to access metabolic function and cellular health [50]. The main reagent of this assay is resazurin, a weakly fluorescent blue indicator dye that permeates into the cells. Resazurin is reduced in living cells, producing resorufin, a pink and highly fluorescent compound. Viable cells continuously convert resazurin to resorufin, generating a quantitative measure of viability and cytotoxicity. Thence, resazurin can be used as an indicator of the cytoplasmic reduction potential, where the intensity of fluorescence produced by resorufin is proportional to the number of living cells [51]. As the reagent has a nontoxic nature, long-term exposure to cells without negative impact is allowed.

In the scope of this thesis, the cell metabolic activity was assessed by AlamarBlue® assay (Bio-Rad Laboratories, Oxford, UK) in Chapter IV and Chapter VIII. Cell culture media supplemented with 10% AlamarBlue® dye was added to each well and incubated for 4 hours at 37 °C and 5% CO₂. Afterwards, medium fluorescence was measured using a microplate reader (Synergy HT, BloTek Instruments, USA) at an excitation/emission of 530/590 nm. The relative metabolic activity was obtained by normalization with the mean fluorescence value obtained for controls. (extraction fluid obtained from a TCPS coverslip). Latex rubber was used as negative control. The experiments were carried out in triplicate (n=9). The percentage of AlamarBlue® reduction was calculated according to the manufacturer's recommendations.

III.7.3 DNA Quantification

DNA quantification was based on the use of PicoGreen® quantitation reagent dye. This reagent selectively binds to nucleic acids, yielding an intense fluorescence signal, with excitation and emission maxima near to fluorescein [52]. Knowing that the quantity of double stranded DNA (dsDNA) is directly proportional to the cell number, it is possible to follow cell proliferation using this assay.

In Chapter VIII, dsDNA quantification was assessed after cells encapsulation, and after each selected timepoint. Quantification was performed using the Quant-iT PicoGreen® dsDNA Assay Kit (Invitrogen, Molecular Probes), according to the manufacturer's instructions. For that, the hydrogels were mechanically destroyed in Milli-Q water and transferred to a water bath at 37 °C. After 1 hour, samples were stored at -80 °C until further use. These steps led to cell lysis both by osmotic and thermal shock. Prior to quantification, samples were thawed, centrifuged, and the supernatant was used for the DNA quantification assay. The fluorescence emission of the PicoGreen dye was measured at an excitation wavelength of 485/20 nm and an emission wavelength of 528/20 nm, in a microplate reader (Gen 5 2.01, Synergy HT, BioTek). At last, DNA concentration for each sample was calculated using a standard curve relating the quantity of DNA with the fluorescence intensity.

III.7.4 Real-time Cell Proliferation

Cell proliferation was monitored in real-time in Chapter IV and Chapter VIII, using an xCELLigence Real-Time Cell Analyzer (RTCA) from Roche. This method allows a label-free and non-invasive real-time monitoring of cell growth by measuring the impedance of sensor electrodes located at the bottom of each well in specific plates. These plates, the E-plates, have gold microelectrodes fused to their bottom surface, which are exposed to cells and the cell culture medium (Figure III-17). While the culture medium is a conductive solution and allows the electron flow from the negative to the positive terminal, the presence of adherent cells at the electrode-solution hinders the electron flow. Thence, upon applying an electric potential (22 mV) is possible to infer about the number, size, and shape of the cells, and the cell-substrate attachment quality, from the magnitude of the recorded impedance.

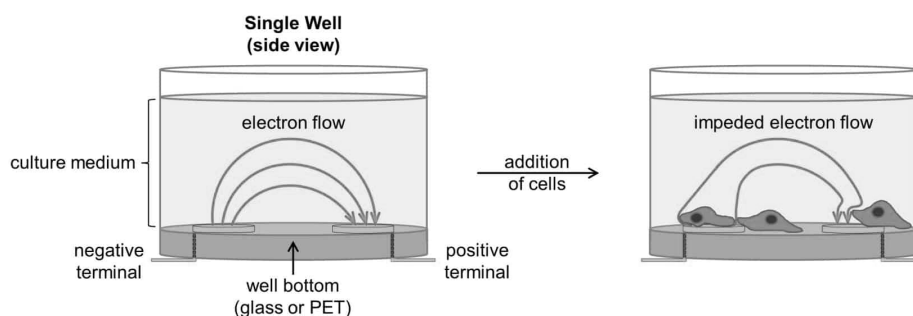


Figure III-17. Schematic representation of the xCELLigence RTCA technology [53].

In this regard, hASCs and macrophage proliferation curves after contact with hydrogel extract fluids were determined using the xCELLigence RTCA DP system (Roche, Basel, Switzerland). hASCs were seeded at 0.01×10^6 cells.mL⁻¹ in 200 mL of α -MEM complete medium and incubated for 24 hours. Media was then replaced by 200 mL of extract fluid, prepared as described in last section. At last, THP-1 cells were seeded at 0.5×10^6 cells.mL⁻¹, using 200 mL of RPMI 1640 complete medium and phorbol12-myristate 13-acetate (PMA, Sigma-Aldrich) at 64 nM. After 48 hours in culture, that allowed THP-1 differentiation into macrophages, culture medium was replaced by fresh medium, and extract fluids were added after additional 24 hours in culture.

III.7.5 Cell Morphology

Cell morphology was accessed using a staining based on 4',6-diamidino-2-phenylindole (DAPI) and tetramethylrhodamine B isothiocyanate-phalloidin (phalloidin-TRITC). DAPI was used to label cell nuclei, since this compound is able to form complexes with double-stranded DNA. When excited by UV light, DAPI emits a strong blue fluorescence, that can be used to detect the nuclei via fluorescence imaging techniques. Phalloidin-TRITC is a fluorescent conjugate of the mushroom toxin, that binds tightly to polymerized F-actin filaments present in the cell cytoplasm. This property is exploited to label the cell cytoskeleton that can be identified by the emitted red fluorescence.

The DAPI/phalloidin staining was performed in Chapter VII and Chapter VIII right after cell encapsulation, and at different timepoints. For staining, the culture medium was removed, and hydrogels were washed three times with PBS. Then, 10 vol.% of formalin was added to each well. After 1 hour at room temperature, formalin was removed and replaced by 0.2 vol.% Triton-X for 5 minutes to permeabilize cells. Upon washing with PBS, 1 mL of PBS containing 1 μ L of DAPI (20 mg.mL⁻¹, Sigma-Aldrich) and 5 μ L of Phalloidin-TRITC (10 mg.mL⁻¹, Sigma-Aldrich) were added to each well. After 45 minutes of incubation at room temperature, and protected from light, samples were washed three times with PBS,

The activation of complement cascade upon interaction with the developed materials was determined using a protocol kindly provided by the Nanotechnology Characterization Laboratory (NCL Method ITA-5.1, version 1.2, 2015), as previously reported by P. Pereira *et al.* [56]. Briefly, a pool of human plasma was collected from five healthy volunteer donors and incubated with the sterile hydrogels at 37 °C, for 60 minutes. Zymosan A from *Saccharomyces cerevisiae* (1 mg.mL⁻¹, Z4250, Sigma-Aldrich) was used as positive control, while PBS (Sigma-Aldrich), Ethylenediamine Tetraacetic Acid (EDTA, 10 mM, E-7889, Sigma-Aldrich), and plasma with PBS incubated at 4 °C, were used as negative controls. Plasma incubated at 37 °C with both EDTA and Zymosan was used as reversion control, to attest the EDTA negative effect on the cascade. Proteins were resolved via 10% SDS–PAGE electrophoresis and transferred to Polyvinylidene fluoride (PVDF) membranes (Immuno-Blot PVDF Membrane, BioRad) using the transblot turbo BioRad transfer equipment (Trans-Blot® Turbo™ Transfer System, BioRad). The resulting membranes were incubated for 60 minutes with a mouse monoclonal antibody against human C3 diluted 1:1000 (ab11871, Abcam), washed and incubated with a secondary polyclonal goat anti-mouse IgG antibody conjugated with alkaline phosphatase diluted 1:2000 (D0486, Dako). The membrane was revealed using 5-Bromo-4-Chloro-3-Indolyl Phosphate (BCIP, Sigma-Aldrich) and scanned with a ChemiDoc™XRS + System (Bio-Rad). Image Lab software™ (version 6.0.1 build 34, Standard Edition 2017, Bio-Rad Laboratories, Inc) was used for further quantification. Procedures using human samples were approved by the Galician Autonomic Ethics Committee at the Concelleria de Sanidade da Xunta de Galicia (Ref 2014/492). All participants included in the study gave their written informed consent.

III.8.2 Cytokine Release

The putative pro-inflammatory and immunogenic properties of the materials developed in Chapter IV and Chapter VIII were assessed using a multiplex analysis of cytokine production by human peripheral blood mononuclear cells (hPBMCs). Cytokines were measured considering both T_H1 and T_H2 possible responses. In this regard, T_H1 profile includes cytokines that mostly induce cellular responses, while the T_H2 profile comprises cytokines involved in humoral responses. IL-8, IL-1β and TNF-α were also studied considering their important role on inducing chemotaxis, mediating the inflammatory response, and triggering systemic inflammations, respectively [57].

Cytokine release was measured following a protocol published by Simon-Vasquez *et al.* [46]. The previously seeded hPBMCs were incubated in the presence of sterile hydrogels, lipopolysaccharide (LPS, InvivoGen) at 20 ng.mL⁻¹ (positive control) and culture medium (negative control). After 24 hours of

incubation at 37 °C with 5% CO₂, the plate was centrifuged (100 g, 5 minutes, 4 °C), the supernatant collected and stored at – 20 °C until further quantification. Cytokines' concentrations were determined using the Milliplex® Map Human Cytokine/Chemokine Magnetic Bead Panel (Millipore Corporation, USA) according to the manufacturer's instructions. Experiments were performed in duplicate, per donor (n=6). Finally, samples were analyzed by Luminex® laser based fluorescent analytical test (MAGPIX®, ThermoFisher) and data evaluated with the xPONENT 4.2 1324.0 Software (Luminex®). Institutional ethics approval to work with human samples from healthy donors was obtained from the Galician Autonomic Ethics Committee at the Concellería de Sanidade da Xunta de Galicia (Ref 2014/492). All participants included in the study gave their written informed consent.

III.9 *In vivo* Tests - Biocompatibility and Function

III.9.1 Mice Models

Animal models still play a central role during the development of tissue engineering constructs [58]. In the present work, mice were used as small animal models to attest the biocompatibility of the hydrogels developed in Chapter IV and Chapter VIII. CD-1 male mice of 5-weeks old and average weight of 27-32 g, at the time of implantation (Charles River, Massachusetts, USA) were used to study biocompatibility and/or bioactivity of the hydrogel beads, *in vivo*. Use and maintenance of animals were carried out in accordance with the Ethics Committee of University of Minho and approved by the Portuguese Licensing Authority (DGAV-DSPA). The hydrogels were prepared under aseptic conditions, using sterile solutions, as aforesaid. At the time of the surgery, each mouse was anesthetized by intraperitoneal injection of Domtor 1 mg.mL⁻¹ (Medetomidine 1 mg.kg⁻¹, Novavet, Braga, Portugal) and Imalgene 100 mg.mL⁻¹ (Ketamine 75 mg.kg⁻¹, Novavet, Braga, Portugal). After anesthesia, the implantation area was shaved, and disinfected with iodine (Life Technologies, Carlsbad, CA, USA). Subcutaneous pockets were formed on the back of each mice. Hydrogels were implanted in each subcutaneous pocket, followed by skin suture. After 2, 4 and 8 weeks, mice were euthanized, by injection of overdose of Eutasil 200 mg.mL⁻¹ (pentobarbital sodium, Novavet, Braga, Portugal), and the beads retrieved. The material was fixed with 10 vol.% formalin solution, followed by dehydration and paraffin embedding.

In Chapter V and Chapter VI, the mice model was used to study hydrogel's functionality when *in vivo*. Double mutant MBP^{sh1/sh1}/rag2 immunocompromised mice (a model of demyelination) were anesthetized with 1.5-2% isoflurane in oxygen and placed in the stereotaxic frame, in a concord-like position [59]. A small incision was made in the midline at the posterior aspect of the skull, and muscles were separated

to expose the atlanto-occipital membrane. The hydrogel was prepared as described above, using 0.1 mM of MnCl_2 . 10 μL of Mn/GG-MA was placed in a Hamilton syringe and injected into the intrathecal, or parenchymal, space with a speed of 10 $\mu\text{L}\cdot\text{min}^{-1}$. After injection, the needle was left in the same place for an additional 1 minute and then slowly withdrawn. Afterwards, skin was sutured, and the animal was placed in MRI scanner.

III.9.2 Histochemistry

III.9.2.1 Hematoxylin & Eosin

The hematoxylin and eosin staining (H&E) is one of the most common histologic stains. Hematoxylin stains in blue-purple substances with a net negative charge, such as the cell nuclei containing DNA. On the other hand, eosin is an acidic pigment that stains in pink-red structures with a positive charge, as cell cytoplasm or collagen [60]. This staining is therefore useful on the evaluation of overall cell morphology in tissue sections collected from *in vivo* studies.

As mentioned before, the materials collected from the *in vivo* studies performed in Chapter VIII were fixed in 10 vol.% formalin, dehydrated and embedded in paraffin wax. Before the H&E staining, the resulting paraffin blocks were sliced into 4 μm -thick sections, using a microtome. These sections were then attached to glass microscope slides and dehydrated. Then, the slides were immersed in a hematoxylin solution, followed by a rinse wash to remove excess staining. At last, slides were counterstained with eosin, washed again and mounted for microscope observation. Experiments were performed in triplicate, with a total number of 9 animals per time-point.

III.9.2.2 Masson's Trichrome

Masson's Trichrome staining is particularly used to stain collagen, being useful on the identification of connective tissue or fibrosis [60]. It uses three different dyes to selectively stain collagen fibers, cell nuclei and muscle that appear as blue, black and red, respectively.

Before the staining, samples were processed as described for H&E. Then, a mordant solution, the Bouin's solution, was used as a mordant to link the dye to the sample, followed by Weigert's hematoxylin, which specifically stains the nuclei. Afterwards, all acidophilic tissue elements such as cytoplasm, muscle, and collagen were stained by the Biebrich scarlet-acid fuchsin solution. Subsequently, phosphomolybdic/phosphotungstic acid was used to remove the Biebrich scarlet-acid fuchsin from collagen fibers, while leaving the muscle cells red. Finally, samples were stained with aniline blue that

marks collagen in blue. Experiments were performed in triplicate, with a total number of 9 animals per time-point.

III.9.2.3 Alizarin Red

Alizarin red (AzR) staining was used in Chapter IV to evaluate the *in vivo* bioactivity of the developed hydrogels. Alizarin has the ability to form complexes with calcium, in a chelation process, that results in a bright red product.

Slides with 4 μm -thick sections were prepared as stated for H&E and stained with AzR. Stained samples were dehydrated using acetone, acetone-xylene, and xylene. Excess xylene was removed, and the slides mounted for microscope observation. Experiments were performed in triplicate, with a total number of 9 animals per time-point.

III.10 Magnetic Resonance Imaging

Magnetic Resonance Imaging (MRI) is a non-invasive technique that relies on the magnetization and relaxation of water protons, wherein the image contrast is typically associated to differences in the proton density found in the sample [45, 61]. Using MRI, it is possible to obtain information about the biomaterial/tissue interface, as well as biomaterial placement and biodistribution, with high anatomical fidelity. Therefore, this technique is one of the most preferable imaging modalities in both pre-clinical and clinical studies, since it is radiation-free and allows a real-time and non-invasive imaging [62].

Magnetic Resonance Imaging (MRI) was performed in Chapter V and Chapter VI, immediately after intrathecal and parenchyma injection of hydrogels. After intrathecal transplantation, a follow-up MRI was performed 24 hours after surgery. For the imaging analysis, animals were anesthetized with isoflurane (1.5-2% in oxygen) and positioned head prone in an MRI-compatible water-heated bed. Body temperature and respiration rate were monitored throughout the study with MRI compatible probes (SA Instruments, Stony Brook, NY, USA). 7T MR scanner (BioSpec 70/30 USR, Bruker, Ettlingen, Germany) equipped with transmit cylindrical radiofrequency coil (8.6 cm inner diameter, Bruker) and a mouse brain dedicated receive-only array surface coil (2x2 elements, Bruker) was used. The structural imaging protocol was performed as previously described [63], using a T1-weighted 3D FLASH sequence (TR = 12 ms; TE = 4 ms; flip angle, FA = 18; NA = 10; field of view, FOV = 15 mm \times 15 mm \times 15 mm, spatial resolution = 117 μm isotropic, scan time near 25 minutes). Structural imaging was followed by T1 parametric imaging with the 2D Saturation Recovery Spin Echo Sequence with varying repetition times (TR = 410 ms

... 8000 ms, TE = 22 ms, rare factor = 4, NA = 3, FOV = 20 mm × 20 mm, 8 slices 0.8 mm thick with no gaps, spatial resolution = 156 μm × 156 μm, scan time near 23 minutes) and T2 parametric imaging with the MSME sequence (TR = 5000 ms, TE = 13 ms ... 416 ms, NA = 1, FOV = 20 mm × 20 mm, 8 slices 0.8 mm thick with no gaps, spatial resolution = 156 μm × 156 μm, scan time near 8 minutes).

Tripilot scan was followed by T1 parametric imaging with the 2D Saturation Recovery Spin Echo Sequence with varying repetition times (TR = 200 ms ... 8000 ms, TE = 9.5 ms, rare factor = 2, NA = 1, FOV = 75 mm × 75 mm, 5 slices 2.0 mm thick with 2.0 mm gaps, spatial resolution = 586 μm × 586 μm, scan time near 13 minutes) and T2 parametric imaging with the MSME sequence (TR = 5000 ms, TE = 15 ms ... 480 ms, NA = 1, FOV = 75 mm × 75 mm, 5 slices 2.0 mm thick with 2.0 mm gaps, spatial resolution = 586 μm × 586 μm, scan time near 8 minutes). To evaluate relative magnetic resonance signal of T1-weighted imaging of hydrogel phantoms with different concentration of manganese ions, identical regions of interest (ROI) were outlined on MR images and the signal intensity was measured with the use of ImageJ software (version 2.0.0-rc-69/1.52p).

Table III-3. Overview of materials and methods used per chapter.

	Chapter IV	Chapter V	Chapter VI	Chapter VII	Chapter VIII	
Materials	Polymers	GG-MA	GG-MA	GG-MA and HA	GG-MA and PLL	GG-MA and PLL
	Crosslinking	Ionic	Ionic	Ionic	PEC	PEC
	Supplementation	CaCl ₂	MnCl ₂	MnCl ₂	n.a.	n.a.
Physicochemical Characterization		SEM	Wight loss profile	Wight loss profile	Wight loss profile	Wight loss profile
		EDS	Rheology	Rheology	Size variation	Size variation
		XRD	Injection ability	Injection ability	SEM	SEM
		μ-CT	ICP	ICP	FTIR	XPS
		Calcium colorimetric assay				Zeta potential
						FTIR
Permeability Studies		Dexa 21P	70 kDa dextran-FITC	70 kDa dextran-FITC	MB	MB
		4, 20 and 70 kDa dextran-FITC	Mn ²⁺	Mn ²⁺	BSA-FITC	BSA-FITC
Optical Microscopy	Material	n.a.	n.a.	n.a.	Brightfield	Brightfield
	Cells	n.a.	Fluorescence	Fluorescence	Fluorescence	Fluorescence
	Tissues	Brightfield	n.a.	n.a.	n.a.	Brightfield
Cells Used		THP-1	hASCs	hASCs	hASCs	hASCs
		hASCs			LNCaP	THP-1
		hPBMCs				Raw 264.7
					hPBMCs	

Table III-3. Continued.

Cell Viability and Morphology		MEM extract RT cell proliferation	Live/Dead	Live/Dead	Live/Dead F-actin, nuclei	Live/Dead MEM extract DNA RT cell proliferation F-actin, nuclei
Immune response		Complement Cytokine release	n.a.	n.a.	n.a.	Complement Cytokine release
<i>In vivo</i>	Mice models	CD-1 male	MBP ^{sh1/sh1} rag2	MBP ^{sh1/sh1} rag2	n.a.	CD-1 male
	Location	Subcutaneous	Intrathecal Parenchymal	Intrathecal	n.a.	Subcutaneous
	Follow-up	Alizarin	MRI	MRI	n.a.	H&E Masson's

III.11 References

1. Coutinho, D.F., et al., *Modified Gellan Gum hydrogels with tunable physical and mechanical properties*. Biomaterials, 2010. **31**(29): p. 7494-502.
2. Silva-Correia, J., et al., *Gellan gum-based hydrogels for intervertebral disc tissue-engineering applications*. Journal of Tissue Engineering and Regenerative Medicine, 2011. **5**(6): p. e97-107.
3. Silva-Correia, J., et al., *Biocompatibility evaluation of ionic- and photo-crosslinked methacrylated gellan gum hydrogels: in vitro and in vivo study*. Advanced Healthcare Materials, 2013. **2**(4): p. 568-75.
4. Pradhan, S., et al., *⁷-NMR, FT-IR and raman characterization of biomaterials*, in *Characterization of Polymeric Biomaterials*, M.C. Tanzi and S. Farè, Editors. 2017, Woodhead Publishing. p. 147-173.
5. Hamcerencu, M., et al., *Synthesis and characterization of new unsaturated esters of Gellan Gum*. Carbohydrate Polymers, 2008. **71**(1): p. 92-100.
6. Slevin, M., et al., *Hyaluronan-mediated angiogenesis in vascular disease: uncovering RHAMM and CD44 receptor signaling pathways*. Matrix Biology, 2007. **26**(1): p. 58-68.
7. Kakehi, K., M. Kinoshita, and S. Yasueda, *Hyaluronic acid: separation and biological implications*. Journal of Chromatography B-Analytical Technologies in the Biomedical and Life Sciences, 2003. **797**(1-2): p. 347-355.
8. Mason, M., et al., *Attachment of hyaluronic acid to polypropylene, polystyrene, and polytetrafluoroethylene*. Biomaterials, 2000. **21**(1): p. 31-36.
9. Allison, D.D. and K.J. Grande-Allen, *Review. Hyaluronan: A powerful tissue engineering tool*. Tissue Engineering, 2006. **12**(8): p. 2131-2140.
10. Ibrahim, S. and A. Ramamurthi, *Hyaluronic acid cues for functional endothelialization of vascular constructs*. Journal of Tissue Engineering and Regenerative Medicine, 2008. **2**(1): p. 22-32.
11. Peattie, R.A., et al., *Dual growth factor-induced angiogenesis in vivo using hyaluronan hydrogel implants*. Biomaterials, 2006. **27**(9): p. 1868-1875.
12. Leach, J.B. and C.E. Schmidt, *Characterization of protein release from photocrosslinkable hyaluronic acid-polyethylene glycol hydrogel tissue engineering scaffolds*. Biomaterials, 2005. **26**(2): p. 125-135.
13. Miller, J.A., et al., *Efficacy of hyaluronic acid nonsteroidal anti-inflammatory drug systems in preventing postsurgical tendon adhesions*. Journal of Biomedical Materials Research, 1997. **38**(1): p. 25-33.
14. King, S.R., et al., *Beneficial Actions of Exogenous Hyaluronic-Acid on Wound-Healing*. Surgery, 1991. **109**(1): p. 76-84.

15. Leach, J.B., et al., *Photocrosslinked hyaluronic acid hydrogels: Natural, biodegradable tissue engineering scaffolds*. Biotechnology and Bioengineering, 2003. **82**(5): p. 578-589.
16. Cristino, S., et al., *Analysis of mesenchymal stem cells grown on a three-dimensional HYAFF 11®-based prototype ligament scaffold*. Journal of Biomedical Materials Research Part A, 2005. **73A**(3): p. 275-283.
17. Correia, C.R., et al., *Chitosan Scaffolds Containing Hyaluronic Acid for Cartilage Tissue Engineering*. Tissue Engineering Part C-Methods, 2011. **17**(7): p. 717-730.
18. Thomas, D., T. O'Brien, and A. Pandit, *Toward Customized Extracellular Niche Engineering: Progress in Cell-Entrapment Technologies*. Advanced Materials, 2017.
19. Juste, S., et al., *Effect of poly-L-lysine coating on macrophage activation by alginate-based microcapsules: assessment using a new in vitro method*. Journal of Biomedical Materials Research Part A, 2005. **72**(4): p. 389-98.
20. Caliari, S.R. and J.A. Burdick, *A practical guide to hydrogels for cell culture*. Nature Methods, 2016. **13**(5): p. 405-14.
21. Hauch, K.D. and B.D. Ratner, *Chapter II.3.8 - Microscopy for Biomaterials Science*, in *Biomaterials Science (Third Edition)*, B.D. Ratner, et al., Editors. 2013, Academic Press. p. 677-692.
22. Sutton, M.A., et al., *Scanning Electron Microscopy for Quantitative Small and Large Deformation Measurements Part I: SEM Imaging at Magnifications from 200 to 10,000*. Experimental Mechanics, 2007. **47**(6): p. 775-787.
23. Omid, M., et al., *7 - Characterization of biomaterials*, in *Biomaterials for Oral and Dental Tissue Engineering*, L. Tayebi and K. Moharamzadeh, Editors. 2017, Woodhead Publishing. p. 97-115.
24. Heath, D.E. and S.L. Cooper, *Chapter I.2.2 - Polymers: Basic Principles A2 - Ratner, Buddy D*, in *Biomaterials Science (Third Edition)*, A.S. Hoffman, F.J. Schoen, and J.E. Lemons, Editors. 2013, Academic Press. p. 64-79.
25. Ermrich, M. and D. Opper, *XRD for the Analyst - Getting Acquainted with the Principles*. 2018: Malvern Panalytical B.V. 93.
26. Chatterjee, A.K., *8 - X-Ray Diffraction*, in *Handbook of Analytical Techniques in Concrete Science and Technology*, V.S. Ramachandran and J.J. Beaudoin, Editors. 2001, William Andrew Publishing: Norwich, NY. p. 275-332.
27. Cengiz, I.F., J.M. Oliveira, and R.L. Reis, *Micro-CT - a digital 3D microstructural voyage into scaffolds: a systematic review of the reported methods and results*. Biomaterials Research, 2018. **22**: p. 26.
28. Malkin, A.Y. and A.I. Isayev, *Rheology: concepts, methods, and applications*. 2017: Elsevier.
29. Xiandeng Hou, R.S.A., Bradley T. Jones, George L. Donati, *Inductively Coupled Plasma Optical Emission Spectrometry*, in *Encyclopedia of Analytical Chemistry*. 2016.

30. Hitachi. *Principle of ICP Optical Emission Spectrometry (ICP-OES)*. [cited 2020 29.02.2020].
31. Shard, A.G., *Chapter 4.3.1 - X-ray photoelectron spectroscopy*, in *Characterization of Nanoparticles*, V.-D. Hodoroaba, W.E.S. Unger, and A.G. Shard, Editors. 2020, Elsevier. p. 349-371.
32. Ratner, B.D., *Chapter 1.1.5 - Surface Properties and Surface Characterization of Biomaterials*, in *Biomaterials Science (Third Edition)*. 2013, Academic Press. p. 34-55.
33. Malvern, *Zeta potential - An introduction in 30 minutes*, in *TN101104ZetaPotentialIntroduction*. 2015, Malvern Instruments Limited.
34. Luo, Y., J. Qin, and B. Lin, *Methods for pumping fluids on biomedical lab-on-a-chip*. *Frontiers in Bioscience*, 2009. **14**: p. 3913-24.
35. Coutinho, D.F., et al., *Microfabricated photocrosslinkable polyelectrolyte-complex of chitosan and methacrylated gellan gum*. *Journal of Materials Chemistry*, 2012. **22**: p. 17262.
36. Olsen, A.L., *Potassium Bromide Pellet Technique*. *Analytical Chemistry*, 1959. **31**(2): p. 321-322.
37. Chen, Y., et al., *Applications of Micro-Fourier Transform Infrared Spectroscopy (FTIR) in the Geological Sciences—A Review*. *International Journal of Molecular Sciences*, 2015. **16**(12): p. 30223-30250.
38. Smith, B.C., *Fundamentals of Fourier Transform Infrared Spectroscopy*. 2011, CRC Press. p. 207.
39. Seo, Y. and W. Jhe, *Atomic force microscopy and spectroscopy*. *Reports on Progress in Physics*, 2007. **71**(1): p. 016101.
40. Majorek, K.A., et al., *Structural and immunologic characterization of bovine, horse, and rabbit serum albumins*. *Molecular Immunology*, 2012. **52**(3-4): p. 174-82.
41. Yuasa, M., et al., *Dexamethasone enhances osteogenic differentiation of bone marrow- and muscle-derived stromal cells and augments ectopic bone formation induced by bone morphogenetic protein-2*. *PLoS ONE*, 2015. **10**(2): p. e0116462.
42. Stevens, M.M., *Biomaterials for bone tissue engineering*. *Materials Today*, 2008. **11**(5): p. 18-25.
43. Kokubo, T. and H. Takadama, *How useful is SBF in predicting in vivo bone bioactivity?* *Biomaterials*, 2006. **27**(15): p. 2907-2915.
44. Lu, X. and Y. Leng, *Theoretical analysis of calcium phosphate precipitation in simulated body fluid*. *Biomaterials*, 2005. **26**(10): p. 1097-108.
45. Appel, A.A., et al., *Imaging challenges in biomaterials and tissue engineering*. *Biomaterials*, 2013. **34**(28): p. 6615-30.
46. Sanderson, M.J., et al., *Fluorescence microscopy*. *Cold Spring Harbor Protocols*, 2014. **2014**(10): p. pdb top071795.

47. Hinton, T.J., et al., *Three-dimensional printing of complex biological structures by freeform reversible embedding of suspended hydrogels*. Science Advances, 2015. **1**(9).
48. Cerqueira, M.T., et al., *Human adipose stem cells cell sheet constructs impact epidermal morphogenesis in full-thickness excisional wounds*. Biomacromolecules, 2013. **14**(11): p. 3997-4008.
49. Standardization, I.O.f., *ISO 10993-5:2009 - Biological evaluation of medical devices, in Part 5: Tests for in vitro cytotoxicity*. 2009.
50. Rampersad, S.N., *Multiple applications of Alamar Blue as an indicator of metabolic function and cellular health in cell viability bioassays*. Sensors (Basel), 2012. **12**(9): p. 12347-60.
51. Wolf, M.F., K.P. Coleman, and G.M. Lewerenz, *Chapter II.3.3 - In Vitro Assessment of Cell and Tissue Compatibility A2 - Ratner, Buddy D*, in *Biomaterials Science (Third Edition)*, A.S. Hoffman, F.J. Schoen, and J.E. Lemons, Editors. 2013, Academic Press. p. 593-608.
52. Singer, V.L., et al., *Characterization of PicoGreen reagent and development of a fluorescence-based solution assay for double-stranded DNA quantitation*. Analytical Biochemistry, 1997. **249**(2): p. 228-38.
53. ACEA Biosciences, I. *Cellular Impedance Explained*. 2020 05.03.2020].
54. Janeway, C., *Immunobiology Five*. 2001: Garland Pub.
55. Trouw, L.A., M.C. Pickering, and A.M. Blom, *The complement system as a potential therapeutic target in rheumatic disease*. Nature Reviews Rheumatology, 2017. **13**(9): p. 538-547.
56. Pereira, P., et al., *Biocompatibility of a self-assembled glycol chitosan nanogel*. Toxicology In Vitro, 2015. **29**(3): p. 638-646.
57. Berger, A., *Th1 and Th2 responses: what are they?* BMJ, 2000. **321**(7258): p. 424.
58. Piedrahita, J.A. and J.K. Williams, *Animal Models in Tissue Engineering. Part I*. Tissue Eng Part C Methods, 2017. **23**(11): p. 641-642.
59. Janowski, M., et al., *Neurotransplantation in mice: The concordance-like position ensures minimal cell leakage and widespread distribution of cells transplanted into the cisterna magna*. Neuroscience Letters, 2008. **430**(2): p. 169-174.
60. Schoen, F.J. and R.N. Mitchell, *Chapter II.1.5 - Tissues, the Extracellular Matrix, and Cell-Biomaterial Interactions*, in *Biomaterials Science (Third Edition)*, B.D. Ratner, et al., Editors. 2013, Academic Press. p. 452-474.
61. Zhang, Y.S. and J. Yao, *Imaging Biomaterial-Tissue Interactions*. Trends in Biotechnology, 2018. **36**(4): p. 403-414.
62. Oliveira, E.P., et al., *Advances in bioinks and in vivo imaging of biomaterials for CNS applications*. Acta Biomaterialia, 2019.

63. Fiedorowicz, M., et al., *Anterograde Transport in Axons of the Retinal Ganglion Cells and its Relationship to the Intraocular Pressure during Aging in Mice with Hereditary Pigmentary Glaucoma*. *Current Eye Research*, 2018. **43**(4): p. 539-546.

SECTION 3: Experimental Part

Chapter IV: Self-mineralizing Ca-enriched Methacrylated Gellan Gum Beads for Bone Tissue Engineering*

ABSTRACT

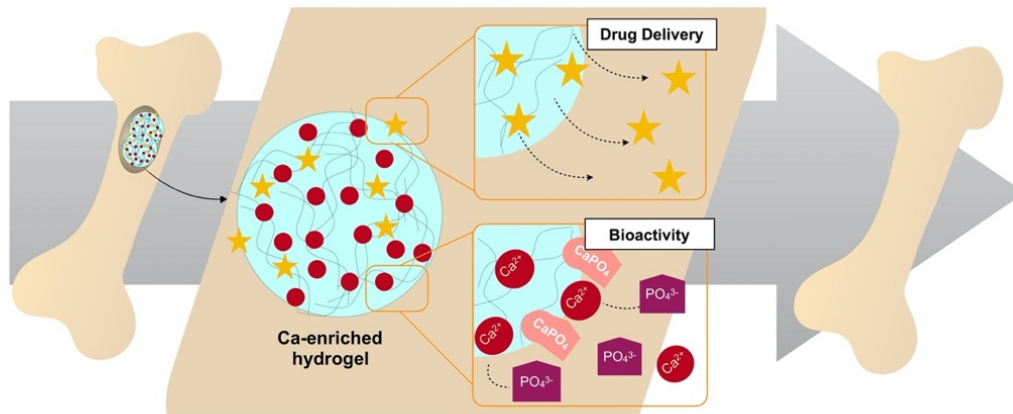
In this study, methacrylated gellan-gum (GG-MA) heteropolysaccharide is proposed as a hydrogel for drug delivery and bone tissue engineering applications. Calcium-enriched beads obtained from the crosslinking of 1% (w/v) GG-MA solutions with 0.1 M CaCl₂ were investigated, considering their intrinsic capacity to promote self-mineralization by ion binding and deposition. Indeed, when immersed in a physiological environment, the Ca-enriched beads promoted the development of a bone-like apatite layer, as confirmed by EDS and XRD chemical analysis. Additionally, the mild production process is compatible with drugs incorporation and release. After encapsulation, Dextran with different molecular weights as well as Dexamethasone 21-phosphate were efficiently released to the surrounding environment. The engineered system was also evaluated considering its biocompatibility, by means of qualitative determination of total complement activation, macrophage proliferation, cytokine release and *in vitro* cell culture. These experiments showed that the developed hydrogels may not stimulate a disproportionate pro-inflammatory reaction once transplanted. At last, when implanted subcutaneously in CD-1 male mice up to 8 weeks, the beads were completely calcified, and no inflammatory reaction was observed. Summing up, these results show that calcium-enriched GG-MA hydrogel beads hold great potential as news tools for bone tissue regeneration and local drug delivery applications.

Keywords: Methacrylated gellan gum; hydrogels; mineralization; bioactivity; drug delivery; bone tissue engineering.

* This chapter is based on the following publication:

"Self-mineralizing Ca-enriched Methacrylated Gellan Gum Beads for Bone Tissue Engineering". Vieira S., Silva Morais A., Garet E., Silva-Correia J., Reis R.L., González-Fernández A., Oliveira J.M., *Acta Biomaterialia*, 93, 74-85, DOI: 10.1016/j.actbio.2019.01.053, 2019.

IV.1 Graphical Abstract



IV.2 Introduction

Traumatic injuries, infections or tumor resections can originate critical-sized bone defects that cannot regenerate *per se*. Bone grafts, mainly autographs from the iliac crest, are widely used as standard procedures for restoration of bone defects. However, the ever-increasing incidence of bone-related disorders, the limited donor supply as well as donor site morbidity, makes the bone grafting strategy far from the ideal clinical needs [1].

Different biomaterials have been explored to engineer functional bone substitutes. Most of the strategies applied in the scope of bone tissue engineering (BTE) focus on the combination of naturally derived polymers with calcium phosphates (CaP), such as hydroxyapatite [2, 3] and β -tricalcium phosphate (β -TCP) [4-6], as well as bioactive glasses [7]. These strategies rely on the development of a calcified surface upon implantation, which confers a bioactive nature to otherwise inert polymers, improving their osteointegration. This biomineralization is attributed to ionic exchange to the surrounding medium that promotes the deposition of calcium and phosphate ions, which in turn leads to the formation of a bone-like apatite layer. That phenomenon is also reported to support stem cell osteodifferentiation [8-10]. Therefore, the inclusion of such ions into different types of scaffolds is gathering a great deal of attention. Biomineralization can also be induced by grafting anionic groups into polymers, as a way to increase ion binding and deposition [11]. Nonetheless, the abovementioned methodologies often require expensive and time-consuming chemistries, leaving room for the development of more cost-effective and straightforward solutions.

Bone-substitute materials can be further improved as regard their biological and functional performance if combined with drugs of interest. These multifunctional three-dimensional BTE structures are considered as a novel generation of osteoinductive scaffolds, that can anticipate new bone formation [12, 13]. Numerous molecules are reported as beneficial for new bone formation [14], including Bone Morphogenetic Proteins (BMP) [15] and dexamethasone [16]. Nevertheless, their systemic and/or erroneous application can result in deleterious side effects [17, 18]. Therefore, much effort has been made on the development of controlled and local drug delivery, taking advantage of BTE strategies.

In this regard, advanced BTE strategies can be achieved using hydrogels. Although hydrogels lack osteoconductivity, they can be functionalized using the abovementioned strategies [19, 20]. As hydrogels are structurally similar to the natural extracellular matrix (ECM), the resulting bioactive matrices can then be used for the delivery of bioactive agents, such as stem cells or drugs, *in situ*. This combined approach is then preferred, since it enables the synergistic effect of cellular therapy and bioactive agents, resulting in a faster osteoinduction and osteointegration. Indeed, different hydrogels were already reported as promising on the scope of BTE [21, 22].

One polymer of particular interest is gellan gum (GG), a heteropolysaccharide, composed by repeating units of 1-4- α -L-rhamnose, 1-3- β -D-glucose and 1,4- β -D-glucuronate [23]. The high acyl form, the native form, has two acyl substituents, both located in the same glucose residue [24, 25]. A low acyl form of GG can be obtained after removal of the acyl residues, via alkaline hydrolysis of native GG [26]. Both forms exhibit a disordered coiled conformation in solution at high temperatures, that changes to a double helix structure when cooled [27], where GG exhibits “weak gel” characteristics. To form a hydrogel, GG can be crosslinked with metallic ions [28, 29], that link the double helices of the polymeric network. The resulting hydrogel properties are closely related to the presence, or absence, of acyl groups [30]. In this regard, high-acyl gellan gum leads to soft, elastic and non-brittle gels, as the acyl residues are located on the periphery of the helix, obstructing the polymer chains packing. In contrast, low-acyl GG produces firm, non-elastic, brittle gels since ions can easily link polymer chains and form a branched network.

GG has been studied for numerous applications on Tissue Engineering (TE), including brain TE [31], dental care [32], cartilage [33-35] and intervertebral disc applications [36-38]. However, as abovementioned, unmodified low acyl GG needs high temperatures, above 50 °C, to be soluble in water. This property hinders its straightforward application as cell-laden material. Methacrylated GG (GG-MA), obtained via chemical modification of low acyl GG [37], is a water-soluble polymer at room temperature.

The obtained GG-MA can be used in place of native GG, thus avoiding the use of high temperatures. Instead, GG-MA hydrogels can be obtained after ionic crosslinking of the pre-gel solution. Different ionic sources were already reported as suitable for GG-MA crosslinking, including phosphate buffered saline (PBS) [39] and CaCl_2 solutions [19, 20]. One asset of GG-MA is its capacity to allow the bidirectional diffusion of oxygen, nutrients, and molecules of different sizes [40]. Hence, GG-MA based matrices are potential candidates for controlled delivery purposes, from stem cells to different drugs, *in situ*.

In this work, the intrinsic bioactive properties of Ca-enriched GG-MA hydrogel beads are investigated. Previous work already reported the potential of ionically crosslinked GG-MA hydrogels for BTE [41]. Nonetheless, to our knowledge, the bioactive nature and self-mineralization capacity of these hydrogels was never exploited. We hypothesize that the presence of calcium ions within the hydrogel matrix facilitates the deposition of phosphate ions and further mineralization, turning the bioinert GG-MA into a strongly bioactive material. For that, bioactive properties of Ca-enriched beads were studied under *in vitro* and *in vivo* conditions. Additionally, the potential to combine an osteoinductive environment with efficient local drug release ability was explored *in vitro*. This could expand the applicability of the Ca-enriched beads, potentially improving its functional and biological outcomes, by providing a sustained release of pharmacological agents or growth factors.

IV.3 Materials and Methods

IV.3.1 Preparation of Methacrylated Gellan Gum (GG-MA) and CaCl_2 Solutions

Methacrylated gellan gum (GG-MA) was obtained following the protocol from Silva-Correia *et al.* [37]. Concisely, glycidyl methacrylate (GMA, 97%, Sigma-Aldrich) was added to a low-acyl gellan gum solution (Gelzan™ CM Gelrite®, Sigma-Aldrich). This mixture was vigorously stirred overnight at room temperature, with a constant control of pH at 8.5. After, cold acetone was used to precipitate the reaction products, which were further purified by dialysis (cellulose membrane, molecular weight cut-off 12 kDa, Sigma-Aldrich) against distilled water. At last, GG-MA was frozen at $-80\text{ }^\circ\text{C}$ and freeze-dried. The dry material was stored protected from light and in a dry place until further use. Then, 1% (w/v) GG-MA solutions were prepared by dissolving the aforementioned dry material in Milli-Q water, using gentle agitation. Calcium chloride (CaCl_2 anhydrous powder, Merck-Millipore, Germany) was used to prepare 0.1 M aqueous solutions, that were further used as crosslinking bath solutions.

IV.3.2 Preparation of Ca-enriched GG-MA Beads

To prepare the hydrogel beads, GG-MA solutions were added dropwise into a CaCl_2 stirred crosslinking bath, using a syringe coupled with 30G needle. Beads, from now on described as Ca-enriched GG-MA, were therefore obtained by ionic crosslinking of the GG-MA chains with the divalent Ca^{2+} ions present in the crosslinking solution. After production, beads were thoroughly washed with phosphate buffer saline (PBS, Sigma-Aldrich), to remove the CaCl_2 excess. Complement activation analysis as well as *in vitro* and *in vivo* studies were carried out using sterile beads. For that, dry GG-MA was sterilized by ethylene oxide gas (EO Gas Sterilizer/Aerator, 5XL, 3M STERI-VAC) before being dissolved. All the solutions were sterilized by filtration (0.22 μm filter) and preparation was performed under aseptic conditions.

IV.3.3 Physicochemical Characterization of Ca-enriched GG-MA Beads

Calcium content was quantified after hydrogel beads production, using a Calcium Colorimetric Assay Kit (Roche), following the manufacturer's instructions. As prepared beads, making up a final GG-MA volume of 100 μL , were mechanically destroyed in 1 mL of Milli-Q water. Then, 5 μL of this solution were mixed with 5 μL of 6 M HCl for 30 minutes, followed by the addition of proper volumes of the commercial reagents provided in the kit. Milli-Q water was used as "blank" control. Surface elemental composition of dehydrated Ca-enriched GG-MA beads was assessed using X-ray photoelectron spectroscopy (XPS, Axis Supra, Kratos, United Kingdom), equipped with monochromatic Al (K) X-ray source operating at 1486.6 eV. Surface charge was reduced by using a co-axial electron neutralizer, which performed the neutralization by itself. Photoelectrons were collected from a take-off angle of 90° relative to the sample surface. Survey spectra was conducted using a Constant Analyzer Energy mode (CAE) with 160 eV pass energy, with high-resolution spectra being recorded at 40 eV pass energy. Charge referencing was performed by setting lower binding energy C 1s photo peak at 285.0 eV. Surface elemental composition was then determined using ESCApe™ software (Kratos, United Kingdom)

IV.3.4 *In vitro* Bioactivity Test

The capability to form an apatite layer *in vitro* was assessed by immersion of the hydrogel beads into Simulated Body Fluid (SBF). The preparation of SBF followed the corrected protocol published by Kokubo and Takadama [42], with ion concentrations as shown in Table III-2 (Chapter III, page 112).

After washing, the hydrogel beads were immersed in SBF solution and incubated at 37 °C, with shaking, for 2, 4 and 8 weeks. At each timepoint, beads were collected, rinsed gently with distilled water, and lyophilized for further characterization. Surface morphology and elemental composition of hydrogel beads

were afterwards assessed by Scanning Electron Microscopy (SEM, FEI Nova NanoSEM 200) and energy dispersive spectroscopy (EDS, QUANTAX200 Bruker, Germany). Crystallinity patterns of the developed apatite shell after incubation in SBF were recorded on a D8 Advance diffractometer (Bruker) using a Cu-K α radiation source, operated at 40 kV and 40 mA (data were collected between 5° and 80° 2 θ). Additionally, apatite formation was followed on hydrated Ca-enriched GG-MA beads, by micro-computed tomography (μ -CT, Skyscan 1772, Bruker, Germany), operated at 50 kV and image pixel size of 5 μ m. ImageJ was used to re-construct the subsequent 3D images. At least, five samples were used per condition and per time point.

IV.3.5 Drug Release Studies

Dexamethasone 21-phosphate disodium salt (Dexa 21P, Mw 516.40 g.mol⁻¹, Sigma-Aldrich) as well as fluorescein isothiocyanate–dextran (Dextran-FITC, Sigma-Aldrich) with different molecular weights (4, 20 and 70 kDa), were loaded into the Ca-enriched GG-MA beads to assess the feasibility of using this system as a platform for drug delivery of molecules with different molecular weight. The model drugs were dissolved in Milli-Q water and added to GG-MA pre-gel solutions at a final concentration of 0.125 mg.mL⁻¹ and 3.5 mg.mL⁻¹ for dextran and Dexa 21P, respectively. For each condition, ten beads were immersed in SBF (5 mL) and incubated at 37 °C with mechanical horizontal shaking (reciprocating motion, 100 min⁻¹) in a thermostatic water bath. At different timepoints, 350 μ L of supernatant was retrieved and replaced by the same amount of fresh SBF. Empty Ca-enriched GG-MA beads incubated in same conditions were used as blanks. At the last time-point, beads were mechanically destroyed by pipetting, centrifuged, and the resulting supernatant was used to calculate the final concentration of FITC-labelled molecules and Dexa21P that could be retained inside the beads. The fluorescence emission of FITC-labelled dextran was measured at an excitation wavelength of 485/20 nm and at an emission wavelength of 528/20 nm, in a microplate reader (Gen 5 2.01, Synergy HT, BioTek); Dexa 21P was quantified by UV-vis spectroscopy (Synergy HT, BioTek) at 243 nm. The released mass after each time point was obtained using calibrations curves prepared with pre-defined standard solutions. Drug loading efficiency was calculated as 43.2 \pm 3.8%, 42.4 \pm 3.4% and 72.9 \pm 0.6% for 4, 20 and 70 kDa Dextran-FITC, respectively; and 74.5 \pm 10.2% for Dex 21P.

IV.3.6 *In vitro* Studies

IV.3.6.1 Cell Culture

Human adipose tissue samples were collected from the knee fat pad of healthy male and female donors with ages between 18 and 57 years, after informed consent, under established cooperative agreements between Hospital da Senhora da Oliveira (Guimarães, Portugal) and 3B's Research Group. hASCs were enzymatically isolated, using a protocol based on a previously published work [43]. Briefly, fat tissue was minced into small pieces and digested overnight at 37 °C, using 0.075% collagenase type II (C6885, Sigma-Aldrich) dissolved in Minimum Essential alpha Medium (α -MEM, Gibco®, Life Technologies), supplemented with 10% (v/v) of heat-inactivated fetal bovine serum (FBS, Gibco®, Life Technologies, reference A3160802, EU approved) and 1% (v/v) antibiotic-antimycotic solution (penicillin 100 units.mL⁻¹ and streptomycin 100 mg.mL⁻¹, Gibco®, Life Technologies). The resulting solution was passed through a 100 μ m cell strainer (Falcon) and centrifuged at 800 *g* for 10 minutes. The pellet was collected, centrifuged again at 300 *g* for more 10 minutes, and resuspended in culture media (α -MEM supplemented with 10% (v/v) FBS and 1% (v/v) antibiotic-antimycotic). Cells were cultured until confluence at 37 °C, 5% CO₂ incubator, changing the culture medium every 2-3 days. THP-1 monocytic cell line as obtained from ATCC (American Type Culture Collection, Middlesex, UK). Cells were seeded in a 75 cm² culture flask (Sarstedt, Nümbrecht, Germany), using RPMI 1640 medium supplemented with 10% heat-inactivated FBS and 2% Penicillin-Streptomycin (Gibco, Life Technologies). Cells were sub-cultured every 2-3 days and maintained in growth in an incubator with humidified air containing 5% CO₂ and at 37 °C.

IV.3.6.2 MEM Extract Test

A MEM extract test, based on ISO 10993-5:2009 guidelines [44], with slight modifications was used to investigate the putative cytotoxic effect of Ca-enriched GG-MA beads. Briefly, hASCs were seeded at 20 x 10³ cells.mL⁻¹ in 24-well plates and allowed to grow until near confluence. Meanwhile, sterile beads were incubated in 20 mL of complete culture α -MEM medium, using a ratio of one bead per mL, for 24 hours at 37 °C under continuous agitation. Sterile TCPS coverslip and latex rubber extracts were used as positive and negative controls, respectively. After one day of culture, hASCs culture media was replaced by 1 mL of extraction fluid and incubated using the aforementioned conditions. After 24, 48, and 72 hours, cell metabolic activity was assessed by AlamarBlue® assay (Bio-Rad Laboratories, Oxford, UK). Cell culture media supplemented with 10% AlamarBlue® dye was added to each well and incubated for 4

hours at 37 °C and 5% CO₂. Afterwards, medium fluorescence was measured using a microplate reader (Synergy HT, BioTek Instruments, USA) at Ex/Em ≈ 530/590 nm. The relative metabolic activity was obtained by normalization with the mean fluorescence value obtained for controls (extraction fluid obtained from a TCPS coverslip). Latex rubber was used as negative control. The experiments were carried out in triplicate (n=9).

IV.3.6.3 Real-time Cell Proliferation: xCELLigence® System

hASCs and macrophage proliferation curves after contact with Ca-enriched GG-MA extract fluids were determined using the xCELLigence RTCA DP system (Roche, Basel, Switzerland). hASCs were seeded at 0.01×10^6 cells.mL⁻¹ in 200 µL of α-MEM complete medium and incubated for 24 hours. Media was then replaced by 200 µL of extract fluid, prepared as described in last section. At last, THP-1 cells were seeded at 0.5×10^6 cells.mL⁻¹, using 200 µL of RPMI 1640 complete medium and phorbol12-myristate 13-acetate (PMA, Sigma-Aldrich) at 64 nM. After 48 hours in culture, that allowed THP-1 differentiation into macrophages, culture medium was replaced by fresh medium, and extract fluids were added after additional 24 hours in culture. Experiments were performed in duplicate (n=4).

IV.3.6.4 Qualitative Determination of Total Complement Activation

The activation of complement cascade upon interaction with Ca-enriched GG-MA beads was determined using a protocol kindly provided by the Nanotechnology Characterization Laboratory (NCL Method ITA-5.1, version 1.2, 2015), as previously reported by P. Pereira *et al.* [45]. Briefly, a pool of human plasma was collected from five healthy volunteer donors and incubated with the sterile hydrogel beads at 37 °C, for 60 minutes. Zymosan A from *Saccharomyces cerevisiae* (1 mg.mL⁻¹, Z4250, Sigma-Aldrich) was used as positive control, while PBS (Sigma-Aldrich), Ethylenediamine Tetraacetic Acid (EDTA, 10 mM, E-7889, Sigma-Aldrich), and plasma with PBS incubated at 4 °C, were used as negative controls. Plasma incubated at 37 °C with both EDTA and Zymosan was used as reversion control, to attest the EDTA negative effect on the cascade. Proteins were resolved via 10% SDS-PAGE electrophoresis and transferred to PVDF membranes (Immuno-Blot PVDF Membrane, BioRad) using the transblot turbo BioRad transfer equipment (Trans-Blot® Turbo™ Transfer System, BioRad). The resulting membranes were incubated for 60 minutes with a mouse monoclonal antibody against human C3 diluted 1:1000 (ab11871, Abcam), washed and incubated with a secondary polyclonal goat anti-mouse IgG antibody conjugated with alkaline phosphatase diluted 1:2000 (D0486, Dako). The membrane was revealed using 5-Bromo-4-Chloro-3-Indolyl Phosphate (BCIP, Sigma-Aldrich) and scanned with a

ChemiDoc™XRS + System (Bio-Rad). Image Lab software™ (version 6.0.1 build 34, Standard Edition 2017, Bio-Rad Laboratories, Inc) was used for further quantification. Procedures using human samples were approved by the Galician Autonomic Ethics Committee at the Concellería de Sanidade da Xunta de Galicia (Ref 2014/492). All participants included in the study gave their written informed consent.

IV.3.6.5 Cytokine Release from Human Peripheral Blood Mononuclear Cells (hPBMCs)

Cytokine release triggered by the presence of Ca-enriched GG-MA hydrogel beads was measured following a protocol published by Simon-Vasquez *et al.* [46]. Blood samples were collected from three different healthy human donors, and hPBMCs were isolated by density gradient using Ficoll-Paque PLUS™ (GE Healthcare). Briefly, EDTA anticoagulated blood was diluted using equal volume of PBS and added to Ficoll in a 7:3 ratio (diluted Blood:Ficoll). This mix was centrifuged at 180 *g* for 30 minutes, at 20 °C, and after centrifugation hPBMCs were located at the interface between Ficoll and plasma. Cells were harvested from the interface, with the help of a Pasteur pipette, and washed twice with complete medium, by centrifugation at 100 *g* for 5 minutes at 20 °C. At last, cells were seeded in a 96-well plate, using a cell density of 1×10^5 cells per well. Seeded hPBMCs were incubated in the presence of sterile Ca-enriched GG-MA beads, lipopolysaccharide (LPS, InvivoGen) at 20 ng.mL⁻¹ (positive control) and culture medium (negative control). After 24 hours of incubation at 37 °C with 5% CO₂, the plate was centrifuged (100 *g*, 5 minutes, 4 °C), the supernatant collected and stored at – 20 °C until further quantification. Ten different cytokines were measured (interleukin-2 (IL-2), interferon gamma (IFN-γ), interleukin-12p70 (IL-12p70), tumor necrosis factor-β (TNF-β), interleukin-4 (IL-4), interleukin-5 (IL-5), interleukin-10 (IL-10), interleukin-8 (IL-8), interleukin-1β (IL-1β), and tumor necrosis factor-α (TNF-α)) and respective concentrations were determined using the Milliplex® Map Human Cytokine/Chemokine Magnetic Bead Panel (Millipore Corporation, USA) according to the manufacturer's instructions. Experiments were performed in duplicate, per donor (n=6). Finally, samples were analyzed by Luminex® laser based fluorescent analytical test (MAGPIX®, ThermoFisher) and data analyzed with the xPONENT 4.2 1324.0 Software (Luminex®). Institutional ethics approval to work with human samples from healthy donors was obtained the Galician Autonomic Ethics Committee at the Concellería de Sanidade da Xunta de Galicia (Ref 2014/492). All participants included in the study gave their written informed consent.

IV.3.7 *In vivo* Subcutaneous Implantation

CD-1 male mice of 5-weeks old and average weight of 27-32 g, at the time of implantation (Charles River, Massachusetts, USA) were used to study biocompatibility and bioactivity of Ca-enriched GG-MA hydrogel

beads *in vivo*. Use and maintenance of animals were carried out in accordance to the Ethics Committee of University of Minho and approved by the Portuguese Licensing Authority (DGAV-DSPA). Ca-enriched GG-MA beads were prepared under aseptic conditions, using sterile solutions as abovementioned in section 2.2. At the time of the surgery, each mouse was anesthetized by intraperitoneal injection of Domtor 1 mg.mL⁻¹ (Medetomidine 1 mg.kg⁻¹, Novavet, Braga, Portugal) and Imalgene 100 mg.mL⁻¹ (Ketamine 75 mg.kg⁻¹, Novavet, Braga, Portugal). After anesthesia, the implantation area was shaved, and disinfected with iodine (Life Technologies, Carlsbad, CA, USA). Subcutaneous pockets were formed on the back of each mice. Three beads were implanted in each subcutaneous pocket, followed by skin suture. After 2, 4 and 8 weeks, mice were euthanized, by injection of overdose of Eutasil 200 mg.mL⁻¹ (pentobarbital sodium, Novavet, Braga, Portugal), and the beads retrieved. The material was fixed with 10 vol.% formalin solution, followed by dehydration and paraffin embedding. Slides with 4 µm-thick sections were prepared and stained with Alizarin Red (AzR) staining. Experiments were performed in triplicate, with a total number of 9 animals per time-point.

IV.3.8 Statistical Analysis

Results are presented as mean ± standard deviation, when appropriate. When applicable, the experimental data was analyzed using both two-way (2way ANOVA) and single-factor analysis of variance (One-way ANOVA) to assess the statistical significance of the results, followed by *post hoc* Tukey tests. Statistical significance was set at a P value of ≤0.05. All statistical analysis was performed using GraphPad Prism version 7.0a.

IV.4 Results

IV.4.1 Ca-enriched GG-MA Hydrogel Beads Characterization

Ca-enriched GG-MA hydrogels were prepared by ionic crosslinking of GG-MA pre-gel solution with 0.1 M CaCl₂. Beads were obtained by extrusion dripping, where drops of GG-MA were dispensed into the stirred CaCl₂ bath, as schematically represented in Figure IV-1A. Beads are formed upon contact of GG-MA with the Ca²⁺ ions, which diffuse from the solution to the hydrogel core, gelifying the whole bead. After washing with PBS, to remove the excess of Ca²⁺ ions, calcium concentration was 80.422 ± 8.15 µg.mL⁻¹. Besides calcium, other ions were found on the surface of Ca-enriched GG-MA beads (Figure IV-1B), including sodium, phosphorus and chloride, that may remain on the surface after PBS washing. Calcium region deconvolution (data not shown) also confirms the presence of this ion on the surface of Ca-enriched GG-MA beads.

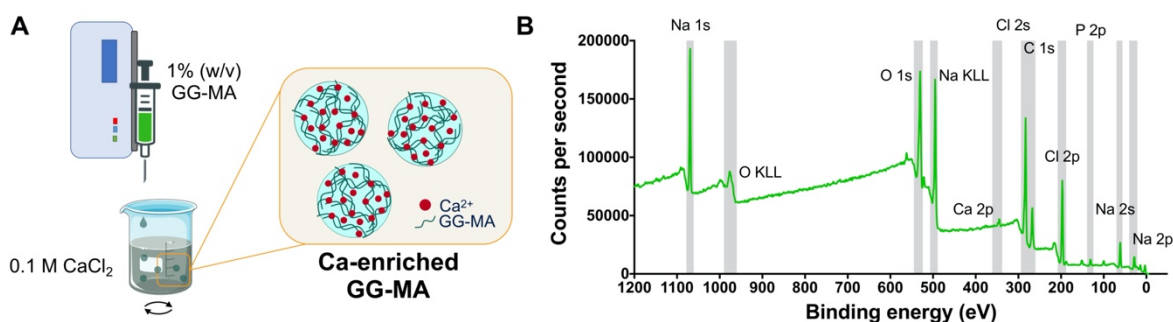


Figure IV-1. Ca-enriched GG-MA beads preparation and characterization. A – Schematic representation of the experimental setting used to prepare the Ca-enriched GG-MA beads; B – Wide XPS spectra of Ca-enriched GG-MA with assigned binding energies.

Mineralization studies were conducted by soaking of Ca-enriched GG-MA beads into Simulated Body Fluid (SBF) solution along 2, 4 and 8 weeks, as schematically represented in Figure IV-2A. At macroscopic level, after SBF immersion, the initially translucent Ca-enriched GG-MA hydrogel beads became white and opaque, suggesting the development of a mineral layer on their top (Figure IV-2B). Indeed, SEM images show that after 2 weeks of incubation, an apatite layer covered the surface of the hydrogels, with the typical cauliflower-like morphology of hydroxyapatite (Figure IV-2C). Further chemical characterization, by means of performing an EDS analysis, confirmed a Ca/P ratio closer to 1.67, the theoretical value of hydroxyapatite (Figure IV-2D). XRD analysis also attested the formation of hydroxyapatite crystals on beads' surface, as the acquired diffractograms, represented in Figure IV-2E, are similar to the diffractogram of semi-crystalline hydroxyapatite [47].

Also, μ CT analysis showed a mineral matrix that was confined to the beads surface (Figure IV-3A), and with increased thickness over time (Figure IV-3A, bottom panel and Figure IV-3B).

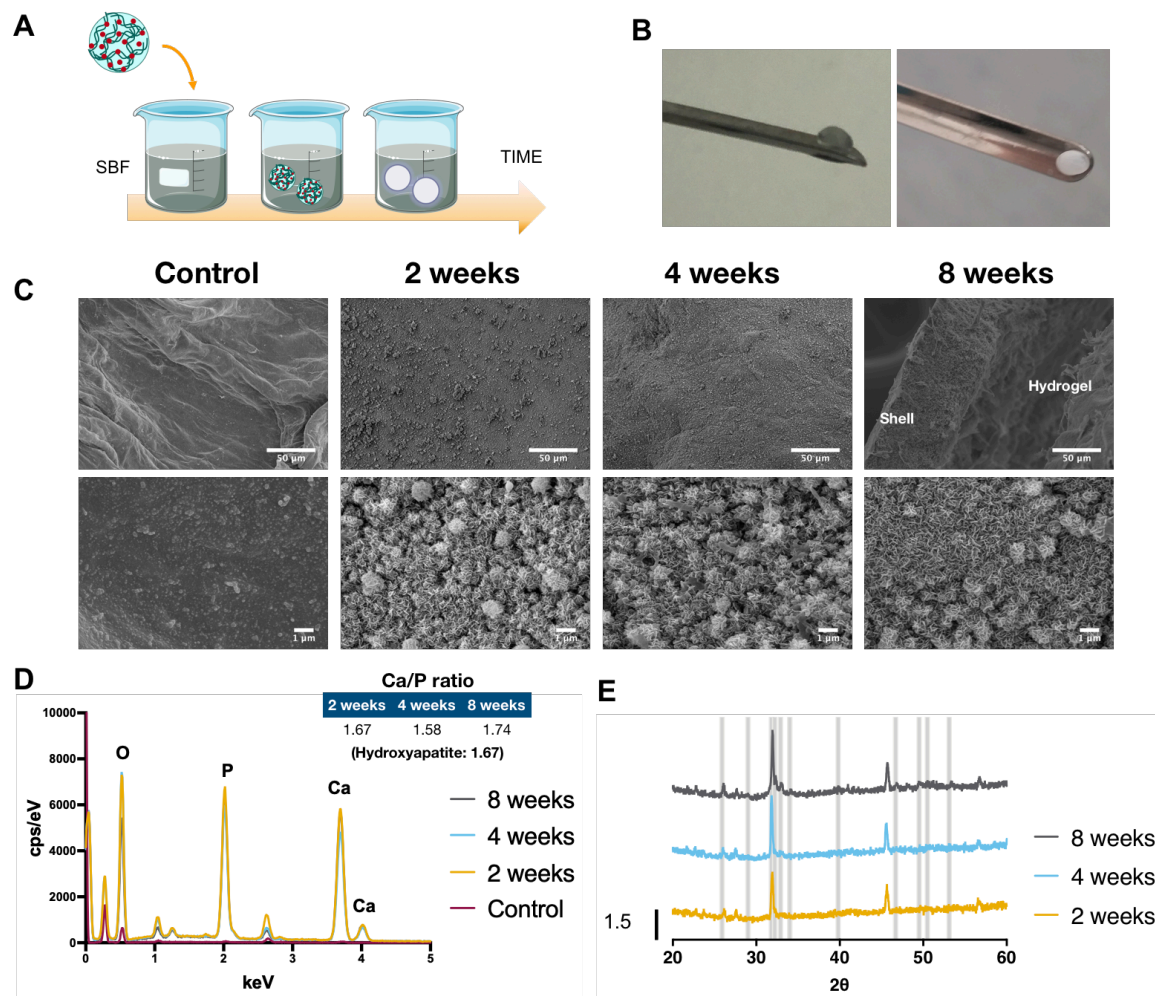


Figure IV-2. *In vitro* bioactivity: SBF immersion. A – Schematic representation of the bioactivity assay; B – Translucent beads before immersion and white opaque beads after SBF immersion for 8 weeks; C – SEM images of the beads before and after 2,4 and 8 weeks of SBF immersion. SEM images highlight the typical cauliflower-like morphology of hydroxyapatite deposited on the surface of beads. Scale bar: 50 μm for SEM 500x magnification (top), 1 μm for SEM 10,000x magnification (bottom); D – EDS spectra acquired before and after 2, 4 and 8 weeks of immersion, for detection of chemical elements and Ca/P ratio; E -XRD spectra of Ca-enriched GG-MA obtained after immersion in SBF. The principal characteristic hydroxyapatite peaks are indicated at $2\theta = 25.9^\circ, 29^\circ, 31.8^\circ, 32.2^\circ, 32.9^\circ, 34^\circ, 39.8^\circ, 46.7^\circ, 49.5^\circ, 50.5^\circ$ and 53.1° .

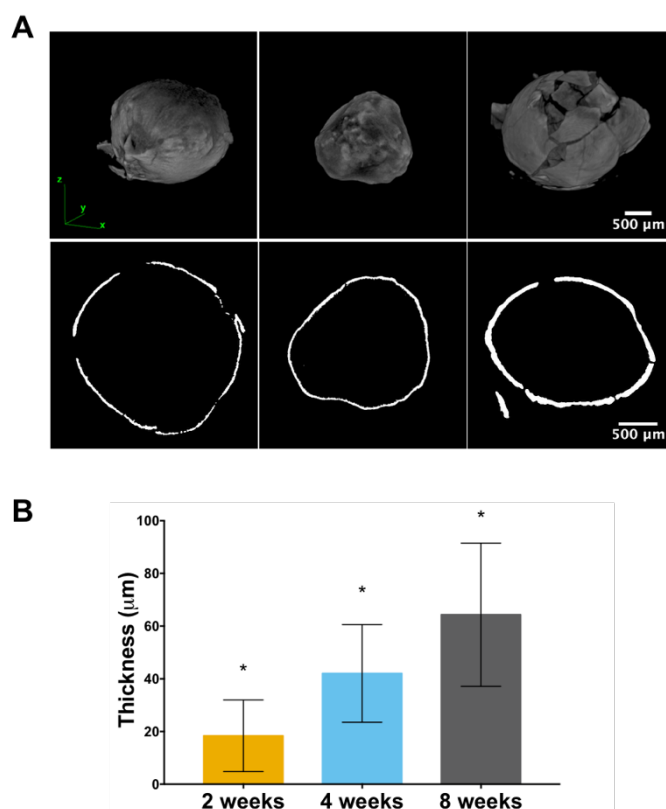


Figure IV-3. *In vitro* bioactivity: μ CT imaging. A - 3D reconstruction of μ CT images (upper panel) also confirm the deposition of a mineral layer on the top of the beads, while the core remains with a high-water content (hydrogel). Representative images of longitudinal sections used to calculate shell thickness (bottom panel). Scale bar: 500 μ m; E - Shell thickness along incubation time. * statistically different from all the other timepoints, with $p < 0.05$.

IV.4.2 Drug Release Profile

Drug delivery capacity was explored by incorporation of different model molecules within the Ca-enriched GG-MA hydrogel matrix, followed by immersion in SBF at 37 °C, in shaking conditions. Dexamethasone 21 phosphate (Dexa 21P, Mw 516.40 g.mol⁻¹) was used as a small model molecule, while 4, 20 and 70 kDa Dextran-FITC were used as a larger molecules model.

The cumulative release profiles are plotted in Figure IV-4. All model drugs reached a plateau after 24 hours of release, except 70 kDa Dextran-FITC molecule, that showed a more sustained release profile. Dexa 21P was totally released in the first two hours, showing a burst release followed by a plateau. Dextran release was dependent on molecule size, where 4 kDa molecules were rapidly released, similarly to Dexa 21P. Conversely, 20 kDa and 70 kDa Dextran-FITC exhibited a hampered diffusion through the hydrogel, resulting in a delayed complete release. After 1 hour, $86.0 \pm 3.12\%$ and $78.3 \pm 3.7\%$ of 20 kDa and 70 kDa Dextran, respectively, were released. The diffusion of Dextran from the inner hydrogel to the

surrounding environment continued and, after 3 hours, the release percentage reached $95.9 \pm 0.94\%$ for 20 kDa molecule and $89.27 \pm 2.18\%$ for 70 kDa Dextran-FITC. Total release of 20 kDa Dextran-FITC was achieved between 6- and 9-hours post incubation, while for 70 kDa, it was necessary to wait nearly 72 hours until a complete release was observed.

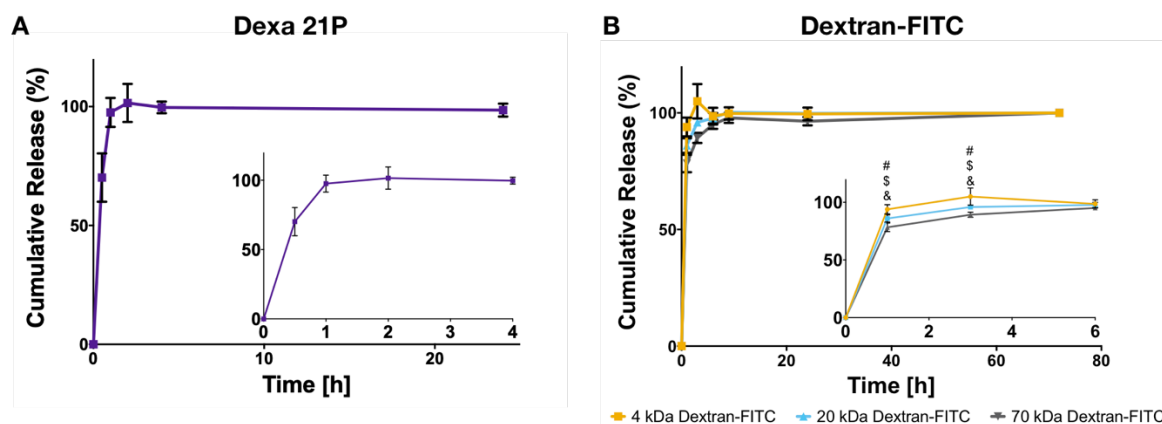


Figure IV-4. Drug Release Profile from Ca-enriched GG-MA Beads. A – Burst release profile observed for Dex 21P molecules; B – Release profile registered for 4, 20 and 70 kDa Dextran-FITC molecules, along 72 hours. Statistical analysis performed by two-way ANOVA, with $p < 0.01$: # - significant difference between 4 and 20 kDa; \$ - significant difference between 4 and 70 kDa; & - significant difference between 20 and 70 kDa. Inserts show the first hours in higher detail. Results presented as average \pm SD, $n=3$.

IV.4.3 Cytocompatibility and Immunocompatibility

IV.4.3.1 Cell Metabolic Activity and Proliferation

The metabolic activity of hASCs, after culture with Ca-enriched GG-MA beads leachable, was measured along 3 days of culturing. As depicted in Figure IV-5A, the possible by-products present in the leachable did not significantly change hASCs metabolic activity, since the obtained values are similar to the control ones (TCPS leachable, 100%). As expected, latex leachable evoked a deleterious effect on cells, drastically decreasing their metabolic activity.

The effect of material leachable on cell proliferation was also studied. For that, hASCs and Human monocytes (THP-1), previously differentiated into M0 macrophages, were cultured with the leachable, and cell proliferation monitored, in real-time, along 3 days (Figure IV-5B and Figure IV-5C). Unsurprisingly, latex leachable rapidly decreased cell proliferation for both hASCs and THP-1 cells. On the other hand, Ca-enriched GG-MA leachable did not significantly change the proliferation pattern, as compared to TCPS control leachable. For hASCs, cell proliferation was slightly higher than control, from day 2 onwards. THP-

1 cell proliferation was lower in the presence of Ca-enriched GG-MA leachable, although the growth trend was comparable to the control (Figure IV-5C).

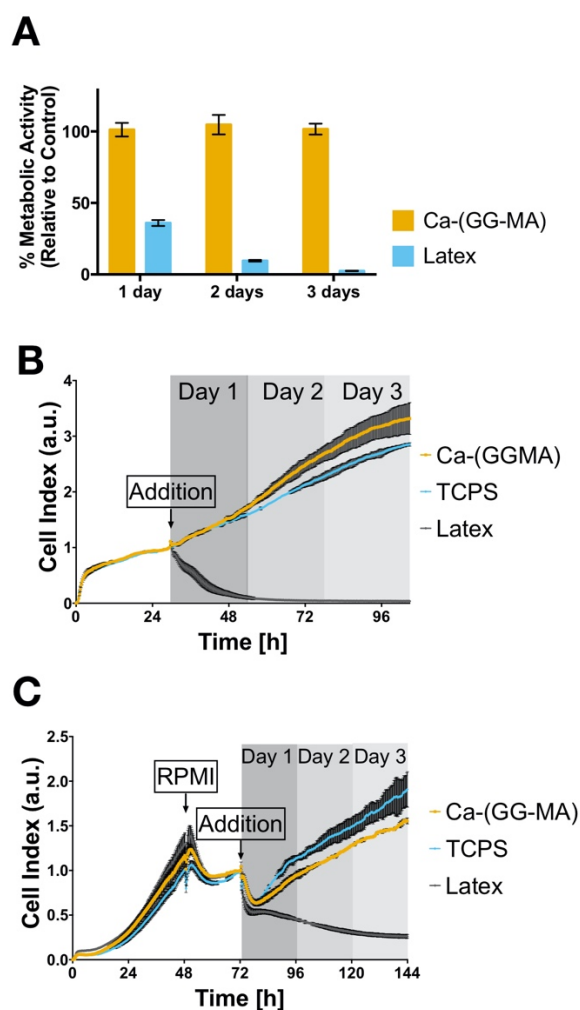


Figure IV-5. *In vitro* assays with Ca-enriched GG-MA beads. A - Metabolic activity of hASCs cultured with Ca-enriched GG-MA and latex leachable, along 3 days of culture, normalized by the cell metabolic activity when in culture with TCPS leachable. Results presented as mean \pm SD, n=9; B - Real-time cell proliferation of hASCs after addition of TCPS (blue line), Ca-enriched GG-MA (orange line) and latex leachable (gray line). Results presented as mean \pm SD, n=4; C- Real-time cell proliferation of THP-1 after addition of TCPS (blue line), Ca-enriched GG-MA (orange line) and latex leachable (gray line). THP-1 differentiation into macrophages was induced by addition of PMA. Results presented as average \pm SD, n=4.

IV.4.3.2 Complement Cascade Activation

The Complement System is one of the routes used to trigger the host innate immune response to a foreign body. Its activation occurs in a cascade fashion, where different serum proteins are locally activated, after contact with the implanted material. Three different routes are reported for Complement

activation (classical, lectin and alternative pathways), but all result in C3 convertase generation followed by the C3 cleavage in C3a and C3b fragments. Since that C3b is considered the main effector of the Complement System [48], the activation of this innate response was evaluated by estimating the C3 cleavage in human plasma samples that were in direct contact with Ca-enriched GG-MA hydrogel beads.

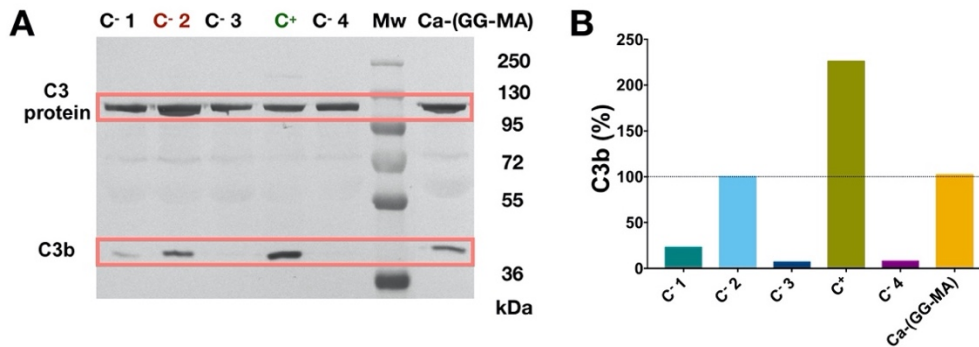


Figure IV-6. Relative C3b protein measured after Complement Activation assay. A - Western Blot membrane after incubation with anti C3/C3b antibody; B - Respective intensity quantification using Image Lab™ software.

C3b was detected in samples only with plasma, due to spontaneous C3 cleavage. Therefore, this value was considered as 100% activation, for reference. Cleavage of C3 also occurred in plasma samples incubated with Ca-enriched GG-MA, as detected by Western Blot (Figure IV-6). However, beads presence did not induce C3 cleavage, as band intensity (Mw ~42) was similar to the reference control (C-2). A residual activation was observed in plasma samples incubated at 4 °C, with EDTA and Zymosan+EDTA (C-1, C-3 and C-4, respectively). As expected, plasma exposure to Zymosan caused C3 cleavage in a higher extension (C+).

IV.4.3.3 Cytokine Release Profile

Multiplex analysis of cytokine production was performed, culturing human peripheral blood mononuclear cells (hPBMCs) in contact with Ca-enriched GG-MA beads. Then, the supernatant was evaluated considering the presence of 9 different cytokines, covering both T_H1 and T_H2 responses as well as others involved in chemotaxis and inflammation [46]. The results show a mild activation of T_H1 cytokines in contrast with a higher activation of T_H2 cytokines (mainly IL-10) as well as chemokine IL-8, and the pro-inflammatory cytokines IL-1 β and TNF- α (Table IV-1). Nevertheless, no activation above the value in the positive control, was found in this study.

Table IV-1. Cytokine release after incubation of hPBMCs with Ca-enriched GG-MA beads.

Panel	Cytokine	Ca-enriched GG-MA
T _H 1 Profile	IFN γ	- - \pm
	IL-12p70	\pm - \pm
	TNF- β	- - -
T _H 2 Profile	IL-4	- \pm -
	IL-5	- \pm -
	IL-10	+ + +
Other	IL-8	+ + +
	IL-1 β	+ + +
	TNF- α	+ + +

Legend: -: cytokine concentration similar to the negative control; \pm : cytokine concentration between the negative and positive control; +: cytokine concentration between the negative and positive control, and at least ten-times higher than the detection limit of the kit; symbols show the average response obtained for each one of the three human donors.

IV.4.4 *In Vivo* Bioactivity

The bioactivity of Ca-enriched GG-MA beads was tested *in vivo*, by means of subcutaneous implantation into CD-1 mice, for 2, 4 and 8 weeks (Figure IV-7A). As showed in Figure IV-7B.2, 2 weeks post-implantation the beads were not translucent but white, possibly due to their complete mineralization, a pattern noticed throughout the whole experiment. The Alizarin Red Staining confirmed the presence of calcium depots in the retrieved beads (Figure IV-7B.2). The histological analysis also shows that calcium deposition starts form beads surface and, after 4 weeks of implantation, it is observed at the whole extent of the material. No signs of inflammation around the beads were observed either macroscopically (Figure IV-7B.2, left side) or microscopically (Figure IV-7B.2, right side).

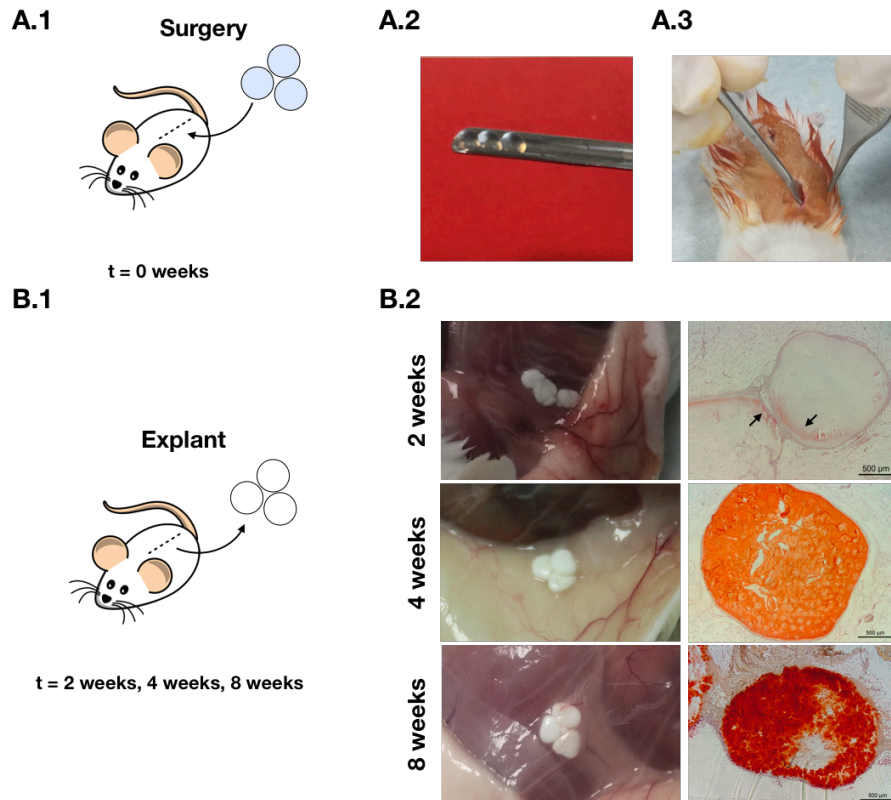


Figure IV-7. *In vivo* bioactivity of Ca-enriched GG-MA beads. A – Schematic drawing of subcutaneous implantation protocol. A.2 shows beads before implantation on the back of CD-1 mice, depicted in A.3; B – Schematic representation of explant protocol. B.2 - Macroscopic (left) and histologic (right) analysis of Ca-enriched GG-MA beads after 2, 4 and 8 weeks of subcutaneous implantation. Beads were stained with Alizarin Red for detection of calcium depots. Scale bar: 500 μm , for right side images.

IV.5 Discussion

The work herein presented aimed to study the bioactive nature of ionically crosslinked GG-MA hydrogels, and their potential to be used as drug delivery vehicles. Interestingly, the potential osteogenic properties of methacrylated gellan gum (GG-MA) hydrogels crosslinked by calcium was already reported by others [41]. However, the differentiation of hASCs towards an osteogenic phenotype was solely attributed to a mechano-transduction phenomenon, driven by different cell binding mechanisms between cells and biomaterials. On the other hand, different works already stressed the positive effect of Ca^{2+} ions and calcium phosphates on stem cells osteogenic differentiation [49, 50], through different pathways, including ATP metabolism and adenosine signaling [10]. Additionally, the self-mineralizing capacity of hydrogels containing anionic residues on their polymeric chains, due to calcium and phosphate deposition, was already reported [20, 41, 51]. As so, this work aimed to explore the potential of GG-MA hydrogels as self-mineralizing matrices, for application in bone tissue engineering. Knowing that GG-MA

as the ability to form hydrogels upon contact with CaCl_2 solutions, an anionic hydrogel network that works as calcium reservoir was engineered. That strategy aims to combine the abovementioned pro-osteogenic factors, joining in one system the possibility to deliver calcium, using an anionic environment. Such approach would promote a rapid self-mineralization of the biomaterials. Ca-enriched GG-MA hydrogels were prepared as spherical beads, envisioning a future *in vivo* application as bone gap fillers, while allowing to control deliver drugs of interest. Following this rationale, spheres are able to pack inside defects, leaving interstitial space for oxygen and nutrient diffusion as well as cell invasion, including vascularization [52].

A biomineralization study was performed by complete immersion of Ca-enriched GG-MA beads in SBF solution (Figure IV-2). This well-established *in vitro* test is often used to predict the ability to form an apatite layer on materials surface [42]. After immersion, it was possible to observe a white coating on the top of the beads (Figure IV-2B). The development of this layer in previously translucent beads may be explained by the deposition of calcium phosphates (CaP) along incubation time. Such deposition was confirmed by Scanning electron microscopy (SEM) and Microcomputed Tomography (μCT) analysis (Figure IV-2C and Figure IV-3, respectively), where a mineral layer was observed. At SEM higher magnifications, it was possible to corroborate the presence of apatite, since the typical cauliflower morphology of hydroxyapatite was observed. The thickness of the mineral shell increased with time, as plotted in Figure IV-3B, pointing out a continuous deposition of ions on the surface of Ca-enriched GG-MA. Further chemical characterization was performed using Energy Dispersive X-ray Spectrometry (EDS) and X-ray Diffraction (XRD). The acquired EDS spectra showed presence of calcium, phosphate and oxygen on the surface of the beads (Figure IV-2D). The Ca and P atomic ratio, an estimation of calcification extent, was similar to the hydroxyapatite stoichiometric theoretical value (~ 1.67). Notably, the Ca/P ratio measured, after 2 weeks of incubation, was the exact same as the theoretical value. However, that did not occur for other timepoints, possible due small ionic exchanges, between the biomaterial and the surrounding fluid. XRD diffractograms confirmed the formation of semi-crystalline hydroxyapatite on bead's surface (Figure IV-2E).

The possibility to combine the observed self-mineralization effect with *in situ* controlled drug release was also evaluated. A drug delivery study was conducted by using model drugs with different molecular weight, to emulate different drug delivery scenarios. Dex 21P, with a molecular weight of $516.40 \text{ g}\cdot\text{mol}^{-1}$, was used as small drug model, while FITC-labelled dextran with different molecular weight (4, 20 and 70 kDa) were applied as larger model molecules. Dex 21P exhibited a burst release profile, with all the cargo

being freed within the first 2 hours of assay (Figure IV-4A). A similar pattern was observed for 4 kDa dextran-FITC. However, a lower dissolution rate and delayed release was registered for larger dextran molecules than for 4 kDa. Although these molecules were also completely released to the surrounding media, a relationship between molecular weight and total release time can be noticed in the first hours of release ($p < 0.01$). Being a larger molecule, the observed delay can be explained by lower diffusivity of larger molecules within the hydrogel network [53]. Contrarily to what was observed by others with bioactive glass nanoparticles [52], the addition of calcium ions as pro-mineralization cues did not compromise the total release of the incorporated cargo. Additionally, considering the reported combined effect of dexamethasone and hydroxyapatite [54], we can postulate combined therapeutic effect of dexamethasone and the Ca-enriched GG-MA hydrogels. While dexamethasone would promote mesenchymal stem cell proliferation in a first stage [55], the Ca-enriched environment provided by the beads will endorse an osteoinductive environment. For a more sustained and/or targeted release, drugs can be conjugated with nanometric drug delivery systems, such as dendrimers [56], and then included in the hydrogel.

Biocompatibility of Ca-enriched GG-MA was also considered. For that, hASCs were supplemented with Ca-enriched GG-MA leachable, in order to quantify the effect of hydrogel by-products on cell metabolic activity. After three days of culture, no significant effect was noticed (Figure IV-5A), although the registered metabolic activity was slightly higher than the observed for control cells (TCPS leachable). However, real-time monitorization of cell proliferation, showed an increased proliferation rate for cells cultured with the Ca-enriched GG-MA leachable, mostly from day two onwards, then explaining the higher metabolic activity. Furthermore, cell proliferation was also followed in a human monocytic cell line (THP-1 cells), after its differentiation into M0 macrophages. These cells showed a small delay on cell proliferation right after leachable supplementation. Still, cells continued to proliferate, following the same trend observed for control group.

Another key point to consider when designing biomaterials for tissue engineering, is the host immune response that occurs after the implantation. Typically, this reaction starts with the activation of complement proteins, upon recognition of some foreign material [57, 58]. Therefore, the complement system activation was studied, as a way to predict a possible *in vivo* innate immune response. The results, depicted in Figure IV-6, show that no differences were observed compared to the spontaneous cleavage of C3 in the negative control (only plasma). Nevertheless, this activation was significantly inferior to the

one observed for positive control, indicating that Ca-enriched GG-MA beads do not induce complement activation by any of the three routes described.

A further insight on the potential inflammatory properties of Ca-enriched GG-MA was explored, using a multiplex analysis of cytokine production by human peripheral blood mononuclear cells (hPBMCs). Representative cytokines of Th1 and Th2 responses were quantified, covering possible in. Additionally, IL-8, IL-1 β and TNF- α were also evaluated, due to their important role on chemotaxis, inflammatory response mediation, and triggering of systemic inflammations, respectively [59, 60]. As summarized in Table IV-1, the presence of Ca-enriched GG-MA by-products triggered the release of some cytokines, but none of them at levels equal or superior to levels observed when lipopolysaccharide was used. Nonetheless, in all donors, IL-10, IL-8, IL-1 β and TNF- α concentrations ranged in between negative and positive controls. While the presence of IL-8, IL-1 β and TNF- α may point out to a pro-inflammatory state, the detection of IL-10 also suggests that a process of inflammation control may be supported [61]. Although immune system effectors are often identified as the responsible for negative host responses, they can be also beneficial for tissue regeneration [57]. As example, there is still no consensus regarding the best immunological environment needed for osteogenesis [62]. Indeed, some studies pointed out the beneficial effect of pro-inflammatory cytokines, secreted by M1 macrophages, on osteogenesis development [63]. The key-point, then, would be the right temporal succession of the different interactions that occur between the different elements of the immune system.

At last, *in vivo* biomineralization was evaluated using a subcutaneous implantation model. Ca-enriched GG-MA beads were placed in subcutaneous pockets, opened on the back of CD-1 mice. As observed in Figure IV-7, after 2 weeks of implantation the translucent beads acquired a white opaque colour, indicating that calcification of the hydrogel has occurred. Histologic analysis, by means of Alizarin Red staining (AzR), showed that calcium depots were present on the surface of the hydrogels. A calcified morphology was noticed in further timepoints, *i.e.* at 4 and 8 weeks of implantation, both at macroscopic level as well as after AzR staining. Noteworthy, contrary to what was observed in biomineralization studies using SBF, mineralization was spread all over the material from 4 weeks afterwards.

Previous reports on GG-based hydrogels for bone tissue engineering, showed that these hydrogels do not elicit a mineralization process *per se* [64]. Indeed, numerous reports showed that GG-based hydrogels are good candidates for cartilage tissue engineering, where mineralization is unwanted [65, 66]. As example, GG-based hydrogels, used to mimic the cartilaginous portion in a bilayered hydrogel for

osteocondral regeneration, did not mineralized once immersed in SBF or implanted in mice dorsum. However, mineralization did occur on the bone-like section of the hydrogels, where GG was previously mixed with hydroxyapatite [67]. It is important to stress that the difference between the aforesaid strategies and the one presented in this work relies on the crosslinking method. As so, we can hypothesize that GG anionic charge is not sufficient to control a mineralization process, as reported for chondroitin sulfate [68] or gelatin methacrylate [20]. However, it might be dependent on the presence of Ca^{2+} ions. The presence of these ions will contribute for the accumulation of phosphate ions, leading to formation and deposition of CaP. Therefore, it is also important to highlight the contribution of these results on the development of future gellan gum, and particularly, methacrylated gellan gum-based hydrogels. By simply changing the preparation method, from thermal gelation to ionic crosslinking using CaCl_2 , it is possible to drastically influence the final biological performance of the material.

Overall, these results head to future synergistic systems, that can combine an efficient and local release of therapeutic molecules with the reported self-mineralization capacity of the beads. This combined effect may potentiate the final therapeutic result of both drugs and biomaterials, while reducing drug resistance and side effects [54].

IV.6 Conclusion

The results presented in this work clearly show the dual mineralizing and drug delivery potential of Ca-enriched GG-MA hydrogel beads. Using a simple fabrication method that takes advantage of the intrinsic properties of the material, GG-MA hydrogels were enriched with Ca^{2+} ions, resulting in a functional bone bioactive material. This Ca-enriched GG-MA hydrogel is able to mineralize, as confirmed by *in vitro* apatite deposition and *in vivo* mineralization. Additionally, this system is compatible with efficient drug delivery applications, in a wide range of molecular weights. Emulation of a possible immune response showed that these hydrogels would trigger some pro-inflammatory cytokines, but also IL-10, which could control the immune response. Moreover, no complement activation was observed. From the obtained *in vivo* results, it is expected a mild controlled reaction, that would be able to further promote osteogenesis. Altogether, this work paves the way for synergistic strategies that can combine a fast drug release with pro-osteogenic signalling, as mineral matrix deposition, in a rapid and low-cost fashion.

IV.7 Acknowledgments

Sílvia Vieira was awarded an FCT PhD scholarship (SFRH/BD/102710/2014). The FCT distinction attributed to J. Miguel Oliveira under the Investigator FCT program (IF/01285/2015) and J. Silva Correia (IF/00115/2015) are also greatly acknowledged. Alain da Silva Morais acknowledges ERC-2012-ADG 20120216–321266 (ComplexiTE) for his Postdoc fellowship. África González Fernández acknowledges funding by Grupo de referencia competitiva IN1 (ED431C 2016041, Xunta de Galicia).

The authors would like to also acknowledge the contribution of Luísa Rodrigues regarding the XPS analysis performed for this work; Elsa Ribeiro that performed the SEM acquisition; Sandra Pina for the acquisition of XRD diffractograms; and Teresa Oliveira for histology samples processing.

IV.8 References

1. Wang, W. and K.W.K. Yeung, *Bone grafts and biomaterials substitutes for bone defect repair: A review*. Bioactive Materials, 2017. **2**(4): p. 224-247.
2. Yang, X., et al., *Hydroxyapatite/collagen coating on PLGA electrospun fibers for osteogenic differentiation of bone marrow mesenchymal stem cells*. Journal of Biomedical Materials Research Part A, 2018.
3. Ye, P., et al., *Application of silk fibroin/chitosan/nano-hydroxyapatite composite scaffold in the repair of rabbit radial bone defect*. Experimental and Therapeutic Medicine, 2017. **14**(6): p. 5547-5553.
4. Maji, K., et al., *Preparation and characterization of gelatin-chitosan-nanobeta-TCP based scaffold for orthopaedic application*. Materials Science & Engineering. C: Materials for Biological Applications, 2018. **86**: p. 83-94.
5. Bergemann, C., et al., *Continuous cellularization of calcium phosphate hybrid scaffolds induced by plasma polymer activation*. Materials Science & Engineering. C: Materials for Biological Applications, 2016. **59**: p. 514-523.
6. Pina, S., J.M. Oliveira, and R.L. Reis, *Natural-Based Nanocomposites for Bone Tissue Engineering and Regenerative Medicine: A Review*. Advanced Materials, 2015. **27**(7): p. 1143-1169.
7. Leite, Á.J., et al., *Screening of Nanocomposite Scaffolds Arrays Using Superhydrophobic-Wettable Micropatterns*. Advanced Functional Materials, 2017. **27**(28): p. 1701219.
8. Barradas, A.M., et al., *A calcium-induced signaling cascade leading to osteogenic differentiation of human bone marrow-derived mesenchymal stromal cells*. Biomaterials, 2012. **33**(11): p. 3205-15.

9. Viti, F., et al., *Osteogenic Differentiation of MSC through Calcium Signaling Activation: Transcriptomics and Functional Analysis*. PLoS ONE, 2016. **11**(2): p. e0148173.
10. Shih, Y.R., et al., *Calcium phosphate-bearing matrices induce osteogenic differentiation of stem cells through adenosine signaling*. Proceedings of the National Academy of Sciences of the United States of America, 2014. **111**(3): p. 990-5.
11. Kepa, K., R. Coleman, and L. Grøndahl, *In vitro mineralization of functional polymers*. Biosurface and Biotribology, 2015. **1**(3): p. 214-227.
12. Costa, P.F., *Bone Tissue Engineering Drug Delivery*. Current Molecular Biology Reports, 2015. **1**(2): p. 87-93.
13. Li, L., et al., *Controlled dual delivery of BMP-2 and dexamethasone by nanoparticle-embedded electrospun nanofibers for the efficient repair of critical-sized rat calvarial defect*. Biomaterials, 2014. **37C**: p. 218-229.
14. Dang, M., et al., *Biomimetic delivery of signals for bone tissue engineering*. Bone Research, 2018. **6**(1): p. 25.
15. Raina, D.B., et al., *Guided tissue engineering for healing of cancellous and cortical bone using a combination of biomaterial based scaffolding and local bone active molecule delivery*. Biomaterials, 2019. **188**: p. 38-49.
16. Chen, Y., N. Kawazoe, and G. Chen, *Preparation of dexamethasone-loaded biphasic calcium phosphate nanoparticles/collagen porous composite scaffolds for bone tissue engineering*. Acta Biomaterialia, 2018. **67**: p. 341-353.
17. den Uyl, D., I.E.M. Bultink, and W.F. Lems, *Glucocorticoid-induced osteoporosis*. Clinical and Experimental Rheumatology, 2011. **29**: p. S93-8.
18. Wong, D.A., et al., *Neurologic impairment from ectopic bone in the lumbar canal: a potential complication of off-label PLIF/TLIF use of bone morphogenetic protein-2 (BMP-2)*. The Spine Journal, 2008. **8**(6): p. 1011-1018.
19. Gantar, A., et al., *Nanoparticulate bioactive-glass-reinforced gellan-gum hydrogels for bone-tissue engineering*. Materials Science & Engineering. C: Materials for Biological Applications, 2014. **43**: p. 27-36.
20. Zhou, L., et al., *Biomimetic mineralization of anionic gelatin hydrogels: effect of degree of methacrylation*. RSC Advances, 2014. **4**(42): p. 21997-22008.
21. Saravanan, S., et al., *A review on injectable chitosan/beta glycerophosphate hydrogels for bone tissue regeneration*. International Journal of Biological Macromolecules, 2018. **121**: p. 38-54.
22. Bai, X., et al., *Bioactive hydrogels for bone regeneration*. Bioactive Materials, 2018. **3**(4): p. 401-417.

23. Milas, M., X. Shi, and M. Rinaudo, *On the physicochemical properties of gellan gum*. Biopolymers, 1990. **30**: p. 451-464.
24. Chandrasekaran, R., A. Radha, and V.G. Thailambal, *Roles of potassium ions, acetyl and L-glyceryl groups in native gellan double helix: An X-ray study*. Carbohydrate Research, 1992. **224**: p. 1-17.
25. Kuo, M.-S., A.J. Mort, and A. Dell, *Identification and location of l-glycerate, an unusual acyl substituent in gellan gum*. Carbohydrate Research, 1986. **156**(0): p. 173-187.
26. Kang, K.S., et al., *Agar-like polysaccharide produced by a pseudomonas species: production and basic properties*. Applied and Environmental Microbiology, 1982. **43**(5): p. 1086-91.
27. Chandrasekaran, R., et al., *The crystal structure of gellan*. Carbohydrate Research, 1988. **175**: p. 1-15.
28. Shimazaki, T., et al., *Influence of Ca²⁺-ion upon viscoelastic properties of gellan gum aqueous solutions*. Polymer Gels and Networks, 1995. **3**(3): p. 295-309.
29. Tang, J., M.A. Tung, and Y. Zeng, *Gelling properties of gellan solutions containing monovalent and divalent cations*. Journal of Food Science, 1997. **62**: p. 688-&.
30. Morris, E.R., K. Nishinari, and M. Rinaudo, *Gelation of gellan – A review*. Food Hydrocolloids, 2012. **28**: p. 373-411.
31. Lozano, R., et al., *3D printing of layered brain-like structures using peptide modified gellan gum substrates*. Biomaterials, 2015. **67**: p. 264-273.
32. Chang, S.J., et al., *In vitro properties of gellan gum sponge as the dental filling to maintain alveolar space*. Carbohydrate Polymers, 2012. **88**(2): p. 684-689.
33. Oliveira, J.T., et al., *Performance of new gellan gum hydrogels combined with human articular chondrocytes for cartilage regeneration when subcutaneously implanted in nude mice*. Journal of Tissue Engineering and Regenerative Medicine, 2009. **3**(7): p. 493-500.
34. Oliveira, J.T., et al., *Gellan gum: a new biomaterial for cartilage tissue engineering applications*. Journal of Biomedical Materials Research Part A. **93**(3): p. 852-63.
35. Oliveira, J.T., et al., *Gellan gum injectable hydrogels for cartilage tissue engineering applications: in vitro studies and preliminary in vivo evaluation*. Tissue Engineering Part A, 2010. **16**(1): p. 343-53.
36. Pereira, D.R., et al., *Development of gellan gum-based microparticles/hydrogel matrices for application in the intervertebral disc regeneration*. Tissue Engineering Part C, 2011. **17**(10): p. 961-72.
37. Silva-Correia, J., et al., *Gellan gum-based hydrogels for intervertebral disc tissue-engineering applications*. Journal of Tissue Engineering and Regenerative Medicine, 2011. **5**: p. e97-107.

38. Silva-Correia, J., et al., *Angiogenic potential of gellan-gum-based hydrogels for application in nucleus pulposus regeneration: in vivo study*. Tissue Engineering. Part A, 2012. **18**(11-12): p. 1203-12.
39. Silva-Correia, J., et al., *Rheological and mechanical properties of acellular and cell-laden methacrylated gellan gum hydrogels*. Journal of Biomedical Materials Research Part A, 2013. **101**(12): p. 3438-3446.
40. Soto, A.M., et al., *Optical Projection Tomography Technique for Image Texture and Mass Transport Studies in Hydrogels Based on Gellan Gum*. Langmuir, 2016. **32**(20): p. 5173-82.
41. Oliveira, M.B., et al., *Autonomous osteogenic differentiation of hASCs encapsulated in methacrylated gellan-gum hydrogels*. Acta Biomaterialia, 2016. **41**: p. 119-32.
42. Kokubo, T. and H. Takadama, *How useful is SBF in predicting in vivo bone bioactivity?* Biomaterials, 2006. **27**(15): p. 2907-2915.
43. Cerqueira, M.T., et al., *Human adipose stem cells cell sheet constructs impact epidermal morphogenesis in full-thickness excisional wounds*. Biomacromolecules, 2013. **14**(11): p. 3997-4008.
44. Standardization, I.O.f., *ISO 10993-5:2009 - Biological evaluation of medical devices – Part 5: Tests for in vitro cytotoxicity*. 2009.
45. Pereira, P., et al., *Biocompatibility of a self-assembled glycol chitosan nanogel*. Toxicology In Vitro, 2015. **29**(3): p. 638-646.
46. Simón-Vázquez, R., et al., *Analysis of the activation routes induced by different metal oxide nanoparticles on human lung epithelial cells*. Future Science OA, 2016. **2**(2): p. FSO118.
47. Hench, L. and S.M. Best, *Ceramics, Glasses, and Glass-Ceramics: Basic Principles*, in *Biomaterials Science (Third Edition)*, B.D. Ratner, et al., Editors. 2013, Academic Press. p. 128-151.
48. Janeway, C., *Immunobiology Five*. 2001: Garland Pub.
49. Jung, G.Y., Y.J. Park, and J.S. Han, *Effects of HA released calcium ion on osteoblast differentiation*. Journal of Materials Science Materials in Medicine, 2010. **21**(5): p. 1649-54.
50. Nakamura, S., et al., *Effect of calcium ion concentrations on osteogenic differentiation and hematopoietic stem cell niche-related protein expression in osteoblasts*. Tissue Engineering Part A, 2010. **16**(8): p. 2467-73.
51. Cha, C., et al., *Integrative design of a poly(ethylene glycol)-poly(propylene glycol)-alginate hydrogel to control three dimensional biomineralization*. Biomaterials, 2011. **32**(11): p. 2695-703.
52. Leite, A.J., et al., *Bioactive Hydrogel Marbles*. Scientific Reports, 2018. **8**(1): p. 15215.

53. Zustiak, S.P., H. Boukari, and J.B. Leach, *Solute diffusion and interactions in cross-linked poly(ethylene glycol) hydrogels studied by Fluorescence Correlation Spectroscopy*. *Soft Matter*, 2010. **6**(15).
54. Oliveira, J.M., et al., *The osteogenic differentiation of rat bone marrow stromal cells cultured with dexamethasone-loaded carboxymethylchitosan/poly(amidoamine) dendrimer nanoparticles*. *Biomaterials*, 2009. **30**(5): p. 804-13.
55. Langenbach, F. and J. Handschel, *Effects of dexamethasone, ascorbic acid and beta-glycerophosphate on the osteogenic differentiation of stem cells in vitro*. *Stem Cell Research & Therapy*, 2013. **4**(5): p. 117.
56. Oliveira, J.M., et al., *Surface Engineered Carboxymethylchitosan/Poly(amidoamine) Dendrimer Nanoparticles for Intracellular Targeting*. *Advanced Functional Materials*, 2008. **18**(12): p. 1840-1853.
57. Crupi, A., et al., *Inflammation in tissue engineering: The Janus between engraftment and rejection*. *European Journal of Immunology*, 2015. **45**(12): p. 3222-3236.
58. Vasconcelos, D.P., et al., *The inflammasome in host response to biomaterials: Bridging inflammation and tissue regeneration*. *Acta Biomaterialia*, 2018.
59. Andorko, J.I. and C.M. Jewell, *Designing biomaterials with immunomodulatory properties for tissue engineering and regenerative medicine*. *Bioengineering & Translational Medicine*, 2017. **2**(2): p. 139-155.
60. Vishwakarma, A., et al., *Engineering Immunomodulatory Biomaterials To Tune the Inflammatory Response*. *Trends in Biotechnology*, 2016. **34**(6): p. 470-482.
61. Ortega-Gomez, A., M. Perretti, and O. Soehnlein, *Resolution of inflammation: an integrated view*. *EMBO Molecular Medicine*, 2013. **5**(5): p. 661-74.
62. Chen, Z., et al., *Osteoimmunomodulation for the development of advanced bone biomaterials*. *Materials Today*, 2016. **19**(6): p. 304-321.
63. Rifas, L., *T-cell cytokine induction of BMP-2 regulates human mesenchymal stromal cell differentiation and mineralization*. *Journal of Cellular Biochemistry*, 2006. **98**(4): p. 706-14.
64. Silva-Correia, J., et al., *Biocompatibility evaluation of ionic- and photo-crosslinked methacrylated gellan gum hydrogels: in vitro and in vivo study*. *Advanced Healthcare Materials*, 2013. **2**(4): p. 568-75.
65. Douglas, T.E.L., et al., *Novel injectable gellan gum hydrogel composites incorporating Zn- and Sr-enriched bioactive glass microparticles: High-resolution X-ray microcomputed tomography, antibacterial and in vitro testing*. *Journal of Tissue Engineering and Regenerative Medicine*, 2018. **12**(6): p. 1313-1326.

66. Vilela, C.A., et al., *In vitro and in vivo performance of methacrylated gellan gum hydrogel formulations for cartilage repair*. Journal of Biomedical Materials Research Part A, 2018. **106**(7): p. 1987-1996.
67. Pereira, D.R., et al., *Injectable gellan-gum/hydroxyapatite-based bilayered hydrogel composites for osteochondral tissue regeneration*. Applied Materials Today, 2018. **12**: p. 309-321.
68. Kim, H.D., et al., *Chondroitin Sulfate-Based Biomineralizing Surface Hydrogels for Bone Tissue Engineering*. ACS Applied Materials and Interfaces, 2017. **9**(26): p. 21639-21650.

Chapter V: Mn-Based Methacrylated Gellan Gum Hydrogels for MRI-Guided Cell Delivery and Imaging*

ABSTRACT

Cell-based therapies are a promising approach for the treatment of several diseases, including multifocal diseases of the central nervous system (CNS). As a consequence, the field of image-guided neural interventions has been growing considerably, as it can allow envisioning a precise control on cell delivery and investigate their fate and therapeutics effects. This work aims to engineer a new injectable Mn-based methacrylated gellan gum (Mn/GG-MA) hydrogel for real-time monitored cell delivery into the CNS. To enable the Mn/GG-MA hydrogel visualization under Magnetic Resonance Imaging (MRI), 0.75% (w/v) GG-MA solutions were supplemented with 0.1 and 1 mM of MnCl_2 . All prepared Mn/GG-MA hydrogel formulations are injectable, with force needed to inject the gel solution being similar to the force needed to inject aCSF. T1-weighted MRI scans of phantom preparations showed that formulations with 0.1 mM MnCl_2 exhibited the best MRI signal. This condition was further used to prepare cell-laden hydrogels, by extrusion of Mn/GG-MA into aCSF. Encapsulated human adipose-derived stem cells remained viable after 7 days of cell culture, as assessed by Live/Dead assay. After transplantation of Mn/GG-MA hydrogels in double mutant $\text{MBP}^{\text{shi/shi}}/\text{rag2}$ immunocompromised mice, the hydrogel was visible on T1-weighted MRI scans. Summing up, the developed Mn/GG-MA hydrogels hold great potential for MRI-guided cell delivery and imaging approaches, when minimally invasive procedures are envisaged.

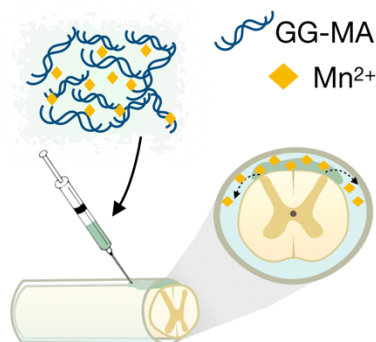
Keywords: Gellan gum; cell delivery; manganese; magnetic resonance imaging; injectable hydrogels.

* This chapter is based on the following publications:

"Hydrogel Comprising Manganese, Methods and Uses Thereof". Oliveira J. M., Vieira S., Oliveira E., Silva-Correia J., Reis R. L., Walczak P., Malysz-Cymborska I., Golubczyk D., Kalkowski L., Majchrzak M., Janowski M., Strymecka P., Stanaszek L., Lukomska B., Svendsen T., Asdahl L. C., and Sætrang H. E. M.. Published as WO/2019/123423 and EP3501553 (A1).

"Mn-Based Methacrylated Gellan Gum Hydrogels for MRI-Guided Cell Delivery and Imaging", S. Vieira, P. Strymecka, L. Stanaszek, J. Silva-Correia, K. Dreha, M. Fiedorowicz, I. Malysz-Cymborska, M. Janowski, R. L. Reis, B. Lukomska, P. Walczak, J. M. Oliveira. (*submitted*)

V.1 Graphical Abstract



V.2 Introduction

Cell-based therapies hold great potential to tackle the central nervous system (CNS) diseases. Indeed, the rationale for transplanting stem cells has been already established in small [1] and large [2] animal models.

On this scope, the CNS can be accessed using different approaches, resulting in cell deposition in different areas. Intraparenchymal cell delivery is performed via direct needle injections into the parenchyma, resulting in a spatially precise cell deposition. This route is currently considered the method of choice for a large number of studies aiming for direct cell delivery into the CNS. In this regard, the safety of intraparenchymal cell injection was already confirmed in studies using large animals [3] as well as in phase I/II clinical trials [4], for direct cell transplantation into the spinal cord and brain. Delivery of therapeutic agents directly near the vicinities of a stroke poses a great advantage of intraparenchymal cell transplantation [5, 6]. However, the hostile environment near the stroke region hampers successful cell transplantation with effective therapeutic effect [7]. To overcome such limitation, cell-laden hydrogels capable of being injected directly into the CNS have been successfully used, showing their potential to promote a pro-survival environment, even near the stroke region [8].

And while significant progress has been made in the CNS field, disseminated or multifocal diseases, where a broad cell distribution is required, pose a particular challenge for cell delivery [9]. Examples of such multifocal disorders include multiple sclerosis or amyotrophic lateral sclerosis (ALS). For the therapy to be effective, cell delivery must be carried to extensive areas of the CNS. Although promising, intraparenchymal delivery is linked with a higher risk when multifocal cell depositions are needed, making room for new, less invasive gateways to the spinal cord [10]. Intrathecal injection is an alternative route

that allows a more widespread delivery of cells in the CNS, and it is therefore considered as an attractive access for spinal cord targeting [11]. With this minimally invasive method, it is possible to dispense cell suspensions, or drugs, directly into the cerebrospinal fluid (CSF), leading to a wide distribution within the CNS. Although intrathecal injection is a routine clinical procedure with a low rate of complications, and numerous stem cell delivery studies (both pre-clinical and clinical) strengthened the feasibility of this route [12-14], there are still some bottlenecks that hamper the development of this technique. The cells injected into the CSF as a suspension in a buffer are subject to gravitational sedimentation, with their accumulation in cauda equina or removal within circulating CSF [11, 15]. One way to avoid these undesirable effects is to embed the transplanted cells within a biomaterial matrix.

In this regard, injectable hydrogel formulations are particularly promising, mainly due to their: (i) soft and pliable nature; (ii) easy transport of nutrients and metabolites; (iii) tissue-like fluidity; (iv) ease of fabrication; and (v) appropriate bio adhesiveness and integration with biological interfaces [16]. After being injected into the CNS, the hydrogel physically supports the encapsulated cells, protects the biological material from an hostile environment, and it can also assure a widespread distribution along the spinal cord when injected in the intrathecal space [17].

Another challenge of CNS direct cell delivery is the correct hydrogel placement and allocation. Particularly, for intraparenchymal injections it is hard to predict the hydrogel placement, as well as possible dilution in the CSF, because the injection is performed into a fluid compartment. Therefore, the possibility to image and monitor the injection procedure in real-time and non-invasive way adds significant value to the whole therapeutic approach. Such control can allow the establishment of new procedures that avoid excessive injection, or biomaterial misplacement, assuring its correct positioning. Tomographic techniques, and particularly Magnetic Resonance Imaging (MRI), are the most appropriate to image deep structures, like the intrathecal space or the parenchyma [18]. Using MRI, it is possible to obtain information about the biomaterial/tissue interface as well as biomaterial placement and biodistribution in both pre-clinical and clinical studies. Another advantage is the non-invasive and radiation-free imaging, thus making MRI one of the most desirable imaging modalities [19].

Visualization of the hydrogel using MRI typically requires hydrogel labeling with a contrast agent. Most frequently used contrasts include iron oxide, gadolinium (Gd), or fluorine in a nanoparticulate form. Although not so popular as other contrast agents, Mn^{2+} ions are increasingly studied and used as a positive contrast [20]. The MRI signal is obtained due to the paramagnetic nature of Mn^{2+} , yielding a high contrast

on T1-weighted MRI images [21, 22]. Manganese presents similar contrast properties as the most commonly used Gd. However, its undeniable advantage relies on the fact that it does not accumulate for long term period and might be incorporated into the organism or expelled, as it represents one of the necessary microelements [23]. Manganese based contrasts can not only be used for anatomy analysis but also for functional studies. Moreover, manganese can be delivered both by systemic and localized routes of delivery [24]. Nevertheless, the concentration of Mn^{2+} must be carefully optimized due to the possible Mn-induced toxicity that might occur when high or repetitive doses of Mn^{2+} are delivered [25, 26].

Regardless the method used to reach the CNS, intraparenchymal or intrathecal, several conditions need to be met to successfully use these methods for delivery of hydrogel-embedded stem cells. The hydrogel needs to withstand the shear forces caused by injection, but also rapidly crosslink upon reaching the CNS to avoid cell and biomaterial escape to unwanted regions. In this regard, gellan gum (GG) presents great potential as injectable material [27]. Indeed, this natural polymer has been successfully used for several tissue engineering applications, including intervertebral disc regeneration [28], nanoparticles coating [29], bioprinting of brain-like tissues [30], among others [31]. In its native form, GG is thermo- and ionic-responsive, and therefore fast gelation can occur *in situ* due to body temperature or presence of metallic ions in body fluids. Nevertheless, GG needs to be heated up to approximately 50 °C to be water-soluble, making cell encapsulation, and delivery a challenging process. Although cells could be mixed with GG near physiological temperatures, the time required for injection could lead to a decrease in temperature and consequent needle clot, as a result of hydrogel crosslink before injection.

On the other hand, the methacrylated GG (GG-MA), obtained through chemical modification of the native low acyl GG, is water-soluble at room temperature. Thus, GG-MA can be easily used for cell encapsulation procedures. Also, GG-MA remains responsive to ionic strength, and rapidly crosslinks in the presence of metallic ions. Bearing in mind that the CSF is rich in Na^+ , Cl^- , HCO_3^- , K^+ , Mg^{2+} , and Ca^{2+} [32], it is highly expected that *in situ* ionic crosslink occurs upon GG-MA injection. More than triggering the desired *in situ* crosslinking of the hydrogel, the ionic interaction between GG and metallic ions can be used to incorporate Mn^{2+} within the hydrogel matrix for further MRI tracking. Indeed, it has been shown that Mn^{2+} strongly interacts with GG, specifically at the carboxyl group of the D-glucuronate unit [33, 34].

In this work, we aim to develop a new injectable Mn-based methacrylated gellan gum (Mn/GG-MA) hydrogel for intrathecal cell delivery that can also be traceable by Mn-enhanced MRI. It is hypothesized

that the Mn/GG-MA hydrogels can be used to support intrathecal cell delivery, but also as reservoirs for Mn²⁺, allowing visualization of hydrogel placement in real-time. To that end, Mn²⁺ concentration was optimized considering the T1-weighted MRI signal but also the final hydrogel stability, rheological properties, injection ability and cytocompatibility.

V.3 Materials and Methods

V.3.1 Preparation of Methacrylated Gellan Gum (GG-MA), MnCl₂ and aCSF Solutions

Preparation of methacrylated gellan gum (GG-MA) was performed following the protocol of Silva-Correia *et al.* [28]. Glycidyl methacrylate (GMA, 97%, Sigma-Aldrich) was added to a low-acyl gellan gum solution (Gelzan™ CM Gelrite®, Sigma-Aldrich), and this mixture was vigorously stirred overnight at room temperature, with constant control of pH at 8.5. Reaction products were precipitated by the addition of cold acetone and further purified by dialysis (cellulose membrane, molecular weight cut-off 12 kDa, Sigma-Aldrich) against distilled water. After one week, the obtained GG-MA was frozen at -80 °C and freeze-dried. The final dry material was stored protected from light, and in a dry place until further use. GG-MA solutions of desired concentrations were prepared by dissolving the dry material in Milli-Q water, using gentle agitation. Manganese (II) chloride powder (MnCl₂ powder, Sigma-Aldrich) was used to prepare MnCl₂ aqueous solutions, that were further used as a supplement for GG-MA hydrogels. Artificial cerebrospinal fluid (aCSF) was prepared following the composition listed in Table V-1, with the final pH adjusted to 7.3 by dropwise addition of NaOH.

All the materials and solutions were sterilized by filtration (0.22 µm filter) before cell *in vitro* and *in vivo* assays, excluding dry GG-MA that was sterilized by UV light for 30 minutes in a laminar flow hood.

Table V-1. Composition of aCSF solution.

	Concentration (mM)
NaCl	125
KCl	2.5
MgCl₂·6H₂O	1
NaH₂PO₄	1.25
CaCl₂·2H₂O	2
NaHCO₃	25
Glucose	25

V.3.2 Preparation of Mn-based GG-MA Hydrogels

Hydrogel solutions were prepared by mixing 1% (w/v) GG-MA with MnCl₂ solutions to obtain hydrogels with different concentrations of Mn²⁺ (0.1 and 1 mM MnCl₂). The final hydrogels were then based on 0.75% (w/v) GG-MA with defined MnCl₂ concentrations. A solution of 0.75% (w/v) of GG-MA was used as

control. To better mimic *in vivo* conditions, further crosslink was obtained by hydrogel interaction with aCSF. For that, Mn-based GG-MA (Mn/GG-MA) hydrogels were poured into cylindrical silicon molds, and excess of aCSF was added dropwise. After 5 minutes of incubation, hydrogels were ready to be analyzed.

V.3.3 Rheological Studies

Rheological analyses were performed using a Kinexus Pro+ rheometer (Malvern Instruments, UK), using the acquisition software rSpace. The measuring system was equipped with stainless steel (316 grade) parallel plates: the upper measurement geometry plate, with 8 mm of diameter, and the 20 mm lower pedestal with roughened finish (to prevent sample slippage and resulting errors on the experiments). First, the Linear Viscoelastic Region was determined, and then single-frequency oscillation experiments were performed at 0.1 Hz for 30 minutes. Pre-gel solutions of 0.75% (w/v) GG-MA, and 0.75% (w/v) GG-MA supplemented with 0.1 mM or 1 mM MnCl₂ were poured in the lower pedestal, while aCSF crosslinked hydrogels (8 mm diameter and 2 mm height) were prepared beforehand, as abovementioned. Shear viscosity and shear stress were determined by rotational experiments, using an upper measurement geometry cone (40 mm diameter and 4° angle). All experiments were performed at 37 °C, and plots are the average of at least 3 experiments.

V.3.4 Injection Ability Test

The possibility to extrude the Mn/GG-MA pre-gel solutions from a 31 G needle was investigated using an injection equipment (Paralab). The measurements were performed using a 10 µL Hamilton syringe coupled with a 31 G needle. The syringe was filled with the Mn/GG-MA solutions, as well as aCSF (control). The material was extruded by applying a force on the syringe piston, using a constant extrusion rate. The load needed to extrude the material through the 31 G needle was measured and recorded using appropriate software.

V.3.5 Permeability Studies

Permeability studies were performed using 70 kDa fluorescein isothiocyanate–dextran molecules (dextran-FITC, Sigma-Aldrich). Dextran-FITC was dissolved in Milli-Q water and added to the GG-MA hydrogel solutions at a final concentration of 125 µg.mL⁻¹. As before, hydrogels were placed inside 8 mm discs, and further crosslinked with aCSF to mimic the delivery of the hydrogels into the intrathecal space. The resulting gels were immersed in aCSF and incubated at 37 °C with mechanical shaking. At different timepoints, 350 µL of supernatant were retrieved and replaced by the same amount of fresh aCSF. At the last timepoint, hydrogels were mechanically destroyed, centrifuged, and the resulting supernatant

was used to calculate the final concentration of FITC-labelled molecules, that could be retained inside the hydrogels. The fluorescence emission of FITC-labelled dextran was measured at an excitation wavelength of 485/20 nm and an emission wavelength of 528/20 nm, in a microplate reader (Gen 5 2.01, Synergy HT, BioTek). The concentration of dextran-FITC in the supernatant was finally calculated using a calibration curve, obtained by the measurement of the fluorescence emission of dextran-FITC solutions of known concentrations.

V.3.6 Degradation Profile

The degradation of Mn-based GG-MA hydrogels upon incubation in aCSF was evaluated by studying its weight loss profile. For this, the different hydrogel formulations, previously crosslinked with aCSF, were weighed (initial weight, m) and incubated in aCSF at 37 °C. All solutions were supplemented with 0.2% (w/v) sodium azide (Sigma-Aldrich) to avoid bacterial contamination. After 1, 3, 24, 72, and 168 hours, the hydrogels were retrieved, the liquid excess was gently removed, and the final mass of samples was determined (m). Equation III-2 (Chapter III, page 97) was applied to calculate the weight loss ratio at each time point.

V.3.7 Manganese Release Profile – Inductively Coupled Plasma-Optical Emission Spectroscopy

The Mn²⁺ release profile from the Mn-based GG-MA hydrogels to the surrounding media was quantified using inductively coupled plasma-optical emission spectroscopy (ICP; JY2000 2, Jobin Yvon, Horiba). Hydrogels were crosslinked with aCSF into 8 mm template discs and then incubated in aCSF, at 37 °C with mechanical shaking. At defined timepoints (0.5, 1, 5, 24, and 48 hours), aCSF was collected and analyzed. Samples were dissolved in nitric acid and injected into the instrument. Manganese ($\lambda_{em}=259.37$ nm) concentrations in the aCSF solutions were obtained by comparison with standard solutions, with a detection limit of 5 ppb.

V.3.8 Human-derived Adipose Stem Cells (hASCs) Isolation and Culture

Lipoaspirate samples were collected from abdominal regions of healthy human male and female donors with ages between 18 and 57 years, after informed consent, under established cooperative agreements between the Hospital da Senhora da Oliveira (Guimarães, Portugal) and the 3B's Research Group – University of Minho. Samples were digested with collagenase NB 6 GMP (good manufacturing practice) Grade (Serva), and 100 mL of fat tissue underwent a first centrifugation to remove all liquids (50 g, 5 minutes). Then, about 50 mL of high quality concentrated adipose tissue, was mixed with the same

volume of collagenase solution, previously diluted with PBS at a final concentration of 0.2 U.mL⁻¹. The tissue in the collagenase solution was incubated for 1 hour and shaken on an orbital shaker at constant low speed of 65 rpm, at 37 °C. Then, the tissue was washed twice with PBS and centrifuged for 10 minutes at 250 *g*. Samples were rewashed with PBS, and the cellular pellet was then ready for use and transferred into the culture dishes in the completed MSC growth medium (MSCGM BulletKit, Lonza). After 48 hours, the fibroblast-like cells were separated from the rest of floating debris, rinsed with PBS, and cultured for the next 7 days or until near confluence.

V.3.9 Cell Encapsulation

Human-derived adipose stem cells (hASCs) were grown as monolayers as described above. At passage 3-4, confluent cells were detached from tissue culture flasks using Trypsin (Gibco®, Life Technologies), and a diluted suspension was centrifuged at 1200 rpm for 5 minutes, forming a cell pellet. Mn-based GG-MA hydrogels with 0.75% (w/v) GG-MA and 0.1 M MnCl₂ were mixed with the hASCs pellet to a final cellular density of 1 x 10⁶ cells.mL⁻¹. Also, 0.75% (w/v) GG-MA hydrogels without MnCl₂ were prepared (controls). Cells were gently resuspended in the biomaterial suspension to obtain a homogeneous cell distribution. Then, 10 µL Hamilton syringe coupled with a 31 G needle was filled with the solution and placed on a stereotaxic syringe pump. The pre-gel solutions were injected into aCSF, using a 10 µL.min⁻¹ extrusion rate, forming Mn/GG-MA fibers. After 5 minutes, aCSF was replaced by 500 µL of cell culture media. Thence, 24-well plates, with 10 µL of gel per well, were incubated for 1, and 7 days at 37 °C, in a humidified air atmosphere of 5% CO₂.

V.3.10 Live/Dead Staining

Live/dead fluorescence assays were performed at each time culture period. LIVE/DEAD Viability/Cytotoxicity Kit for mammalian cells (ThermoFisher Scientific) was used to perform a Live/Dead assay, where Calcein-AM stained live cells and ethidium homodimer-1 (EthD-1) stain dead cells. At each timepoint, the culture medium was removed, and 150 µL of Calcein and EthD-1 diluted in PBS (0.5 µL of Calcein-AM and 2 µL of EthD-1 per 1 mL PBS) was added to each well. Samples were then incubated 20 minutes at room temperature (RT), protected from light and visualized in the dark using a fluorescence microscope Cell Observer SD (Carl Zeiss, Germany) in Z-stack mode. Image acquisition was performed at the Laboratory of Advanced Microscopy Techniques, Mossakowski Medical Research Centre, Polish Academy of Sciences. The percentage of live cells in each fiber was then calculated using ImageJ software (version 2.0.0-rc-69/1.52p).

V.3.11 Animal Surgeries

All the procedures were performed with the approval of the Ethical Committee (IV Local Committee in Warsaw, 117/2015). Double mutant MBP^{shiv/shiv}/rag2 immunocompromised mice (a model of demyelination) were anesthetized with 1.5-2% isoflurane in oxygen, and placed in the stereotaxic frame in a concord-like position [35]. A small incision was made in the midline at the posterior aspect of the skull, and muscles were separated to expose the atlanto-occipital membrane. The hydrogel was prepared as described above, using 0.1 mM of MnCl₂. 10 µL of Mn/GG-MA was placed in Hamilton syringe and injected into the intrathecal space with a speed of 10 µL.min⁻¹. After injection, the needle was left in the same place for an additional 1 minute and then slowly withdrawn. Afterwards, skin was sutured, and the animal was placed in MRI scanner.

V.3.12 Phantom Magnetic Resonance Imaging

Tripilot scan was followed by T1 parametric imaging with the 2D Saturation Recovery Spin Echo Sequence with varying repetition times (TR = 200 ms ... 8000 ms, TE = 9.5 ms, rare factor = 2, NA = 1, FOV = 75 mm × 75 mm, 5 slices 2.0 mm thick with 2.0 mm gaps, spatial resolution = 586 µm × 586 µm, scan time ~13 min) and T2 parametric imaging with the MSME sequence (TR = 5000 ms, TE = 15 ms ... 480 ms, NA = 1, FOV = 75 mm × 75 mm, 5 slices 2.0 mm thick with 2.0 mm gaps, spatial resolution = 586 µm × 586 µm, scan time ~8 min).

To evaluate relative magnetic resonance signal of T1-weighted imaging of GG-MA phantoms with different concentration of manganese ions, identical regions of interest (ROI) were outlined on MR images and the signal intensity was measured with the use of ImageJ software.

V.3.13 *In vivo* Magnetic Resonance Imaging

MR imaging was performed immediately after intrathecal and intracerebral implantation of hydrogel. After intrathecal transplantation additional MR imaging was performed 24 hours after surgery. For the imaging animals were anesthetized with isoflurane (1.5-2% in oxygen) and position head prone in MRI-compatible water-heated bed. Body temperature and respiration rate were monitored throughout the study with MRI compatible probes (SA Instruments, Stony Brook, NY, USA). 7T MR scanner (BioSpec 70/30 USR, Bruker, Ettlingen, Germany) equipped with transmit cylindrical radiofrequency coil (8.6 cm inner diameter, Bruker) and a mouse brain dedicated receive-only array surface coil (2x2 elements, Bruker) was used. The structural imaging protocol was performed as we described previously [36]. Briefly, we used T1-weighted 3D FLASH sequence (TR = 12 ms; TE = 4 ms; flip angle, FA = 18; NA = 10; field of

view, FOV = 15 mm × 15 mm × 15 mm, spatial resolution = 117 μm isotropic, scan time ~25 min). Structural imaging was followed by T1 parametric imaging with the 2D Saturation Recovery Spin Echo Sequence with varying repetition times (TR = 410 ms ... 8000 ms, TE = 22 ms, rare factor = 4, NA = 3, FOV = 20 mm × 20 mm, 8 slices 0.8 mm thick with no gaps, spatial resolution = 156 μm × 156 μm, scan time ~23 min) and T2 parametric imaging with the MSME sequence (TR = 5000 ms, TE = 13 ms ... 416 ms, NA = 1, FOV = 20 mm × 20 mm, 8 slices 0.8 mm thick with no gaps, spatial resolution = 156 μm × 156 μm, scan time ~8 min).

V.3.14 Statistical Analysis

Results are presented as mean ± standard deviation, when appropriate. When applicable, the experimental data were analyzed using a single-factor analysis of variance (One-way ANOVA) to assess the statistical significance of the results, followed by post hoc Tukey tests. Statistical significance was set at a P value of ≤0.05. All statistical analysis was performed using GraphPad Prism version 7.0a.

V.4 Results and Discussion

V.4.1 Preparation of Mn-based GG-MA Hydrogels

Mn-based GG-MA hydrogels (Mn/GG-MA) were prepared using methacrylated gellan gum (GG-MA) as a hydrogel matrix (Figure V-1A). Solutions of 1% (w/v) GG-MA were mixed with MnCl₂ solutions to obtain the desired final concentration of MnCl₂ (0, 0.1, and 1 mM), in a final GG-MA concentration of 0.75% (w/v). All formulations were studied by rheological techniques to assess their mechanical properties. Time sweep curves, plotted in Figure V-1B, were performed to study a possible gelation effect over time. Particularly, the evolution of the storage modulus (G'), loss modulus (G''), and phase angle (δ) upon the addition of ionic solutions was considered. While G' is regarded as the stiffness of the material, G'' represents the liquid-like behavior of the hydrogel. Therefore, these parameters allow the determination of the elastic (G') and viscous (G'') character of the tested hydrogels, and the ratio between these parcels (δ) giving a quantitative measure of the material mechanical properties [18].

Without the addition of MnCl₂, 0.75% (w/v) GG-MA hydrogels showed a G' value of 0.65 ± 0.18 Pa, which was similar to the obtained G'' value (0.35 ± 0.09 Pa). Considering the higher G' value over G'', one can assume this formulation as viscoelastic solid, as confirmed by the phase angle value of 28.51 ± 4.58°, that is between the purely elastic (δ = 0°) and purely viscous (δ = 90°) values [37, 38] (Supplementary Figure V-1A). The addition of 0.1 mM MnCl₂ leads to a modest increase in G' value to 0.80 ± 0.23 Pa,

with G'' following the same trend (0.39 ± 0.10 Pa). By its turn, GG-MA hydrogels with 1 mM $MnCl_2$ showed a considerably high G' and G'' values after a 30 minutes sweep, due to the electrostatic interaction between the Mn^{2+} ions and the carboxylic groups of GG-MA. Interestingly, both parameters increased over time, showing a time-dependent interaction between GG-MA polymeric networks and the Mn^{2+} ions. After the time sweep, it was registered a G' and G'' value of 34.54 ± 18.78 Pa and 5.34 ± 1.71 Pa, respectively. As expected, the measured phase angle was lower for hydrogels with 1 mM, $9.69 \pm 1.81^\circ$, showing that the lag time between strain and shear stress decreases upon addition of $MnCl_2$. Thence, one can assume that this formulation has already a “gel-like” character, although with insufficient mechanical stability.

Although the presence of 1 mM $MnCl_2$ changed the rheological properties of the GG-MA hydrogel, with a slight increase in its stiffness, none of the formulations acquired a defined, self-supporting shape. It is known that GG-MA crosslinks in the presence of ions, particularly divalent ions such as Mn^{2+} . However, the obtained results showed that the ionic concentration used to prepare the hydrogels was not sufficient to overcome the intramolecular electrostatic repulsions of the carboxylic groups in the GG-MA network, thus giving origin to a “weak gel” [39].

The addition of artificial cerebrospinal fluid (aCSF), a salt-rich solution, to the GG-MA formulations led to a more efficient crosslink of the hydrogel network. The ions present in the aCSF can interact with the GG-MA polymer, resulting in a chemical bonding between the divalent ions (e.g Ca^{2+} or Mg^{2+}) and the polymeric network. Additionally, the presence of monovalent ions, such as K^+ or Na^+ , also contributed to hydrogel crosslink by screening the electrostatic repulsion between the GG-MA ionized carboxylate groups [40]. Indeed, after incubation in aCSF for 24 hours, the Mn/GG-MA hydrogel acquired a definite shape, possible to be handled. Alongside, G' values significantly increased to 1463.02 ± 666.19 Pa, 5157.52 ± 2330.58 Pa and 4490.19 ± 1488.04 Pa, for solutions with 0 mM, 0.1 mM and 1 mM respectively, confirming the increase of the material stiffness upon aCSF-driven crosslinking. An increase in G'' values was also noticed together with the changes in G' . However, significant differences on the phase angle, thus in the ratio G''/G' , were noticed for GG-MA hydrogels and hydrogels supplemented with 0.1 mM $MnCl_2$, when compared to values without aCSF (Supplementary Figure V-1A). Although all formulations showed a viscoelastic nature, the phase angle value was smaller for the GG-MA hydrogels after aCSF incubation, confirming a more elastic behavior of these hydrogels.

intraparenchymal space, a self-supporting, defined, viscoelastic hydrogel is formed. Therefore, the CSF can be used to ionically crosslink the Mn/GG-MA hydrogels *in situ*, without the use of further stimuli.

V.4.2 Injection Ability

From the obtained rheology data, it is possible to infer that the ions present in the aCSF physically crosslink all Mn/GG-MA hydrogel formulations. Yet, it is still necessary to study the hydrogel response to high shear rates, similar to what happens during injection, as well as to measure the force needed to inject the material.

Using steady-state shear measurements, it was possible to observe a decrease in viscosity as shear rate increases, typical of shear-thinning solutions (Supplementary Figure V-1B). The non-Newtonian behavior, noticed for all formulations, strongly suggests the feasibility of hydrogel injection. This capacity to decrease viscosity as a response to increasing shear is highly advantageous for injectable formulations [41].

Regardless, a biomaterial is only clinically relevant for injection if the injection force needed is not damaging to embedded cells and it is feasible in a clinical scenario. The force needed to extrude the biomaterial through a 31G needle was then measured, as this type of needle size is frequently used for injection for neurological applications in small animals. As plotted in Figure V-1C, the force needed to extrude the pre-gel solutions was 0.309 ± 0.063 N for GG-MA only; 0.238 ± 0.063 N for 0.1 mM; 0.238 ± 0.024 N for 1 mM; and 0.294 ± 0.090 N for aCSF. All formulations tested are injectable, with force needed to inject gel solution being similar to the force needed to inject aCSF. No needle clotting was observed during the experiment, and the maximal force used to inject the hydrogel in each experiment was similar for all formulations, with no significant differences observed. Interestingly, after injection into a tube filled with aCSF, the pre-gel solution rapidly crosslinks, forming a well-defined fiber structure (Figure V-1D). This is particularly important for intrathecal injections, as it shows that Mn-based hydrogels will not disperse within the aCSF due to delayed crosslink leading to undesired stem cell sedimentation.

V.4.3 Hydrogel Permeability

One important feature to consider when designing hydrogels for cell-based therapies is the permeability to nutrients and signaling molecules. Mostly, it is of utmost importance that the neurotrophic factors released by transplanted cells do not face additional diffusional barriers that may hinder their release from the hydrogel to the nervous tissue.

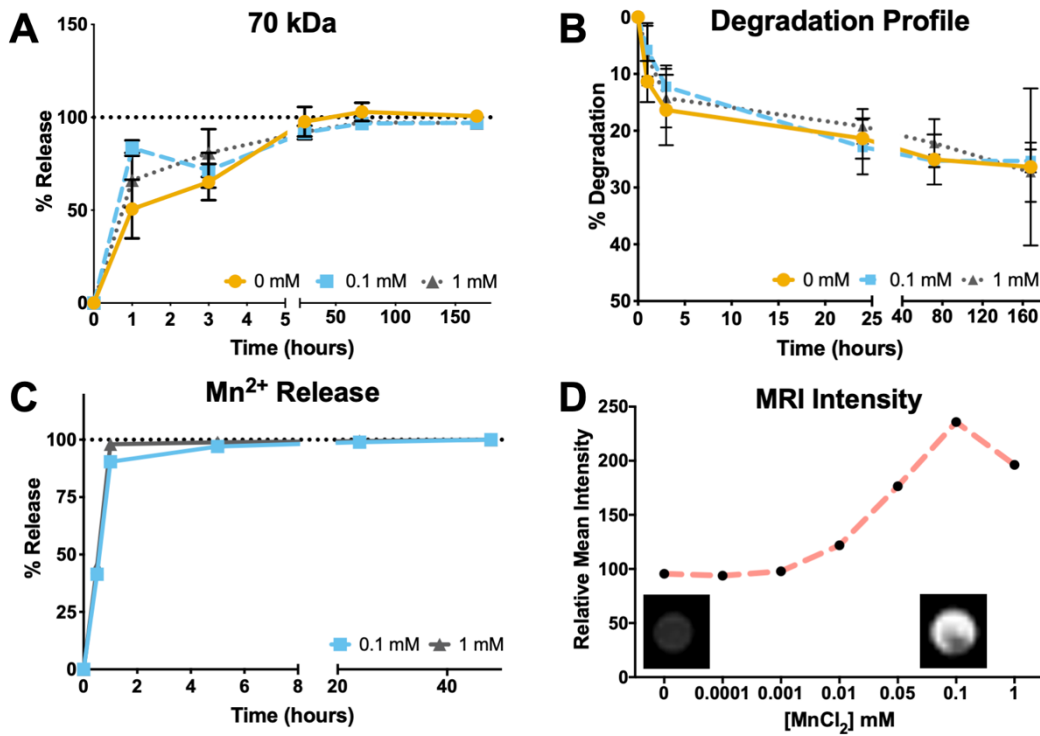


Figure V-2. Release and degradation profiles of Mn-based GG-MA hydrogels. A – Release profile of 70 kDa Dextran-FITC, from the hydrogel to surrounding aCSF; B – Degradation profile of Mn-based hydrogels along time; C – Time-dependent Mn²⁺ release from the prepared hydrogels. Results presented as average±SD, n=5. D – Relative magnetic resonance signal of T1-weighted imaging of GG-MA phantoms with different concentration of manganese ions (ex vivo).

To study the hydrogel permeability, 70 kDa dextran molecules coupled with FITC were mixed with pre-gel solutions followed by crosslinking and incubation in aCSF for 7 days. As depicted in Figure V-2A, for all formulations most of the dextran molecules were released within the first 2 days of incubation. The presence of different amounts of Mn²⁺ does not significantly change the release profile of dextran, as no significant differences were found between the tested formulations. Thenceforth, it is predictable that molecules within this size range, as most of the key neurotrophic factors released by MSCs, will freely diffuse between the encapsulated cells and the surrounding environment. As an example, recent studies [42, 43] showed that intrathecal delivery of mesenchymal stem cells (MSCs) could ameliorate ALS symptoms due to the secretion of neurotrophic factors to the surrounding media. These include glial cell-line derived neurotrophic factor (GDNF, 30 kDa), insulin growth factor type-1 (IGF-1, 7.65 kDa), brain-derived neurotrophic factor (BDNF, 14 kDa), neural growth factor (NGF, 27 kDa) among others. Consequently, one can assume that the hydrogel herein proposed will not interfere with the delivery of the aforementioned neurotrophic factors.

V.4.4 Degradation Profile

The degradation profiles of the different hydrogels were also monitored for 7 days while incubated in aCSF, as plotted in Figure V-2B. After 1 day of incubation, there was a mass loss of $21.36 \pm 3.53\%$ for GG-MA only and $22.86 \pm 4.77\%$ and $19.22 \pm 3.04\%$ for hydrogels with 0.1 and 1 mM MnCl_2 , respectively. During the following 2 days, mass loss was less evident, and the final hydrogel weight variations were $25.31 \pm 1.98\%$ on hydrogels supplemented with 0.1 mM MnCl_2 and $27.30 \pm 5.17\%$ when 1 mM MnCl_2 was used. Although herein the hydrogels were incubated in aCSF, the obtained degradation profile is aligned with previous studies on GG hydrogels stability in PBS. Different works already pointed to a high stability of GG-based hydrogel, both in the low acyl form or after methacrylation, with a weight loss of only 20% after incubation in PB for up to 90 days [28, 44, 45]. When compared with GG-MA only hydrogels, the difference in degradation is not significant, showing again that the introduction of MnCl_2 ions does not change the GG-MA properties in a substantial way. More importantly, the observed stability suggests that Mn/GG-MA hydrogels can hold the delivered cells for long periods, avoiding the undesired sedimentation at cauda equina.

V.4.5 Manganese Release Profile and Magnetic Resonance Imaging

The possibility to perform image-guided interventions is highly appealing, as it can facilitate the precise deposition of the cell-laden hydrogel into the intrathecal space or parenchyma. With that being said, it is expected that the Mn^{2+} ions present in the GG-MA matrix remain in the hydrogel long enough to be detected during the procedure of gel injection. Thus, the Mn^{2+} release profile was obtained via ICP detection. As plotted in Figure V-2C, Mn^{2+} ions are quickly released from the hydrogel. Specifically, after 30 minutes of incubation in aCSF, roughly 50% of the Mn^{2+} ions were released to the surrounding media ($45 \pm 4\%$ and $46 \pm 1\%$ for 0.1 and 1 mM, respectively). It was already shown that Mn^{2+} ions interact with the carboxyl group of the D-glucuronate unit of GG [33, 34]. However, when in contact with the aCSF, other divalent ions start to diffuse into the hydrogel and to interact with the polymeric network leading to hydrogel crosslink [39, 46]. The Mn^{2+} ions are then substituted by other divalent ions, as Ca^{2+} and Mg^{2+} , and consequently released from the hydrogel to the aCSF.

Although the total release of Mn^{2+} was noticed after 1 hour of incubation, it should be taken into consideration that Mn^{2+} start to diffuse only when in contact with the CSF solution. Hence, besides the burst release of the paramagnetic ions, the timeframe until a complete a release is achieved is enough for tracking the delivery, placement and initial biodistribution of the hydrogel within the CSF space. Rapid

clearance of the Mn^{2+} contrast signal may be considered as advantageous in situations when T1 MRI is further utilized for diagnostic purposes to follow treatment outcomes [47, 48].

To verify appropriate Mn^{2+} concentration for Mn/GG-MA hydrogel visualization in MRI, phantoms of GG-MA with different concentrations of $MnCl_2$ were prepared followed by T1 and T2 weighted MR imaging acquisition (Figure V-2D). The MR signal was detected with an $MnCl_2$ concentration as low as 0.01 mM. The signal intensity increased with $MnCl_2$ concentration, reaching an intensity peak for 0.1 mM, with a 2.4-fold increase in MR signal as compared to aCSF. Interestingly, the signal intensity decreased for higher concentrations (1 mM $MnCl_2$), which can be attributed to a T2 effect that results in a signal loss [49].

The possibility to retrieve an MRI signal with low $MnCl_2$ concentrations ensures that, besides the rapid Mn^{2+} release from the hydrogels, the biomaterial is still identifiable by MRI during the transplant procedure. Also, the use of low Mn^{2+} concentrations prevents possible deleterious effects caused by manganese-induced toxicity [50]. From the obtained results, the formulation using 0.1 mM $MnCl_2$ was selected to be used in further studies, as it gives the highest MR signal.

V.4.6 Cell Viability: hASCs Encapsulation

In vitro biocompatibility was studied by encapsulating human-derived adipose stem cells (hASCs) into the developed hydrogels. To better mimic a possible *in vivo* scenario, hydrogels were extruded into aCSF using a 31G needle, which is typically used for small animal studies (Figure V-3A). Considering the aforementioned MRI results, *in vitro* biocompatibility was assessed using hydrogels prepared with 0.1 mM $MnCl_2$, while GG-MA only hydrogels were used as controls. As plotted in Figure V-3B, cell viability was not significantly impaired by the presence of $MnCl_2$ along the 7 days of culture. As expected, hydrogels were successfully extruded as fibers, and their shape was maintained throughout the culture time, as depicted in Figure V-3C. As a proof-of-concept, hydrogels with 0.1 mM $MnCl_2$ were also extruded using an 18G needle, envisioning future large-animal studies (Supplementary Figure V-2). Similarly, cells remained viable after being encapsulated within the hydrogel matrix, with $92 \pm 3\%$ of cells viable 7 days after extrusion. Considering the potential of mesenchymal stem cells [51] and in particular adipose stem cells [52, 53], on the treatment of multifocal CNS diseases, the obtained results pave the way for the application of the Mn/GG-MA hydrogels as physical support in non-invasive cell-based therapies.

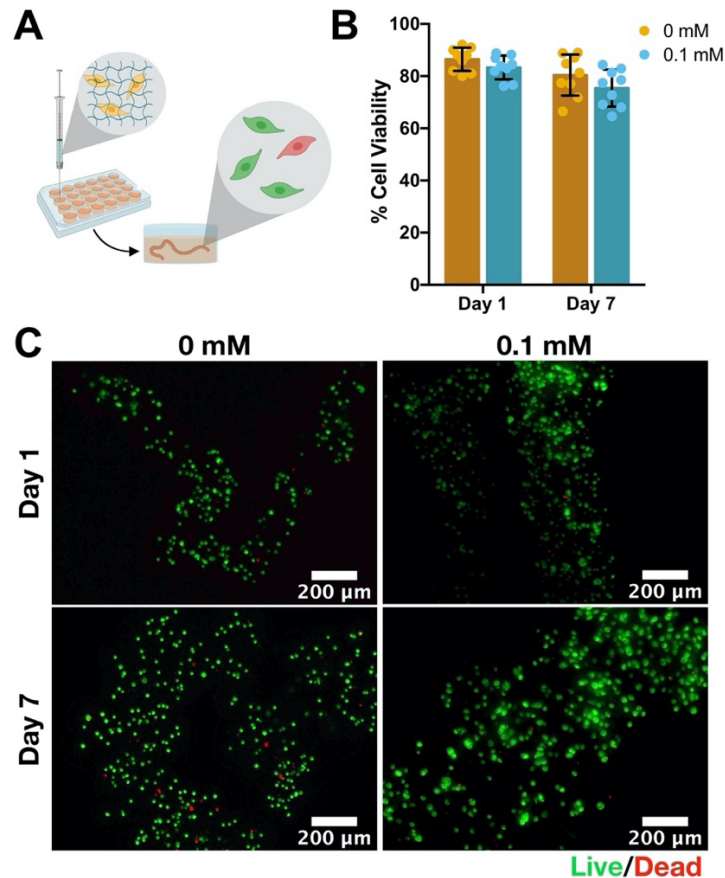


Figure V-3. Cell encapsulation within Mn-based GG-MA hydrogel fibers. A – Schematic representation of the experimental setup. Cells were injected directly into aCSF using a Hamilton syringe coupled with a 31G needle, and then cultured for different periods of time; B – Cell viability after 1 and 7 days of encapsulation in hydrogels with 0.1 mM MnCl₂ and GG-MA only (used as control). Results presented as average±SD, n=3; C – Fluorescence microscopy images of Live/dead staining after 1 and 7 days of incubation. Live cells showed as green and dead cells as red. Scale bar: 200 μm.

V.4.7 *In Vivo* Magnetic Resonance Imaging

The feasibility of using the developed Mn-based GG-MA hydrogels for image-guided cell delivery was further investigated *in vivo*. For that, hydrogels were injected into the intrathecal space and intraparenchymally in double mutant MBP^{shi/shi}/rag2 mice, and followed by MR imaging, as schematically represented in Figure V-4A and Figure V-4C.

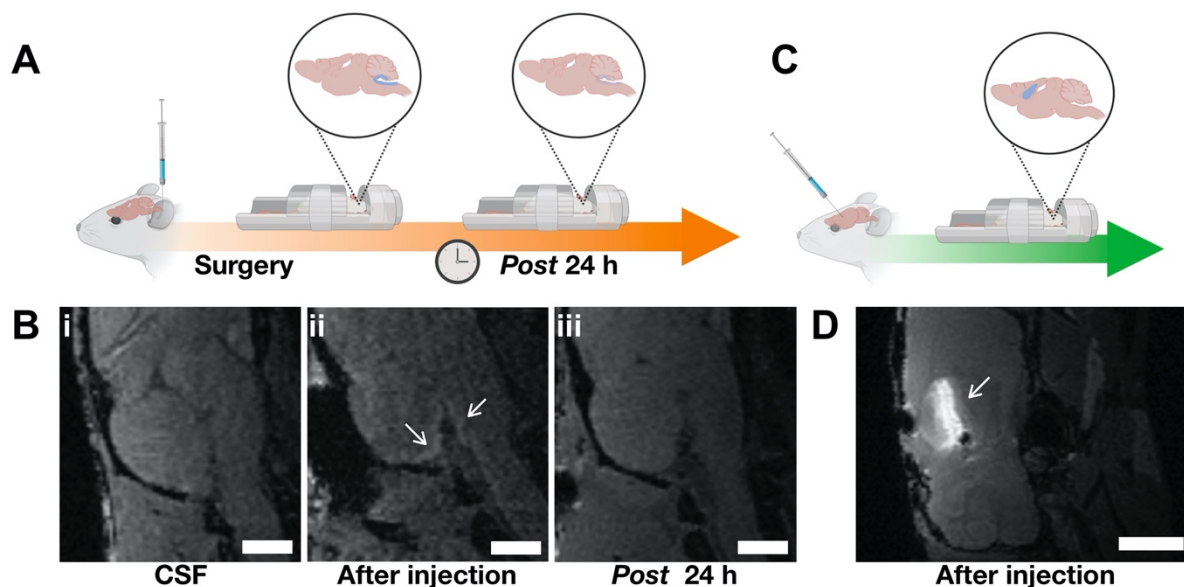


Figure V-4. Magnetic resonance T1 weighted imaging of Mn-based GG-MA hydrogels. A- Schematic representation of the *in vivo* assessment of MRI signal; B - T1 weighted image of (i) control *MBP^{sh/shi}/rag2* mouse; (ii) hyperintense signal (arrows) on MR image represent Mn-based GG-MA hydrogel directly after intrathecal transplantation in *MBP^{sh/shi}/rag2* mice; (iii) MR scan 24 hours after transplantation, where hydrogels are not visible in intrathecal space; C- Schematic drawing of intraparenchymal injection and MR scanning; D - MR scan after transplantation of Mn-based GG-MA hydrogel in the parenchyma of *MBP^{sh/shi}/rag2* mice with prominent hyperintensity (arrow) showing biodistribution of Mn-based GG-MA hydrogel. Scale bar: 2mm.

Hydrogels were visible as a hyperintense signal in T1 MRI (Figure V-4B.ii, arrows) directly after transplantation, confirming the *in vitro* MR results. However, none of the injected GG-MA hydrogels could be visualized 24 hours *post*transplantation (Figure V-4B.iii), which is in accordance with the Mn²⁺ release profile previously discussed. Indeed, the CSF circulation in the intrathecal space is likely responsible for elution of the Mn²⁺ ions, thus decreasing the hyperintense signal with time. Hence, the engineered hydrogel can be a potential tool for the correct placement of cells along the spinal cord, using a considerably lower amount of MnCl₂ as compared to other Mn-based hydrogels [21]. As showed before, the MnCl₂ concentration used to prepare the hydrogels is not deleterious for cells and the rapid release to the CSF prevents a local accumulation of Mn²⁺ ions, which might be harmful to the local neuronal cells, and induce Mn-related toxicity [26]. Mn/GG-MA hydrogels were also visible when hydrogels were injected directly into the parenchyma (Figure V-4C and Figure V-4D). MRI-guided intraparenchymal cell delivery is also feasible using the designed hydrogel system, which might be useful for stem cell delivery after a stroke event [8]. As shown in Figure V-4D, the MR signal was more intense when the hydrogel was injected into the parenchyma. This shows the importance of the CSF on the clearance of the Mn²⁺ from the

hydrogel, since in the parenchyma the ionic diffusion between the hydrogel and the fluid is reduced, thence increasing the signal. Therefore, one should be aware that Mn^{2+} concentration must be optimized for each of the intended cell delivery route for better imaging outcomes.

V.5 Conclusion

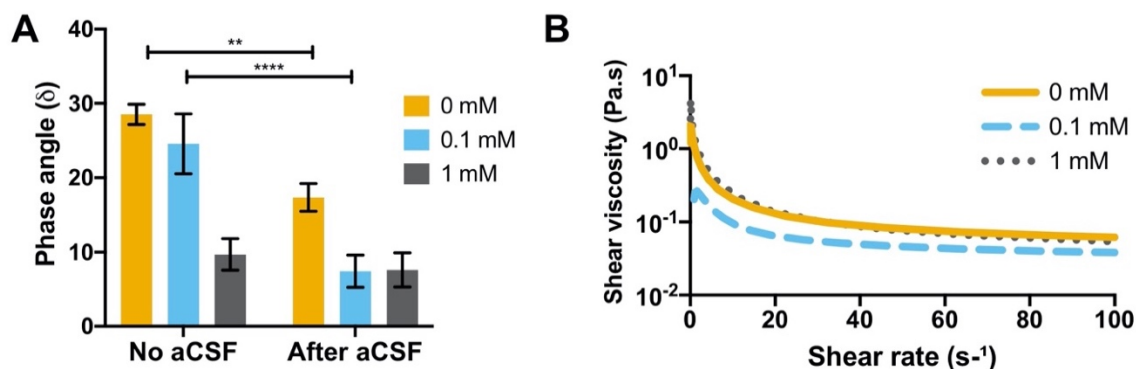
The present work aimed to design a new traceable hydrogel for image-guided intrathecal cell delivery. By taking advantage of the inherent affinity of methacrylated gellan gum to divalent ions, it was possible to incorporate paramagnetic Mn^{2+} ions within the hydrogel network. Such Mn^{2+} labeled hydrogels can then be used for MRI-guided injection to visualize their biodistribution. The resulting hydrogel was easily injectable, forming distinct, stable, and biocompatible fibers upon injection in a simulated cerebrospinal fluid environment. While the hydrogel formulation would prevent cell removal due to sedimentation or CSF circulation, Mn^{2+} allows real-time visualization of hydrogel position, avoiding an incorrect placement, as evaluated by *in vitro* and *in vivo* MR imaging. Thus, the Mn-based methacrylated gellan gum hydrogels developed herein hold great potential on minimally invasive intrathecal cell delivery, tackling two of the main drawbacks reported to date, and possibly open up other applications as a cell/drug delivery matrix for neurological applications when an imaging guidance is required.

V.6 Acknowledgements

Silvia Vieira acknowledges FCT PhD scholarship (SFRH/BD/102710/2014). The FCT distinction attributed to J. Miguel Oliveira under the Investigator FCT program (IF/01285/2015) and J. Silva-Correia (IF/00115/2015) are also greatly acknowledged. The authors also acknowledge the funds provided under the project NanoTech4ALS, funded under the EU FP7 M-ERA.NET program, and to FCT for the funds provided under the 3BioMeD project (JICAM/0001/2017).

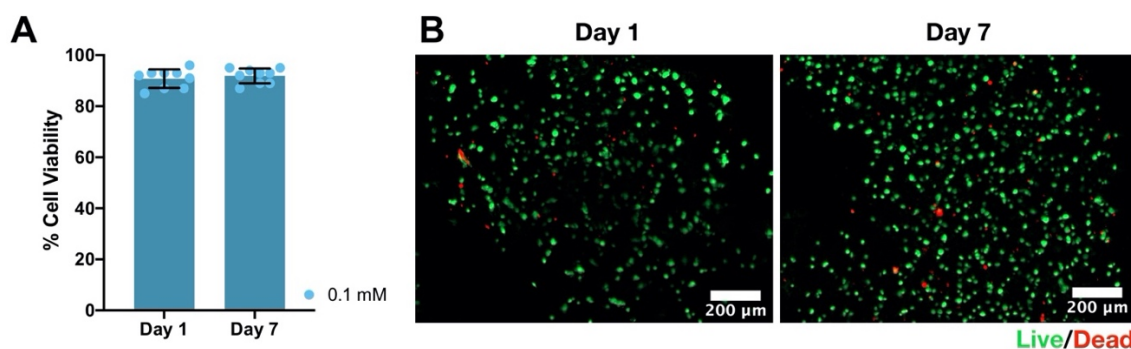
V.7 Supporting Information

V.7.1 Rheological Characterization: Phase Angle and Shear Viscosity



Supplementary Figure V-1. Rheologic characterization of Mn-based hydrogels. A - Hydrogels phase angle before and after addition of aCSF. Results presented as average \pm SD of the last registered minute, of at least 3 different samples; B - Shear viscosity of the different hydrogel formulations, along a shear rate ramp. Shear viscosity drastically decreases upon increasing on the shear rate. Results presented as average, n=4.

V.7.2 Biocompatibility: Injection with 18G Needle



Supplementary Figure V-2. Cell encapsulation in GG-MA hydrogel supplemented with 0.1 mM Mn. A- Cell viability after 1 and 7 days of culture (average \pm SD, n=3); B- Fluorescence microscopy images of Live/dead staining after 1 and 7 days of incubation. Live cells showed as green and dead cells as red. Scale bar: 200 μ m.

V.8 References

1. Lyczek, A., et al., *Transplanted human glial-restricted progenitors can rescue the survival of dysmyelinated mice independent of the production of mature, compact myelin*. *Experimental Neurology*, 2017. **291**: p. 74-86.
2. Golubczyk, D., et al., *The Role of Glia in Canine Degenerative Myelopathy: Relevance to Human Amyotrophic Lateral Sclerosis*. *Molecular Neurobiology*, 2019. **56**(8): p. 5740-5748.
3. Gutierrez, J., et al., *Preclinical Validation of Multilevel Intraparenchymal Stem Cell Therapy in the Porcine Spinal Cord*. *Neurosurgery*, 2015. **77**(4): p. 604-12; discussion 612.

4. Glass, J.D., et al., *Transplantation of spinal cord-derived neural stem cells for ALS: Analysis of phase 1 and 2 trials*. *Neurology*, 2016. **87**(4): p. 392-400.
5. Huang, H., et al., *Intraparenchymal Neural Stem/Progenitor Cell Transplantation for Ischemic Stroke Animals: A Meta-Analysis and Systematic Review*. *Stem Cells International*, 2018. **2018**: p. 4826407.
6. Chen, L., et al., *Multiple cell transplantation based on an intraparenchymal approach for patients with chronic phase stroke*. *Cell Transplantation*, 2013. **22 Suppl 1**: p. S83-91.
7. Kelly, S., et al., *Transplanted human fetal neural stem cells survive, migrate, and differentiate in ischemic rat cerebral cortex*. *Proceedings of the National Academy of Sciences of the United States of America*, 2004. **101**(32): p. 11839-44.
8. Zhong, J., et al., *Hydrogel matrix to support stem cell survival after brain transplantation in stroke*. *Neurorehabilitation and Neural Repair*, 2010. **24**(7): p. 636-44.
9. Goldman, S.A., *Stem and Progenitor Cell-Based Therapy of the Central Nervous System: Hopes, Hype, and Wishful Thinking*. *Cell Stem Cell*, 2016. **18**(2): p. 174-88.
10. Boltze, J., et al., *The Dark Side of the Force - Constraints and Complications of Cell Therapies for Stroke*. *Frontiers in Neurology*, 2015. **6**: p. 155.
11. Oliveira, J.M., et al., *Hydrogel-based scaffolds to support intrathecal stem cell transplantation as a gateway to the spinal cord: clinical needs, biomaterials, and imaging technologies*. *npj Regenerative Medicine*, 2018. **3**: p. 8.
12. Nabavi, S.M., et al., *Safety, Feasibility of Intravenous and Intrathecal Injection of Autologous Bone Marrow Derived Mesenchymal Stromal Cells in Patients with Amyotrophic Lateral Sclerosis: An Open Label Phase I Clinical Trial*. *Cell journal*, 2019. **20**(4): p. 592-598.
13. Barczewska, M., et al., *Safety of intrathecal injection of Wharton's jelly-derived mesenchymal stem cells in amyotrophic lateral sclerosis therapy*. *Neural Regeneration Research*, 2019. **14**(2): p. 313-318.
14. Habisch, H.J., et al., *Intrathecal application of neuroectodermally converted stem cells into a mouse model of ALS: limited intraparenchymal migration and survival narrows therapeutic effects*. *Journal of Neural Transmission*, 2007. **114**(11): p. 1395-406.
15. Chotivichit, A., et al., *Chronic spinal cord injury treated with transplanted autologous bone marrow-derived mesenchymal stem cells tracked by magnetic resonance imaging: a case report*. *Journal of Medical Case Reports*, 2015. **9**: p. 79.
16. Gasperini, L., J.F. Mano, and R.L. Reis, *Natural polymers for the microencapsulation of cells*. *Journal of The Royal Society Interface*, 2014. **11**: p. 20140817-20140817.
17. Malysz-Cymborska, I., et al., *MRI-guided intrathecal transplantation of hydrogel-embedded glial progenitors in large animals*. *Scientific Reports*, 2018. **8**(1): p. 16490.

18. Fratini, M., et al., *Multiscale Imaging Approach for Studying the Central Nervous System: Methodology and Perspective*. *Frontiers in Neuroscience*, 2020. **14**: p. 72.
19. Oliveira, E.P., et al., *Advances in bioinks and in vivo imaging of biomaterials for CNS applications*. *Acta Biomaterialia*, 2019.
20. Gale, E.M., et al., *A Manganese-based Alternative to Gadolinium: Contrast-enhanced MR Angiography, Excretion, Pharmacokinetics, and Metabolism*. *Radiology*, 2018. **286**(3): p. 865-872.
21. Morch, Y.A., et al., *Mn-alginate gels as a novel system for controlled release of Mn²⁺ in manganese-enhanced MRI*. *Contrast Media and Molecular Imaging*, 2012. **7**(2): p. 265-75.
22. Addisu, K.D., et al., *Bioinspired, Manganese-Chelated Alginate-Polydopamine Nanomaterials for Efficient in Vivo T1-Weighted Magnetic Resonance Imaging*. *ACS Applied Materials and Interfaces*, 2018. **10**(6): p. 5147-5160.
23. Wang, J., et al., *Manganese-Based Contrast Agents for Magnetic Resonance Imaging of Liver Tumors: Structure-Activity Relationships and Lead Candidate Evaluation*. *Journal of Medicinal Chemistry*, 2018. **61**(19): p. 8811-8824.
24. Cloyd, R.A., S.A. Koren, and J.F. Abisambra, *Manganese-Enhanced Magnetic Resonance Imaging: Overview and Central Nervous System Applications With a Focus on Neurodegeneration*. *Frontiers in Aging Neuroscience*, 2018. **10**: p. 403.
25. Roth, J.A., B. Ganapathy, and A.J. Ghio, *Manganese-induced toxicity in normal and human B lymphocyte cell lines containing a homozygous mutation in parkin*. *Toxicology In Vitro*, 2012. **26**(7): p. 1143-9.
26. Ding, D., J. Roth, and R. Salvi, *Manganese is toxic to spiral ganglion neurons and hair cells in vitro*. *Neurotoxicology*, 2011. **32**(2): p. 233-41.
27. Oliveira, J.T., et al., *Gellan gum injectable hydrogels for cartilage tissue engineering applications: in vitro studies and preliminary in vivo evaluation*. *Tissue Engineering Part A*, 2010. **16**(1): p. 343-53.
28. Silva-Correia, J., et al., *Gellan gum-based hydrogels for intervertebral disc tissue-engineering applications*. *Journal of Tissue Engineering and Regenerative Medicine*, 2011. **5**(6): p. e97-107.
29. Vieira, S., et al., *Gellan gum-coated gold nanorods: an intracellular nanosystem for bone tissue engineering*. *RSC Advances*, 2015. **5**(95): p. 77996-78005.
30. Lozano, R., et al., *3D printing of layered brain-like structures using peptide modified gellan gum substrates*. *Biomaterials*, 2015. **67**: p. 264-273.
31. Stevens, L.R., et al., *Tissue engineering with gellan gum*. *Biomaterials Science*, 2016. **4**(9): p. 1276-1290.

32. Spector, R., S. Robert Snodgrass, and C.E. Johanson, *A balanced view of the cerebrospinal fluid composition and functions: Focus on adult humans*. Experimental Neurology, 2015. **273**: p. 57-68.
33. Kawahara, S., et al., *Interactions of paramagnetic metal ions with gellan gum studied by ESR and NMR methods*. Carbohydrate Polymers, 1996. **30**(2-3): p. 129-133.
34. Akihiro Tsutsumi, et al., *ESR studies of Mn(II) binding to gellan and carrageenan gels*. Food Hydrocolloids, 1993. **7**(5): p. 427-434.
35. Janowski, M., et al., *Neurotransplantation in mice: The concordance-like position ensures minimal cell leakage and widespread distribution of cells transplanted into the cisterna magna*. Neuroscience Letters, 2008. **430**(2): p. 169-174.
36. Fiedorowicz, M., et al., *Anterograde Transport in Axons of the Retinal Ganglion Cells and its Relationship to the Intraocular Pressure during Aging in Mice with Hereditary Pigmentary Glaucoma*. Current Eye Research, 2018. **43**(4): p. 539-546.
37. Yan, C. and D.J. Pochan, *Rheological properties of peptide-based hydrogels for biomedical and other applications*. Chemical Society Reviews, 2010. **39**(9): p. 3528-40.
38. Malkin, A.Y. and A.I. Isayev, *Rheology: concepts, methods, and applications*. 2017: Elsevier.
39. Morris, E.R., K. Nishinari, and M. Rinaudo, *Gelation of gellan - A review*. Food Hydrocolloids, 2012. **28**(2): p. 373-411.
40. Bacelar, A.H., et al., *Recent progress in gellan gum hydrogels provided by functionalization strategies*. Journal of Materials Chemistry B, 2016. **4**(37): p. 6164-6174.
41. Chen, M.H., et al., *Methods To Assess Shear-Thinning Hydrogels for Application As Injectable Biomaterials*. ACS Biomaterials Science & Engineering, 2017. **3**(12): p. 3146-3160.
42. Forostyak, S. and E. Sykova, *Neuroprotective Potential of Cell-Based Therapies in ALS: From Bench to Bedside*. Frontiers in Neuroscience, 2017. **11**: p. 591.
43. Chen, K.S., S.A. Sakowski, and E.L. Feldman, *Intraspinal stem cell transplantation for amyotrophic lateral sclerosis*. Annals of Neurology, 2016. **79**(3): p. 342-53.
44. Xu, Z.H., et al., *Chemically Modified Gellan Gum Hydrogels with Tunable Properties for Use as Tissue Engineering Scaffolds*. ACS Omega, 2018. **3**(6): p. 6998-7007.
45. Silva-Correia, J., et al., *Biocompatibility evaluation of ionic- and photo-crosslinked methacrylated gellan gum hydrogels: in vitro and in vivo study*. Advanced Healthcare Materials, 2013. **2**(4): p. 568-75.
46. Grasdalen, H. and O. Smidsrød, *Gelation of gellan gum*. 1987. p. 371-393.
47. Turner, M.R. and M. Modo, *Advances in the application of MRI to amyotrophic lateral sclerosis*. Expert Opinion on Medical Diagnostics, 2010. **4**(6): p. 483-496.

48. Grolez, G., et al., *The value of magnetic resonance imaging as a biomarker for amyotrophic lateral sclerosis: a systematic review*. BMC Neurology, 2016. **16**(1): p. 155.
49. Mørch, Y.A., et al., *Mn-alginate gels as a novel system for controlled release of Mn 2+ in manganese-enhanced MRI*. Contrast Media and Molecular Imaging, 2012. **7**(2): p. 265-275.
50. Malheiros, J.M., et al., *Manganese-Enhanced MRI: Biological Applications in Neuroscience*. Frontiers in Neurology, 2015. **6**: p. 161.
51. Gugliandolo, A., P. Bramanti, and E. Mazzon, *Mesenchymal Stem Cells: A Potential Therapeutic Approach for Amyotrophic Lateral Sclerosis?* Stem Cells International, 2019. **2019**: p. 3675627.
52. Kim, K.S., et al., *Transplantation of human adipose tissue-derived stem cells delays clinical onset and prolongs life span in ALS mouse model*. Cell Transplantation, 2014. **23**(12): p. 1585-97.
53. Walker, C.L., *Adipose-derived stem cell conditioned medium for the treatment of amyotrophic lateral sclerosis: pre-clinical evidence and potential for clinical application*. Neural Regeneration Research, 2019. **14**(9): p. 1522-1524.

Chapter VI: Methacrylated Gellan Gum and Hyaluronic Acid Hydrogel Blends for Image-Guided Neurointerventions*

ABSTRACT

Cell-based therapies delivered via intrathecal injection are considered as one of the most promising solutions for the treatment of amyotrophic lateral sclerosis (ALS). Herein, injectable manganese-based biocompatible hydrogel blends were developed, that can allow image-guided cell delivery. The hydrogels can also provide physical support for cells during injection, and at the intrathecal space after transplantation, while assuring cell survival. In this regard, different formulations of methacrylated gellan gum/hyaluronic acid hydrogel blends (GG-MA/HA) were considered as a vehicle for cell delivery. The hydrogels blends were supplemented with paramagnetic Mn^{2+} to allow a real-time monitorization of hydrogel deposition via T1-weighted magnetic resonance imaging (MRI). The developed hydrogels were easily extruded and formed a stable fiber upon injection into the cerebrospinal fluid. Hydrogels prepared with a 75:25 GG-MA to HA ratio supplemented with $MnCl_2$ at 0.1 mM showed controlled hydrogel degradation, suitable permeability, and a distinct MRI signal *in vitro* and *in vivo*. Additionally, human-derived adipose stem cells encapsulated in 75:25 GG-MA/HA hydrogels remained viable up to 14 days of culture *in vitro*. Therefore, the engineered hydrogels can be an excellent tool for injectable image-guided cell delivery approaches.

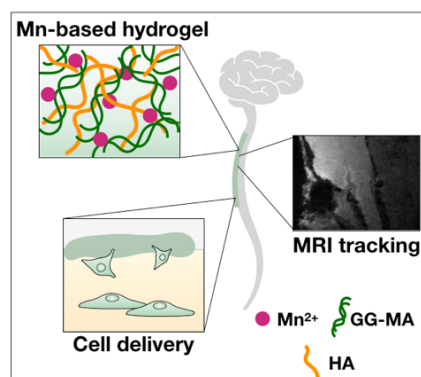
Keywords: gellan gum hydrogels, hyaluronic acid, manganese, magnetic resonance imaging, neuro intervention.

* This chapter is based on the following publication:

"Hydrogel Comprising Manganese, Methods and Uses Thereof". Oliveira J. M., Vieira S., Oliveira E., Silva-Correia J., Reis R. L., Walczak P., Malysz-Cymborska I., Golubczyk D., Kalkowski L., Majchrzak M., Janowski M., Strymecka P., Stanaszek L., Lukomska B., Svendsen T., Asdahl L. C., and Sætrang H. E. M.. Published as WO/2019/123423 and EP3501553 (A1).

"Methacrylated Gellan Gum and Hyaluronic Acid Hydrogel Blends for Image-Guided Neuro interventions", Vieira S., Strymecka P., Stanaszek L., Silva-Correia J., Drela K., Fiedorowicz M., Malysz-Cymborska I., Rogujski P., Janowski M., Reis R. L., Lukomska B., Walczak P., Oliveira J. M. *Journal of Materials Chemistry B*, 8, 5928-5937, DOI: 10.1039/d0tb00877j, 2020.

VI.1 Graphical Abstract



VI.2 Introduction

Disseminated or multifocal diseases are a challenging pathological scenario, as there is no particular target for therapy. As an example, amyotrophic lateral sclerosis (ALS) is a disseminated disease of the central nervous system (CNS), characterized by progressive degeneration of both upper and lower motor neurons [1]. Although ALS is a relatively rare condition, with an incidence of 0.6 to 3.8 per 100000 person-years, this disease can be fatal in 2–5 years [2, 3]. The estimated worldwide mortality is about 30,000 patients a year, and the socioeconomic burden of the disease is also quite relevant [4].

Recently, different studies have shown the potential of cell-based therapy on ALS treatment, namely strategies using stem cells [5, 6]. Indeed, strategies using mesenchymal stem cells (MSCs) showed that the cells are capable of supporting neural recovery, either by cell replacement or by trophic support [7–9]. After transplantation, MSCs can secrete different neurotrophic factors, such as the glial cell line-derived neurotrophic factor (GDNF), vascular endothelial growth factor (VEGF), or insulin-like growth factor 1 (IGF-1), that improve the function, differentiation, and proliferation of neural cells [10]. Also, MSCs can reduce inflammation, and stimulate tissue regeneration, thus ameliorating ALS symptoms [11, 12].

Due to the multifocal nature of ALS, it is necessary to ensure that the therapeutic cells are delivered in extensive areas of the CNS. In this regard, intrathecal cell delivery is considered as one of the most suitable routes to reach broad areas of the CNS [13–16]. This approach relies on direct injection of cells into the cerebrospinal fluid (CSF), providing a straightforward gateway for the CNS through a minimally invasive procedure [17]. Nonetheless, the low cell survival rate and ineffective post-transplantation engraftment are still hampering the clinical application of cell-based therapies for ALS. Specifically, cell

sedimentation at cauda equina due to the gravity effect distorts one of the main advantages of the intrathecal approach: its broad distribution [18].

However, the abovementioned sedimentation can be avoided by encapsulating cells within biocompatible hydrogels. These three-dimensional, highly hydrated structures would provide a cell-friendly environment while narrowing cell distribution to the vicinities of the hydrogel matrix [19]. Nevertheless, that strategy must be carefully designed as hydrogels need to fulfill several requirements to be suitable for an intrathecal approach. Among them, suitable crosslink kinetics upon reaching the CSF is of particular importance. It should be quick to avoid a random material distribution on the CSF space but also controlled not to cause needle clotting and stagnation. Hence, the development of hydrogels, capable of delivery cells within a broad area and using a minimally invasive procedure, is a compelling requisite.

Considering that intrathecal cell delivery implies an injection near the delicate spinal cord tissue, all precautions must be taken to avoid an inaccurate needle placement, or an incorrect hydrogel settlement. Image-guided neuro interventions are then considered a safer method to perform this procedure [19, 20]. Through non-invasive imaging techniques, such as magnetic resonance imaging, it is possible to track in real-time the whole procedure, from needle placement to hydrogel deposition [21, 22]. In this regard, the possibility to label the hydrogels with suitable imaging probes is an advantage for hydrogels intended to be used in the CNS.

With this work, we aim to design a new advanced hydrogel to tackle the main bottlenecks of intrathecal cell delivery. For that, we used methacrylated gellan gum (GG-MA) and hyaluronic acid (HA) hydrogel blends to give cells appropriate physical support. GG-MA is an ionic-responsive hydrogel, that rapidly crosslinks after contact with an ionic solution, such as the CSF [23]. However, GG-MA hydrogels are particularly stable in physiological conditions, since they are degraded only via hydrolytic processes, which might hamper MSCs' distribution in the spinal cord tissue [24, 25]. Therefore, HA was blended with GG-MA to increase the degradation kinetics of the hydrogels. Contrarily to GG-MA, HA has a widespread distribution in the human body, including in the CNS. Its degradation is controlled by hyaluronidases, which are also present in several tissues of the human body [26]. As a result, the hydrogel blends are timely degraded by the action of hyaluronidases, allowing a phased cell escape, but in a controlled fashion due to the presence of stable GG-MA. Additionally, HA has shown promising results as an immunoprotective and immunomodulatory biomaterial, thus contributing to cell survival after transplantation [27, 28].

Additionally, this work also aims to address the issue of uncertainty about hydrogel location after implantation. For this, the intrinsic properties of GG-MA are exploited, namely its affinity to divalent metallic cations, to incorporate Mn^{2+} ions in the hydrogel. Due to their paramagnetic nature, Mn^{2+} can be used as contrast agents for MRI imaging techniques [29, 30]. Thence, the resulting hydrogel can be easily monitored without the addition of standard, potentially toxic, contrast agents, as gadolinium [31].

In this work, we propose a tissue engineering approach for ALS treatment by designing a hydrogel that addresses the main bottlenecks of intrathecal cell-delivery. The resulting hydrogel material allows a minimal-invasive delivery of therapeutic cells as well as the cell escape to the surrounding spinal cord environment, due to sustained hydrogel degradation. Indeed, the developed hydrogels were easily injected, both in *in vitro* and *in vivo* conditions. The hydrogels also supported the *in vitro* encapsulation of human adipose-derived stem cells for up to 14 days. Interestingly, cells could migrate from the hydrogel to the surrounding environment, strengthening the feasibility of using these hydrogels in cell delivery approaches. Last, the engineered hydrogels are compatible with non-invasive MRI tracking, due to the presence of Mn^{2+} ions. This feature might be useful in the scope of image-guided neuro interventions, making the hydrogel placement a safer procedure.

VI.3 Materials and Methods

VI.3.1 Gellan Gum Methacrylation

Methacrylated gellan gum (GG-MA) was prepared following the protocol of Silva-Correia *et al.* [32]. Briefly, low acyl gellan gum (Gelzan™ CM Gelrite®, Sigma-Aldrich) was dissolved in ultra-pure water at 90 °C at a concentration of 1% (w/v). After complete dissolution, glycidyl methacrylate (GMA, 97%, Sigma-Aldrich) was added to the low-acyl gellan gum solution, and this mixture was vigorously stirred overnight at room temperature. The pH of the solution was set as 8.5. After the overnight period, cold acetone was used to precipitate the resulting reaction products. Thence, the obtained material was purified by dialysis (cellulose membrane, molecular weight cut-off 12 kDa, Sigma-Aldrich) against distilled water. After one week of dialysis, the obtained GG-MA was frozen at -80 °C and freeze-dried. Once dried, the material was stored protected from light, and in a dry place until further use.

VI.3.2 Artificial Cerebrospinal Fluid (aCSF)

aCSF was prepared by sequential addition of the different reagents listed in Table V-1 (Chapter V, page 168) in a defined volume of ultra-pure water. After mixing all the reagents, the solution pH was adjusted to 7.3 by the dropwise addition of NaOH. All the reagents were purchased to Sigma-Aldrich.

VI.3.3 Methacrylated Gellan Gum Pre-gel Solutions Supplemented with MnCl₂ (MnGG-MA)

Dry GG-MA was first dissolved in ultra-pure water, using gentle agitation, to prepare 1% (w/v) GG-MA stock solutions. The stock GG-MA solution was then diluted by addition of a suitable volume of manganese (II) chloride solutions (MnCl₂ powder, Sigma-Aldrich), to obtain a final solution with 0.75% (w/v) GG-MA and either 0.1 or 1 mM in MnCl₂. Controls without MnCl₂ were prepared using ultra-pure water for GG-MA dilution.

VI.3.4 Methacrylated Gellan Gum/Sodium Hyaluronate Blends (MnGG-MA/HA)

Sodium hyaluronate solutions were prepared at a concentration of 1% (w/v) by dissolving the sodium hyaluronate powder (HA, 1200-1900 kDa Sodium Hyaluronate pharma-grade 80, Novamatrix® Dupont) in ultra-pure water. After complete dissolution, HA was mixed via gentle agitation with Mn/GG-MA solutions, using volume ratios of 75:25 and 50:50 in Mn/GG-MA and HA, respectively. Hydrogel crosslink was achieved by the interaction of the MnGG-MA/HA with aCSF. For that, MnGG-MA/HA pre-gel solutions were poured into cylindrical silicon molds, and an excess of aCSF was added dropwise. After 5 minutes, hydrogels were recovered from the silicon templates and further analyzed using different techniques.

VI.3.5 Rheological Studies

The rheological properties of the MnGG-MA/HA hydrogels were studied using a Kinexus Pro+ rheometer (Malvern Instruments, UK), and the acquisition software rSpace. The measurements were performed using stainless steel (316 grade) parallel plates: the upper measurement geometry plate, with 8 mm of diameter, and the 20 mm lower pedestal. Pre-gel solutions were poured in the lower pedestal, while aCSF crosslinked hydrogels (8 mm diameter and 2 mm height) were prepared beforehand, with an incubation period in aCSF of 24h. For each hydrogel formulation, the Linear Viscoelastic Region (LVER) was determined. Then, single-frequency oscillation experiments were performed at 0.1 Hz for 30 minutes. Shear viscosity and shear stress were determined by rotational experiments, using an upper measurement geometry cone (40 mm diameter and 4° angle). All experiments were performed at 37 °C, and plots are the average of at least 3 experiments.

VI.3.6 Injection Ability Test

The force needed to extrude the MnGG-MA/HA solutions was measured using an injectability equipment (Paralab). The pre-gel solutions were used to fill a 10 μL Hamilton syringe coupled with a 31 G needle. The material was extruded into a tube filled with aCSF by applying a force on the syringe piston, using a constant extrusion rate. Thus, the load needed to extrude the material through the 31 G needle was measured and recorded using appropriate software. Extrusion of aCSF was used as control.

VI.3.7 Permeability Studies

Hydrogel permeability was studied using 70 kDa fluorescein isothiocyanate–dextran molecules (Dextran-FITC, Sigma-Aldrich). Pre-gel solutions of MnGG-MA/HA were mixed with dextran-FITC, with a final dextran concentration of 125 $\mu\text{g mL}^{-1}$. Hydrogels were crosslinked inside 8 mm silicon cylinders using aCSF as a crosslinker to mimic the hydrogels' properties into the intrathecal space. Upon crosslinking, the hydrogels were immersed in aCSF and incubated at 37 $^{\circ}\text{C}$, with mechanical shaking. At defined time-points, 350 μL of supernatant was retrieved and replaced by the same amount of fresh aCSF. The amount of dextran-FITC that remained inside the hydrogels was calculated at the last time-point. For that, hydrogels were mechanically destroyed, centrifuged, and the resulting supernatant was used to calculate the final concentration of dextran-FITC. The fluorescence emission of FITC-labelled dextran was measured at an excitation wavelength of 485/20 nm and an emission wavelength of 528/20 nm in a microplate reader (Gen 5 2.01, Synergy HT, BioTek). After the reading, the concentration of dextran-FITC in the supernatant was calculated using a calibration curve obtained by measuring the fluorescence emission of dextran-FITC solutions of known concentrations.

VI.3.8 Degradation Profile

Different hydrogel formulations were prepared using aCSF, weighted (initial weight, m), and incubated in aCSF at 37 $^{\circ}\text{C}$, with mechanical shaking. aCSF solutions supplemented with hyaluronidase near plasma concentration (2.6 U, Sigma-Aldrich) were also used to study the effect of enzymatic degradation along time. Hydrogel degradation was monitored by studying its weight loss profile along the incubation time. After 1, 3, 24, 72, and 168 hours, the hydrogels were retrieved, the liquid excess was gently removed, and the final mass of samples was determined (m). Equation III-2 (Chapter III, page 97) was applied to calculate the weight loss ratio at each time point.

VI.3.9 Manganese Release Profile – Inductively Coupled Plasma-Optical Emission Spectroscopy (ICP)

The release of Mn²⁺ ions from the MnGG-MA/HA hydrogels to the surrounding media was quantified using inductively coupled plasma optical emission spectroscopy (ICP; JY2000 2, Jobin Yvon, Horiba). Hydrogels were prepared as mentioned before and incubated in aCSF, at 37 °C with mechanical shaking. At defined time-points (0.5, 1, 5, 24, and 48 hours), aCSF was collected and analyzed. Before analysis, all samples were dissolved in nitric acid, filtered using a 0.22 µm filter, and finally injected into the instrument. Manganese ($\lambda_{em}=259.37$ nm) concentrations in the aCSF solutions were obtained by comparison with standard solutions, with a detection limit of 5 ppb.

VI.3.10 Human-derived Adipose Stem Cells Isolation and Culture

Abdominal lipoaspirate samples were collected under established cooperative agreements between the Hospital da Senhora da Oliveira (Guimarães, Portugal) and the 3B's Research Group – University of Minho, and after donors' informed consent. The fat tissue was retrieved from the abdominal regions of healthy human male and female donors with ages between 18 and 57 years. After collection, samples were digested with collagenase NB 6 GMP Grade (Serva), and 100 mL of fat tissue was centrifuged to remove all liquids (50 g, 5 minutes). Then, about 50 mL of concentrated adipose tissue was mixed with the same volume of collagenase solution, diluted in PBS at a final concentration of 0.2 U mL⁻¹. The tissue in the collagenase solution was incubated for 1 hour and shaken on an orbital shaker at a constant low speed of 65 rpm, at 37 °C. After digestion, the resulting solution was washed three times with PBS and centrifuged for 10 minutes at 250 g. The cellular pellet obtained after the third wash was resuspended in completed MSC growth medium (MSCGM BulletKit, Lonza) and transferred into the cell culture dishes. After 48 hours, the fibroblast-like cells were separated from the rest of floating debris, rinsed with PBS, and cultured for the next 7 days or until near confluence.

VI.3.11 Cell Encapsulation

Human-derived adipose stem cells (hASCs) were grown as monolayers, as abovementioned, until passage 3-4, when confluent cells were detached from tissue culture flasks using Trypsin (Gibco®, Life Technologies). The resulting diluted cell suspension was centrifuged at 1200 rpm for 5 minutes, forming a cell pellet. After removing the supernatant, 75:25 and 50:50 MnGG-MA/HA with 0.1 M MnCl₂ were mixed with the hASCs pellet, making up a final cellular density of 1×10⁶ cells mL⁻¹. Hydrogels without MnCl₂ were used as controls. After gentle resuspension of the cell pellet in the biomaterial suspension, to assure a homogeneous cell distribution, the cell-laden solution was used to fill a 10 µL Hamilton syringe

coupled with a 31 G needle (inner \varnothing 133 μ m). The syringe was then placed on a stereotaxic syringe pump and the pre-gel solutions injected into aCSF, using a 10 μ L min⁻¹ extrusion rate, forming hydrogel fibers. After 5 minutes, aCSF was replaced by 500 μ L of cell culture media. Thence, 24-well plates, with 10 μ L of gel per well, were incubated for 1 and 7 days at 37 °C in a humidified air atmosphere of 5% CO₂. Fibers were also obtained using a 1 mL syringe coupled with an 18G needle (inner \varnothing 840 μ m), using a 1 mL min⁻¹ extrusion rate. All the materials and solutions were sterilized by filtration (0.22 μ m filter) before cell *in vitro* and *in vivo* assays, excluding dry GG-MA that was sterilized by UV light for 30 minutes in a laminar flow hood.

VI.3.12 Live/Dead Staining

LIVE/DEAD Viability/Cytotoxicity Kit for mammalian cells (ThermoFisher Scientific) was used to perform a Live/Dead assay, where calcein-AM stained live cells and ethidium homodimer-1 (EthD-1) stain dead cells. At each time-point, the culture medium was removed, and a solution containing 150 μ L of Calcein and EthD-1 diluted in PBS (0.5 μ L of Calcein-AM and 2 μ L of EthD-1 per 1mL PBS) was added to each well, followed by sample incubation for 20 minutes at room temperature (RT), protected from light. Stained hydrogels were visualized in the dark using a fluorescence microscope Cell Observer SD (Carl Zeiss, Germany) in Z-stack mode, performed at the Laboratory of Advanced Microscopy Techniques, Mossakowski Medical Research Centre, Polish Academy of Sciences. At last, the percentage of live cells in each fiber was calculated using ImageJ software (version 2.0.0-rc-69/1.52p).

VI.3.13 MnGG-MA/HA *In Vivo* Transplantation

All the procedures were performed with the approval of the Ethical Committee (IV Local Committee in Warsaw, 117/2015). The *in vitro* assays were performed using double mutant MBP^{sh1/sh1}/rag2 immunocompromised mice, a typical demyelination model. Before the surgical procedure, all animals were anesthetized with 1.5-2% isoflurane in oxygen and placed in the stereotaxic frame in a concord-like position [33]. A small incision was then made in the midline at the posterior aspect of the skull, and muscles were separated to expose the atlanto-occipital membrane. Hydrogels made of 75:25 MnGG-MA/HA with 0.1 M MnCl₂, prepared as described above, were placed in a Hamilton syringe and injected into the intrathecal space with a speed of 10 μ L min⁻¹. After injection, the needle was left in the same place for an additional 1 minute and then slowly withdrawn. Afterward, the skin was sutured, and the animal was placed in the MRI scanner.

VI.3.14 Magnetic Resonance Imaging - Phantom Imaging

Tripilot scan was followed by T1 parametric imaging with the 2D Saturation Recovery Spin Echo Sequence with varying repetition times (TR = 200 ms ... 8000 ms, TE = 9.5 ms, rare factor = 2, NA = 1, FOV = 75 mm × 75 mm, 5 slices 2.0 mm thick with 2.0 mm gaps, spatial resolution = 586 μm × 586 μm, scan time ~13 min) and T2 parametric imaging with the MSME sequence (TR = 5000 ms, TE = 15 ms ... 480 ms, NA = 1, FOV = 75 mm × 75 mm, 5 slices 2.0 mm thick with 2.0 mm gaps, spatial resolution = 586 μm × 586 μm, scan time ~8 min). To evaluate the relative magnetic resonance signal of T1-weighted imaging of MnGG-MA/HA phantoms with different concentrations of manganese ions, identical regions of interest (ROI) were outlined on MR images, and the signal intensity was measured with the use of ImageJ software.

VI.3.15 Magnetic Resonance Imaging – *In Vivo* Imaging

MR imaging was performed immediately after intrathecal and intracerebral implantation of a hydrogel. After intrathecal transplantation, additional MR imaging was performed 24 hours after surgery. For the imaging, animals were anesthetized with isoflurane (1.5-2% in oxygen) and position head prone in MRI-compatible water-heated bed. Body temperature and respiration rate were monitored throughout the study with MRI compatible probes (SA Instruments, Stony Brook, NY, USA). 7T MR scanner (BioSpec 70/30 USR, Bruker, Ettlingen, Germany) equipped with transmit cylindrical radiofrequency coil (8.6 cm inner diameter, Bruker) and a mouse brain dedicated receive-only array surface coil (2x2 elements, Bruker) was used. The structural imaging protocol was performed as we described previously [34]. Briefly, a T1-weighted 3D FLASH sequence (TR = 12 ms; TE = 4 ms; flip angle, FA = 18; NA = 10; field of view, FOV = 15 mm × 15 mm × 15 mm, spatial resolution = 117 μm isotropic, scan time ~25 min) was used. Structural imaging was followed by T1 parametric imaging with the 2D Saturation Recovery Spin Echo Sequence with varying repetition times (TR = 410 ms ... 8000 ms, TE = 22 ms, rare factor = 4, NA = 3, FOV = 20 mm × 20 mm, 8 slices 0.8 mm thick with no gaps, spatial resolution = 156 μm × 156 μm, scan time ~23 min) and T2 parametric imaging with the MSME sequence (TR = 5000 ms, TE = 13 ms ... 416 ms, NA = 1, FOV = 20 mm × 20 mm, 8 slices 0.8 mm thick with no gaps, spatial resolution = 156 μm × 156 μm, scan time ~8 min).

VI.3.16 Statistical Analysis

Results are presented as mean ± standard deviation. When applicable, the experimental data were analyzed using single-factor analysis of variance (One-way ANOVA) to assess the statistical significance of

the results, followed by post hoc Tukey tests. Statistical significance was set at a p-value of ≤ 0.05 . All statistical analysis was performed using GraphPad Prism version 7.0a.

VI.4 Results and Discussion

VI.4.1 Preparation and Characterization of MnGG-MA/HA Hydrogel Blends

VI.4.1.1 Rheology and Injection Ability

Hydrogels blends, prepared from Mn-supplemented methacrylated gellan gum (MnGG-MA), and hyaluronic acid (HA), were prepared and characterized envisioning biomedical applications. Formulations were prepared from 0.75% (w/v) GG-MA solutions supplemented with 0.1 or 1 mM MnCl_2 . The obtained solutions were then mixed with 1% (w/v) HA solutions, using an MnGG-MA to HA ratio of 75:25 and 50:50. First, the hydrogel's rheological properties were evaluated before and after contact with artificial cerebrospinal fluid (aCSF). The contact between the MnGG-MA/HA blends and aCSF lead to an increase in storage (G') and loss (G'') moduli, as plotted in Figure VI-1A. This increase translates into the formation of a crosslinked three-dimensional structure, with viscoelastic gel properties, as confirmed by the higher G' values over G'' . Herein, hydrogel formation, schematically represented in Figure VI-1B, is mainly driven by the presence of cationic species in the aCSF, as Mg^{2+} , K^+ or Na^+ , that interact with the negatively charged groups of GG-MA. As a result, the polymeric chains of GG-MA start to crosslink, finally leading to a stable hydrogel. Indeed, blends with a higher HA content showed lower G' values, which can be attributed to a lower GG-MA content. As aforesaid, only GG-MA is crosslinked by the ions present in the aCSF. Thus, a higher HA to GG-MA ratio hinders the ionic crosslink of GG-MA as the polymeric networks are more dispersed in the HA polymer. However, this difference was only statistically significant for formulations prepared with 0.1 mM MnCl_2 .

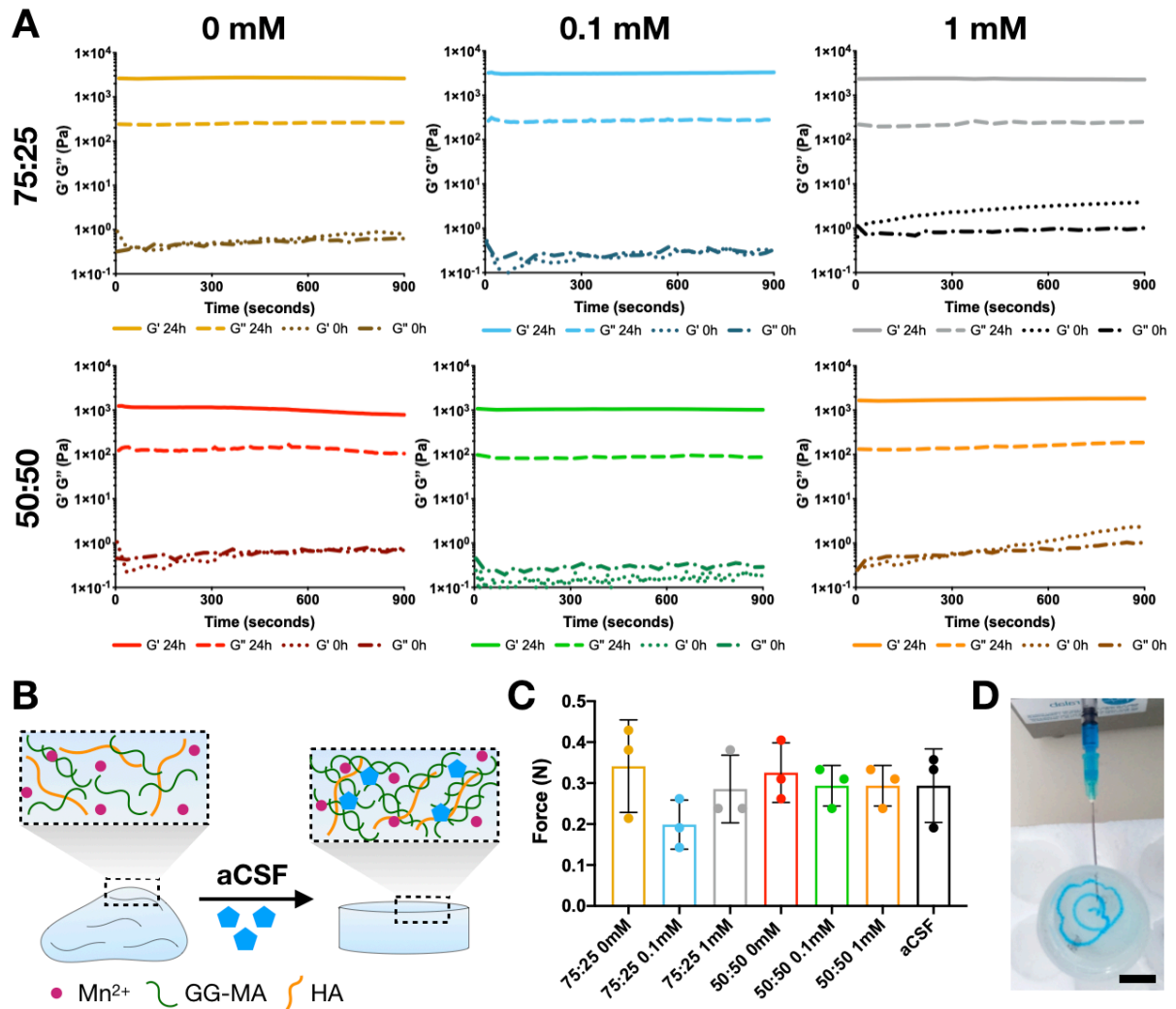


Figure VI-1. Characterization of MnGG-MA/HA hydrogels. A – Rheological characterization of the resulting MnGG-MA/HA hydrogels using different polymeric weight ratios and supplemented with 0.1 or 1 mM $MnCl_2$. Samples without manganese were used as control. Values presented as average. $n=4$; B – Schematic representation of hydrogel's formation upon contact with aCSF; C – Extrusion force (N) measured while injecting different MnGG-MA/HA formulations into aCSF, using a 31G needle. Data presented as average \pm SD, $n=3$; D – Representative image of hydrogel extrusion into aCSF solution. A continuous fiber is formed as the material is extruded. Scale bar: 1 cm.

Regarding the presence of $MnCl_2$, it did not significantly change the viscoelastic properties of the hydrogel blends after crosslinking with aCSF. Regardless, the viscoelastic properties of hydrogel precursor solutions (before aCSF) changed when supplemented with 1mM $MnCl_2$. Both the G' and G'' of these solutions were slightly increased, showing that for this concentration, the presence of Mn^{2+} started to affect the packing of GG-MA polymeric chains. Interestingly, for this condition, it was verified a time dependency of G' and G'' . This dependence, which was more accentuated for G' , can be due to a chain rearrangement of the GG-MA network upon diffusion and distribution of Mn^{2+} throughout the polymeric matrix.

Although the rheological characterization confirmed the hydrogel formation, it is still necessary to ascertain the compatibility of the developed blends with minimally invasive procedures, particularly injection. The force needed to extrude each formulation was monitored while the formulations were injected into a falcon tube filled with aCSF. As depicted in Figure VI-1C, there was no significant difference between the force needed to extrude aCSF and the forces measured in all of the formulations tested. This fact can be attributed to the rapid ionic crosslink that occurs immediately after the contact between the hydrogel precursor and the aCSF. Importantly, the obtained hydrogel does not block the syringe flow, resulting in a continuous hydrogel fiber, as illustrated in Figure VI-1D. This timely crosslink process is of utmost importance on the design of injectable formulation. While rapid crosslink prevents unwanted distribution of hydrogel precursor outside the region of interest, it is still possible to extrude the hydrogel precursor into the fluid, without needle clotting.

VI.4.1.2 Hydrogel Stability

One aspect that must be considered while designing hydrogels for cell delivery is the biomaterial's degradation profile. Although it is crucial to assure a certain degree of degradation that will allow cell proliferation and diffusion to the external environment, it must be assured that such degradation occurs gradually. Intrathecal cell delivery approaches much depend on such steady degradation kinetics to be successful. A rapid hydrogel degradation kinetics can lead to cell deposition at cauda equina after a short period of injection, thus subverting the rationale for using a hydrogel. On the other hand, a stable hydrogel that shows little to no degradation would also impair the therapy, as cells would not be able to reach the spinal cord tissue.

Bearing this in mind, the stability of the developed hydrogels was assessed *in vitro* after immersion in aCSF, with and without hyaluronidase (Figure VI-2). Surprisingly, the presence of hyaluronidase only caused significant changes in the degradation profile of hydrogels prepared using a 50:50 ratio and 1 mM MnCl₂. After the incubation time, *i.e.*, 7 days, 45.19±10.94% of the hydrogel degraded in aCSF, while the degradation percentage for samples incubated with enzyme was, on average, 75.30±3.25%. All other formulations were not affected by the presence of the enzyme, although 50:50 hydrogels showed a trend to degrade faster in such conditions. As expected, the presence of HA fragilizes the polymeric network, allowing its degradation along time. Nevertheless, the hydrogel shows a slow degradation profile due to the presence of GG-MA, a more stable polymer.

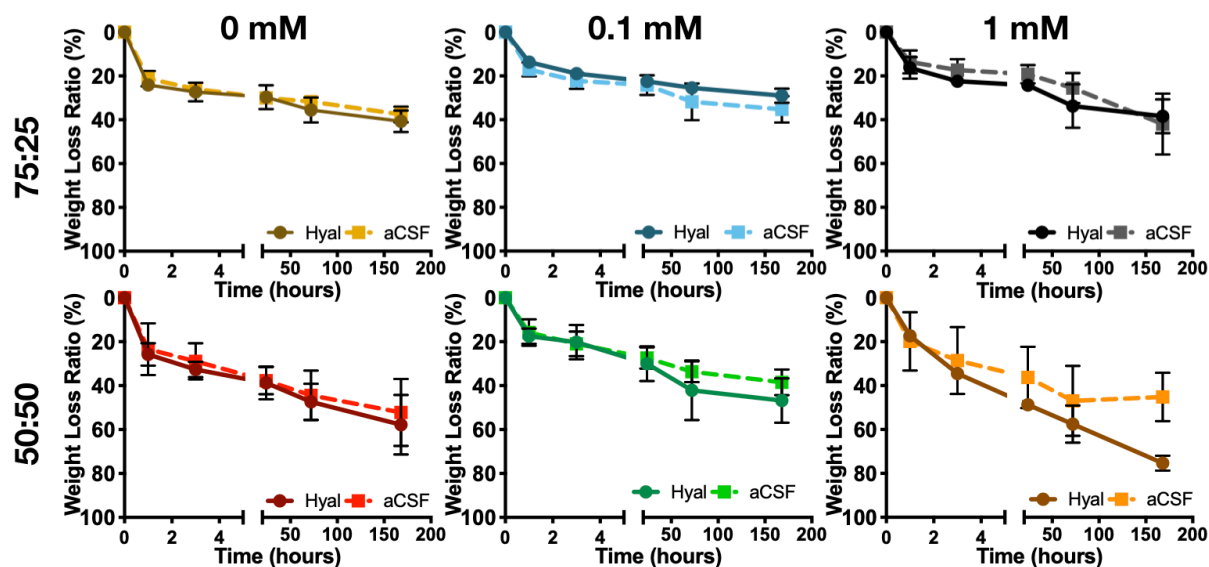


Figure VI-2. Degradation profile of MnGG-MA/HA hydrogels. Degradation profile of different MnGG-MA/HA formulations measured with incubation in aCSF or aCSF supplemented with hyaluronidase (Hyal). Data presented as average \pm SD, n=3.

VI.4.1.3 Hydrogel Permeability

Another essential aspect to consider when designing hydrogels for cell delivery approaches is the permeability of the biomaterial. Besides the diffusion of essential nutrients, it is also necessary to assure that the therapeutic molecules produced by the transplanted cells can reach the central nervous system. It is known that MSCs can exert a neuroprotective role in an ALS scenario, which is highly attributable to the secretion of growth factors as nerve growth factor (NGF, 27 kDa), brain-derived neurotrophic factor (BDNF, 28 kDa), insulin-like growth factor 1 (IGF-1, 7.5 kDa), and vascular endothelial growth factor (VEGF, 20-40 kDa) [35]. Thus, the presence of the hydrogel must not block the diffusion of these factors.

In this regard, the permeability of the different MnGG-MA/HA blends was assessed using a 70 kDa dextran-FITC. As plotted in Figure VI-3A, blends with a ratio of 75:25 allowed a sustained release of dextran for up to 72 hours. The presence of Mn²⁺ did not significantly change the release profile of the model drug, although some differences were noticed in the early time-points. A similar pattern was noticed for the 50:50 hydrogel blends (Figure VI-3B), showing that the presence of a higher amount of HA does not change the permeability of the obtained hydrogels.

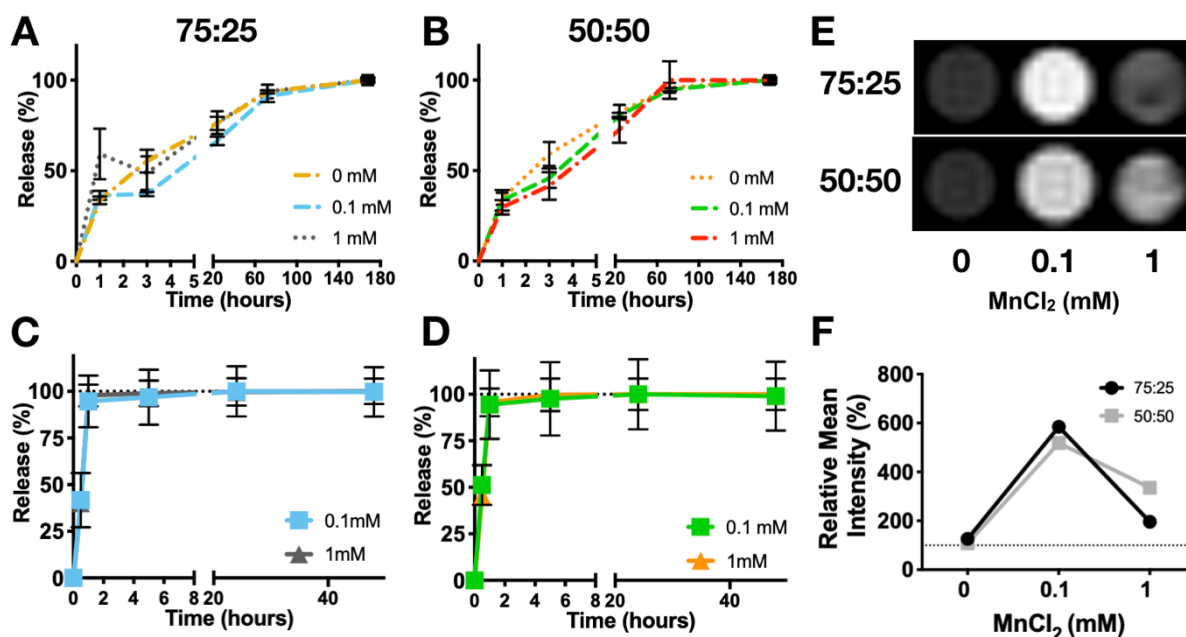


Figure VI-3. Permeability of MnGG-MA/HA hydrogels. A – Release profile of 70 kDa dextran-FITC from hydrogels prepared with 75:25 MnGG-MA/HA hydrogels, supplemented with 0, 0.1 or 1 mM MnCl₂; B - Release profile of 70 kDa dextran-FITC from hydrogels prepared with 50:50 MnGG-MA/HA hydrogels, supplemented with 0, 0.1 or 1 mM MnCl₂; C – Release profile of Mn²⁺ from hydrogels prepared with 75:25 MnGG-MA/HA hydrogels, supplemented with 0.1 or 1 mM MnCl₂; D – Release profile of Mn²⁺ from hydrogels prepared with 50:50 MnGG-MA/HA hydrogels, supplemented with 0.1 or 1 mM MnCl₂; E – T1-weighted MRI phantoms of hydrogels prepared with 75:25 or 50:50 MnGG-MA/HA hydrogels, supplemented with 0, 0.1 or 1 mM MnCl₂; F – Relative mean intensity of the acquired MRI signal.

VI.4.2 MRI Imaging

VI.4.2.1 Manganese Release Profile

One of the primary purposes of the present work is to take advantage of the electrostatic interactions between Mn²⁺ cations and anionic GG-MA, to visualize the resulting hydrogels via MR. Therefore, it is important to understand how long the Mn²⁺ remains inside the hydrogel network and if the ionic concentration is sufficient to retrieve a clear and traceable MRI signal.

First, the release profile of Mn²⁺ was monitored after hydrogels immersion into aCSF. As plotted in Figure VI-3C and Figure VI-3D, Mn²⁺ is released rapidly from hydrogels, independently of the GG-MA to HA ratio. It is expected an ionic substitution of the Mn²⁺ coupled to the GG-MA by the ions present in the aCSF that show a higher affinity to the polymer, particularly Ca²⁺. Indeed, a complete release was observed only after 1 hour of incubation, and no significant differences were noticed regarding the initial Mn²⁺ concentration. As aforesaid, the release profile was monitored only after the contact with aCSF, thus

mimicking what would happen in an *in vivo* scenario. That means a time-frame window of nearly 1 hour, where it would be possible to track hydrogel's administration, placement, and biodistribution effectively.

Although the release profile of Mn^{2+} was similar for all formulations, it must be noticed that the final amount of Mn^{2+} in aCSF is different due to the different initial concentrations of $MnCl_2$ used. Such fact may result in distinct MRI signals, which was confirmed by MRI imaging of different hydrogel phantoms. Figure VI-3E shows T1-weighted MRI images retrieved from hydrogels placed into Eppendorf's filled with aCSF. Hydrogels prepared with 0.1 mM $MnCl_2$ result in a more intense MRI signal, as confirmed by the signal quantification (Figure VI-3F). Interestingly, higher concentrations resulted in a saturated, less intense signal, and therefore harder to detect. Besides Mn^{2+} concentration, also the ratio between MnGG-MA and HA impacted the detected MRI signal. In this regard, hydrogels with a 75:25 ratio showed a slightly better MR signal compared to the hydrogel prepared with a 50:50 ratio.

Formulations prepared by means of using 1 mM $MnCl_2$ showed a higher signal in a 50:50 ratio than in 75:25. Considering that the final hydrogels are obtained using MnGG-MA previously prepared, the final Mn^{2+} concentration is lower in 50:50 blends. Thus, the signal is less saturated on these blends, as compared to 75:25.

VI.4.3 *In Vivo* Magnetic Resonance Imaging

The possibility to track the obtained hydrogels was also validated *in vivo*, upon intrathecal injection of the hydrogels in double mutant $MBP^{shi/shi}/rag2$ immunocompromised mice. In light of the previous results, this assay was performed using 75:25 MnGG-MA/HA blends prepared with 0.1 mM $MnCl_2$.

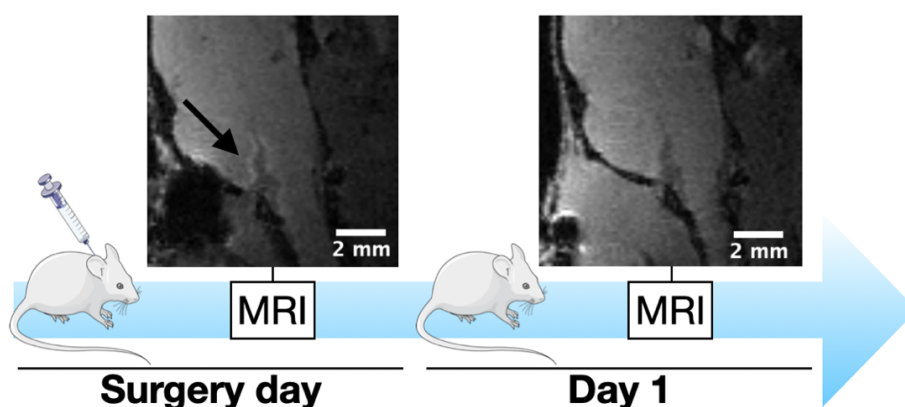


Figure VI-4. Magnetic resonance T1 weighted imaging of MnGG-MA/HA hydrogels. Hyperintense signal (arrow) on MR image corresponds to MnGG-MA/HA hydrogel directly after intrathecal transplantation in shiverer mice. After 1 day of surgery, the hydrogels are not detectable on the MR scans. Scale bar: 2 mm.

After injection, it was possible to visualize the hydrogels within the intrathecal space, visible as a hyperintense signal in T1 MRI, as shown in Figure VI-4. As expected from the *in vitro* results, the MR signal is lost 24 hours *post*transplantation (Figure VI-4, Day 1). In mice, the total CSF volume, near 40 μL , turn over near 12-13 time per day [36]. Therefore, the Mn^{2+} released from the hydrogels starts to dissolve due to CSF circulation, decreasing the MRI signal due to probe dilution. The rapid release and dilution of Mn^{2+} into the CSF avoids a local accumulation of this ion near the CNS structures, thus preventing the occurrence of harmful Mn-induced toxicity [37].

VI.4.4 hASCs Encapsulation and Viability

Bearing in mind the results obtained while studying the MR signal, cell studies were performed using hydrogels prepared with 75:25 MnGG-MA/HA blends supplemented with 0.1 mM MnCl_2 . Cell-laden fibers were obtained by direct hydrogel extrusion into aCSF solution, followed by incubation in a suitable cell culture media. Cell viability was then assessed by live/dead staining at different time-points (Figure VI-5A).

First, cell viability was studied using human-derived adipose stem cells (hASCs) encapsulated in hydrogel fibers obtained with a 31G needle, a frequent setup in small animal studies. After 1 day of incubation, $79.27 \pm 7.52\%$ of cells remained viable, and no statistical differences were noticed along the 14 days of study (Figure VI-5B and Figure VI-5C). The presence of MnCl_2 did not impair cell viability, as similar values were measured for fibers prepared without this constituent (Figure VI-5G and Figure VI-5H). Remarkably, after 14 days of incubation, it was possible to observe cell growth as a monolayer at the well bottom, thus confirming the feasibility of using the developed hydrogels as cell delivery carriers.

Besides the injection via a 31G needle, cell viability was evaluated after extrusion with an 18G needle, foreseeing studies using large-animal models. As expected, fiber diameter was larger ($886.11 \pm 30.55 \mu\text{m}$ vs. $189.13 \pm 36.80 \mu\text{m}$), but their size was still compatible with the rapid ionic crosslink observed for smaller fibers. Regarding cell viability, the extrusion with an 18G needle revealed superior viability after 1 day of incubation ($87.94 \pm 5.48\%$), as depicted in Figure VI-5D and Figure VI-5E. Also, an increase in this parameter was noticed along the culture time, with measured cell viability of $95.29 \pm 1.32\%$ after 7 days of culturing. Compared to a 31G needle, the mechanical stress caused on cells by an 18G needle is smaller, leading to a high cell viability and recovery rate [38]. Similar to what was observed with the thinner fibers, cells were also able to escape from the hydrogel. However, the cell escape was noticed earlier, after only 7 days of culture (Figure VI-5F), which can be attributed to the higher cell cargo obtained with these fibers.

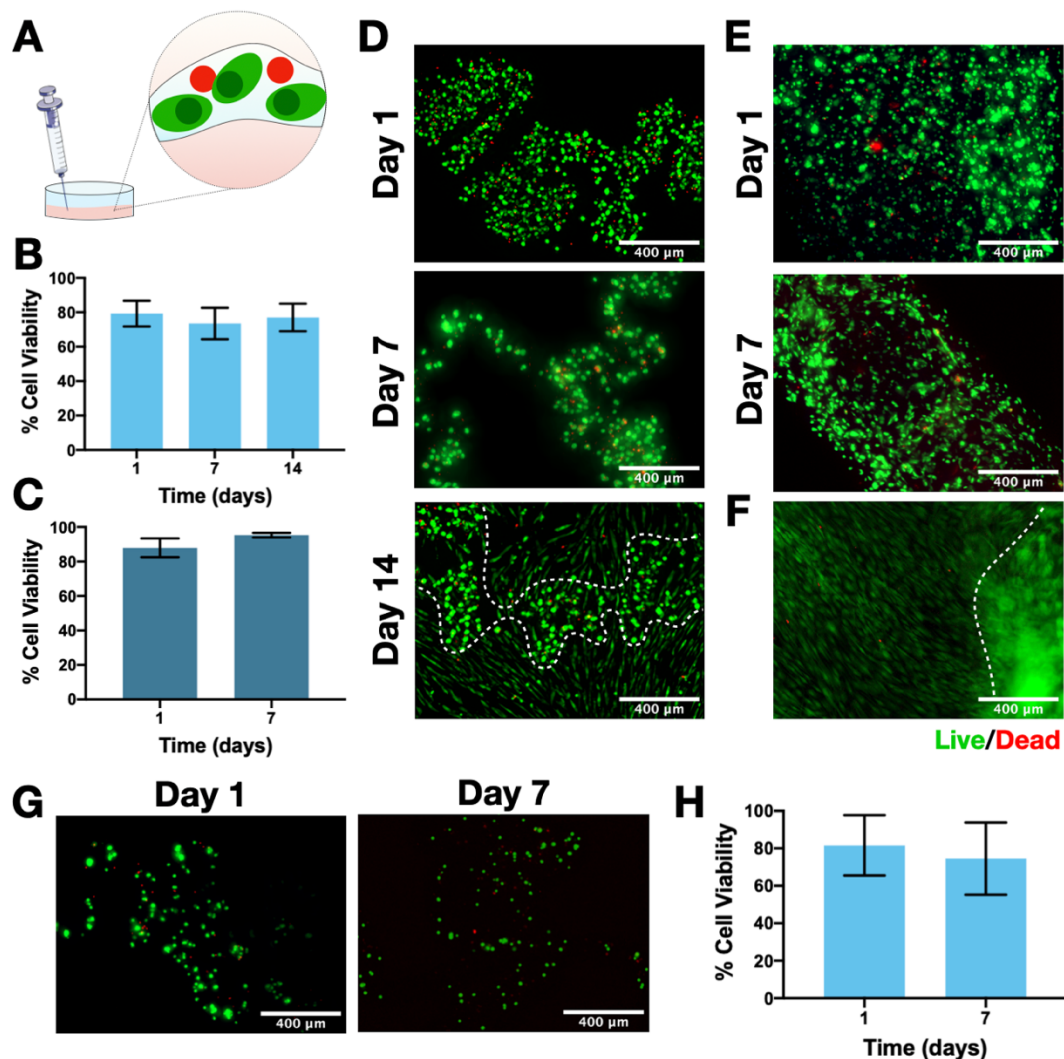


Figure VI-5. Cell encapsulation within MnGG-MA/HA hydrogel fibers. A – Schematic representation of the experimental setup, showing the direct extrusion of cell-laden hydrogels into aCSF. Fibers are then cultured for different periods of time and cell viability assessed by means of Live/dead staining; B – Cell viability after 1, 7 and 14 days of culture in hydrogels prepared with 75:25 MnGG-MA/HA and 0.1 mM MnCl₂ using a Hamilton syringe coupled with a 31G needle. Results presented as average±SD, n=3; C – Cell viability after 1 and 7 days of culture in hydrogels prepared with 75:25 MnGG-MA/HA and 0.1 mM MnCl₂ and extruded using an 18G needle. Results presented as average±SD, n=3; D - Fluorescence microscopy images of hydrogels extruded from a 31G needle after live/dead staining 1,7, and 14 days post extrusion. E - Fluorescence microscopy images of hydrogels extruded from an 18G needle after live/dead staining at 1- and 7-days post extrusion. F – Confluent hASCs present at the bottom of the well after 7 days of incubation, showing cell extrusion capacity. Live cells showed as green and dead cells as red. Scale bar: 400 μm; G - Fluorescence microscopy images of Live/dead staining of hASCs encapsulated in MnGG-MA/HA hydrogels without MnCl₂ after 1 and 7 days of incubation. Live cells showed as green and dead cells as red. Scale bar: 400 μm; H - Cell viability of hASCs encapsulated in MnGG-MA/HA hydrogels without MnCl₂ after 1 and 7 days of culture (average±SD, n=3).

VI.5 Conclusion

This work explores the potential of hydrogels as cell delivery vehicles and imaging probes. Particularly, a hydrogel blend prepared from methacrylated gellan gum and hyaluronic acid was supplemented with paramagnetic Mn^{2+} ions that are suitable markers for magnetic resonance imaging. The affinity between the gellan gum network and the divalent manganese ions allowed the use of this polymeric hydrogel as a manganese reservoir, thus permitting the real-time visualization of the hydrogels by magnetic resonance imaging. Additionally, the rapid ionic crosslink of gellan gum makes the developed hydrogel highly suitable for minimally invasive procedures, such as intrathecal injection. Overall, the hydrogel was successfully injected in the intrathecal space of a small-model animal, the double mutant $MBP^{shi/shi}/rag2$ immunocompromised mice, and it could be traced by T1-weighted magnetic resonance imaging. Also, the resulting hydrogel showed to be compatible with the encapsulation of human-derived adipose stem cells that remained viable upon hydrogel extrusion with needles with different diameters. The presence of hyaluronic acid allowed a timely hydrogel degradation, crucial for cell escape from the hydrogel to the external environment. Therefore, the hydrogels developed in this work hold great potential for image-guided neuro-procedures, particularly minimal invasive interventions for cell-based therapy.

VI.6 Conflict of Interest

The authors declare no conflict of interest.

VI.7 Acknowledgments

Silvia Vieira acknowledges FCT PhD scholarship (SFRH/BD/102710/2014). The FCT distinction attributed to J. Miguel Oliveira under the Investigator FCT program (IF/01285/2015) and J. Silva-Correia (IF/00115/2015) are also greatly acknowledged. The authors also acknowledge the funds provided under the project NanoTech4ALS, funded under the EU FP7 M-ERA.NET program, and ESF (POWR.03.02.00-00-I028/17-00).

VI.8 References

1. Hardiman, O., et al., *Amyotrophic lateral sclerosis*. Nat Rev Dis Primers, 2017. **3**: p. 17071.
2. Longinetti, E. and F. Fang, *Epidemiology of amyotrophic lateral sclerosis: an update of recent literature*. Current Opinion in Neurology, 2019. **32**(5): p. 771-776.
3. Mathis, S., et al., *Genetics of amyotrophic lateral sclerosis: A review*. Journal of the Neurological Sciences, 2019. **399**: p. 217-226.
4. Arthur, K.C., et al., *Projected increase in amyotrophic lateral sclerosis from 2015 to 2040*. Nature Communications, 2016. **7**: p. 12408.
5. Baloh, R.H., J.D. Glass, and C.N. Svendsen, *Stem cell transplantation for amyotrophic lateral sclerosis*. Current Opinion in Neurology, 2018. **31**(5): p. 655-661.
6. Mao, Z., S. Zhang, and H. Chen, *Stem cell therapy for amyotrophic lateral sclerosis*. Cell Regeneration, 2015. **4**: p. 11.
7. Oh, K.W., et al., *Repeated Intrathecal Mesenchymal Stem Cells for Amyotrophic Lateral Sclerosis*. Annals of Neurology, 2018. **84**(3): p. 361-373.
8. Petrou, P., et al., *Safety and Clinical Effects of Mesenchymal Stem Cells Secreting Neurotrophic Factor Transplantation in Patients With Amyotrophic Lateral Sclerosis: Results of Phase 1/2 and 2a Clinical Trials*. JAMA Neurology, 2016. **73**(3): p. 337-44.
9. Sykova, E., et al., *Transplantation of Mesenchymal Stromal Cells in Patients With Amyotrophic Lateral Sclerosis: Results of Phase I/IIa Clinical Trial*. Cell Transplantation, 2017. **26**(4): p. 647-658.
10. Lewis, C.M. and M. Suzuki, *Therapeutic applications of mesenchymal stem cells for amyotrophic lateral sclerosis*. Stem Cell Research & Therapy, 2014. **5**(2): p. 32.
11. Bonafede, R. and R. Mariotti, *ALS Pathogenesis and Therapeutic Approaches: The Role of Mesenchymal Stem Cells and Extracellular Vesicles*. Frontiers in Cellular Neuroscience, 2017. **11**: p. 80.
12. Forostyak, S. and E. Sykova, *Neuroprotective Potential of Cell-Based Therapies in ALS: From Bench to Bedside*. Frontiers in Neuroscience, 2017. **11**: p. 591.
13. Forostyak, S., et al., *Intrathecal delivery of mesenchymal stromal cells protects the structure of altered perineuronal nets in SOD1 rats and amends the course of ALS*. Stem Cells, 2014. **32**(12): p. 3163-72.
14. Aebischer, P., et al., *Intrathecal delivery of CNTF using encapsulated genetically modified xenogeneic cells in amyotrophic lateral sclerosis patients*. Nature Medicine, 1996. **2**(6): p. 696-9.
15. Yan, L., et al., *Intrathecal delivery of human ESC-derived mesenchymal stem cell spheres promotes recovery of a primate multiple sclerosis model*. Cell Death Discovery, 2018. **4**: p. 28.

16. Ciervo, Y., et al., *Advances, challenges and future directions for stem cell therapy in amyotrophic lateral sclerosis*. *Molecular Neurodegeneration*, 2017. **12**(1): p. 85.
17. Barczewska, M., et al., *Safety of intrathecal injection of Wharton's jelly-derived mesenchymal stem cells in amyotrophic lateral sclerosis therapy*. *Neural Regeneration Research*, 2019. **14**(2): p. 313-318.
18. Oliveira, J.M., et al., *Hydrogel-based scaffolds to support intrathecal stem cell transplantation as a gateway to the spinal cord: clinical needs, biomaterials, and imaging technologies*. *npj Regenerative Medicine*, 2018. **3**: p. 8.
19. Malysz-Cymborska, I., et al., *MRI-guided intrathecal transplantation of hydrogel-embedded glial progenitors in large animals*. *Scientific Reports*, 2018. **8**(1): p. 16490.
20. Hall, W.A., *Magnetic resonance imaging in neurointervention*. *Topics in Magnetic Resonance Imaging*, 2009. **19**(4): p. 177.
21. Walczak, P., et al., *Real-time MRI for precise and predictable intra-arterial stem cell delivery to the central nervous system*. *Journal of Cerebral Blood Flow and Metabolism*, 2017. **37**(7): p. 2346-2358.
22. Ohno, K., et al., *Kinetics and MR-Based Monitoring of AAV9 Vector Delivery into Cerebrospinal Fluid of Nonhuman Primates*. *Molecular Therapy-Methods & Clinical Development*, 2019. **13**: p. 47-54.
23. Hladky, S.B. and M.A. Barrand, *Fluid and ion transfer across the blood-brain and blood-cerebrospinal fluid barriers; a comparative account of mechanisms and roles*. *Fluids and Barriers of the CNS*, 2016. **13**(1): p. 19.
24. Silva-Correia, J., et al., *Biocompatibility evaluation of ionic- and photo-crosslinked methacrylated gellan gum hydrogels: in vitro and in vivo study*. *Advanced Healthcare Materials*, 2013. **2**(4): p. 568-75.
25. Oliveira, J.T., et al., *Gellan gum: a new biomaterial for cartilage tissue engineering applications*. *Journal of Biomedical Materials Research Part A*. **93**(3): p. 852-63.
26. Dicker, K.T., et al., *Hyaluronan: a simple polysaccharide with diverse biological functions*. *Acta Biomaterialia*, 2014. **10**(4): p. 1558-70.
27. Zamboni, F., et al., *The potential of hyaluronic acid in immunoprotection and immunomodulation: Chemistry, processing and function*. *Progress in Materials Science*, 2018. **97**: p. 97-122.
28. Burdick, J.A. and G.D. Prestwich, *Hyaluronic acid hydrogels for biomedical applications*. *Advanced Materials*, 2011. **23**(12): p. H41-56.
29. Addisu, K.D., et al., *Bioinspired, Manganese-Chelated Alginate-Polydopamine Nanomaterials for Efficient in Vivo T1-Weighted Magnetic Resonance Imaging*. *ACS Applied Materials and Interfaces*, 2018. **10**(6): p. 5147-5160.

30. Brzozowski, P., et al., *Gellan gum-based gels with tunable relaxation properties for MRI phantoms*. Magnetic Resonance Imaging, 2019. **57**: p. 40-49.
31. Gale, E.M., et al., *A Manganese-based Alternative to Gadolinium: Contrast-enhanced MR Angiography, Excretion, Pharmacokinetics, and Metabolism*. Radiology, 2018. **286**(3): p. 865-872.
32. Silva-Correia, J., et al., *Gellan gum-based hydrogels for intervertebral disc tissue-engineering applications*. Journal of Tissue Engineering and Regenerative Medicine, 2011. **5**(6): p. e97-107.
33. Janowski, M., et al., *Neurotransplantation in mice: The concordance-like position ensures minimal cell leakage and widespread distribution of cells transplanted into the cisterna magna*. Neuroscience Letters, 2008. **430**(2): p. 169-174.
34. Fiedorowicz, M., et al., *Anterograde Transport in Axons of the Retinal Ganglion Cells and its Relationship to the Intraocular Pressure during Aging in Mice with Hereditary Pigmentary Glaucoma*. Current Eye Research, 2018. **43**(4): p. 539-546.
35. Gugliandolo, A., P. Bramanti, and E. Mazzon, *Mesenchymal Stem Cells: A Potential Therapeutic Approach for Amyotrophic Lateral Sclerosis?* Stem Cells International, 2019. **2019**: p. 3675627.
36. Simon, M.J. and J.J. Iliff, *Regulation of cerebrospinal fluid (CSF) flow in neurodegenerative, neurovascular and neuroinflammatory disease*. Biochimica et Biophysica Acta (BBA) - Molecular Basis of Disease, 2016. **1862**(3): p. 442-51.
37. Ding, D., J. Roth, and R. Salvi, *Manganese is toxic to spiral ganglion neurons and hair cells in vitro*. Neurotoxicology, 2011. **32**(2): p. 233-41.
38. Chang, R., J. Nam, and W. Sun, *Effects of dispensing pressure and nozzle diameter on cell survival from solid freeform fabrication-based direct cell writing*. Tissue Engineering Part A, 2008. **14**(1): p. 41-8.

Chapter VII: Composition Comprising Polyelectrolyte Complexes, Methods and Uses Thereof*

ABSTRACT

The present disclosure relates to a composition of at least one predominantly positively charged polyelectrolyte polymer and at least one predominantly negatively charged polyelectrolyte polymer, a preferred composition comprises poly-L-lysine and a gellan gum, preferably a methacrylate gellan gum.

The present subject-matter further relates to methods for generating composition of the present disclosure and to uses of a mixture according to the disclosure for biomedical applications such as cellular and acellular systems for tissue engineering and regenerative medicine applications or as drug delivery systems, for the treatment of several diseases namely diabetes mellitus.

* This chapter is based on the following publications:

"Composition Comprising Polyelectrolyte Complexes, Methods and Uses Thereof". Vieira S., Silva-Correia J., Oliveira J.M., Reis R.L. Published as WO/2017/089974, EP3380078 (A1) and US20180344652 (B2).

VII.1 Technical Field

The present disclosure relates to a composition of at least one predominantly positively charged polyelectrolyte polymer and at least one predominantly negatively charged polyelectrolyte polymer, a preferred composition comprises poly-L-lysine and a gellan gum (GG), preferably a methacrylate gellan gum (GG-MA).

The present subject-matter further relates to methods for generating composition of the present disclosure and to uses of a mixture according to the disclosure for biomedical applications such as cellular and acellular systems for tissue engineering and regenerative medicine applications or as drug delivery systems (DDS), for the treatment of several diseases namely diabetes mellitus.

VII.2 Background

Polyelectrolyte complexes (PEC) are produced by the interfacial complexation of polyelectrolytes. This process is mainly driven by the electrostatic bonds formed between the two oppositely charged polyelectrolytes. One of the great advantages of this process is its compatibility with mild conditions, namely room temperature, aqueous environment and physiological pH, and its non-deleterious effect on cells or drugs. Thence, cells, drugs, small peptides and others can easily be incorporated in structures produced by polyelectrolyte complexation without compromising their viability and bioactivity. PEC shape and size is easily adjustable (e.g. capsules (3D), fibers, membranes (2D), sacs (with an aperture), and microbioreactors) making possible their use on a plethora of biomedical applications. On a tissue engineering perspective, the possibility to include different components – as cells and drugs – into very specific structures is attractive, thus composing a multicomponent system. PEC can then be used alone as scaffolds or in combination with hydrogels as a way to enhance their mechanical properties.

Gellan gum is a linear anionic heteropolysaccharide secreted by the bacteria *Sphingomonas elodea*. Its molecular structure is based in one repeating unit consisting of glucose-glucuronic acid-glucose-rhamnose. In the native form, or high acyl form, two types of acyl substituents are present: acetyl and L-glyceryl. Low acyl gellan gum is obtained through alkaline hydrolysis of native gellan gum, which removes both of the acyl residues. Both forms of gellan gum form hydrogels in presence of metallic ions, and upon temperature decrease.

It is acid and heat resistant and has a free carboxylic group per repeating unit, which can be used for improvement of functionalization. Moreover, the presence of this carboxylic group confers to gellan gum

a negative charge at neutral pH ($pK_a=3.1$). Thus, gellan gum can be combined with positively charged polymers in order to prepare PEC systems.

Poly-L-lysine is a lysine homopolymer. Therefore, it results from the polymerization of a lysine amino acid. Since lysines have two different amines, polymerization process can start either from the amine located at ϵ -carbon (ϵ -polylysine) or from the amine located at the α -carbon (α -polylysine), which applies to poly-L-lysine. Due to the presence of a positively charged hydrophilic amino group, poly-L-lysine is positively charged at physiological pH.

Several patent documents are based on the application of PEC for different purposes, including cell encapsulation.

Document US5334640 refers to crosslinked biocompatible compositions comprising an ionically crosslinked component and a covalently crosslinked component for encapsulating biologic compounds. Crosslinkable mixtures and method are also disclosed.

Document WO 2013133705 A1 relates to a composition comprising a polyelectrolyte complex and comprising at least one biocide. A preferred composition comprises lignosulfonate and chitosan. The document further relates to methods for generating a composition and to uses of a mixture for protecting an agricultural plant or plant part against a pathogen.

Document US9005662 B2 describes a polyelectrolyte complex comprising an interpenetrating network. The polyelectrolyte complex further comprises a plurality of closed-shell pores, having at least one average transverse dimension between about 100 nanometers and about 1000 micrometers.

Document WO 2000001373 A1 defines a method for encapsulating a core material within a capsule having a permeable or semipermeable membrane. A complex formation reaction between oppositely charged polymers is used wherein one of the polymers is an oligosaccharide such as chitosan and the reaction is carried out at a pH between about 6.6 and 7.5.

Document WO 2004032881 A3 relates to compositions for treating a disease by implanting encapsulated biological material into a patient. The components of the used coatings can include natural and synthetic polymers, macromers, accelerants, co-catalysts, photo-initiators, and radiation and can be manipulated in order to obtain different degrees of biocompatibility, protein diffusivity characteristics, strength, and biodegradability.

These facts are disclosed in order to illustrate the technical problem addressed by the present disclosure.

VII.3 General Description

The present disclosure provides a PEC systems based on gellan gum and poly-L-lysine. These systems may be processed with different architectures, including capsules, micro- and nanofibers, membranes, sacs with inner micro-nanofibers or hydrogels, and microbioreactors, and it is useful for tissue engineering and regenerative medicine applications, as well as for drug delivery.

Taking advantage of self-assembly processes, as the aforementioned PEC, it is possible to develop stable materials with specific tailored design. As they are oppositely charged, in particular gellan gum and poly-L-lysine can be used as platform to obtain self-assembly PEC systems.

Herein, it is disclosed the use of a gellan gum-based polyelectrolyte complex that can be applied for cell encapsulation purposes. Although a number of hydrogel systems based in natural polymers (e.g., alginate and chitosan) have been developed to tackle cell encapsulation, they still present several problems such as variability of production, poor nutrient supply, insufficient mechanical properties or desired stability and tuned permeability to cells. Using the aforesaid PEC, it is possible to construct a thin membrane with adjusted permeability that surrounds a biocompatible core, preferably liquefied. This membrane allows the inflow of essential nutrients and oxygen and outflow of cell waste and metabolites while blocking the recognition by immune cells. This immunoprotective device permits cell transplantation-based therapies without the using of deleterious immunosuppression drugs.

One aspect of the present subject-matter discloses a composition for use in veterinary or in human medicine comprising a polyelectrolyte complex comprising a cationic polymer, poly-L-lysine, and a gellan gum.

In one embodiment for better results, the polyelectrolyte complex material of the present subject-matter may comprise a gellan gum and a poly-L-lysine. In particular suitable for tissue engineering and regenerative medicine applications or as drug delivery systems.

In one embodiment for better results, the composition of the present subject-matter may comprise 0.05-1% (w/v) of poly-L-lysine, 0.5-10% (w/v) of gellan gum.

In other embodiment for better results, the composition of the present subject-matter may comprise 0.05-0.1% (w/v) of poly-L-lysine, 0.5-3% (w/v) of gellan gum. Preferably 0.5-1.5% (w/v) of gellan gum; more preferably, 0.5-1.5% (w/v) of low acyl GG.

In other embodiment for better results the gellan gum may be a low-acyl gellan gum, a high-acyl gellan gum, a methacrylated gellan gum, and combinations thereof.

In another embodiment for better results the gellan gum acylation degree may be from no acyl groups up to two acyl substituents - acetate and glycerate - both located on the same glucose residue.

In another embodiment for better results the gellan gum acylation degree may be one glycerate per repeat and one acetate per every two repeats.

In another embodiment for better results the methacrylated gellan gum may comprises a methacrylation degree up to 10%, preferably between 0.5-5%, more preferably 1-3%, even more preferably 1-1.5%. Formulations of gellan gum with different degrees of acylation (from low to high) and poly-L-lysine serve as precursor materials. When in contact, these materials interact and form a stable polyelectrolyte complex material with tunable shape and size. The material can be then tailored to form capsules to withstand the encapsulation of human and animal cells and/or drugs; fibers; 3D structures or scaffolds; micro- or nanoparticles; and any combination thereof.

In other embodiment for better results the gellan gum molecular weight may be between $5-10 \times 10^4$ Da (methacrylated), $2-3 \times 10^5$ Da (low acyl) and $1-2 \times 10^6$ Da (high acyl).

In another embodiment for better results the poly-L-lysine molecular weight may be between 30-500 kDa, preferably between 70-300 kDa. By varying the molecular weight of gellan gum and poly-L-lysine it is possible to adjust both biological and physicochemical properties (such as strength, flexibility, softness, degradability, chemical resistance and permeability) of the polyelectrolyte complex material, to meet specific needs.

In another embodiment for better results the composition of the present disclosure may further comprise an anti-inflammatory agent, an antiseptic agent, an antipyretic agent, an anesthetic agent, a therapeutic agent, a biological cell, a biological tissue and combinations thereof. Preferably, may comprise an animal or human cell, or stem cell, or combinations thereof. More preferably, may comprise an animal or human pancreatic β -cell.

In another embodiment for better results the composition may further comprise a plurality of hydrogels. More preferably, the second, or more hydrogels, is selected from a list consisting of carbopol, Matrigel®, hyaluronic acid, carboxymethylchitosan, dextran, alginate, collagen, and mixtures thereof.

In another embodiment for better results the composition may further comprise a coupling agent, in particular the coupling agent may be selected from the group consisting of 4-(4,6-dimethoxy-1,3,5-triazin-2-yl)-4-methylmorpholinium chloride, glutaraldehyde, epichlorohydrin, dianhydrides, diamines, and mixtures thereof.

Another aspect of the present invention relates with the use of the composition of the present subject-matter in the treatment of diseases that involve the repair or regeneration of tissues; or the use as a drug delivery system; or use in cell therapy or advanced-therapy medicinal product.

Another aspect of the present invention relates with the use of the composition of the present subject-matter in the treatment or prevention of diabetes; in particular for the treatment of type 1 diabetes mellitus, type 2 diabetes mellitus, or gestational diabetes; or obesity, ageing related-diseases, tumors or pancreatic diseases.

Another aspect of the present invention relates to the use of the composition of the present subject-matter in the treatment or prevention of female infertility, in particular the use of the sac/membranes/capsules for ovarian protection, or for ovarian follicle protection or for oocyte protection.

Another aspect of the present invention relates to capsule, sac, fiber, membrane, or microbio reactors comprising the compositions of the present subject-matter.

In another embodiment the external size of the capsules may be less than 20 mm, in particular up to 3 mm.

In another embodiment the sacs may comprise inner fibers, or hydrogel, or combinations thereof. In particular, the inner fibers are microfibers, or nanofibers or combinations thereof.

Throughout the description and claims the word "comprise" and variations of the word, are not intended to exclude other technical features, additives, components, or steps. Additional objects, advantages and features of the disclosure will become apparent to those skilled in the art upon examination of the description or may be learned by practice of the disclosure. The following examples and drawings are provided by way of illustration, and they are not intended to be limiting of the present disclosure. Furthermore, the present disclosure covers all possible combinations of particular and preferred embodiments described herein.

VII.4 Brief Description of the Drawings

The following figures provide preferred embodiments for illustrating the description and should not be seen as limiting the scope of invention.

Figure VII-1: Schematic representation of a FTIR spectra of (A) GG/PLL complex, (B) GG and (C) PLL.

Figure VII-2: Size comparison of capsules before (black) and after (grey) immersion in distilled water, PBS and DMEM. Different formulations were used to produce the capsules, namely: A - 0.5% GG-LA 0.1% PLL; B – 0.5% GG-LA 0.05% PLL; C – 1% GG-LA 0.1% PLL; D – 1% GG-LA 0.05% PLL; E – 1% GG-MA 0.1% PLL; and F – Size variation after immersion in distilled water, PBS and DMEM as compared to capsules measured before incubation.

Figure VII-3: Pictures of different formulations of GG/PLL capsules, before and after incubation with distilled water, PBS and DMEM. Scale bar = 500 μm .

Figure VII-4: SEM images of GG/PLL capsules at different magnifications. A – 0.5% GG-LA 0.1% PLL after one week in distilled water; B – 1% GG-LA 0.1% PLL after one week in distilled water; C – 1% GG-LA 0.1% PLL after one week in PBS; D – 1% GG-MA 0.1% PLL after one week in distilled water; E – 1% GG-MA 0.1% PLL after one week in DMEM.

Figure VII-5: Live/dead assay on encapsulated androgen-sensitive human prostate adenocarcinoma (LNCaP) cells after 24 hours and 3 days (from left to right).

Figure VII-6: Schematic representation of GG-PLL spheres, and method of obtaining thereof.

Figure VII-7: Characterization of an embodiment of GG microcapsules of the present disclosure, specifically 1% GG-MA 0.1% PLL. A – Micrographs of 1% GG-MA 0.1% PLL capsules immersed in water, PBS or DMEM at 37 °C throughout 14 days; B – SEM images of different magnification of 1% GG-MA 0.1% PLL capsules after 14 days of incubation in PBS (left) or DMEM (right); C – Size of 1% GG-MA 0.1% PLL capsules along the 14 days of incubation. In water, capsules were disrupted after 14 days hampering their measuring; D – Size variation of 1% GG-MA 0.1% PLL capsules as compared to initial capsules (before incubation).

Figure VII-8: Schematic representation of a controlled release of BSA-FITC or Methylene Blue from two different formulations, 1% GG-MA 0.1% PLL capsules and 1% GG-MA 0.05% PLL capsules.

Figure VII-9: Pictures confirming that live cells are found inside the PEC capsules of the present disclosure. Live/dead assay and cytoskeleton analysis by DAPI/Phalloidin staining on human adipose derived stem cells.

VII.5 Detailed Description

The present disclosure provides polyelectrolyte complexes in particular compositions comprising poly-L-lysine and gellan gum, their processing methods and use in the field of tissue engineering and regenerative medicine or drug delivery systems.

Gellan gum is an anionic heteropolysaccharide that form hydrogels in the presence of mono-, di-, and tri-valent ions and exists in two different forms, the high-acyl gellan gum and the low-acyl gellan gum. In high-acyl gellan gum, the acyl residues are located on the periphery of the helix, obstructing the polymer chain association, resulting in soft, elastic and non-brittle gels. In contrast, low-acyl gellan gum produces firm, non-elastic, brittle gels since ions can easily link polymer chains and form a branched network.

Poly-L-lysine is a cationic polymer, synthetically produced, commonly used as a charge enhancer and surface coating for adhesion purposes. It is available on formulations with different molecular weight that can vary from 30-70 kDa (lower molecular weight) to more than 300 kDa (high molecular weight).

Due to the anionic nature of gellan gum, it can be conjugated with other positively charged polymers, in particular poly-L-lysine, forming stable PEC systems.

PEC based on gellan gum and poly-L-lysine are formed by combination of the two compounds at controlled pH and temperature. By varying the components ratio, it was possible to obtain materials with different physicochemical properties. The materials are stable under physiological conditions due to the formed electrostatic bounds. The formation of PEC was verified by Fourier-transform Infra-red (FTIR) analysis performed before and after PEC formation. The biological properties of the obtained material were assessed *in vitro* and using different cell types and cell agglomerates (see embodiments of Figure VII-1 and Figure VII-6).

The final physicochemical and biological properties, as well as the shape, of the PEC systems can be tailored by applying different formulations and processing conditions.

An aspect of the disclosure is to improve both the mechanical performance of gellan gum hydrogel capsules and their permeability to nutrients and cell metabolites. Formulations can use different gellan gum forms and types of poly-L-lysine, *i.e.* with different degrees of acylation and molecular weight that

self-assemble into PEC as a result of their opposite charge. This process allows the production of capsules with tuned physical properties (e.g., strength, softness, flexibility, degradability and permeability to solutes, bioactive molecules and cells) according to the desired use. Along with having adaptable properties, these systems can also provide the advantage of being straightforward, with no need of other chelating agents for capsule formation, and under physiological-like conditions (37 °C and pH 7.4).

In an embodiment, the PEC systems of the present subject-matter used alone or together with cells and/or bioactive molecules, can provide a plethora of potential applications in tissue replacement and regenerative approaches, mostly for cell encapsulation technologies, namely pancreatic cells.

The description of this disclosure is complemented through the following examples that are intended to provide a better understanding of the same, although these examples should not be addressed with a restrictive nature.

Synthesis of PEC system as capsules – In an embodiment, the PEC capsules were prepared by reacting gellan gum with poly-L-lysine. Two commercially available gellan gum were used, namely: 1) low-acyl gellan gum (Sigma, St. Louis, MO, USA) and 2) methacrylated gellan gum (mimsys® G, Irisbiosciences, Portugal). For that, gellan gum solutions, with a final concentration varying from 0.5 to 3% (w/v), were prepared by dissolving the material in distilled water under constant stirring. For low-acyl gellan gum, the solutions were heated until 90 °C to obtain a homogenous dispersion. Then, solutions were cooled down 10 °C above the respective setting temperature.

In an embodiment, PEC capsules were produced as follows: the well-dispersed gellan gum solution was extruded dropwise from a 30G needle into a poly-L-lysine bath (Mw from 30,000 to 300,000, Sigma, St. Louis, MO, USA) using a peristaltic pump to control the flow rate. The formed capsules were maintained on poly-L-lysine solution to allow the formation of a complete PEC membrane, and then transferred to PBS (Phosphate-buffered saline).

Synthesis of PEC system as particles – In an embodiment, the PEC capsules were prepared by reacting gellan gum with poly-L-lysine. Two commercially available gellan gum were used, namely: 1) low-acyl gellan gum (Sigma, St. Louis, MO, USA); and 2) methacrylated gellan gum (mimsys® G, Irisbiosciences, Portugal). For that, gellan gum solutions, with a final concentration varying from 0.5 to 3% (w/v), were prepared by dissolving the material in distilled water under constant stirring. For low-acyl gellan gum, the solutions were heated until 90 °C to obtain a homogenous dispersion. Then, solutions were cooled down 10 °C above the respective setting temperature.

The well-dispersed gellan gum solution can be then extruded dropwise from a 30G needle into a poly-L-lysine bath (Mw from 30,000 to 300,000, Sigma, St. Louis, MO, USA) using a peristaltic pump to control the flow rate. The formed capsules were maintained on poly-L-lysine solution to allow the formation of a complete PEC membrane.

In an embodiment, to obtain particles, as-prepared capsules can be transferred into a 3% CaCl₂ bath to allow the ionic crosslinking of the inner hydrogel. At last, particles were immersed in PBS until further use.

PEC system with encapsulated cells – In an embodiment, the PEC capsules with encapsulated cells were prepared by reacting gellan gum with poly-L-lysine. Two commercially available gellan gum were used, namely: 1) low-acyl gellan gum (Sigma, St. Louis, MO, USA); and 2) methacrylated gellan gum (mimsys[®] G, Irisbiosciences, Portugal). For that, gellan gum solutions, with a final concentration varying from 0.5 to 3% (w/v), were prepared by dissolving the material in distilled water under constant stirring. For low-acyl gellan gum, the solutions were heated until 90 °C to obtain a homogenous dispersion. Then, solutions were cooled down 10 °C above the respective setting temperature.

In an embodiment, cells were carefully mixed with the different gellan gum suspensions and the mix was extruded dropwise from a 30G needle into a poly-L-lysine bath (Mw from 30,000 to 300,000, Sigma, St. Louis, MO, USA) using a peristaltic pump to form capsules. The formed capsules were maintained on poly-L-lysine solution for 10 minutes, to allow the formation of a complete membrane and the resulting PEC capsules with loaded cells.

In an embodiment, PEC capsules can be subsequently cultured together with the previously described growth medium and kept at 37 °C with 5% CO₂ in a standard tissue culture incubator.

In an embodiment, the FTIR spectra of GG/PLL complex of the present disclosure, are present in Figure VII-1 herein (a) is the FTIR spectra of GG/PLL complex of the present disclosure, (b) is the FTIR spectra of GG and (c) is the FTIR spectra of PLL.

An embodiment for measuring the size and morphology of Capsules - Capsules of the present disclosure were placed either in water, PBS (Phosphate-buffered saline) or DMEM (Dulbecco's Modified Eagle Medium) for 1 week. Particles size was measured before and after the environmental change.

As it is possible to observe in Figure VII-3, when in contact with PBS and DMEM particles size decreases for all conditions. Regarding the presence of water, particles size increases for all conditions except when

GG-MA (methacrylated gellan gum) was used. A morphological difference is also noticed when capsules were observed using a magnifying glass (Figure VII-3) and SEM (Figure VII-4).

The observed shrinkage can be a consequence of ionic crosslinking of inner GG-based polymers, that changes the conformation of gellan. Such modification may cause changes on PEC membrane, including the “crease-like” structures observed.

An embodiment of release studies – The albumin-fluorescein isothiocyanate conjugate (albumin-FITC) was used as a model drug to study the release profile from GG/PLL capsules. Briefly, 1% low acyl gellan gum (GG-LA) solution was heated until 90 °C and then cooled to 37 °C. At this point, albumin-FITC (100 µg.mL⁻¹) was added to the hydrogel and the solution was stirred until complete dissolution, under dark conditions. The mixture was then extruded to a 0.1% (w/v) PLL bath using a 30G needle. The resulted capsules were distributed by three different wells, where each well had three capsules immersed in 1.5 mL of PBS. The release of albumin-FITC was tested at 0.5, 1, 2, 3, 4, 5 and 6 hours. At each time point, the supernatant was removed, and equal volume of fresh PBS was added. The fluorescence intensity of 100 µL supernatant of the removed PBS was read by a microplate reader (excitation wavelength at 485/20 nm and the emission wavelength at 528/20) to quantify the albumin-FITC released. The total amount of albumin-FITC incorporated inside the capsules was estimated through their volume.

As depicted in Figure VII-5, during the experiment albumin-FITC was slowly released from de capsules. At last, almost 50% of the albumin present in each well was released.

Live Dead Assay – In an embodiment to evaluate the biocompatibility of GG/PLL capsules, androgen-sensitive human prostate adenocarcinoma cells (LNCaP) cells were mixed with 1% GG-MA, and then extruded to a 0.1% PLL solution. After complexation, particles were washed with PBS and then cultured for three days in RPMI 1640 media, supplemented with 10% FBS and 1% antibiotic/antimycotic.

As depicted in Figure VII-5, the material did not significantly affect cell viability through the three days of experiment. It is also possible to observe a uniform cell distribution within the capsule.

The present disclosure also describes a biomaterial to encapsulate pancreatic islet cells for type I diabetes treatment. The chemical structure of gellan gum (GG), based on a linear anionic heteropolysaccharide, and was exploited to encapsulate cells through its bio-adhesive and thermo-reversible gel properties. Methacrylate, and low acyl forms of GG were studied to obtain gels with different mechanical properties and permeability to biomacromolecules.

At the end, the microcapsule should be able to fully protect the encapsulated cells from the host immune system while allowing the free diffusion of small molecules such as nutrients and oxygen.

In an embodiment, capsules were formed by gravitational dripping, as illustrated in Figure VII-6. Drops with different GG concentrations (0.5, 1 and 1.5% (w/v) of low acyl GG; 1 and 1.5% GG methacrylate (GG-MA)) were extruded from a 30G syringe into a Poly-L-lysine bath (PLL) with two different concentrations: 0.1 and 0.05% (w/v). This results in the formation of spheres due to the interaction between free carboxylic groups of the GG and the PLL amines, forming polyelectrolyte complexes (PEC). Among the tested conditions, 1% (w/v) GG-MA with 0.1% PLL was the most reproducible and easy to manipulate. Therefore, the following experiments were performed using this condition.

In an embodiment morphology of GG microcapsules of the present disclosure, was assessed using both scanning electron microscopy (SEM) and micrographs (Figure VII-8).

In an embodiment, the diameter of the spheres - GG microcapsules of the present disclosure was, on average, 2.3 ± 0.145 mm after production (Figure VII-7C). Then, particles were incubated in water, PBS and DMEM for 14 days at 37 °C to assess the effect of each solution on capsule's size. After the incubation time, it was possible to observe a decrease on spheres diameter of 11% and 14% on capsules incubated respectively with PBS and DMEM (Figure VII-7D). This can be due to the diffusion of ions, present in PBS and DMEM, into the capsules, leading to GG gelation. Furthermore, it was possible to observe the formation of a creases on the surface of these capsules that may result from the tightening of the GG chains as result of the ionic crosslinking. SEM images confirm the presence of the crease-like structures only on the surface of capsules incubated with PBS and DMEM.

In an embodiment, the drug release ability of the PEC capsules was assessed using two model molecules. BSA-FITC, with a molecular weight of approximately 66 kDa, was used as a model of large molecules while Methylene Blue, with a molecular weight of 319.85 Da, was used as a small molecule model.

Both compounds were mixed with the GG solutions before the dripping process. After processing, capsules were incubated in PBS at 37 °C. Solutions with defined concentrations of BSA-FITC and Methylene Blue were also incubated under the same conditions of the samples, to be used as controls. Furthermore, nine as-prepared capsules were randomly separated into three different eppendorfs, and stored at 4 °C with PBS, to be analysed as t=0h samples. At each time point, a sample of the supernatant was retrieved, and the same volume of fresh PBS was added.

The results, presented in Figure VII-8, have shown a controlled release of BSA-FITC (Figure VII-8). Moreover, it was possible to tune capsules' permeability by changing the concentration of PLL. For 0.1% PLL (w/v), capsules have released 37% of the incorporated BSA-FITC while capsules produced using 0.05% PLL (w/v) released 49% of their content. On the other hand, Methylene Blue was rapidly released from the capsules, with all the material being released within 1 hour (Figure VII-9). These results show that PEC capsules have a selective permeability that can be useful for several TE applications.

In an embodiment at last, biocompatibility was also evaluated using human adipose stem cells (hASC). For that, cells were properly mixed in GG-MA solution solutions, at a concentration of 1×10^6 cell.mL⁻¹, and microparticles were produced as stated before. Then, cell viability was studied using a Live/Dead staining, followed by fluorescent microscope observation, after defined timepoints.

As depicted in Figure VII-9, live cells were found inside the PEC capsules after the experimental timeframe.

The results herein presented show the effect of GG-MA and PLL particles disclosed in the present subject-matter for cell encapsulation strategies. These capsules are easy to produce, using one-step only instead of the commonly used alginate-PLL-alginate system. The spheres are stable on culture media (DMEM) and PBS for at least 14 days and are compatible with hASC, since live cells were found after 7 days of culture.

All references recited in this document are incorporated herein in their entirety by reference, as if each and every reference had been incorporated by reference individually.

Those skilled in the art will recognize or be able to ascertain using no more than routine experimentation, many equivalents to the specific embodiments of the invention described herein. The scope of the present invention is not intended to be limited to the above description, but rather is as set forth in the appended claims.

Where singular forms of elements or features are used in the specification of the claims, the plural form is also included, and vice versa, if not specifically excluded. For example, the term "a cell" or "the cell" also includes the plural forms "cells" or "the cells," and vice versa. In the claims, articles such as "a," "an," and "the" may mean one or more than one unless indicated to the contrary or otherwise evident from the context. Claims or descriptions that include "or" between one or more members of a group are considered satisfied if one, more than one, or all of the group members are present in, employed in, or otherwise relevant to a given product or process unless indicated to the contrary or otherwise evident from the context. The invention includes embodiments in which exactly one member of the group is

present in, employed in, or otherwise relevant to a given product or process. The invention also includes embodiments in which more than one, or all of the group members are present in, employed in, or otherwise relevant to a given product or process.

Furthermore, it is to be understood that the invention encompasses all variations, combinations, and permutations in which one or more limitations, elements, clauses, descriptive terms, etc., from one or more of the claims or from relevant portions of the description is introduced into another claim. For example, any claim that is dependent on another claim can be modified to include one or more limitations found in any other claim that is dependent on the same base claim. Furthermore, where the claims recite a composition, it is to be understood that methods of using the composition for any of the purposes disclosed herein are included, and methods of making the composition according to any of the methods of making disclosed herein or other methods known in the art are included, unless otherwise indicated or unless it would be evident to one of ordinary skill in the art that a contradiction or inconsistency would arise.

Where ranges are given, endpoints are included. Furthermore, it is to be understood that unless otherwise indicated or otherwise evident from the context and/or the understanding of one of ordinary skill in the art, values that are expressed as ranges can assume any specific value within the stated ranges in different embodiments of the invention, to the tenth of the unit of the lower limit of the range, unless the context clearly dictates otherwise. It is also to be understood that unless otherwise indicated or otherwise evident from the context and/or the understanding of one of ordinary skill in the art, values expressed as ranges can assume any subrange within the given range, wherein the endpoints of the subrange are expressed to the same degree of accuracy as the tenth of the unit of the lower limit of the range.

The above described embodiments are combinable.

The disclosure should not be seen in any way restricted to the embodiments described and a person with ordinary skill in the art will foresee many possibilities to modifications thereof.

The following claims further set out particular embodiments of the disclosure.

VII.6 Claims

1. A composition comprising gellan gum and poly-L-lysine for use in veterinary or in human medicine.
2. The composition according to the previous claim comprising:
0.05-1% (w/v) of poly-L-lysine,
0.5-10% (w/v) of gellan gum.
3. The composition according to the previous claim comprising:
0.05-0.1% (w/v) of poly-L-lysine,
0.5-3% (w/v) of gellan gum.
4. The composition according to any one of the previous claims wherein the gellan gum is a low-acyl gellan gum, a high-acyl gellan gum, a methacrylated gellan gum, and combinations thereof.
5. The composition according to the previous claim wherein the gellan gum acylation degree is from no acyl groups up to two acyl substituents - acetate and glycerate - both located on the same glucose residue.
6. The composition according to any one of the previous claims wherein the gellan gum acylation degree is one glycerate per repeat and one acetate per every two repeats.
7. The composition according to any of the claims 4-6 wherein the methacrylated gellan gum comprises a methacrylation degree up to 10%, preferably between 0.5-5%.
8. The composition according to the previous claim, wherein the methacrylation degree is between 1-2%.
9. The composition according to any one of the previous claims wherein the gellan gum molecular weight is between 5×10^4 Da to 2×10^6 Da, in particular 5×10^4 Da to 10×10^4 Da.
10. The composition according to any one of the previous claims wherein the poly-L-lysine molecular weight is between 30-500 kDa, preferably between 70-300 kDa.
11. The composition according to any one of the previous claims further comprising an anti-inflammatory agent, an antiseptic agent, an antipyretic agent, an anaesthetic agent, a therapeutic agent, a biological cell, a biological tissue and combinations thereof.

12. The composition according to the previous claim comprising an animal or human cell, or stem cell, or combinations thereof.
13. The composition according to the previous claim comprising an animal or human pancreatic β -cell or androgen-sensitive human prostate adenocarcinoma cell.
14. The composition according to any one of the previous claims comprising human tissue.
15. The composition according to any one of the previous claims further comprising at least a second hydrogel.
16. The composition according to any one of the previous claims wherein the second, or more hydrogels, is selected from a list consisting of carbopol, hyaluronic acid, carboxymethylchitosan, dextran, alginate, collagen, and mixtures thereof.
17. The composition according to any one of the previous claims further comprising a coupling agent.
18. The composition according to any one of the previous claims wherein said coupling agent is selected from the group consisting of 4-(4,6-dimethoxy-1,3,5-triazin-2-yl)-4-methylmorpholinium chloride, glutaraldehyde, epichlorohydrin, dianhydrides, diamines, and mixtures thereof.
19. A composition according to any of the previous claims for use in the treatment or prevention of diseases that involve the repair or regeneration of tissues.
20. A composition according to any of the previous claims for use as a drug delivery system.
21. The composition according to any one of the previous claims wherein the composition is an injectable formulation, in particular an intravenous injection.
22. The composition according to any of the previous claims for use in cell therapy or advanced-therapy medicinal product.
23. The composition according to any of the previous claims for use in the treatment or prevention of diabetes, obesity, ageing-related diseases, tumors or pancreatic diseases.
24. The composition according to any of the previous claims for use in the treatment or prevention of pancreatic cancer.
25. The composition according to any one of the previous claims for the treatment or prevention of female infertility.

26. A capsule, sac, fibre, membrane, or microbioreactor comprising any one of the compositions of the previous claims.
27. The sac according to the previous claim wherein the external size is up to 3 mm.
28. The sac according to any of the claims 25-26 comprising inner fibers, or hydrogel, or combinations thereof.
29. The sac according to any of the claims 25-27, wherein the inner fibers are microfibers, or nanofibers or combinations thereof.
30. The capsule according to claim 25 wherein the external size less than 20 mm.

VII.6.1 Amended Claims (Pursuant to Rule 161(1) and 162 of the European Patent Convention)

1. A composition comprising gellan gum and poly-L-lysine for use in veterinary or in human medicine, wherein the composition comprises:
0.05-0.1% (w/v) of poly-L-lysine,
0.5-3% (w/v) of a methacrylated gellan gum.
2. The composition according to the previous claim, wherein the methacrylated gellan gum comprises a methacrylation degree up to 10%.
3. The composition according to the previous claim, wherein the methacrylation degree is between 0.5-5%.
4. The composition according to the previous claim, wherein the methacrylation degree is between 1-2%.
5. The composition according to any one of the previous claims wherein the gellan gum molecular weight is between 5×10^4 Da to 2×10^6 Da, in particular 5×10^4 Da to 10×10^4 Da.
6. The composition according to any one of the previous claims wherein the poly-L-lysine molecular weight is between 30-500 kDa, preferably between 70-300 kDa.
7. The composition according to any one of the previous claims further comprising an anti-inflammatory agent, an antiseptic agent, an antipyretic agent, an anaesthetic agent, a therapeutic agent, a biological cell, a biological tissue and combinations thereof, preferably an animal or human cell, or stem cell, or combinations thereof.

8. The composition according to the previous claim comprising an animal or human pancreatic β -cell, or androgen-sensitive human prostate adenocarcinoma cell and/or human tissue.
9. The composition according to any one of the previous claims further comprising at least a second hydrogel, preferably wherein the second, or more hydrogels, is selected from a list consisting of carbopol, hyaluronic acid, carboxymethylchitosan, dextran, alginate, collagen, and mixtures thereof.
10. The composition according to any one of the previous claims further comprising a coupling agent, in particular wherein said coupling agent is selected from the group consisting of 4-(4,6-dimethoxy-1,3,5-triazin-2-yl)-4-methylmorpholinium chloride, glutaraldehyde, epichlorohydrin, dianhydrides, diamines, and mixtures thereof.
11. A composition according to any of the previous claims for use in the treatment or prevention of diseases that involve the repair or regeneration of tissues, and/or for use as a drug delivery system, and/or for use in cell therapy or advanced-therapy medicinal product, and/or for use in the treatment or prevention of diabetes, obesity, ageing related-diseases, tumors or pancreatic diseases, and/or for use in the treatment or prevention of pancreatic cancer and/or for use for the treatment or prevention of female infertility.
12. The composition according to any one of the previous claims wherein the composition is an injectable formulation, in particular an intravenous injection.
13. A capsule, sac, fiber, membrane, or microreactor comprising any one of the compositions of the previous claims, preferably wherein the sac has an external size up to 3 mm or preferably wherein the capsule has an external size less than 20 mm.
14. The sac according to the previous claim comprising inner fibers, or hydrogel, or combinations thereof and/or wherein the inner fibers are microfibers, or nanofibers or combinations thereof.

VII.7 Drawings

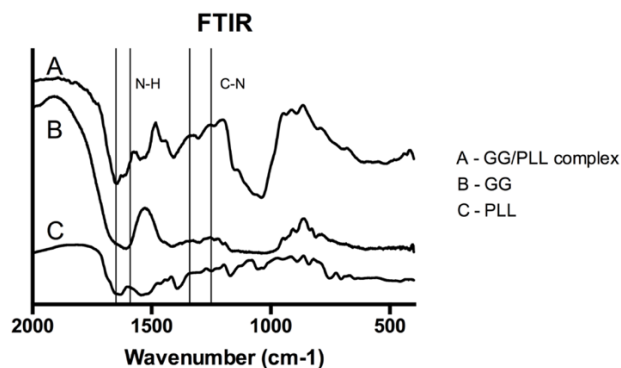


Figure VII-1. Schematic representation of a FTIR spectra. A - GG/PLL complex, B - GG and D - PLL.

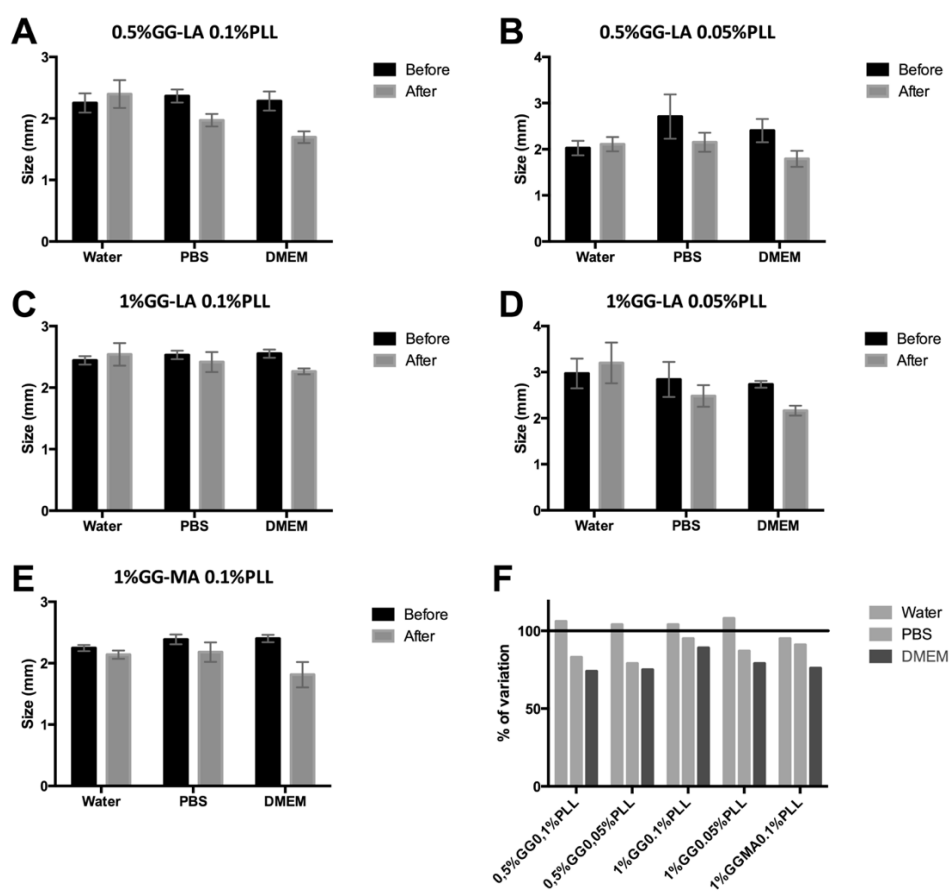


Figure VII-2. Size comparison of capsules before and after immersion in distilled water, PBS and DMEM. Different formulations were used to produce the capsules, namely: A - 0.5% GG-LA 0.1% PLL; B - 0.5%GG-LA 0.05% PLL; C - 1% GG-LA 0.1% PLL; D - 1% GG-LA 0.05% PLL; E - 1% GG-MA 0.1% PLL; and F - Size variation after immersion in distilled water, PBS and DMEM (grey) as compared to capsules measured before incubation (black).

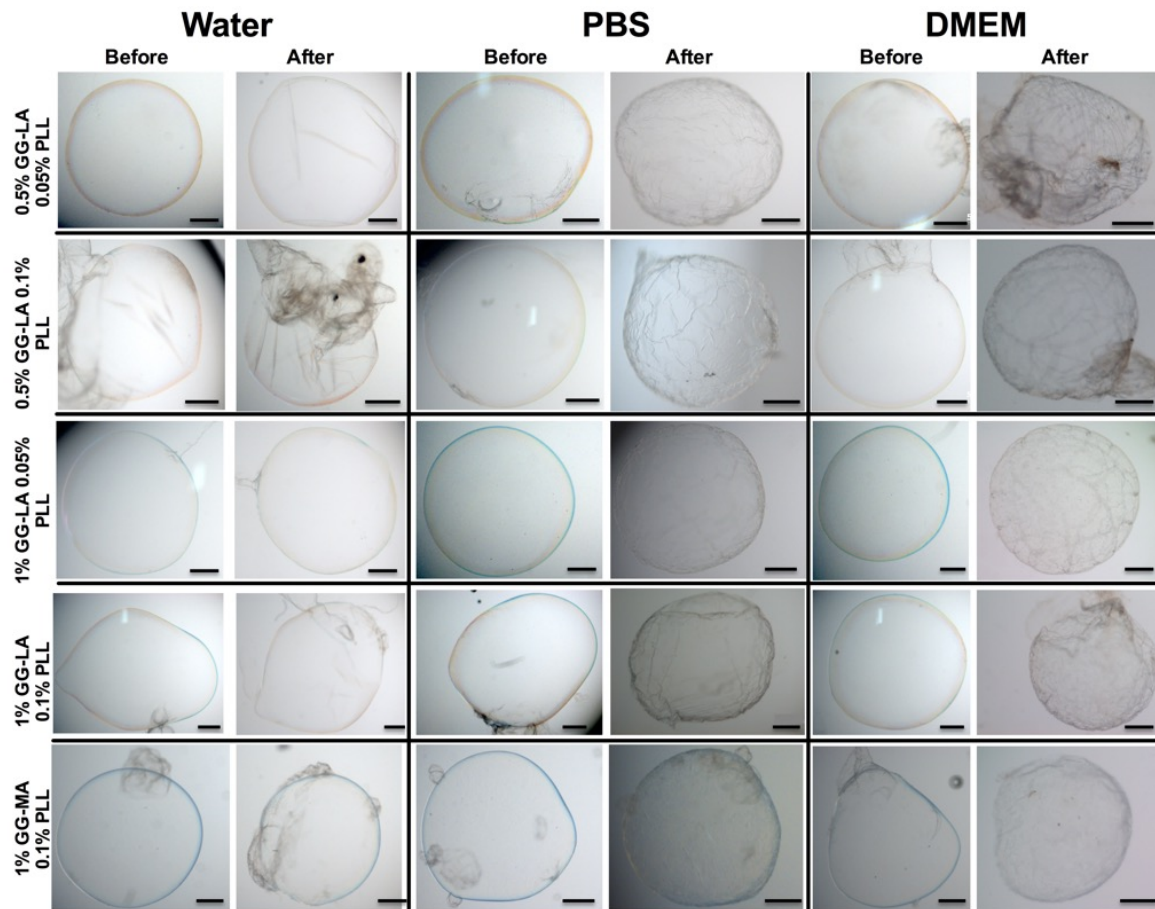


Figure VII-3. Pictures of different formulations of GG/PLL capsules, before and after incubation with distilled water. PBS and DMEM. Scale bar = 500 μ m.

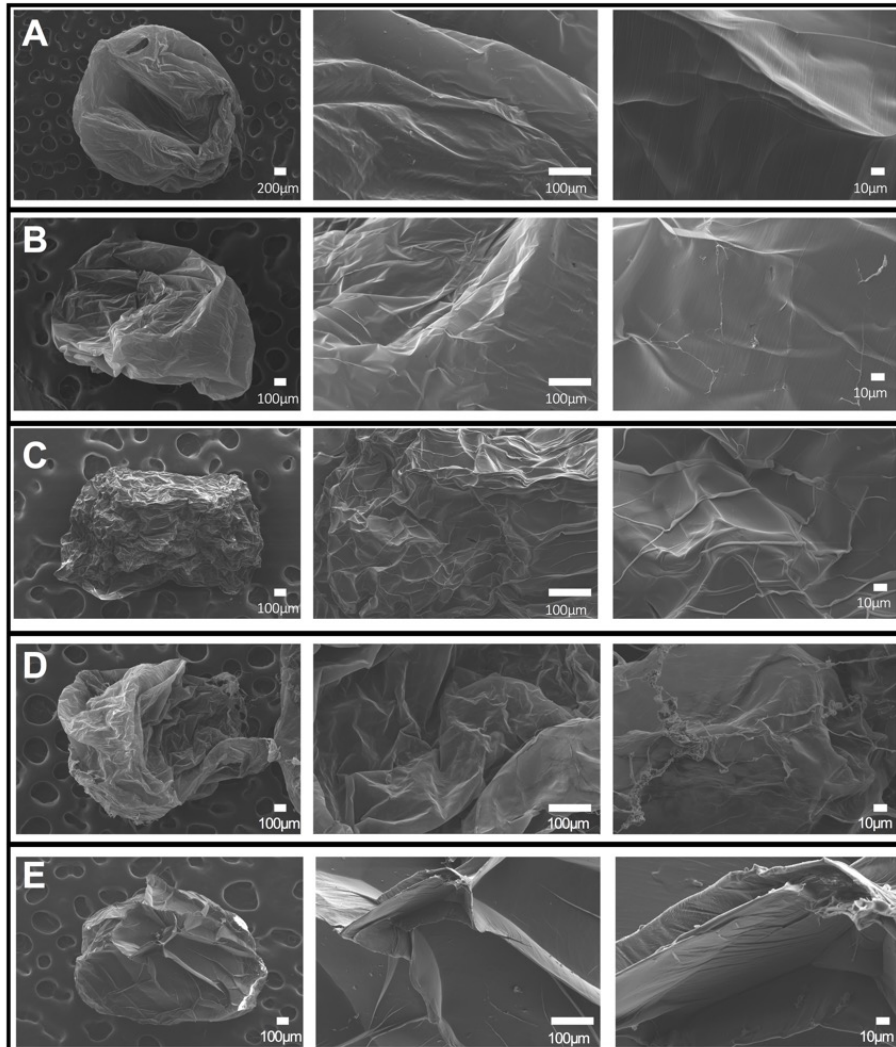


Figure VII-4. SEM images of GG/PLL capsules at different magnifications. A – 0.5% GG-LA 0.1% PLL after one week in distilled water; B – 1% GG-LA 0.1% PLL after one week in distilled water; C – 1% GG-LA 0.1% PLL after one week in PBS; D – 1% GG-MA 0.1% PLL after one week in distilled water; E – 1% GG-MA 0.1% PLL after one week in DMEM.

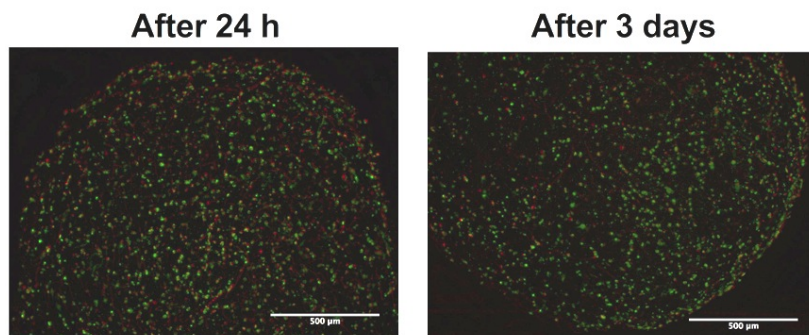


Figure VII-5. Live/dead assay on encapsulated androgen-sensitive human prostate adenocarcinoma (LNCaP) cells. Left image: after 24 hours of incubation; and right image: after 3 days of incubation.

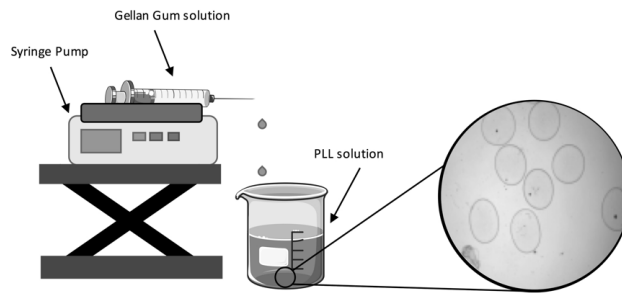


Figure VII-6. Schematic representation of GG-PLL spheres, and method of obtaining thereof.

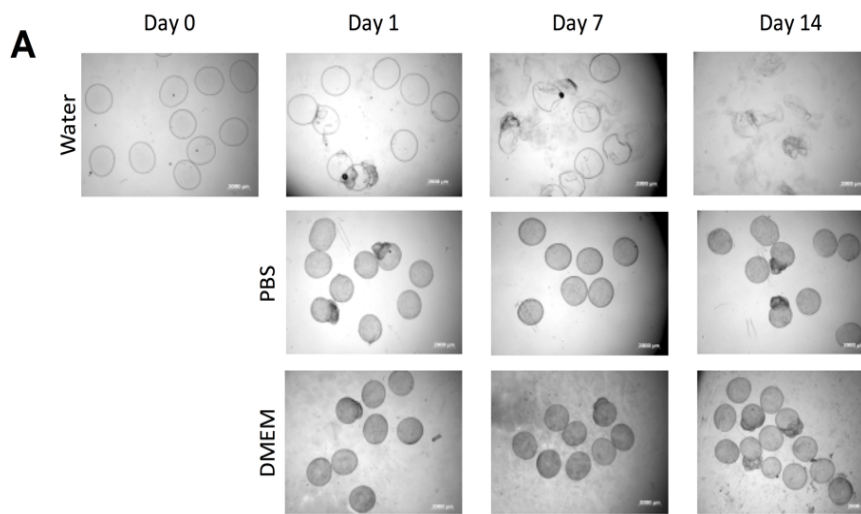
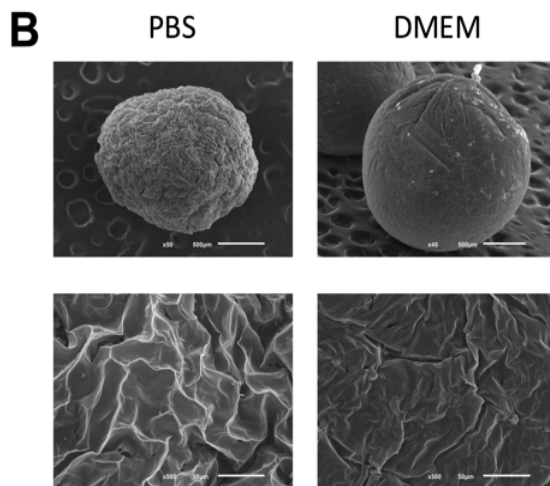


Figure VII-7. Characterization of an embodiment of GG microcapsules of the present disclosure, specifically 1% GG-MA 0.1% PLL. A - Micrographs of 1% GG-MA 0.1% PLL capsules immersed in water, PBS or DMEM



at 37 °C throughout 14 days.

Figure VII-7B. SEM images of different magnification of 1% GG-MA 0.1% PLL capsules. Left panel: after 14 days of incubation in PBS; right panel: after 14 days of incubation in DMEM.

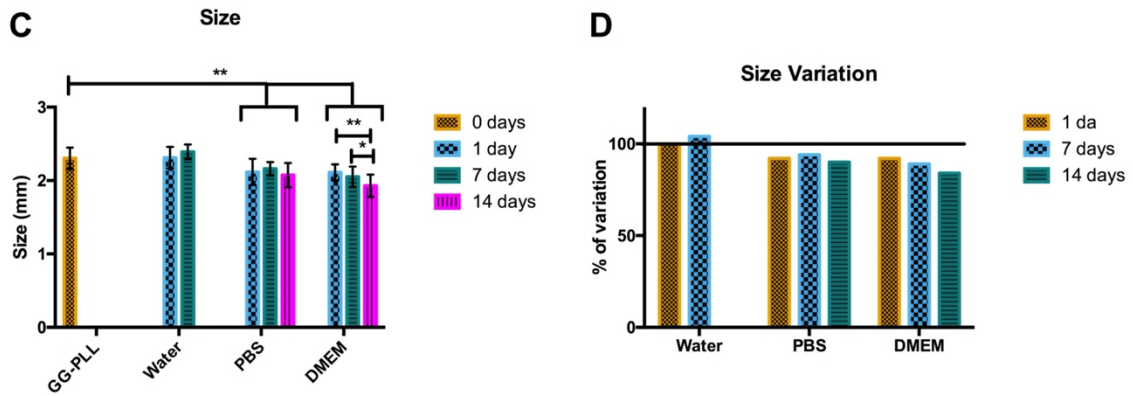


Figure VII-7C. Size of 1% GG-MA 0.1% PLL capsules along the 14 days of incubation. In water, capsules were disrupted after 14 days hampering their measuring; D - Size variation of 1% GG-MA 0.1% PLL capsules as compared to initial capsules (before incubation).

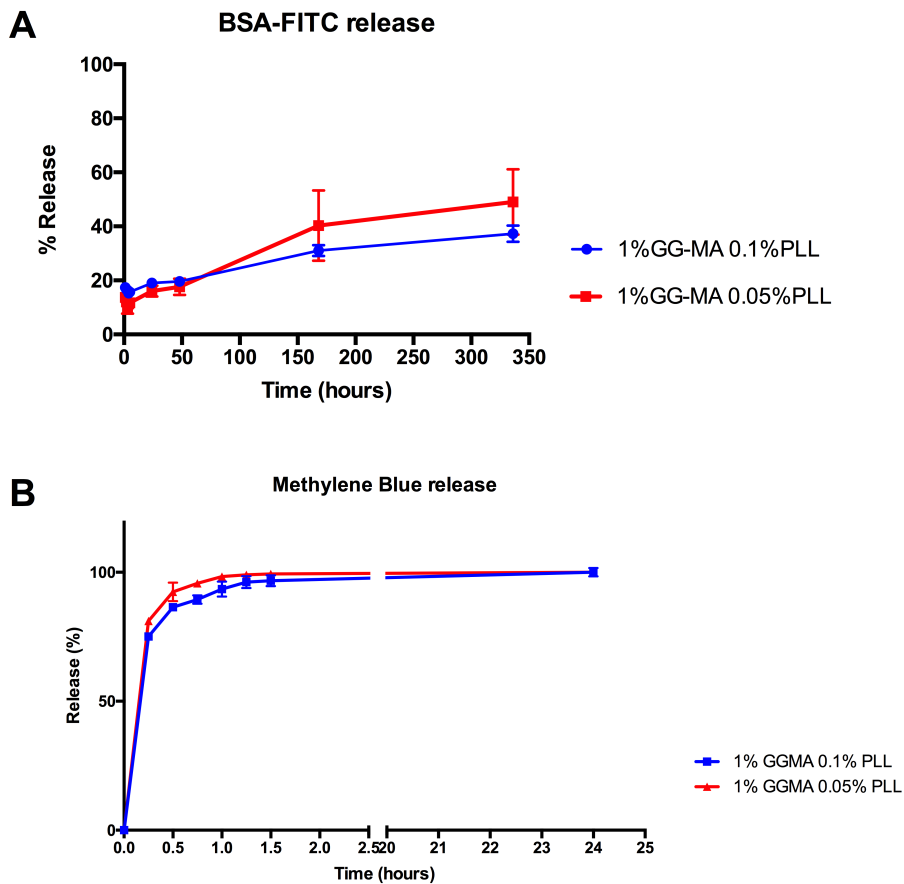


Figure VII-8. Schematic representation of a controlled release of BSA-FITC or Methylene Blue from two different formulations. A - Release of BSA-FITC from 1% GG-MA 0.1% PLL capsules; and B - Release of Methylene Blue from 1% GG-MA 0.05% PLL capsules.

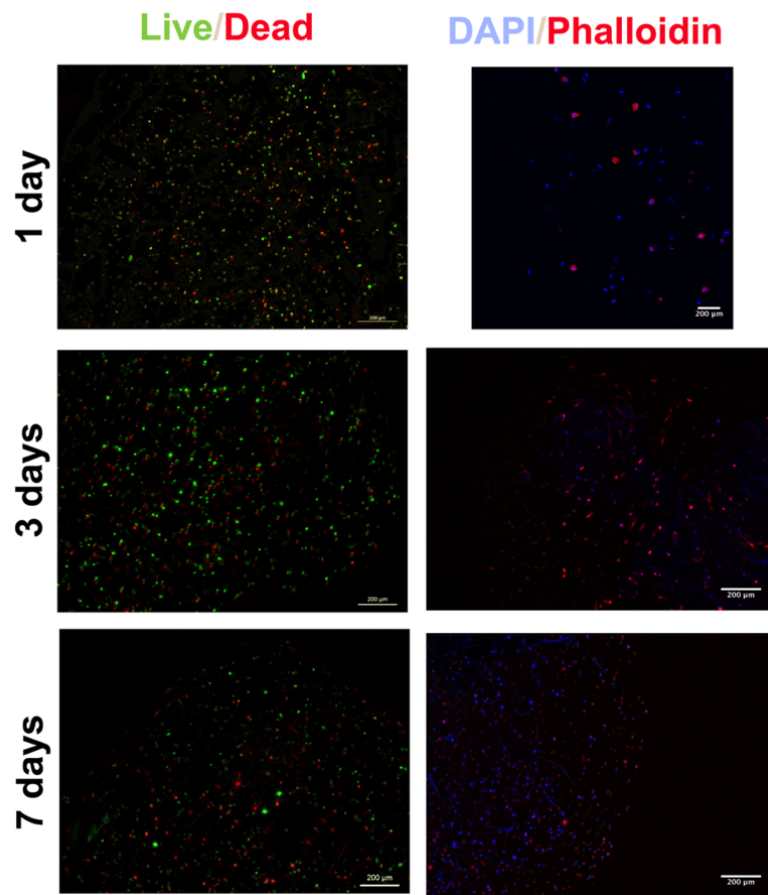


Figure VII-9. Pictures confirming that live cells are found inside the PEC capsules of the present disclosure. Live/dead assay and cytoskeleton analysis by DAPI/Phalloidin staining on human adipose derived stem cells.

Chapter VIII: Methacrylated Gellan Gum/Poly-L-lysine Polyelectrolyte Complex Beads for Cell-Based Therapies*

ABSTRACT

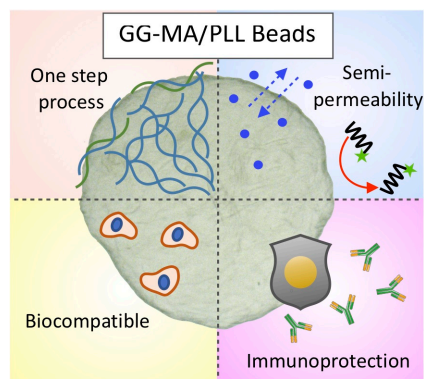
Cell encapsulation strategies using hydrogel beads have been considered as an alternative to immunosuppression in cell-based therapies. They rely on layer-by-layer (LbL) deposition of polymers to tune beads' permeability, creating a physical barrier to the host immune system. However, the LbL approach can also create diffusion barriers, hampering the flow of essential nutrients and therapeutic cell products. In this work, polyelectrolyte complex (PEC) methodology was used to induce hydrogel beads formation, comprising a complex semipermeable membrane of methacrylated gellan gum (GG-MA) with poly-L-lysine (PLL) and a cell-friendly GG-MA hydrogel core. The beads showed great *in vitro* stability over time, a semi-permeable behavior, and supported human adipose-derived stem cells encapsulation. Additionally, and regarding immune recognition, the *in vitro* and *in vivo* studies pointed out that the hydrogel beads behave as an immunocompatible system. Overall, the engineered beads showed great potential for hydrogel-mediated cell therapies, when immunoprotection is required, as when treating different metabolic disorders.

Keywords: Cell therapies, gellan gum, poly-L-lysine, polyelectrolyte complexes, tissue engineering.

* This chapter is based on the following publication:

"Methacrylated Gellan Gum/Poly-L-lysine Polyelectrolyte Complex Beads for Cell-Based Therapies". Vieira S., Silva Morais A., Garet E., Silva-Correia J., Reis R.L., González-Fernández A., Oliveira J.M. (*submitted*).

VIII.1 Graphical Abstract



VIII.2 Introduction

Cell transplantation strategies have emerged as tentative treatments for several diseases, as type I diabetes mellitus (T1DM) or hepatic [1] and central nervous system disorders [2]. However, the outcome of such approaches is often unsatisfactory, mostly due to immune rejection and consequent compulsive need of immunosuppressant drugs [3]. In an attempt to prevent this unsuccessful scenario, biomaterials have been used as platforms for cell encapsulation, where living cells and cell aggregates, became protected from the immune system. For doing so, the biomaterial must allow the diffusion of essential nutrients, oxygen and therapeutic proteins secreted by the cells, but also block host immune system recognition [4].

Hydrogels are the most common choice for engineering immunoisolation platforms. The first immunoisolation systems were developed by Bisceglie *et al.* [5], being later adapted by Algire [6]. However, only in 1980, with the work of Lim and Sun, who used an alginate-poly-L-lysine-alginate (APA) system to encapsulate porcine islets [7], microencapsulation started to be considered an immunoisolation strategy. Similarly, other authors reported the successful application of alginate microcapsules in T1DM treatment, using different diabetic models like rodent [8], porcine [9], canine [10], and non-human primates [11]. Human clinical trials have also been performed with encouraging results, but researchers are still facing and reporting some complications, including finite normoglycemia, lack of functionality of encapsulated cells, and exacerbated fibrotic overgrowth [12].

The most used cell encapsulation strategy still relies on a layer-by-layer (LbL) deposition of the materials to form stable capsules. However, such LbL strategy may hinder the diffusion of essential nutrients, since flow properties can decrease with increasing number of layers [13]. By its turn, polyelectrolyte complex

(PEC) hydrogels result from a one-step reaction between two polyelectrolyte polymers of opposite charge. The interaction is mainly driven by electrostatic bonds, but it can also include inter-macromolecular interactions as hydrogen bonding, van der Waals forces, hydrophobic, and dipole interactions [14]. The process leads to stable macromolecular complexes, at room temperature, where harsh crosslinking agents or organic solvents can be avoided. Therefore, PEC hydrogels are significantly advantageous for Tissue Engineering and Regenerative Medicine (TERM) applications and are being applied for microfabrication [15], drug delivery [16], cell encapsulation [17] and scaffold design [18], and to form multilayered polyelectrolyte assemblies [19].

Gellan Gum (GG) is a linear anionic heteropolysaccharide secreted by the bacteria *Sphingomonas elodea* [20] that exists in two different forms – low and high acyl – depending on the number of acyl substituents present on the molecule [21]. GG is insoluble in water at room temperature, which hinders its straightforward application on cell-based strategies. Thence, before being used as cell encapsulation matrix, GG solutions must be heated up to 90 °C, and then cooled in controlled conditions to avoid the thermal gelation of the material before cell incorporation. Also, the stability of physically crosslinked GG hydrogels is often compromised when implanted *in vivo* [22]. These drawbacks can be surpassed via chemical modification of the carboxylic group of GG by the addition of a methacrylate group [23], as shown in our previous works regarding the development of injectable hydrogels for intervertebral disc regeneration. Indeed, the addition of methacrylate groups leads to an improved water solubility and processability at physiological temperature [23]. The obtained methacrylated gellan gum (GG-MA) hydrogels are then compatible with cell encapsulation, and their mechanical properties, as well as their stability, are improved as compared to unmodified GG hydrogels [23]. Therefore, GG-MA can be used to prepare cell-laden pre-gels at physiological temperature which is ideal for cell normal functioning and growth. On the other hand, poly-L-lysine (PLL) is a cationic polymer, routinely used to improve the durability and tune permeability of bulk anionic polymeric beads [24]. However, it is often necessary to mask PLL with other polymers, PLL is known to be immunogenic, as activated macrophages have high affinity to positively charged surfaces [25].

In this study, the properties of GG-MA and PLL were exploited to form novel PEC hydrogels. Beads were formed using a one-step approach, by extrusion dripping of GG-MA into a PLL bath. It is hypothesized that the free carboxyl groups of GG-MA would interact with the cationic amino groups of PLL, producing robust PEC semi-permeable membranes that would surround the GG-MA hydrogel, thus creating a microenvironment that can protect the encapsulated cells from the host immune system while allowing

the free diffusion of small molecules, metabolites and nutrients. The obtained GG-MA/PLL PEC beads were tested as regard to their permeability to small and large model molecules in both directions of flow. Methylene blue (0.32 kDa) was used as small model molecule while fluorescein isothiocyanate–dextran with different molecular weights (4, 20 and 70 kDa) were used as larger molecules. Also, the fluorescent bovine serum albumin (BSA-FITC) was used in order to assess the diffusion of glomerular proteins through the PEC membrane. Immunocompatibility was evaluated by performing the Complement cascade activation assessment, cytokine production and *in vivo* subcutaneous implantation in CD-1 male mice. Cytocompatibility of GG-MA/PLL PEC beads was also evaluated as proof-of-concept, using encapsulated human adipose tissue-derived stem cells (hASCs).

VIII.3 Materials and Methods

VIII.3.1 Production of GG-MA/PLL Beads

Methacrylated gellan gum (GG-MA) was prepared following the protocol published by Silva-Correia *et al.* [23]. A proper volume of glycidyl methacrylate (GMA, 97%, Sigma-Aldrich) was added to low-acyl gellan gum (Gelzan™ CM Gelrite®, Sigma-Aldrich) solution and the mixture was vigorously stirred for overnight at room temperature, with a constant pH of 8.5. The reaction products were precipitated with cold acetone and purified by dialysis (cellulose membrane, molecular weight cut-off 12 kDa, Sigma-Aldrich) against distilled water. Afterwards, GG-MA was frozen at -80 °C and freeze-dried.

The degree of substitution (DS, fraction of modified carboxyl groups per repeating unit) of GG was assessed by proton nuclear magnetic resonance (¹H NMR) spectroscopy. ¹H NMR spectra were recorded with a 400 MHz Bruker Avance II spectrometer at 70 °C. Lyophilized materials were dissolved in D₂O at a concentration of 10 mg.mL⁻¹. Chemical shifts were referred to the methyl group of rhamnose as an internal standard (δ 1.45 ppm [26]). The final DS obtained was 5.1%, determined using Equation III-1 (Chapter III, page 95) [22].

As prepared GG-MA powder was dissolved in Milli-Q water at concentrations of 1 and 1.5% (w/v). Then, GG-MA solutions were added dropwise to aqueous PLL solutions (Mw 150,000-300,000, Sigma-Aldrich) at a concentration of 0.1 and 0.05% (w/v), using a 30G needle. Beads were formed using an extrusion dripping technique, by polyelectrolyte complexation between GG-MA (anionic) and PLL (cationic) polymers. After production, beads were washed with phosphate buffer saline (PBS, Sigma-Aldrich) solution to remove the excess of PLL. Although the work herein presented is based on spherical beads

with approximately 2 mm in diameter, other sizes and shapes can be obtained (Supplementary Figure VIII-2d).

VIII.3.2 Injection Ability Tests

The ability of GG-MA solutions to be extruded from a 30G needle was investigated by employing an injection measurement equipment (Paralab). The measurements were performed using a 1 mL syringe with a 30 G needle. The syringe was filled with the GG-MA at different concentrations as well as distilled water. Then, each solution was injected through the needle by applying a constant rate of 20 $\mu\text{L}\cdot\text{min}^{-1}$. The load applied to the piston for injecting the material through the 30 G needle was measured and recorded using an appropriate software.

VIII.3.3 Zeta Potential Measurements

The Zeta Potential of 1% (w/v) GG-MA and 0.1% (w/v) PLL solutions was measured using a Zetasizer (Malvern Instruments, NanoZS). Independent triplicate experiments were performed for obtaining statistical significance. Each sample was equilibrated for 120 seconds at 25 °C prior reading and surface charge was calculated using the Smoluchowski model with an $F(Ka)$ value of 1.50. The surface Zeta Potential of GG-MA/PLL complexes was measured using a SurPASS Electrokinetic Analyzer (Anton Paar GmbH), combined with a cylindrical cell. For that, GG-MA/PLL beads were produced as before, washed with distilled water and freeze-dried (LyoAlfa 10/15, Telstar). The measurements were carried out in 0.01 M KCl electrolyte solution, and pH variation was controlled by adding 0.05 M HCl or 0.05 M NaCl.

VIII.3.4 Fourier-Transformed Infrared (FTIR) Spectroscopy

FTIR analysis was applied to confirm the complex formation in GG-MA/PLL beads. Infrared spectra were recorded using the FTIR Spectrometer IR-Prestige-21 (Shimadzu) controlled by IRsolution software. GG-MA powder, dehydrated PLL and dehydrated GG-MA/PLL beads were individually crushed with potassium bromide (Sigma-Aldrich) to prepare a tablet. Spectra were taken in the wavelength range of 4500-400 cm^{-1} .

VIII.3.5 X-ray Photoelectron Spectroscopy (XPS) Measurements

Surface elemental composition of dehydrated GG-MA, PLL, GG-MA/PLL beads and GG-LA was assessed using X-ray photoelectron spectroscopy (XPS, Axis Supra, Kratos) equipped with monochromatic Al (K) X-ray source operating at 1486.6 eV. A co-axial electron neutralizer was used to minimize surface charging, which performed the neutralization by itself. Photoelectrons were collected from a take-off angle of 90° relative to the sample surface. Constant Analyzer energy mode (CAE) with 160 eV pass energy was used

for survey spectra while high-resolution spectra were recorded at 40 eV pass energy. Charge referencing was performed by setting lower binding energy C 1s photo peak at 285.0 eV. Surface elemental composition was then determined using ESCApe™ software.

VIII.3.6 Beads' Surface Morphology and Size

Surface morphology of GG-MA/PLL beads was characterized by scanning electron microscopy (SEM), stereo light microscopy and atomic force microscopy (AFM). For SEM, beads were quickly frozen within liquid nitrogen and then freeze-dried (LyoAlfa 10/15, Telstar). Prior to SEM visualization, samples were fixed by mutual conductive adhesive tape and coated with a thin layer of gold using a sputter coater (EM ACE600, Leica). Then, beads were visualized using a FEI Nova NanoSEM 200 operating at 15 kV accelerating voltage. A Stereo Light Microscope (Stemi 2000-C, Zeiss) with a camera (AxioCam ICC1) was used to assess surface morphology and size in a wet state. Beads' diameter was then measured using the ImageJ software (version 2.0, NIH). AFM measurements were executed using a Nanowizard III (JPK Instruments) at room temperature in QI™ mode. Beads were attached to glass microscopy slides using a glue supplied by JPK Instruments, and then immersed in PBS. A silicon nitride cantilever with silicon tip (MSNL-10, Bruker AFM Probes, Bruker) was used to scan the surface of beads on $10 \times 10 \mu\text{m}^2$ areas. AFM data was then analyzed using the JPK Data Processing software.

VIII.3.7 Size Variation and Weight Loss Profile

GG-MA/PLL beads were incubated in PBS solution with different pH (pH 4, pH 7.4 and pH 10) and cell culture media (α -MEM, Gibco®, Life Technologies), supplemented with 10 vol.% of heat-inactivated fetal bovine serum (FBS, Gibco®, Life Technologies, reference A3160802, EU approved) and 1 vol.% antibiotic-antimycotic solution (penicillin $100 \text{ units.mL}^{-1}$ and streptomycin 100 mg.mL^{-1} , Gibco®, Life Technologies) to evaluate size variations along time. Optical images were obtained at defined timepoints, and beads' diameter measured as abovementioned. Considering that the size obtained at day 0 is the initial size (s) and that each time point a new size value was obtained (s_t), size variation was then obtained by applying Equation III-3 (Chapter III, page 98).

Beads degradation upon incubation with different enzymes was evaluated by studying its weight loss profile. Five as prepared and washed GG-MA/PLL beads were placed into a wet $100 \mu\text{m}$ cell strainer (Falcon). The initial weight (m) was obtained, after careful removal of the liquid excess using a filter paper. Then, the strainers were placed in different solutions of PBS and PBS supplemented with α -amylase (150 U.L^{-1} , Sigma-Aldrich) or 0.1% (w/v) trypsin (Gibco®, Thermo Fisher) and incubated at $37 \text{ }^\circ\text{C}$. All

solutions were supplemented with 0.2% (w/v) sodium azide (Sigma-Aldrich) to avoid bacterial contamination. After 0.08 (2 hours), 0.16 (4 hours), 0.25 (6 hours), 1, 4, 7, 14 and 33 days the liquid excess was gently removed, and the final mass of the samples was determined (m). Equation III-2 (Chapter III, page 97) was applied to calculate the weight loss ratio at each time point.

VIII.3.8 Mechanical Stability

The mechanical stability of GG-MA/PLL beads was evaluated using a rotational stress test ($n=5$, in triplicate). As prepared, beads were placed in centrifuge tubes containing 5 mL of PBS. Then, tubes were rotated at a speed of 200 g for 60 minutes, at room temperature, divided in four 15 minutes steps. After every 15 minutes of rotation, the number of damaged beads was observed and counted under a Stereo Light Microscope. The intact beads were placed again inside the centrifuge tubes to continue the test.

VIII.3.9 Permeability Tests

The permeability of GG-MA/PLL beads was measured using fluorescently labelled molecules with different molecular weight. Fluorescein isothiocyanate–dextran (dextran-FITC, Sigma-Aldrich) with different molecular weights (4, 20 and 70 kDa), and Albumin–fluorescein isothiocyanate conjugate (BSA-FITC, 66 kDa, Sigma-Aldrich), were mixed with GG-MA solutions to obtain a final concentration of 125 $\mu\text{g}\cdot\text{mL}^{-1}$ of dextran-FITC (or BSA-FITC) in 1% (w/v) GG-MA solution. Then, beads were produced as abovementioned and incubated up to 168 hours in PBS, using a shaking water bath at 37 °C. At different timepoints, a small amount of the supernatant was retrieved, and the same amount of fresh PBS was added to each sample. At the last timepoint, beads were collected, mechanically destroyed in 1 mL of PBS, centrifuged, and the resulting supernatant was used to calculate the concentration of FITC-labelled molecules that have remained inside the beads. The fluorescence emission of the retrieved supernatant was measured at an excitation wavelength of 485/20 nm and at an emission wavelength of 528/20 nm, in a microplate reader (Gen 5 2.01, Synergy HT, BioTek). The final concentration of released fluorescent-labelled molecules was obtained using a standard curve with defined concentrations. Initial mass was calculated by summation of the total mass released along the assay and the mass that remained inside the beads at the last timepoint. Ionically crosslinked beads were prepared as published elsewhere [27], and used as controls.

A similar protocol was used for the release of methylene blue (MB, 0.32 kDa, Sigma-Aldrich), but its concentration in the supernatant was quantified by absorbance reading at 665 nm, in a microplate reader (Gen 5 2.01, Synergy HT, BioTek).

Molecular diffusion into GG-MA/PLL beads was quantified using FITC-labelled dextran (4, 20 and 70 kDa) and BSA (66 kDa), as reported elsewhere [28]. Briefly, beads were prepared as before and placed in Eppendorf tubes previously filled with each probing solution. After each timepoint, beads ($n=3$ per timepoint) were collected and visualized using an Inverted Laser Scanning Confocal Microscope (TCS SP8, Leica). Quantification was performed using ImageJ software (version 2.0, NIH), by selecting three random localizations and measuring the mean gray value of defining areas, both inside and outside the beads. For MB diffusion study, as prepared beads were placed in an MB solution and its diffusion was recorded using a Stereo Light Microscope.

VIII.3.10 Qualitative Determination of Total Complement Activation

The activation of Complement cascade upon interaction with GG-MA/PLL complexes was determined as previously reported [29], following the protocol kindly provided by the Nanotechnology Characterization Laboratory (NCL Method ITA-5.1, version 1.2, 2015), with slight modifications. A pool of human plasma, from five healthy volunteer donors, was incubated with GG-MA/PLL beads at 37 °C, for 60 minutes. Zymosan A from *Saccharomyces cerevisiae* (1 mg.mL⁻¹, Z4250, Sigma-Aldrich) was used as positive control, while PBS (Sigma-Aldrich) and Ethylenediamine Tetra acetic Acid (EDTA, 10 mM, E-7889, Sigma-Aldrich) were used as negative controls. A sample with PBS and plasma incubated at 4 °C were also used as negative control. The reversion control, comprised by plasma incubated both with EDTA and Zymosan incubated at 37 °C, for 60 minutes, was included to attest the EDTA negative effect on the cascade. At last, proteins were resolved by 10% SDS-PAGE electrophoresis and transferred to membranes (Immuno-Blot PVDF Membrane, BioRad) using the transblot turbo BioRad transfer equipment (Trans-Blot® Turbo™ Transfer System, BioRad). Membranes were incubated for 60 minutes with a mouse monoclonal antibody against human C3/C3b diluted 1:1000 (ab11871, Abcam), washed and incubated with a secondary polyclonal goat anti-mouse IgG antibody conjugated with alkaline phosphatase diluted 1:2000 (D0486, Dako). The membrane was revealed with 5-Bromo-4-Chloro-3-Indolyl Phosphate (BCIP, Sigma-Aldrich) and then scanned with ChemiDoc™XRS + System (Bio-Rad). ImageJ software (version 2.0, NIH) was used for further quantification.

VIII.3.11 Cytokine Release from Human Peripheral Blood Mononuclear Cells (hPBMCs)

Blood samples were collected from three different healthy donors and hPBMCs were isolated by density gradient using Ficoll-Paque PLUS™ (GE Healthcare). EDTA anticoagulated blood was diluted using equal volume of PBS and added to Ficoll in a 7:3 ratio (diluted Blood:Ficoll) and centrifuged at 180 *g* for 30 min, at 20 °C. After centrifugation, hPBMCs were located at the interface between Ficoll and plasma,

allowing their collection with a Pasteur pipette for further cell culture. Institutional ethics approval to work with human samples from healthy donors was obtained by the Galician Autonomic Ethics Committee at the Concelleria de Sanidade da Xunta de Galicia (Ref 2014/492). All participants included in the study gave their written informed consent.

Cytokine release triggered by the presence of GG-MA/PLL beads was studied, considering a protocol already published [30]. For that, isolated hPBMCs were washed twice with complete medium by centrifugation at 100 *g* for 5 minutes at 20 °C, and seeded in a 96-well plate, using a cell density of 1×10^5 cells per well. Seeded hPBMCs were incubated in the presence of the GG-MA/PLL beads. Cells incubated with lipopolysaccharide (LPS, InvivoGen) at 20 ng.mL⁻¹ were used as positive control and culture medium served as a negative control. After 24 hours of incubation at 37 °C with 5% CO₂, the plate was centrifuged (100 *g*, 5 minutes, 4 °C) and the supernatant collected and stored at -20 °C. The concentrations of nine different cytokines (IFN- γ , IL-12p70, TNF- β , IL-4, IL-5, IL-10, IL-8, IL-1 β , and TNF- α) were determined using the Milliplex® Map Human Cytokine/Chemokine Magnetic Bead Panel (Millipore Corporation, USA) according to the manufacturer's instructions. Finally, samples were analyzed by Luminex® laser based fluorescent analytical test (MAGPIX®, ThermoFisher) and data analyzed with the xPONENT 4.2 1324.0 Software (Luminex®).

VIII.3.12 *In vivo* Tests

VIII.3.12.1 Biocompatibility and Integrity

The biocompatibility and integrity of GG-MA/PLL beads was studied *in vivo* using CD-1 male mice of 5 weeks old and average weight of 27-32 g, at the time of implantation (Charles River, Massachusetts, USA). The maintenance and use of animals were carried out in accordance to the Ethics Committee of University of Minho and approved by the Portuguese Licensing Authority (DGAV-DSPA). Each mouse was anesthetized by intraperitoneal injection of Domtor 1 mg.mL⁻¹ (Medetomidine 1 mg.Kg⁻¹, Novavet, Braga, Portugal) and Imalgene 100 mg.mL⁻¹ (Ketamine 75 mg.Kg⁻¹, Novavet, Braga, Portugal). After anesthesia, the hair at the implantation area was shaved, followed by disinfection with iodine (Life Technologies, Carlsbad, CA, USA). Subcutaneous pockets were formed on the back of each mice, following standard procedures. Afterwards, three beads were implanted subcutaneously per pocket, and the skin was sutured. After 2, 4 and 8 weeks, mice were euthanized, by injection of overdose of Eutasil 200 mg.mL⁻¹ (pentobarbital sodium, Novavet, Braga, Portugal), and the beads retrieved. The material was fixed with

10 vol.% formalin solution, followed by dehydration and paraffin embedding. Slides with 4 μm -thick sections were prepared and stained with Hematoxylin and Eosin (H&E) and Masson's Trichrome (MT).

VIII.3.13 *In Vitro* Tests: Biocompatibility, Cell Morphology, and Proliferation

VIII.3.13.1 Cell Culture

Cell proliferation upon contact with GG-MA/PLL beads' leachable was assessed using human adipose tissue-derived stem cells (hASCs), human macrophages cell line (THP-1) and mouse macrophage cell line (Raw 264.7).

Human adipose tissue samples were retrieved from the knee fat pad of healthy male and female donors with ages between 18 and 57 years, after informed consent, under established cooperative agreements between Hospital da Senhora da Oliveira (Guimarães, Portugal) and 3B's Research Group. All the samples were processed within 24 hours after tissue collection, and hASCs were enzymatically isolated, as previously described [31] with slight modifications. Briefly, fat tissue was minced into small pieces and digested with 0.075% collagenase type II (C6885, Sigma-Aldrich) dissolved in MEM cell culture media (Minimum Essential alpha Medium, α -MEM, Gibco®, Life Technologies), supplemented with 10 vol.% of heat-inactivated fetal bovine serum (FBS, Gibco®, Life Technologies, reference A3160802, EU approved) and 1 vol.% antibiotic-antimycotic solution (penicillin 100 units.mL⁻¹ and streptomycin 100 mg.mL⁻¹, Gibco®, Life Technologies). Tissue digestion took place overnight in a water bath at 37 °C, with shaking. Next, the resulting solution was passed through a 100 μm cell strainer (Falcon) and centrifuged at 800 *g* for 10 minutes. The resulting pellet was collected and centrifuged again at 300 *g* for more 10 minutes. The pellet was then resuspended in culture media and expanded in tissue culture flasks. Cells were cultured until confluence at 37 °C, in a 5% CO₂ incubator, by changing the culture medium every 2-3 days. THP-1 and Raw 264.7 cell lines were obtained from ATCC (American Type Culture Collection, Middlesex, UK). Cells were seeded in a 75 cm² culture flask (Sarstedt, Nümbrecht, Germany), using RPMI 1640 medium supplemented with 10 vol.% heat-inactivated FBS and 2 vol.% Penicillin-Streptomycin (Gibco, Life Technologies). Cells were subculture every 2–3 days and maintained in culture in an incubator with humidified air containing 5% CO₂ and at 37 °C.

VIII.3.13.2 MEM Extract Test

The putative cytotoxic effect of GG-MA/PLL leachable was assessed using a MEM extract test, based on ISO 10993-5:2009 guidelines [32], with slight modifications. hASCs were seeded at 20 x 10³ cells.mL⁻¹ in 24-well plates and allowed to grow until near confluence. The materials were incubated in 20 mL of

complete culture medium, using a ratio of one bead per mL, for 24 hours at 37 °C under continuous agitation. The culture medium of 24-well plates was replaced by 1 mL of extraction fluid and incubated using the aforementioned conditions. After 24, 48 and 72 hours, cell metabolic activity was assessed by AlamarBlue® assay (Bio-Rad Laboratories, Oxford, UK). Briefly, cell culture medium supplemented with 10% (v/v) AlamarBlue® dye (AB) was added to each well and incubated for 4 hours at 37 °C and 5% CO₂. Afterwards, medium fluorescence was measured using a microplate reader (Synergy HT, BioTek Instruments, USA) at Ex/Em ≈ 530/590 nm. The relative metabolic activity was obtained by normalization with the mean fluorescence value obtained for controls (extraction fluid obtained from a TCPS coverslip).

VIII.3.13.3 Real-time Cell Proliferation: xCELLigence® System

The effect of extract fluids from GG-MA/PLL beads on cell proliferation was determined using the xCELLigence RTCA DP system (Roche, Basel, Switzerland). For this, hASCs were seeded at 0.01×10^6 cells.mL⁻¹ in 200 µL of α-MEM complete medium and incubated for 24 hours. The medium was then replaced by 200 µL of extract fluid, using TCPS coverslip extract as control. Similarly, THP-1 cells were seeded at 0.5×10^6 cells.mL⁻¹ per well in 200 µL of RPMI complete medium and phorbol 12-myristate 13-acetate (PMA, Sigma-Aldrich) at 64 nM. After 48 hours in culture, that allowed THP-1 differentiation into macrophages, the medium was replaced by fresh medium. Extract fluids were then added after additional 24 hours in culture.

VIII.3.13.4 Preparation of Cell-laden GG-MA/PLL Beads

hASCs were grown as monolayers as described in Supplementary Information - Methods. At passage 3-4, confluent cells were detached from tissue culture flasks using TrypLE™ Express Enzyme (Gibco®, Life Technologies) and a diluted suspension was centrifuged at 1200 rpm for 5 minutes, forming a cell pellet. GG-MA solution at 1% (w/v) was mixed with the hASCs pellet to a final cellular density of 1×10^6 cells.mL⁻¹. Cells were gently resuspended in the biomaterial suspension to obtain a homogeneous cell distribution. Then, GG-MA/PLL beads were formed by gravitational dripping into a PLL solution, as stated above. Produced beads were washed three times with sterile DPBS (Dulbecco's phosphate-buffered saline, no calcium, no magnesium, reference 21600-044, Gibco), to remove the excess of PLL, and transferred to 24-well plates (Corning). Each well was previously filled with 1 mL of cell culture media and received three beads. GG-MA/PLL beads ($n=3$ beads per well, in triplicate) were incubated for 1, 3, and 7 days at 37 °C, in a humidified air atmosphere of 5% CO₂.

All the materials and solutions were sterilized by filtration (0.22 μm filter) before cell encapsulation, excluding dry GG-MA that was sterilized by ethylene oxide gas (EO Gas Sterilizer/Aerator, 5XL, 3M STERIVAC).

VIII.3.13.5 Viability Assay Using Live/Dead Staining

Live/dead fluorescence assays were performed right after encapsulation and at each time culturing period. Calcein-AM and Propidium Iodide (PI) dyes (1 $\text{mg}\cdot\text{mL}^{-1}$, Molecular Probes, Invitrogen, USA) were used to perform the Live/Dead assay ($n=3$ beads per well, in triplicate). At each timepoint, the culture medium was removed, and 1 mL of PBS containing 2 μL of Calcein-AM and 1 μL of PI was added to each well. Samples were then incubated 10 minutes at 37 $^{\circ}\text{C}$, protected from light. Then, samples were washed three times with PBS and immediately visualized in the dark using a Fluorescence Microscope (Axioimage RZ1M, Zeiss, Germany) in Z-stack mode and using the AxioVision software. Percentage of live cells in each bead was then calculated using ImageJ software.

VIII.3.13.6 DAPI/Phalloidin Staining

As for Live/Dead fluorescence assay, DAPI/Phalloidin staining was performed right after encapsulation and at each time culturing period. Culture medium was removed, and beads were washed three times with PBS. Then, 10% of formalin was added to each well. After 1 hour at room temperature, formalin was removed and replaced by 0.2% Triton-X for 5 minutes to permeabilize cells. Upon washing with PBS, 1 mL of PBS containing 1 μL of DAPI (4,6-Diaminidino-2-phenylindole-dilactate, 20 $\text{mg}\cdot\text{mL}^{-1}$, Sigma-Aldrich) and 5 μL of Phalloidin (phalloidin tetramethyl rhodamine B isothiocyanate, 10 $\text{mg}\cdot\text{mL}^{-1}$, Sigma-Aldrich) were added to each well. After 45 minutes of incubation at room temperature and protected from light, samples were washed three times with PBS and immediately visualized in the dark using an Inverted Confocal Microscope (TCS SP8, Leica). Cell nuclei appeared bright blue, and F-actin filaments looked bright red due to DAPI and Phalloidin dyes, respectively.

VIII.3.13.7 DNA Quantification

Cell proliferation was quantified by the total amount of double-stranded DNA, once cells were encapsulated and after each selected timepoint. Quantification was performed using the Quant-iT PicoGreen[®] dsDNA Assay Kit (Invitrogen, Molecular Probes), according to the manufacturer's instructions. Beads were mechanically destroyed in Milli-Q water and transferred to a water bath at 37 $^{\circ}\text{C}$. After 1 hour, samples were stored at -80 $^{\circ}\text{C}$ until further use. These steps lead to cell lysis both by osmotic and thermal shock. Thence, samples were centrifuged, and the supernatant was used for the DNA

quantification assay. The fluorescence emission of the PicoGreen dye was measured at an excitation wavelength of 485/20 nm and an emission wavelength of 528/20 nm, in a microplate reader (Gen 5 2.01, Synergy HT, BioTek). At last, DNA concentration for each sample was calculated using a standard curve relating the quantity of DNA with the fluorescence intensity.

VIII.3.14 Statistical Analysis

Each experiment was carried out, at least, in triplicate. Results are presented as mean \pm standard deviation, when appropriate. When applicable, the experimental data was analyzed using single-factor or two-way analysis of variance (One-way ANOVA and Two-way ANOVA, respectively) to assess the statistical significance of the results, followed by *post hoc* Tukey tests. Statistical significance was set at a *p*-values of 0.05 (*); 0.001 (**); 0.0001 (***) or <0.0001 (****). All statistical analysis was performed using GraphPad Prism version 7.0a.

VIII.4 Results and Discussion

VIII.4.1 Preparation and Characterization of GG-MA/PLL PEC Beads

PEC hydrogel beads were obtained by means of combining two oppositely charged polymers, the anionic GG-MA and cationic PLL. Both polymers were dispersed in aqueous solutions at room temperature, and beads were formed via extrusion dripping, as illustrated in Figure VIII-1a. The resulting beads were then characterized using different techniques, such as Fourier-transformed infrared spectroscopy (FTIR), X-ray photoelectron spectroscopy (XPS) and SurPass Electrokinetic Analyzer (Figure VIII-1b).

Drops with two different GG-MA concentrations (1 and 1.5% (w/v)) were extruded into a PLL bath with two different concentrations: 0.05 and 0.1% (w/v). When GG-MA reached the PLL bath, a fast, electrostatic interaction occurred between the positively charged amino groups of PLL and the negatively charged carboxyl groups of GG-MA (Supplementary Figure VIII-1). As previously reported [33], it is hypothesized that first, the polyelectrolyte chains form a random structure, based on electrostatic bonds formed upon contact. Then, this random complex structure starts to rearrange into a more stable form, with formation of new electrostatic bonds and polymer chain organization. As a result, a stable and spherical PEC membrane of desired size can be formed at the interface of both polymers, enclosing the GG-MA hydrogel in the center, while some amount of PLL remains in solution. As demonstrated by Coutinho *et al.* [15], the reminiscent quantity of PLL that is observed in solution after the complexation can result from an excess of positive charges as compared to negative ones. As plotted in Figure VIII-1c, GG-MA presents a charge of -37.6 ± 2.1 mV, while PLL has a higher surface charge, of 129.7 ± 9.6 mV.

Therefore, the negative charges of GG-MA are quickly complexed with the excess of positive charges of PLL chains, resulting in an excess of PLL in solution.

Among the tested conditions, 1.5% (w/v) GG-MA solutions demanded a higher force to be extruded and needle clotting was frequently observed (Supplementary Figure VIII-2a and Supplementary Figure VIII-2b). On the other hand, beads formed using a 0.05% (w/v) PLL bath were too fragile, with irregular shape, and difficult to manipulate (Supplementary Figure VIII-2c). Considering that PEC formation is highly dependent on polymer concentration and its mixing ratio [34, 35], we hypothesize that a concentration of 0.05% (w/v) in PLL is not sufficient to instantly form a stable and continuous PEC membrane around GG-MA. Therefore, GG-MA present in the inner core of the bead can be partially released to the external environment, where it reacts with PLL that remains in solution, forming protrusions on the surface of the beads (Supplementary Figure VIII-2c). The 1% (w/v) GG-MA extruded into 0.1% (w/v) PLL bath allowed producing robust spherical beads, which were effortlessly handled. Therefore, the following experiments were performed extruding a 1% (w/v) GG-MA into a 0.1% PLL (w/v) bath (Supplementary Movie VIII-1).

FTIR and XPS analysis were performed to confirm the interaction between GG-MA and PLL. As represented in Figure VIII-1d, the FTIR spectrum of GG-MA/PLL complex shows bands characteristic of both GG-MA and PLL. Mainly, it is possible to distinguish the bands corresponding to Amide I at 1645 cm^{-1} and Amide II at 1540 cm^{-1} from PLL [36, 37]. It is also possible to detect three peaks in $1200\text{-}950\text{ cm}^{-1}$ region assigned to C-O, C-C and C-OH vibrations of the carbohydrate ring attributed to GG-MA [23].

The surface elemental quantification of the beads and their main constituents (PLL and GG-MA), all in a dehydrated state was assessed using XPS analysis. Figure VIII-1e depicts the elemental composition of GG-MA/PLL complexes, and PLL and GG-MA alone (see also Supplementary Table VIII-1). The presence of carbon (C, $63.02 \pm 0.20\%$), oxygen (O, $33.68 \pm 0.19\%$) and nitrogen (N, $3.30 \pm 0.11\%$) on beads' surface was confirmed, and these elements were also found in PLL ($73.89 \pm 0.54\%$ C, $15.10 \pm 0.49\%$ O and $11.01 \pm 0.31\%$ N) and GG-MA ($65.67 \pm 0.22\%$ C, $33.88 \pm 0.21\%$ O and $0.45 \pm 0.09\%$ N). As depicted in Figure VIII-1f, the presence of nitrogen on the GG-MA/PLL complex derives mainly from the PLL molecules. By dividing the C/N ratio of PLL by the C/N ratio of GG-MA/PLL, it became possible to estimate that 35% of the carbon atoms present in GG-MA/PLL complexes derive from PLL molecules.[36] Considering that the amount of PLL in the membrane can be estimated using the quantity of nitrogen on its surface, these results confirmed the successful complexation between PLL and GG-MA and its presence in GG-MA/PLL complexes. Interestingly, the percentage of nitrogen atoms, and consequently of PLL molecules, present in GG-MA/PLL beads is slightly lower than the previously observed for APA beads

[38, 39]. Considering the reported deleterious effect of remaining PLL on the surface of APA beads [40], this result is encouraging for the use of GG-MA/PLL complexes in cell encapsulation strategies.

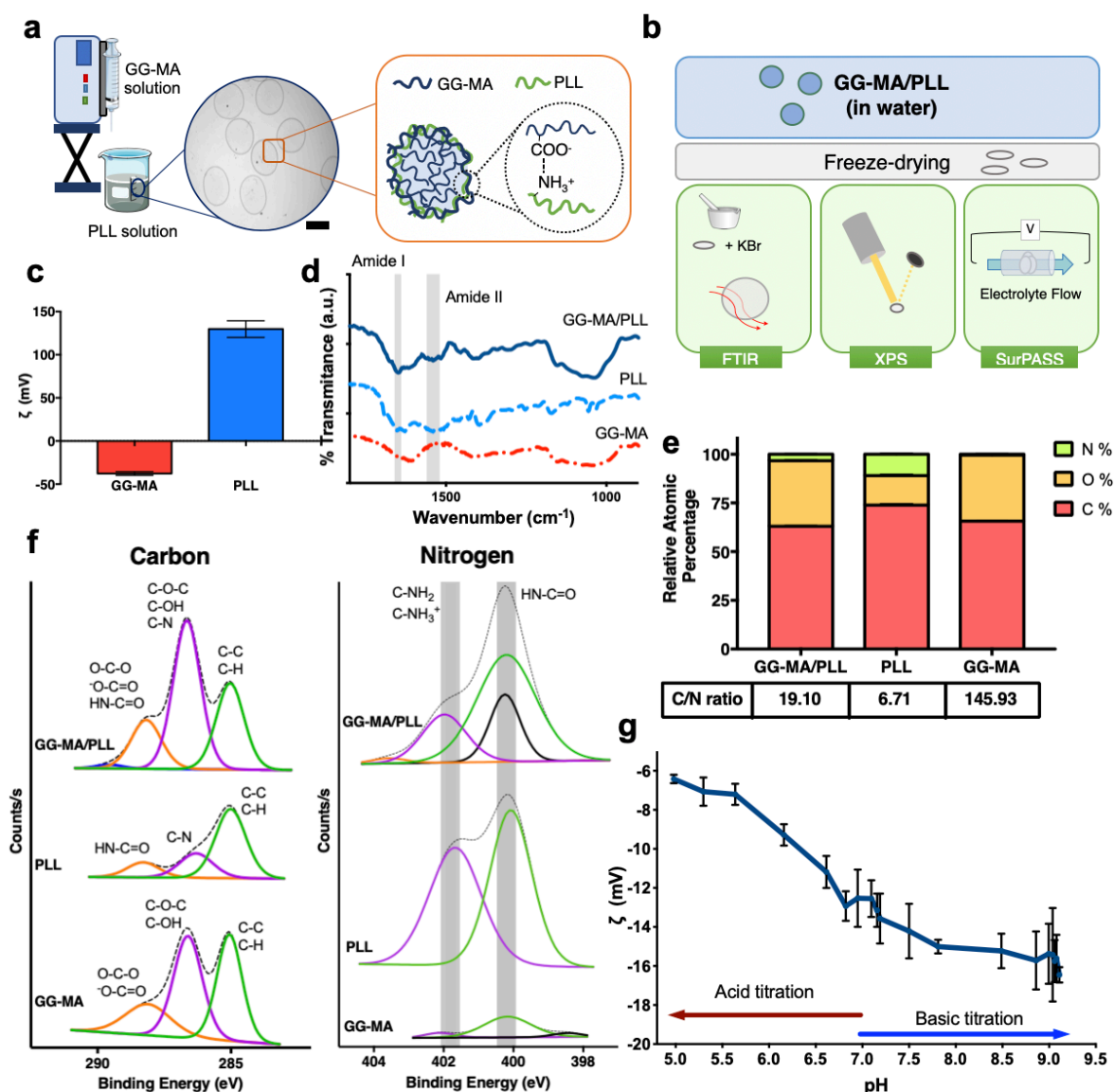


Figure VIII-1. Preparation and characterization of GG-MA/PLL PEC beads. a - Schematic representation of the processing method. GG-MA is extruded dropwise into a PLL solution, using a syringe pump, forming spherical beads upon contact with the cationic bath; b - GG-MA/PLL sample preparation for further chemical characterization by FTIR, XPS and SurPASS electrokinetic analyzer; c - Surface charge of GG-MA and PLL solutions; d - FTIR spectra of GG-MA/PLL (top), PLL (middle) and GG-MA (bottom) with Amide I and Amide II specific wavenumbers (1645 cm⁻¹ and 1540 cm⁻¹, respectively); e - Elemental surface composition (relative atomic percentages) of GG-MA/PLL beads, PLL and GG-MA as measured by XPS. Carbon to nitrogen ratio (C/N ratio) is depicted as a table; f - Comparison of XPS spectra of dehydrated GG-MA/PLL, PLL and GG-MA. Deconvoluted peaks are assigned to chemical groups based on its binding energy: Carbon (C1s) and Nitrogen (N1s); g - Surface charge of GG-MA/PLL beads upon pH titration. Results presented as mean \pm SD, n=3.

The streaming potential of GG-MA/PLL beads was also assessed, using a SurPASS Electrokinetic Analyzer under acidic, neutral, and basic conditions. As illustrated in Figure VIII-1g, at physiological conditions, the measured surface charge was -14.21 ± 1.40 mV (pH near 7.4). By means of comparing to the surface charge of both GG-MA and PLL (-37.6 ± 2.1 mV, and 129.7 ± 9.6 mV, respectively), it is possible to state that PLL is present on the surface of the beads, as the surface charge is higher than the observed for GG-MA alone. Bearing in mind that activated macrophages have an affinity to adhere to positively charged surfaces, it is of utmost importance to consider this parameter when designing a device for cell encapsulation. Therefore, more than confirming the interaction between GG-MA and PLL, this result can be indicative of the *in vivo* immunocompatibility of the beads [12]. In comparison with literature, the surface charge of GG-MA/PLL complexes is substantially decreased as compared to reported values for other biomaterials' capsules [41], which may indicate an improved immunocompatibility of GG-MA/PLL beads. Under acidic conditions (pH 4.98), typical of the inflammatory scenario observed after surgery, the measured surface charge was -6.42 ± 0.22 mV. This value is inferior to that observed by Vos *et al.* [41] for intermediate-G alginate beads at pH 7, the formulation showing better *in vivo* outcome. Thence, it is expected that GG-MA/PLL PEC beads can cope with the hostile inflammatory environment generated from surgical procedures. Under basic conditions (pH 9.11), the surface charge decreased to -16.45 ± 0.39 mV. Considering that PLL has a pK_a of 9.4 [42], it is highly expected that this polyelectrolyte turns electrostatically neutral at a pH near its pK_a . Thenceforth, the interaction between GG-MA and PLL molecules weakens, possibly leading to some release of PLL molecules from the beads' surface and to a consequent decrease of its charge.

Afterwards, beads' morphology and stability were assessed using different conditions, including distinct pH environments and enzymatic solutions (Figure VIII-2a). Optical microscopy, scanning electron microscopy (SEM) and atomic force microscopy (AFM) were performed for further characterization. After production, GG-MA/PLL beads have a smooth surface, round shape (Figure VIII-2b) and an average diameter of 2.30 ± 0.15 mm. Interestingly, upon washing and immersion in PBS, beads' surface changes to a rougher morphology, as observed by optical microscopy and SEM (Figure VIII-2b). To gain a deeper insight on surface topography AFM studies were carried out (Figure VIII-2c). As depicted in Figure VIII-2d, ridges were found through the whole sampled surface, which can be as high as 600 nm (Figure VIII-2d, right image). Although a change on morphology was noticed right after immersion in PBS, and also in Minimum Essential Medium (MEM), no significant changes were observed for the following 14 days (Figure VIII-2e). In addition to the morphological changes observed, it was possible to perceive a decrease

of beads diameter after immersion in PBS and MEM solutions (Figure VIII-2f). This reduction was more pronounced for initial timepoints, with a size variation of $-3.67 \pm 2.56\%$ and $-10.90 \pm 1.61\%$ after 1 day of incubation in PBS and MEM, respectively. Beads' size continued to decrease gradually, and after 14 days of incubation it was observed a size reduction of $8.45 \pm 1.81\%$ in PBS and $12.73 \pm 1.63\%$ in MEM. This shrinkage, as well as the aforementioned ridges' formation on the surface, may be explained by the ionic crosslinking of GG-MA. After PEC formation, the GG-MA coils are organized in double-helix structures. However, this conformational organization does not translate into a true gel, since electrostatic repulsion between helices prevents the formation of stable aggregates [43]. When the divalent ions from PBS solution and MEM culture media, which are not present in deionized water, diffuse from the solution into the GG-MA core, this repulsion is lowered. Ions associate with the free carboxylate groups present on the GG-MA network, reducing the repulsion between the GG-MA double helices, that leads to helix association via cation-mediated aggregates [43]. As a result, the packaging of the hydrogel network is more effective, causing the size reduction, and the previously formed PEC membrane contracts, forming the observed ridges. Regarding size variation on acidic or basic conditions (Figure VIII-2f), it was also observed a slight decrease on beads' size on both environments. However, after 14 days, beads' size variation in acidic conditions was higher than in basic solutions ($-11.00 \pm 1.80\%$ vs. $-7.92 \pm 1.85\%$, respectively), which is in accordance with the reported tightening effect of high concentrations of H^+ ions on GG hydrogel networks [44].

Enzymatic degradation was also studied by means of soaking the GG-MA/PLL PEC beads into PBS solutions containing either α -amylase or trypsin, two enzymes typically used on biodegradation studies [22, 45]. As depicted in Figure VIII-2g, the weight variation profile was similar, regardless the presence of enzymes in solution. During the timeframe of this study, *i.e.* 35 days, the maximum weight loss observed was $2.7 \pm 0.5\%$, showing the great stability of the developed beads. Interestingly, after 35 days of soaking, the higher weight variation was observed for the beads incubated in PBS only ($2.6 \pm 0.8\%$). Nevertheless, this result is not significantly different to the values obtained in the other tested solutions: $2.2 \pm 0.1\%$ and $1.9 \pm 1.1\%$ in the presence of α -amylase and trypsin, respectively. In addition, the mechanical resistance of GG-MA/PLL complexes was tested using a rotational stress test, as described elsewhere [46]. After four series of centrifugation, no modification was found in beads' shape (Supplementary Figure VIII-3), attesting the mechanical stability of the system under this stress test.

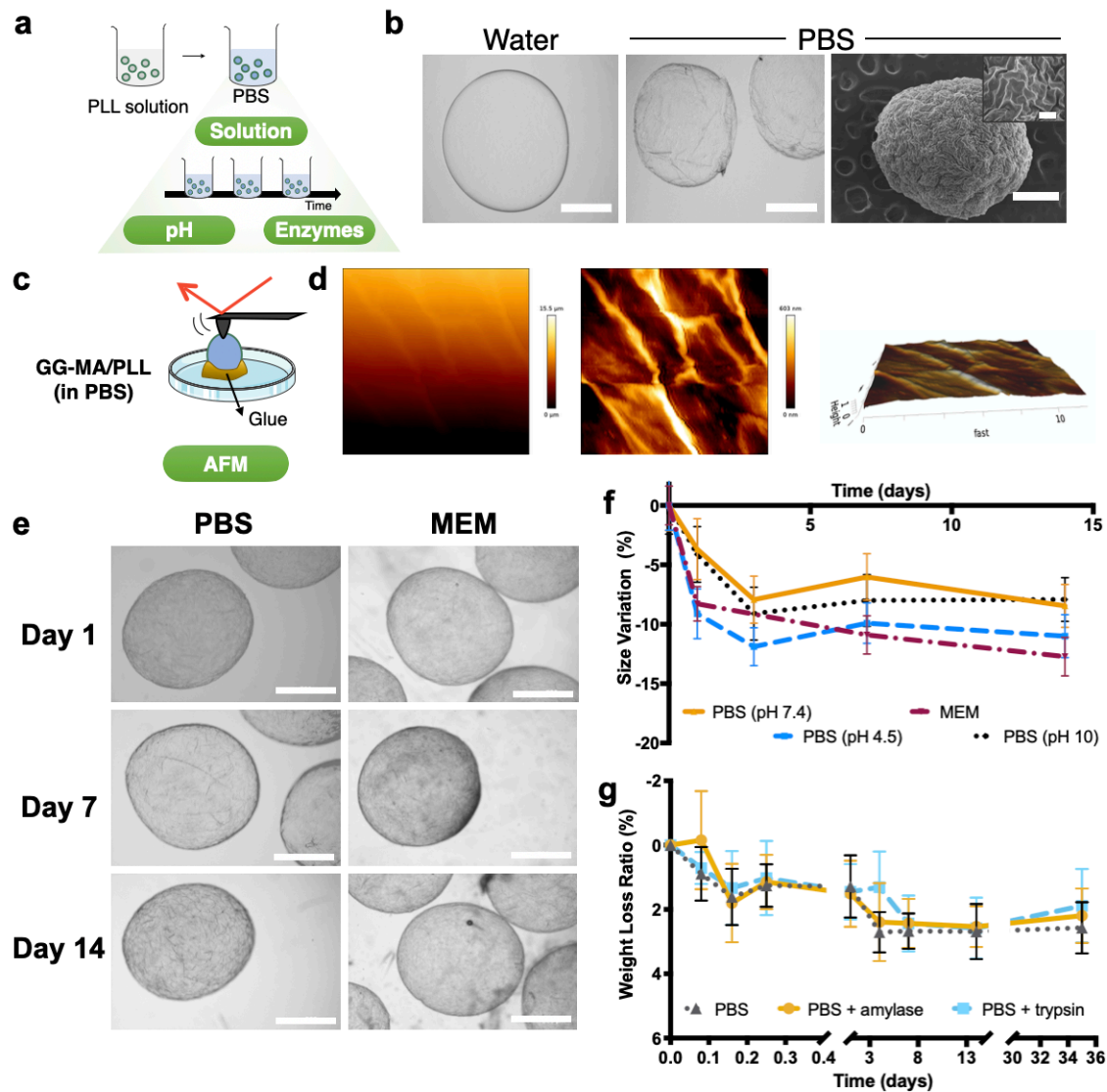


Figure VIII-2. Surface morphology and stability of GG-MA/PLL PEC beads. a - After production, beads were washed with PBS and then submitted to different experimental set-ups to test their morphology and stability; b - Before being washed, beads have a smooth surface. However, after immersion in PBS their surface changes to a rough morphology due to the ionic crosslinking of inner GG-MA, as demonstrated by optical microscopy and SEM. Scale bar: 1 mm for optical images and 500 μm to SEM images; c - Schematic representation of the experimental set-up used to perform the AFM acquisition; d - Surface topography of the bead immersed in PBS (left side), and after tilt correction (middle and right side); e - Micrographs showing GG-MA/PLL beads incubated in PBS and cell culture media (MEM) for 14 days. Scale bar: 1 mm; f - Size variation along time upon incubation in PBS (pH 7.4), acidic PBS (pH 4.5), basic PBS (pH 10) and cell culture media (MEM); and g - Weight variation profile of GG-MA/PLL beads after immersion in PBS, and PBS supplemented with trypsin or amylase. Data represents average \pm SD (n=20).

VIII.4.2 Permeability Studies

Immunoprotection is a central requirement when allo- or xeno-transplantation is envisaged. As stated before, the materials used on such approaches should allow the diffusion of nutrients, therapeutic agents, and cell waste while blocking harmful components of the host immune system [47]. Thence, the performance of encapsulated cells is tightly correlated with the permeability of the device. One important parameter available that possibly evaluates membrane permeability is the molecular weight cut-off (MWCO), that must be tailored to meet the immunoprotection requirements.

The drug release ability of the PEC hydrogels was assessed using three model molecules, as schematically illustrated in Figure VIII-3a. The BSA-FITC, a glomerular protein with a molecular weight of approximately 66 kDa, was used as a model of protein molecules. By its turn, dextran-FITC with 4, 20 and 70 kDa were used as models for different molecular weights. Finally, methylene blue (MB), with a molecular weight of 0.32 kDa, was used as a small molecule model.

As represented in Figure VIII-3b and Figure VIII-3c, it was observed a rapid release of the smallest molecules (4 kDa dextran-FITC and MB), which reached a complete release within 1 hour, in agreement with Fickian diffusion (Supplementary Figure VIII-4a and Supplementary Figure VIII-4b). These results suggest that insulin (MW ~5.8 kDa), as well as other small nutrients, would be quickly released from the hydrogel matrix as a function of its concentration, without facing diffusional resistance. On the other hand, the 20 and 70 kDa dextran-FITC molecules exhibited a hampered outflow (Figure VIII-3c). Although 20 kDa dextran-FITC molecules were completely released after the incubation, these molecules took more time to diffuse from the beads (approximately 72 hours) as compared to the smaller 4 kDa dextran-FITC. By its turn, the 70 kDa dextran-FITC was not completely released from the beads during the timeframe of this experiment, as only $62 \pm 10\%$ of the material was released after 168 hours of incubation. For both molecules, the observed release profile followed an anomalous transport model (Supplementary Figure VIII-4c), suggesting that their diffusion is not only dependent on molecule concentration, but also on the polymeric rearrangements of the matrix [48, 49]. Similarly, BSA-FITC showed a limited release, with only $31 \pm 2\%$ of the protein being released after 168 hours, following a quasi-Fickian transport model (Supplementary Figure VIII-4d and Supplementary Figure VIII-4e).

Side-by-side analyses of these results with the release profiles obtained from ionically crosslinked GG-MA hydrogels, allows us to conclude about the effect of the PEC membrane as diffusion barrier against large molecules. Ionically crosslinked GG-MA hydrogels rapidly release their cargo, with a complete release of both 20 and 70 kDa dextran-FITC, after 6 hours of incubation (Supplementary Figure VIII-4f). This is in

accordance with our previous work, that showed a rapid cargo release from Ca-enriched GG-MA hydrogel beads incubated in simulated body fluid [27].

Membrane's permeability to the inflow of molecules present outside the beads was also assessed, to estimate the potential flow of host antibodies and essential nutrients into the hydrogel matrix. For that, beads were immersed into different solutions containing the same molecules used in the previous assay (Figure VIII-3d). When GG-MA/PLL beads were immersed into a MB solution, it was possible to observe a quick impregnation of MB into the hydrogel (Supplementary Movie VIII-2), confirming the permeability of the PEC membrane to small molecules, needed for cell survival. As shown in Figure VIII-3e, the 4 kDa dextran-FITC readily diffused through the membrane. After 0.5 hours, significant inflow was observed, a trend that was preserved along 7 days. Contrarily, the diffusion of 20 kDa dextran-FITC was considerably hampered and it was only possible to observe a significant permeation of the molecule through the membrane of the beads after 24 hours of incubation. Surprisingly, the inflow of 70 kDa dextran-FITC molecules into the beads is not comparable to its release from the material. Indeed, the diffusion of these molecules to the interior of the beads was substantially blocked by the PEC membrane. When using BSA-FITC, an accumulation of the signal on the border of the bead was observed, and only a vestigial diffusion was noticed, after 168 hours of incubation. This result is in agreement with the results obtained from the BSA-FITC release, where the diffusion of the protein was highly hampered.

For gaining a deeper understanding of PEC membrane permeability, the relative fluorescence of dextran-FITC was quantified at different regions of the bead over time (Figure VIII-3f). As expected, the relative fluorescence of 4 kDa was always higher than $76.43 \pm 1.40\%$, confirming that GG-MA/PLL membrane is highly permeable to small molecules. The delayed diffusion of 20 kDa molecules was also confirmed. The relative fluorescence obtained after 24 hours was $51.38 \pm 1.82\%$, and the equilibrium between the inside and the outside media was not achieved, since the relative fluorescence calculated for 168 hours was $69.54 \pm 7.82\%$. Only traces of diffusion of 70 kDa molecules was noted, but fluorescence values were never higher than $22.10 \pm 1.85\%$, reached after 72 hours of soaking. Considering these results, one can assume that large proteins will have a more limited diffusion into the GG-MA/PLL PEC beads. Bearing in mind that the smallest antibody, immunoglobulin G (IgG), has ≈ 150 kDa, these results suggest that GG-MA/PLL system would block its permeation to the inner space, protecting encapsulated cells from a host humoral immune rejection. Other hydrogels made from GG showed a completely different behavior from the one reported by us. Lozano *et al.* [50] reported a full equilibrium between a 0.5% (w/v) GG hydrogel and a BSA-FITC solution after 48 hours of incubation. Soto *et al.* [51] showed

that 20 kDa dextran-FITC can easily diffuse into a 2% (w/v) ionically crosslinked GG-MA hydrogel. That being said, one can conclude that the presence of a PEC membrane is responsible for the semi-permeable behavior of the GG-MA/PLL PEC beads, essential for appropriate cell immunoprotection.

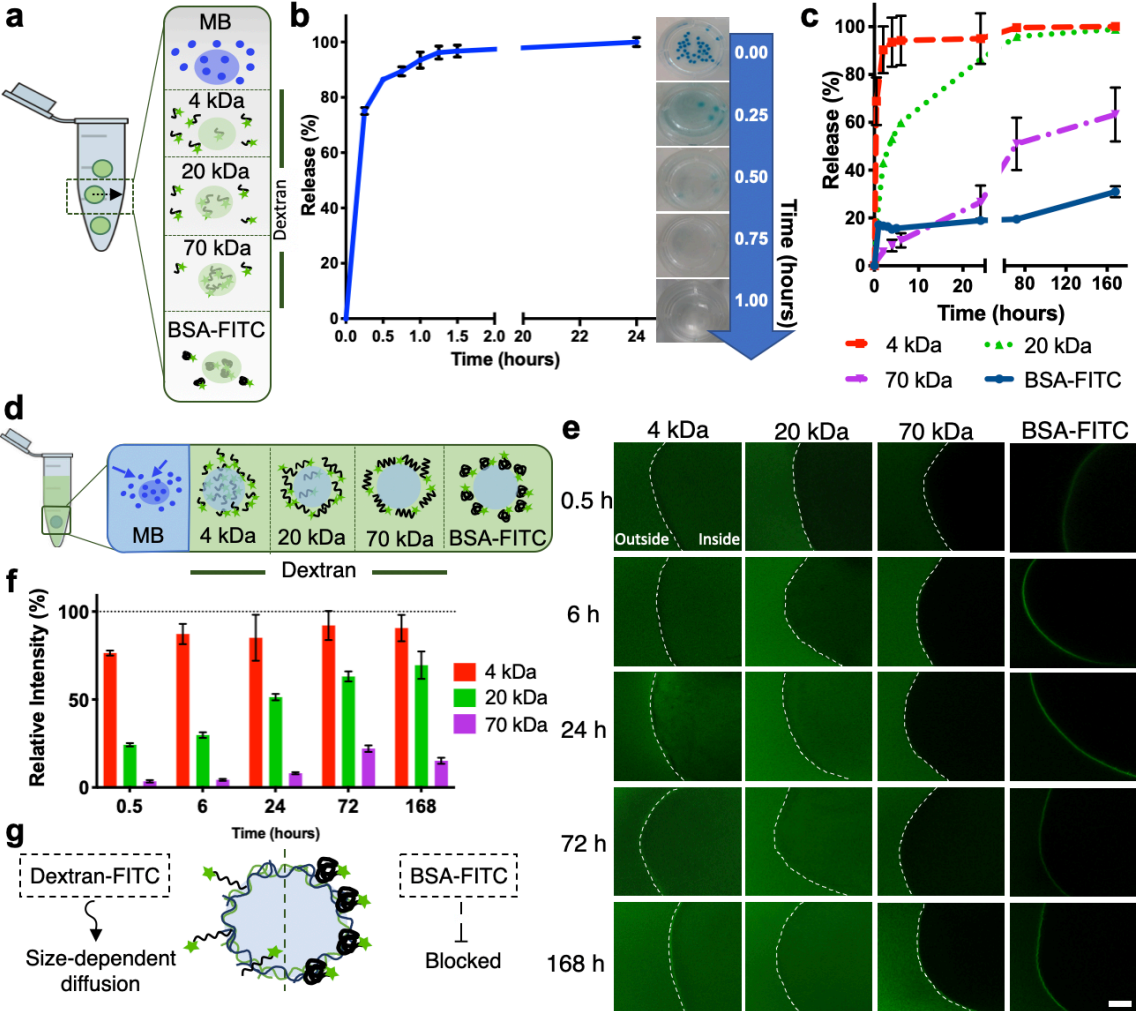


Figure VIII-3. Permeability of GG-MA/PLL PEC beads. a - Schematic representation of the experimental conditions used to test the release capacity of GG-MA/PLL beads; b - Rapid release profile observed for encapsulated methylene blue (MB) in GG-MA/PLL. Representative images of the observed release profile along the period of 1 hour show that the characteristic blue color of MB is almost undetectable inside the beads after 30 minutes of experiment; c - Release profile of BSA-FITC and dextran-FITC with different molecular weights (4, 20, and 70 kDa) from GG-MA/PLL PEC beads. While small molecules (4 kDa) are rapidly released, larger ones (20, 70 kDa, and BSA) show a restrict flow to the surrounding media; Data presented as the average \pm SD with $n=3$; d - Schematic representation of the experimental design used to assess the inflow of model molecules into GG-MA/PLL PEC hydrogels; e - Laser Scanning Confocal Microscope (LSCM) images of beads after 0.5, 6, 24, 72, and 168 hours of incubation. Whereas 4 kDa and 20 kDa dextran-FITC passed through the beads' membrane, 70 kDa dextran-FITC could not pass the membrane after 168 hours of immersion, resulting in a dark core surrounded by a green background when observed under a LSCM. Similarly, BSA-FITC was not detectable inside the PEC hydrogels, but only on their

surface. Scale bar = 200 μm ; f - Relative fluorescence of dextran-FITC diffusion into GG-MA/PLL beads. Fluorescence was normalized to the liquid medium and showed data represents the average \pm SD % of the gray value of all pixels; and g - Schematic drawing comparing the interaction between the surface membrane and linear dextran or BSA proteins.

VIII.4.3 Immunoprotection

An important feature of an encapsulating material is its immunoprotection capacity, in order to be able to efficiently avoid graft rejection in immunocompetent hosts [52]. Herein, the putative immunoprotection conferred by the GG-MA/PLL PEC beads was evaluated by different ways, namely: *in vitro* (i) Complement cascade activation; (ii) macrophage proliferation; (iii) cytokine release profile; and (iv) *in vivo* subcutaneous implantation.

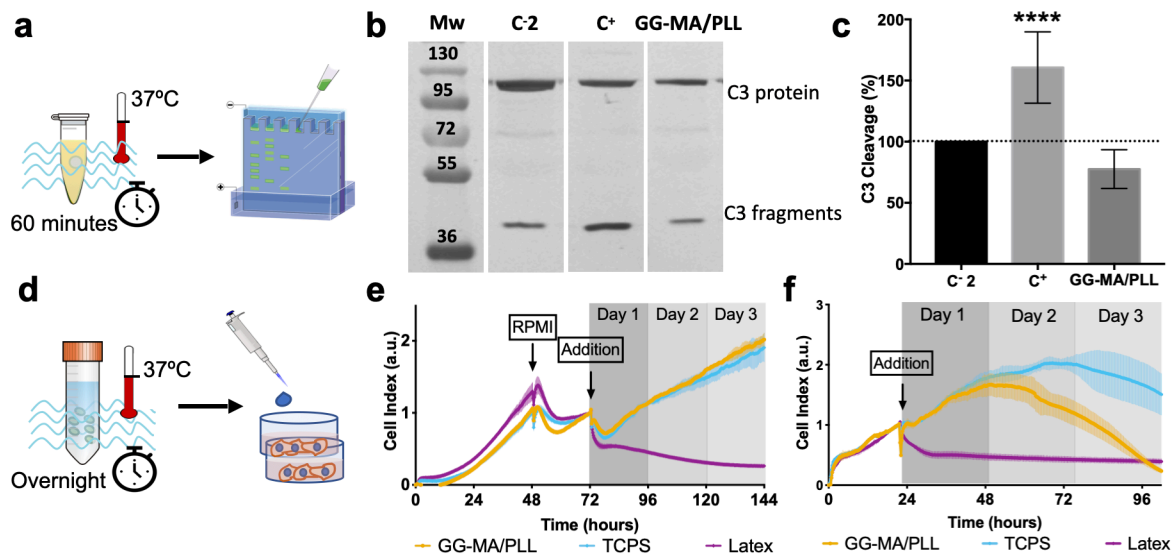


Figure VIII-4. Assessment of GG-MA/PLL PEC beads immunocompatibility (*in vitro*). a - Schematic drawing of the preparation methodology used to assess Complement system activation; b - Western Blot membrane incubated with a monoclonal antibody against human C3 and C3 fragments, followed by incubation with a secondary antibody conjugated with alkaline phosphatase, for detection. From left to right, molecular weight standard (Mw, kDa); negative control without sample (C-2); positive control (C+); and GG-MA/PLL beads sample; c - Relative quantification of C3 fragments measured on GG-MA/PLL beads and positive control, using C-2 as reference value. **** represents statistical difference of C+ relative to the other samples, with $p < 0.0001$. ($F_{5,30} = 97.7$, $p < 0.0001$); d - Schematic drawing of the experimental protocol followed to study macrophage proliferation; e - Real-time proliferation of THP-1 cell line upon contact with GG-MA/PLL, TCPS and Latex leachable; f - Real-time proliferation of Raw 264.7 cell line after contact with GG-MA/PLL, TCPS and Latex leachable. Results presented as average \pm SD, $n=4$.

VIII.4.3.1 Complement Cascade Activation

Once a material is implanted *in vivo*, the innate immune response to a foreign body takes place. This is a rather non-specific host defense, triggered by different ways, including the Complement system. The Complement comprises a set of serum proteins that upon contact with a foreign body (like pathogens or biomaterials), or by the presence of immunocomplexes (antibody-antigen), could be locally activated, through a triggered enzyme cascade. Although the complement cascade can be activated via three different pathways, (classical, lectins and alternative), all of them converge to cleavage C3 into C3a and C3b fragments, followed by the C3b degradation to other fragments (C3c, C3dg). C3 cleavage usually results in large amounts of C3b, the main effector of the complement system [53]. Therefore, the study of complement system activation was performed by estimating the extent of C3 cleavage upon contact of GG-MA/PLL PEC beads with human plasma (Figure VIII-4a). As shown in Figure VIII-4b, a C3 spontaneous cleavage occurred in the negative control used, *i.e.* only human plasma incubated at 37 °C (C2). Therefore, this value was considered as 100% for reference. The exposure of plasma to Zymosan led to a high C3 cleavage (C⁺), as shown in Figure VIII-4b lane 3, while in plasma incubated at 4 °C (C1), or in the presence of EDTA (C3 and C4), the amount of degraded C3 was almost neglectable (Supplementary Figure VIII-5). After incubation with human plasma, GG-MA/PLL PEC beads triggered the cleavage of C3 protein, as two bands were detected by Western Blot (Figure VIII-4b, lane 4). Taking the negative control as reference, the amount of the small fragments of C3 protein measured for the positive control and GG-MA/PLL beads was $160.60 \pm 29.18\%$ and $77.56 \pm 15.85\%$, respectively (Figure VIII-4c). There was no significant difference between the reference value and the one measured for GG-MA/PLL ($p=0.122$). Considering these results, GG-MA/PLL PEC beads do not strongly influence the Complement system activation, which is a good indicator for the final performance of the GG-MA/PLL PEC beads.

VIII.4.3.2 Macrophage Proliferation

Human (THP-1) and murine (Raw 264.7) macrophages proliferation was observed in real-time, along 3 days, after addition of GG-MA/PLL leachable to culture media, as illustrated in Figure VIII-4d. These cell lines are regarded as good models for immunomodulation approaches, as they closely mimic monocyte and macrophage cells, which are effectors of the innate immune response [54-56]. Upon activation, macrophages start to proliferate to increase the number of cells capable of eradicate the element that triggered the immune response [57]. Therefore, the effect of the GG-MA/PLL leachable on the proliferation of these cells gives a deeper insight on the effect of the biomaterial in the immune response. The obtained proliferation curves are depicted in Figure VIII-4e and Figure VIII-4f, respectively.

For THP-1 cell line (Figure VIII-4e), the proliferation pattern was similar between the control and beads' leachable. When the leachable was added to Raw 264.7 cells, the proliferation was similar to the control (TCPS leachable) for day 1, but a decrease on cell index was noticed afterwards, indicating cell detachment from the well bottom. As depicted in Figure VIII-4f, the same pattern was also observed for the control sample, although delayed for 0.5 days. These results indicated that GG-MA/PLL leachable would not trigger an over-proliferative status on both human and murine macrophages, which would be deleterious for future *in vivo* applications, in particular the ones related to cell-based therapies.

VIII.4.3.3 Cytokine Release Profile

A further insight on the putative pro-inflammatory and immunogenic properties of PEC hydrogels was evaluated by a multiplex analysis of cytokine production by human peripheral blood mononuclear cells (hPBMCs). Cytokines have a key role on the interplay between immune cells, and are responsible for the activation and differentiation of various immune cells [58]. Therefore, the balance between pro- and anti-inflammatory cytokines released by hPBMCs upon interaction with the PEC hydrogels can give a deeper insight on the immune response triggered by the biomaterial [59]. In total, nine cytokines were measured considering both T_H1 and T_H2 possible responses. In this regard, T_H1 profile includes cytokines that mostly induce cellular responses, while the T_H2 profile comprises cytokines involved in humoral responses [60]. IL-8, IL-1 β and TNF- α were also studied considering their important role on inducing chemotaxis, mediating the inflammatory response and triggering of systemic inflammations, respectively [61]. As represented in Table VIII-1, IFN- γ , TNF- β , IL-4 and TNF- α were detected in concentrations similar to the negative control (-), meaning that their synthesis was not greatly affected by the presence of GG-MA/PLL PEC beads. However, minor cytokine secretion was noticed for IL-12p70, IL-5, IL-10, IL-8 and IL-1 β , with measured values between the negative and positive control (\pm). Additionally, IL-10, IL-8 and IL-1 β were observed in concentrations at least ten-times higher than the detection limit of the kit (+), in donor 2 sample. Indeed, cytokine production was different among the three different donors. Donor 1 showed a mild T_H1 and T_H2 profile responses, via the pro-inflammatory IL-12p70 and IL-5, respectively [62]. Interestingly, both pro-inflammatory (IL-8 and IL-1 β) and anti-inflammatory cytokines (IL-10) were detected in donor 2. While IL-8 and IL-1 β are related to immune rejection, IL-10 inhibits the production of different pro-inflammatory cytokines, including IL-8 and IL-1 β , and is associated with immune acceptance [59]. In this regard, the results obtained for donor 2, point to a controlled immune response, where the secretion of pro- and anti-inflammatory cytokines is balanced [63]. At last, in the sample derived from donor 3, only IL-1 β was detected in intermediate levels between the observed for negative and

positive control, suggesting a mild pro-inflammatory reaction. However, it must be stressed out that none of the values were above the ones measured when in presence of lipopolysaccharide, the positive control. This result suggests that GG-MA/PLL PEC beads do not exerted *per se* a serious inflammatory reaction that could compromise the functionality of this system as immunoprotective matrix for cells.

Table VIII-1. Cytokine release after incubation of hPBMCs with GG-MA/PLL PEC beads.

Panel	Cytokine	GG-MA/PLL
T _H 1 Profile	IFN- γ	---
	IL-12p70	\pm --
	TNF- β	---
T _H 2 Profile	IL-4	---
	IL-5	\pm --
	IL-10	- + -
Other	IL-8	- + -
	IL-1 β	- + \pm
	TNF- α	---

Legend: -: cytokine concentration similar to the negative control; \pm : cytokine concentration between the negative and positive control; +: cytokine concentration between the negative and positive control and at least ten-times higher than the detection limit of the kit. Symbols shows the average response obtained for each one of the three human donors.

VIII.4.4 Subcutaneous Implantation of GG-MA/PLL PEC Beads

In vivo biocompatibility of GG-MA/PLL beads was assessed by implanting the materials subcutaneously into the back of CD-1 male mice, up to 8 weeks (Figure VIII-5a). At defined timepoints (2, 4 and 8 weeks), beads were retrieved from the back of the animals and processed for histological analysis. From Figure VIII-5b, it can be observed that all beads remained translucent, showing no signs of calcification. Additionally, no signs of acute inflammation or necrosis were found at the macroscopic level. After hematoxylin & eosin (H&E) staining (Figure VIII-5c), it was possible to observe a thin layer of connective tissue between the beads and the surrounding adipose tissue (black arrows).

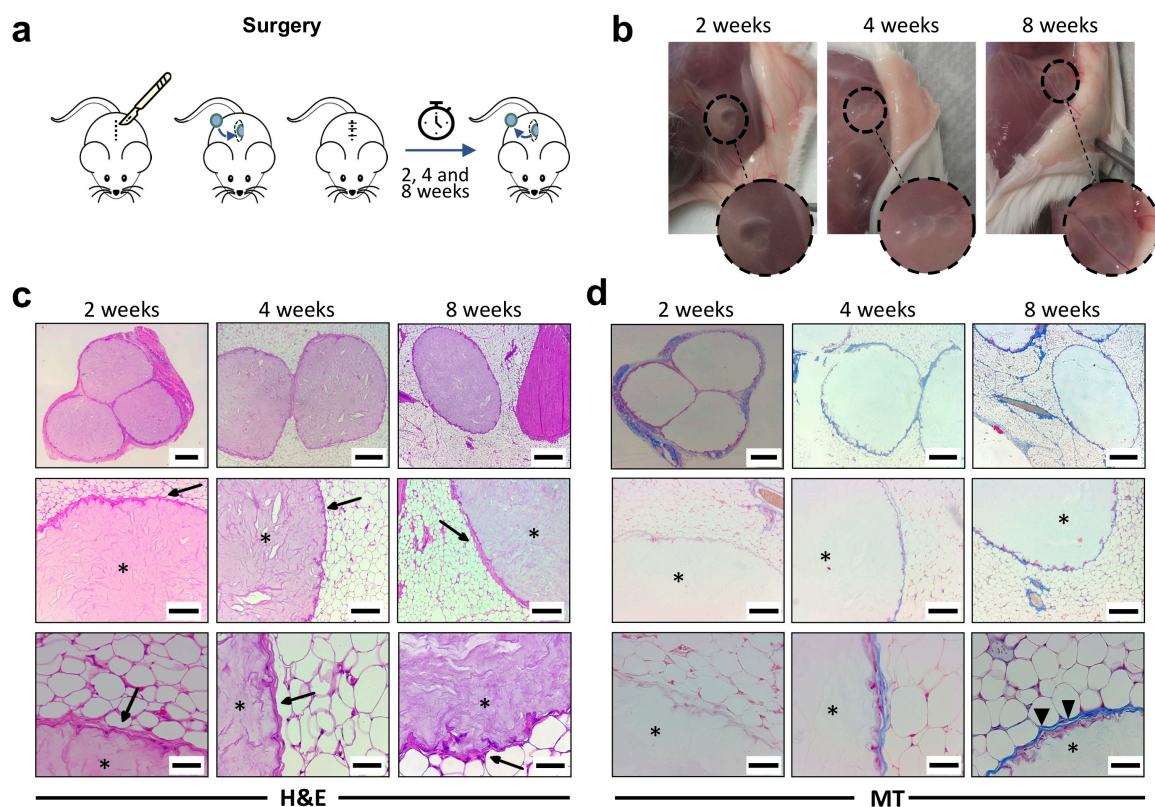


Figure VIII-5. *In vivo* biocompatibility of GG-MA/PLL PEC beads. a - Drawing of the surgical procedure; b - GG-MA/PLL PEC beads explants at different timepoints; c - Hematoxylin & eosin (H&E) staining of GG-MA/PLL PEC beads explants retrieved from mice after 2, 4 and 8 weeks; d - Masson's Trichrome (MT) staining of retrieved beads after 2, 4 and 8 weeks of subcutaneous implantation. Stars mark the material and black arrows the thin layer of newly formed connective tissue. Blue stains for collagen. Black triangles point to small blood vessels. Scale bars (c-d): 500 μm (upper row), 200 μm (middle row), and 50 μm (lower row).

Macrophages or foreign body giant cells were not found on the vicinity of intact beads in all the tested timepoints. Cell infiltration towards the inside of the beads was also not observed, contrarily to the observed by others when using ionically crosslinked GG-MA hydrogels [64]. The Masson's Trichrome staining (Figure VIII-5d) confirmed the collagenous nature of the thin layer observed on the borders of the beads, as showed by the blue color after the staining procedure. Interestingly, small blood vessels were found close to the beads, after 8 weeks of implant (black triangles), which may be beneficial to aid on the diffusion process in a cell encapsulation scenario.

VIII.4.5 *In vitro* Assay Using hASC-laden GG-MA/PLL PEC Beads

As a proof-of-concept, cell viability upon encapsulation was evaluated using human adipose-derived stem cells (hASCs) from knee fat pad. For that, hASCs were mixed with sterile GG-MA solution, at a final concentration of 1×10^6 cells.mL⁻¹. Then, cell-laden GG-MA/PLL beads were formed, as aforementioned

(Figure VIII-6a). The biocompatibility of the beads was assessed by Live/Dead and DAPI/Phalloidin staining (Figure VIII-6b), followed by quantification of live cells (Figure VIII-6c), up to 7 days of culturing. Viable cells, colored as green in Figure VIII-6b, were observed in all the tested timepoints (0, 1, 3 and 7 days) after encapsulation. Indeed, after the encapsulation process, nearly $62.43 \pm 4.36\%$ of cells were viable. The percentage of live cells increased along the culture time, and a significant increase on cell viability was observed after 7 days, with $87.09 \pm 6.16\%$ of encapsulated cells being viable (Figure VIII-6c).

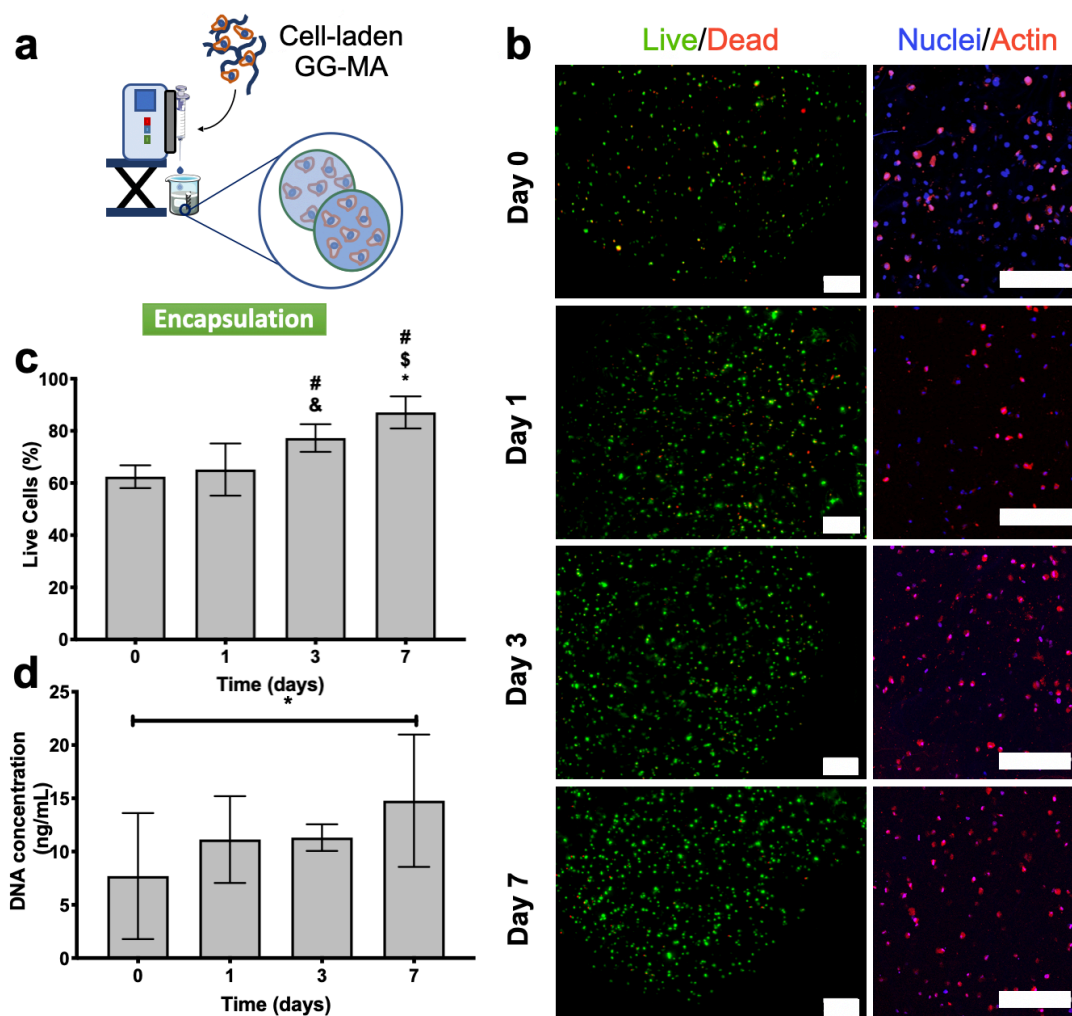


Figure VIII-6. *In vitro* assessment of GG-MA/PLL PEC beads effect on hASCs. a - Graphical representation of the encapsulation process, where hASCs are first embedded on GG-MA pre-gel that is then extruded to a PLL bath; b - Live/Dead and DAPI/Phalloidin stainings of hASCs, at different timepoints (0, 1, 3 and 7 days). For the Live/Dead staining, live cells are imaged as green (Calcein) and dead cells as red (PI). On the Nuclei/Actin staining, nuclei are stained in blue (DAPI) and the actin filaments of the cytoskeleton in red (Phalloidin); c - Percentage of live cells calculated from the Live/Dead staining. # - significant results to day 0 ($p < 0.0001$); & - significant results to day 1 ($p < 0.001$); & - significant results to day 1 ($p < 0.0001$); * - significant results to day 3 ($p < 0.01$); e - DNA quantification of encapsulated cells along culturing time. * represents p -value of 0.05. Results presented as average \pm SD ($n=9$).

DAPI/Phalloidin staining, used to mark respectively, the nuclei and actin filaments, allowed the visualization of cell morphology upon encapsulation. As expected, cells have a round morphology when encapsulated in GG-MA/PLL PEC beads, due to the 3D environment in which they are embedded. DNA quantification was also performed to estimate cell proliferation inside GG-MA/PLL PEC beads (Figure VIII-6d), and results show higher values of DNA at the latest timepoint, *i.e.* 7 days. Indeed, although DNA amount was nearly constant until this timepoint, a significative increase was noticed as compared to the moment of encapsulation.

To further investigate the possible cytotoxic effect of GG-MA/PLL PEC beads on surrounding cells, hASCs were cultured with GG-MA/PLL PEC leachable (Figure VIII-7a) followed by assessment of cell proliferation and metabolic activity (Figure VIII-7b and Figure VIII-7c, respectively). As depicted in Figure VIII-7b, hASCs culture showed a faster growth profile, as compared to the positive control (TCPS leachable), although this difference is not significant. As expected, cells incubated with latex leachable did not proliferate and after 1 day of incubation, cells were detached from the well, as shown by the cell index close to zero. As plotted in Figure VIII-7c, the metabolic activity of hASCs incubated with the leachable released from the beads was similar to the measured for cells incubated with TCPS leachable (positive control, reference value of 100%). Again, the incubation with latex resulted in deleterious toxic effect to cells, as noticed by the drastic decrease on metabolic activity.

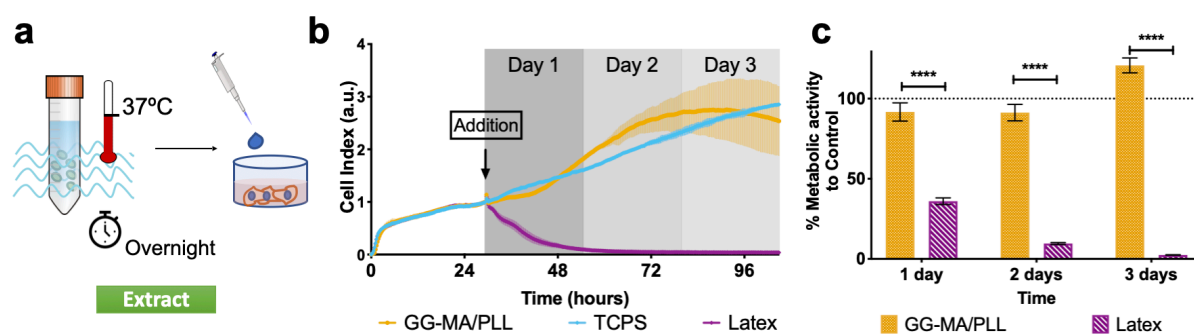


Figure VIII-7. *In vitro* assessment of the effect of GG-MA/PLL PEC leachable on hASCs. a - Schematic representation of the leachables extraction process. Beads are incubated overnight at 37 °C in MEM culture media, and the resulting conditioned media is then added to cell culture; b - Real-time proliferation of hASCs upon contact with GG-MA/PLL leachables; and c - Metabolic activity of hASCs after contact with GG-MA/PLL leachables, normalized by the metabolic activity measured for cells incubated with culture media. Scale bars (b,d): 200 μ m. **** shows statistical difference with $p < 0.0001$. Results presented as average \pm SD ($n=9$).

Previous studies on GG-MA hydrogels showed the biocompatible nature of these hydrogels [64, 65]. Nevertheless, the use of GG-MA/PLL PEC beads is new, and its biocompatibility must be addressed,

mostly due to the toxic effect attributed to PLL [66]. The effect of biomaterial leachable on cell's proliferation and metabolic activity is considered a standard procedure and a good indicator of biomaterial's biocompatibility [67]. Therefore, the obtained results confirmed that the possible by-products released from the GG-MA/PLL beads would not affect the neighbor cells, and that the developed beads are biocompatible, grounding the potential of GG-MA/PLL beads to be used as cell encapsulation system.

VIII.5 Conclusion

Methacrylated gellan gum/poly-L-lysine beads can be easily prepared using a low-cost, one-step protocol, in opposition to the actual gold-standard method - the APA system - that requires several steps for production and encapsulation. The obtained beads are stable upon immersion in cell culture media as well as in phosphate buffered saline for at least 14 days. With only one polyelectrolyte complex layer, it was possible to obtain a semi-permeable membrane, which protects the hydrogel core from infiltration of high molecular weight molecules. Additionally, the flow of small molecules through the bead's membrane in both directions (in and out), is not affected. This is a crucial need when cell encapsulation strategies, and thenceforth immunoprotection, are envisaged. The feasibility of using this type of beads for cell-based therapies was additionally strengthened by the immunocompatibility study. The data herein collected suggests that the developed beads do not exert a significative immune reaction, both *in vitro* and *in vivo*. In addition, methacrylated gellan gum/poly-L-lysine polyelectrolyte complex beads showed great promise as vehicles for cell delivery, as human adipose-derived stem cells were encapsulated within the hydrogel core of these beads and remained viable along the culturing periods. Thus, a new methodology for the production of cell-laden polyelectrolyte complex methacrylated gellan gum/poly-L-lysine beads was proposed which can be easily applied to cell-based therapies requiring immunoprotection, such as Type I diabetes and hepatic disorders.

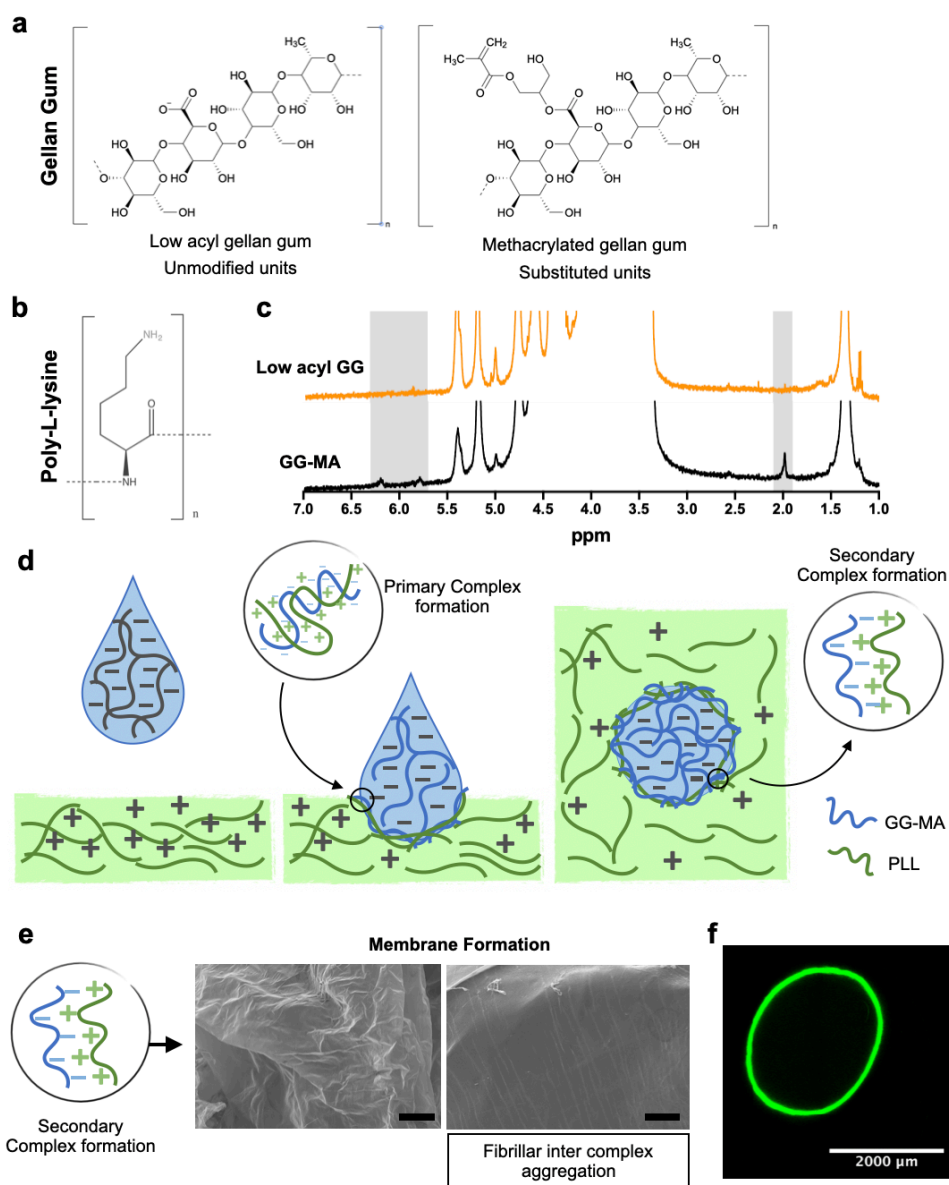
VIII.6 Acknowledgements

Silvia Vieira was awarded an FCT PhD scholarship (SFRH/BD/102710/2014) and also acknowledges the IACOBUS scholarship (Erorregión Galicia - Norte de Portugal, Agrupación Europea de Cooperación Territorial) and Award "Príncipe da Beira for Biomedical Sciences, 2017". The FCT distinctions attributed to J. Miguel Oliveira (IF/01285/2015) and J. Silva-Correia (IF/00115/2015) under the Investigator FCT program are also greatly acknowledged. Alain da Silva Morais acknowledges ERC-2012-ADG 20120216-

321266 (ComplexiTE) for his Postdoc fellowship. This work was also partially supported by Xunta de Galicia (Grupo de referencia competitiva ED431C 2016/041) and the project FROnTHERA (No. NORTE-01-0145-FEDER-000023), supported by Norte Portugal Regional Operational Programme (No. NORTE 2020), under the PORTUGAL 2020 Partnership Agreement, through the European Regional Development Fund (ERDF). The authors are also thankful to FCT for the funds provided under the 3BioMeD project (JICAM/0001/2017). The authors would like to also acknowledge the contribution of Luísa Rodrigues regarding the XPS analysis performed for this work; Elsa Ribeiro and Isabel Leonor that performed the SEM and bioAFM acquisition; and Teresa Oliveira for histology samples processing.

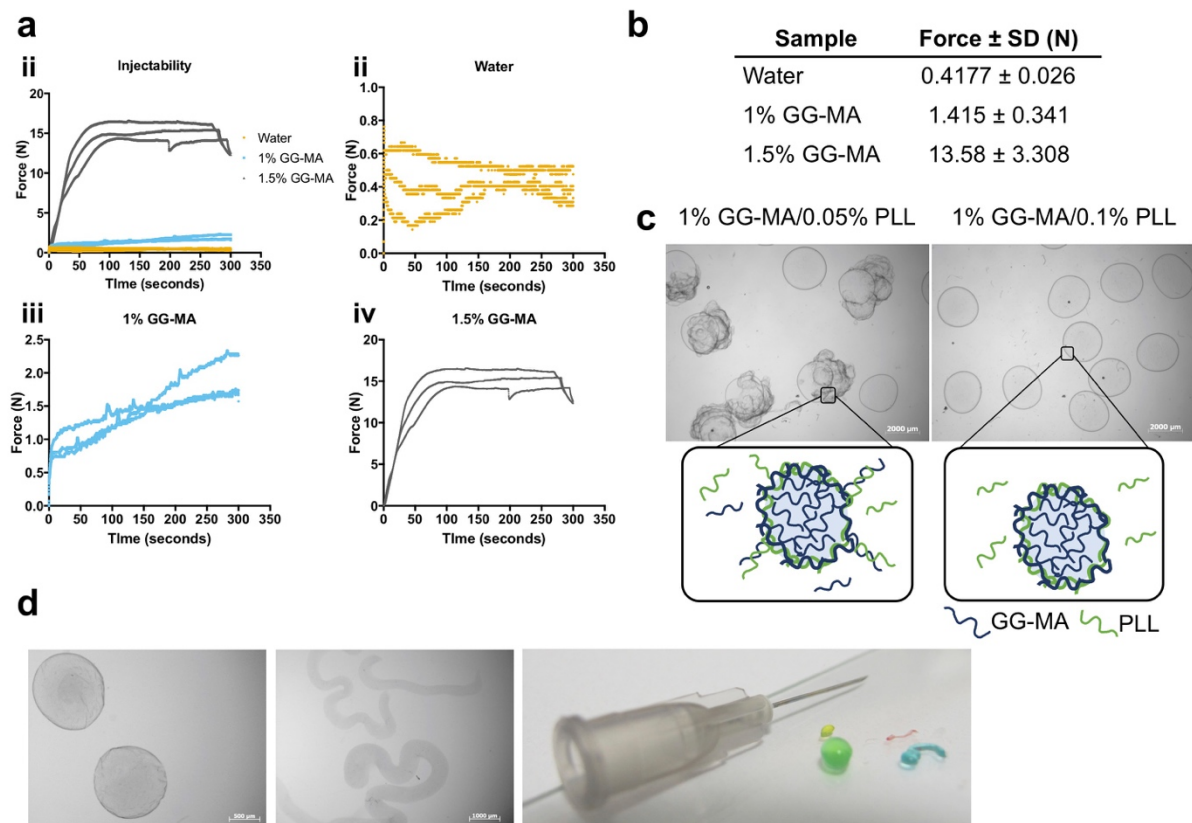
VIII.7 Supplementary Information

VIII.7.1 PEC Formation Reaction



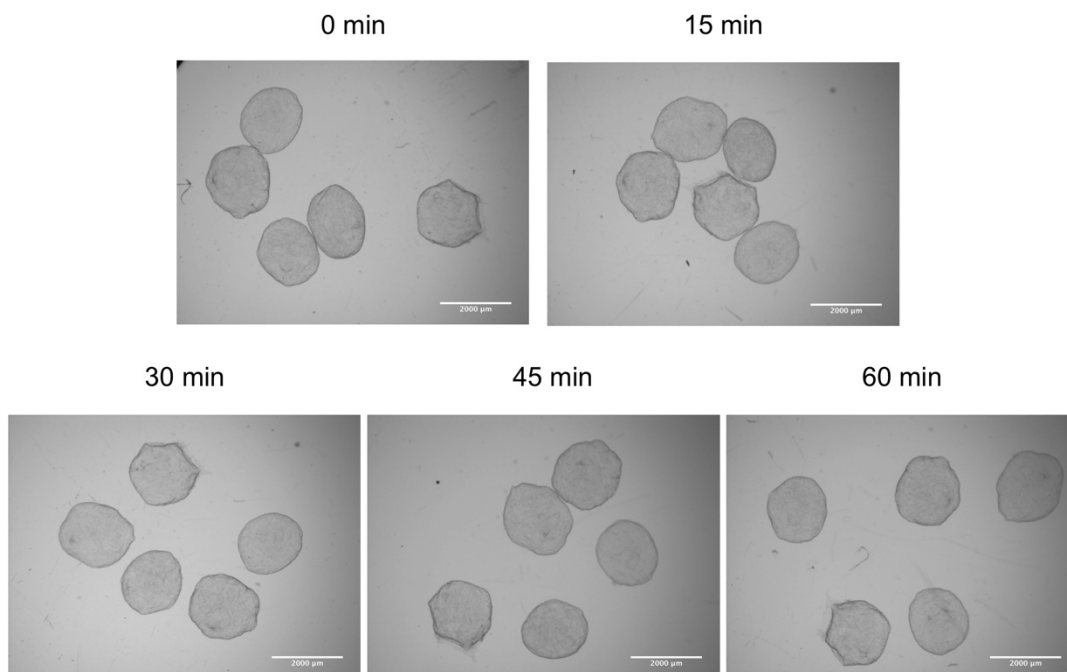
Supplementary Figure VIII-1. Polyelectrolyte formation. a - Methacrylated gellan gum (GG-MA) chemical structure: non-modified repeating units and substituted units. b - Chemical structure of Poly-L-lysine (PLL); c - ^1H -NMR spectra of GG-MA and low acyl GG; d - Schematic representation of the polyelectrolyte complex (PEC) formation upon contact between the GG-MA solution with the PLL bath. Firstly, the polyelectrolyte networks interact via electrostatic forces, forming a random primary complex. Then, chains start to organize into secondary complex structures, where new bonds are formed, and polymeric distortion is corrected. e - As a result of PEC formation a membrane is formed, that surrounds a hydrogel core made from GG-MA. SEM analysis shows nanofibers on the PEC membrane that point to a fibrillar inter complex aggregation of the PEC. Scale bar: 100 μm (left image) and 10 μm (right image). f - Confocal images of PEC formed with FITC-labelled PLL showed that PLL is located only at the surface of the hydrogel bead.

VIII.7.2 PEC Formation Conditions



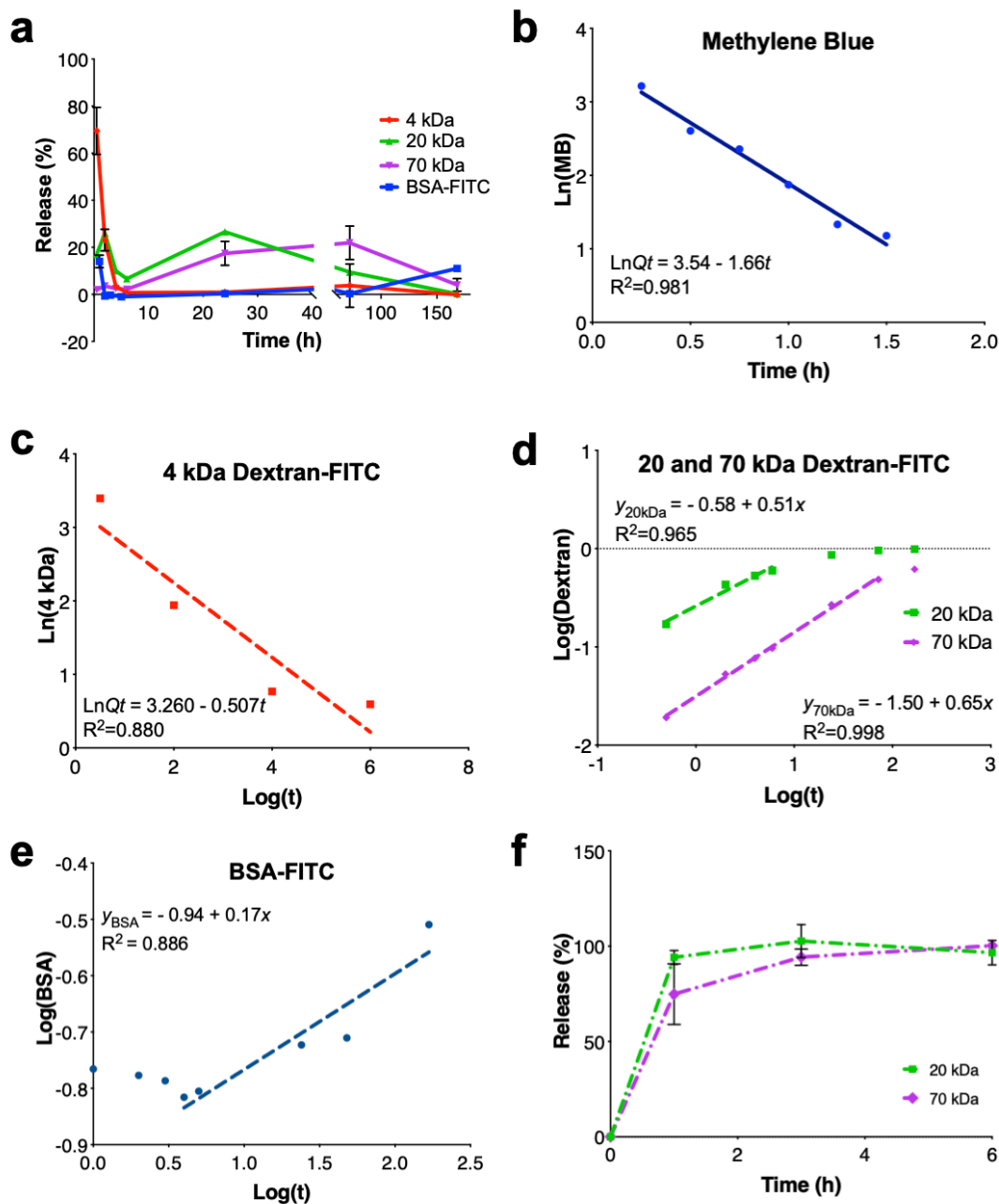
Supplementary Figure VIII-2. Polyelectrolyte complex optimization. a - Two concentrations of methacrylated gellan gum (GG-MA) were tested, however 1.5% (w/v) had to be discarded due to its poor injection ability. b - Quantitative comparison of the force (N) needed to extrude GG-MA solutions through a 30 G needle. As compared to 1% (w/v) GG-MA, the injection of 1.5% (w/v) solutions required more than three times the force used to inject the 1% (w/v) solution, which resulted in frequent needle clothing. c - Two different concentrations of poly-L-lysine were tested for the formation of the PEC hydrogels. While 0.05% (w/v) resulted in irregular beads, 0.1% (w/v) solution made close round beads. d - Besides beads, other shapes can be prepared using this technique as smaller beads or fibers.

VIII.7.3 Mechanical Stability



Supplementary Figure VIII-3. Mechanical stability of the GG-MA/PLL PEC beads. The mechanical stability of the beads was attested via a rotational stress test. For that, the beads were centrifuged in PBS media under a speed of 200 g at room temperature. After 15 minutes of rotation, the material was retrieved and observed to assess the damage caused by centrifugation. After 60 minutes of rotation no significant damage was observed.

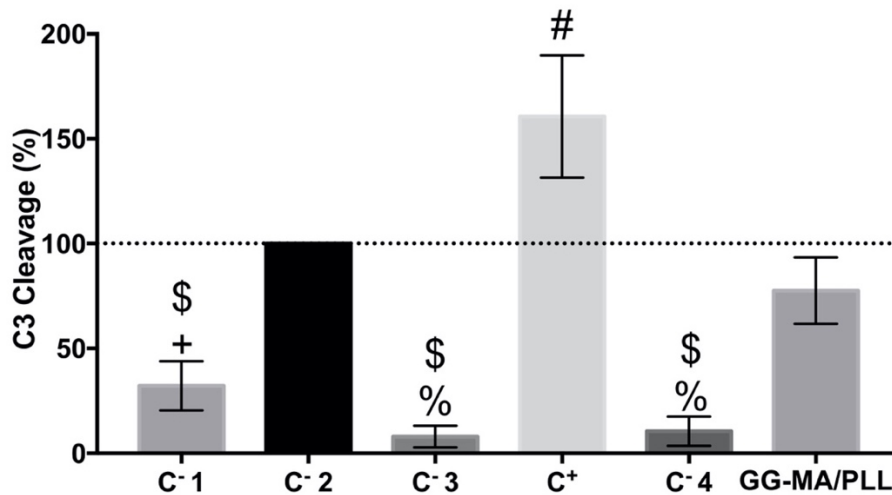
VIII.7.4 Release Analysis and Modeling



Supplementary Figure VIII-4. Release analysis a - Release profiles of 4, 20 and 70 kDa dextran-FITC and BSA-FITC. 4 kDa showed a burst release from the GG-MA/PLL PEC beads, due to its small molecular weight. On the other hand, BSA-FITC as well as 20 and 70 kDa dextran-FITC showed a more controlled release profile. Interestingly, BSA-FITC registered a small release at early timepoints ($14.0 \pm 2.65\%$), that can be attributed to a release of BSA molecules that were entrapped in the PEC membrane, and not in the hydrogel matrix. Afterwards, no considerable release from the hydrogel matrix was noticed until 168 hours of incubation ($11.0 \pm 1.0\%$); b - Modeling of the release kinetics of MB by the First-order model, $\text{Ln}(Q_t) = \text{Ln}(Q_0) - kt$, where Q_t is the non-released amount of active agent on time t , Q_0 is the initial amount of drug dissolved, and k is the first-order constant; c - Release kinetics of 4 kDa dextran-FITC, using the First-order kinetics

model; d - Modeling of release kinetics for 20 and 70 kDa dextran-FITC by the Korsmeyer-Peppas power law ($M_i/M_\infty = kt^n$, where M_i is drug released over time t , M_∞ is drug at the equilibrium state, k is the release velocity constant, and n is the release exponent in function of time t , determined by the portion of release curve where $M_i/M_\infty < 0.60$). Here, we used its logarithmic version for linearity ($y = b + mx$): $\log(M_i/M_\infty) = \log(k) + n \log(t)$. The obtained n values were 0.51 and 0.65 for 20 and 70 kDa dextran-FITC, respectively. These are between $0.43 < n < 0.85$, which is the theoretical value for spherical matrices. Thence, this modulation suggests a non-Fickian transport, with release being governed by diffusion and swelling processes; e - Korsmeyer-Peppas modulation of BSA-FITC release showed a n of 0.17. This value is below the theoretical range of this model, pointing to a quasi-Fickian release kinetics, that is hindered by the presence of a PEC membrane; f - Release profile of 20 and 70 kDa dextran-FITC from ionically crosslinked GG-MA beads, showing its rapid release to the surrounding PBS solution.

VIII.7.5 Complement System Activation



Supplementary Figure VIII-5. Quantification of the complement system activation. Quantification of the degradation of the C3 protein in plasma incubated at 4 °C (C-1); plasma incubated with EDTA (C-3); plasma incubated with Zymosan (C+); plasma incubated with EDTA and Zymosan (C-4); and plasma incubated with GG-MA/PLL PEC beads. C3 degradation products were detected by Western Blot, using plasma incubated with PBS as reference value (C-2). Results presented as average \pm SD; # - significant results to all other conditions ($p < 0.0001$); \$ - significant results compared to C2 ($p < 0.0001$); + - significant results to GG-MA/PLL ($p = 0.0001$); % - significant results as compared to GG-MA/PLL ($p < 0.0001$). ($F_{5,30} = 97.7$, $p < 0.0001$).

VIII.7.6 Surface Elemental Composition

Supplementary Table VIII-1. Surface elemental composition measured by XPS. The relative atomic percentages of nitrogen, oxygen and carbon, found in GG-MA/PLL, PLL and GG-MA are presented. Analysis was also performed in GG-LA to confirm that the vestigial amounts of nitrogen found in GG-MA powder, comes from external impurities present in the raw material. Carbon to nitrogen ratios are also presented. Results showed as average \pm SD of at least three independent measurements.

	N %	O %	C %	C/N
GG-MA/PLL	3.30 \pm 0.11	33.68 \pm 0.19	63.02 \pm 0.20	19.10
PLL	11.01 \pm 0.31	15.10 \pm 0.49	73.89 \pm 0.54	6.71
GG-MA	0.45 \pm 0.09	33.88 \pm 0.21	65.67 \pm 0.22	145.93
GG-LA	0.91 \pm 0.12	27.33 \pm 0.21	71.77 \pm 0.23	78.87

VIII.7.7 Supplementary Movies



Supplementary Movie VIII-1. Formation of PEC beads.



Supplementary Movie VIII-2. Diffusion of Methylene Blue into a GG-MA/PLL PEC bead.

VIII.8 References

1. Zhang, C., et al., *Therapeutic potential of human minor salivary gland epithelial progenitor cells in liver regeneration*. Scientific Reports, 2017. **7**: p. 11.
2. Zong, X.M., et al., *Transplantation of VEGF-mediated bone marrow mesenchymal stem cells promotes functional improvement in a rat acute cerebral infarction model*. Brain Research, 2017. **1676**: p. 9-18.
3. Jin, X., T. Lin, and Y. Xu, *Stem Cell Therapy and Immunological Rejection in Animal Models*. Current Molecular Pharmacology, 2016. **9**(4): p. 284-288.

4. Orive, G., et al., *Cell encapsulation: technical and clinical advances*. Trends in Pharmacological Sciences, 2015. **36**(8): p. 537-46.
5. Bisceglie, V., *Über die antineoplastische Immunität*. Zeitschrift für Krebsforschung, 1934. **40**: p. 122-140.
6. Algire, G.H., *An Adaptation of the Transparent-Chamber Technique to the Mouse*. Journal of the National Cancer Institute, 1943. **4**: p. 1-11.
7. Lim, F. and A.M. Sun, *Microencapsulated islets as bioartificial endocrine pancreas*. Science (New York, N.Y.), 1980. **210**: p. 908-910.
8. Vegas, A.J., et al., *Long-term glycemic control using polymer-encapsulated human stem cell-derived beta cells in immune-competent mice*. Nature Medicine, 2016.
9. Arifin, D.R., et al., *Magnetoencapsulated human islets xenotransplanted into swine: a comparison of different transplantation sites*. Xenotransplantation, 2016. **23**(3): p. 211-221.
10. Scharp, D.W. and P. Marchetti, *Encapsulated islets for diabetes therapy: history, current progress, and critical issues requiring solution*. Advanced Drug Delivery Reviews, 2014. **67-68**: p. 35-73.
11. Bochenek, M.A., et al., *Alginate encapsulation as long-term immune protection of allogeneic pancreatic islet cells transplanted into the omental bursa of macaques*. Nature Biomedical Engineering, 2018. **2**(11): p. 810-821.
12. Orive, G., et al., *Engineering a Clinically Translatable Bioartificial Pancreas to Treat Type I Diabetes*. Trends in Biotechnology, 2018. **36**(4): p. 445-456.
13. Wang, Q. and B.Z. Newby, *Layer-by-layer Polyelectrolytes Coating of Alginate Microgels for Sustained Release of Sodium Benzoate and Zosteric Acid*. Journal of Drug Delivery Science and Technology, 2018. **46**: p. 46-54.
14. Meka, V.S., et al., *A comprehensive review on polyelectrolyte complexes*. Drug Discovery Today, 2017. **22**(11): p. 1697-1706.
15. Coutinho, D.F., et al., *Microfabricated photocrosslinkable polyelectrolyte-complex of chitosan and methacrylated gellan gum*. Journal of Materials Chemistry, 2012. **22**: p. 17262.
16. Minkal, M. Ahuja, and D.C. Bhatt, *Polyelectrolyte complex of carboxymethyl gum katira-chitosan: Preparation and characterization*. International Journal of Biological Macromolecules, 2018. **106**: p. 1184-1191.
17. Wan, A.C., et al., *Multicomponent fibers by multi-interfacial polyelectrolyte complexation*. Advanced Healthcare Materials, 2012. **1**(1): p. 101-5.
18. Yim, E.K., et al., *Proliferation and differentiation of human mesenchymal stem cell encapsulated in polyelectrolyte complexation fibrous scaffold*. Biomaterials, 2006. **27**(36): p. 6111-22.
19. Costa, R.R. and J.F. Mano, *Polyelectrolyte multilayered assemblies in biomedical technologies*. Chemical Society Reviews, 2014. **43**(10): p. 3453-79.

20. Kang, K.S., et al., *Agar-like polysaccharide produced by a pseudomonas species: production and basic properties*. Applied and Environmental Microbiology, 1982. **43**(5): p. 1086-91.
21. Chandrasekaran, R., et al., *The crystal structure of gellan*. Carbohydrate Research, 1988. **175**: p. 1-15.
22. Coutinho, D.F., et al., *Modified Gellan Gum hydrogels with tunable physical and mechanical properties*. Biomaterials, 2010. **31**(29): p. 7494-502.
23. Silva-Correia, J., et al., *Gellan gum-based hydrogels for intervertebral disc tissue-engineering applications*. Journal of Tissue Engineering and Regenerative Medicine, 2011. **5**: p. e97-107.
24. Thomas, D., T. O'Brien, and A. Pandit, *Toward Customized Extracellular Niche Engineering: Progress in Cell-Entrapment Technologies*. Advanced Materials, 2017.
25. Juste, S., et al., *Effect of poly-L-lysine coating on macrophage activation by alginate-based microcapsules: assessment using a new in vitro method*. Journal of Biomedical Materials Research Part A, 2005. **72**(4): p. 389-98.
26. Hamcerencu, M., et al., *Synthesis and characterization of new unsaturated esters of Gellan Gum*. Carbohydrate Polymers, 2008. **71**(1): p. 92-100.
27. Vieira, S., et al., *Self-mineralizing Ca-enriched methacrylated gellan gum beads for bone tissue engineering*. Acta Biomaterialia, 2019.
28. Harrington, S., et al., *Hyaluronic Acid/Collagen Hydrogel as an Alternative to Alginate for Long-Term Immunoprotected Islet Transplantation*. Tissue Engineering Part A, 2017.
29. Pereira, P., et al., *Biocompatibility of a self-assembled glycol chitosan nanogel*. Toxicology In Vitro, 2015. **29**(3): p. 638-646.
30. Simón-Vázquez, R., et al., *Analysis of the activation routes induced by different metal oxide nanoparticles on human lung epithelial cells*. Future Science OA, 2016. **2**(2): p. FSO118.
31. Cerqueira, M.T., et al., *Human adipose stem cells cell sheet constructs impact epidermal morphogenesis in full-thickness excisional wounds*. Biomacromolecules, 2013. **14**(11): p. 3997-4008.
32. Standardization, I.O.f., *ISO 10993-5:2009 - Biological evaluation of medical devices, in Part 5: Tests for in vitro cytotoxicity*. 2009.
33. Tsuchida, E., *Formation of Polyelectrolyte Complexes and Their Structures*. Journal of Macromolecular Science-Pure and Applied Chemistry, 1994. **A31**(1): p. 1-15.
34. Luo, Y. and Q. Wang, *Recent development of chitosan-based polyelectrolyte complexes with natural polysaccharides for drug delivery*. International Journal of Biological Macromolecules, 2014. **64**: p. 353-67.
35. Zhang, Y., et al., *The influence of ionic strength and mixing ratio on the colloidal stability of PDAC/PSS polyelectrolyte complexes*. Soft Matter, 2015. **11**(37): p. 7392-401.

36. Tam, S.K., et al., *Physicochemical model of alginate-poly-L-lysine microcapsules defined at the micrometric/nanometric scale using ATR-FTIR, XPS, and ToF-SIMS*. *Biomaterials*, 2005. **26**: p. 6950-61.
37. Amorim, S., et al., *Hyaluronic acid/poly-L-lysine bilayered silica nanoparticles enhance the osteogenic differentiation of human mesenchymal stem cells*. *Journal of Materials Chemistry B*, 2014. **2**(40): p. 6939-6946.
38. de Vos, P., et al., *The association between in vivo physicochemical changes and inflammatory responses against alginate based microcapsules*. *Biomaterials*, 2012. **33**(22): p. 5552-9.
39. de Vos, P., C.G. Hoogmoed, and H.J. Busscher, *Chemistry and biocompatibility of alginate-PLL capsules for immunoprotection of mammalian cells*. *Journal of Biomedical Materials Research*, 2002. **60**(2): p. 252-9.
40. de Vos, P., et al., *Alginate-based microcapsules for immunoisolation of pancreatic islets*. *Biomaterials*, 2006. **27**: p. 5603-5617.
41. de Vos, P., et al., *Zeta-potentials of alginate-PLL capsules: a predictive measure for biocompatibility?* *Journal of Biomedical Materials Research Part A*, 2007. **80**(4): p. 813-9.
42. Burke, S.E. and C.J. Barrett, *pH-Responsive Properties of Multilayered Poly(L-lysine)/Hyaluronic Acid Surfaces*. *Biomacromolecules*, 2003. **4**(6): p. 1773-1783.
43. Morris, E.R., K. Nishinari, and M. Rinaudo, *Gelation of gellan – A review*. *Food Hydrocolloids*, 2012. **28**: p. 373-411.
44. Picone, C.S.F. and R.L. Cunha, *Influence of pH on formation and properties of gellan gels*. *Carbohydrate Polymers*, 2011. **84**: p. 662-668.
45. Suri, S. and R. Banerjee, *In vitro evaluation of in situ gels as short term vitreous substitutes*. *Journal of Biomedical Materials Research Part A*, 2006. **79**(3): p. 650-64.
46. Correia, C.R., et al., *Liquified chitosan-alginate multilayer capsules incorporating poly(L-lactic acid) microparticles as cell carriers*. *Soft Matter*, 2013. **9**(7): p. 2125-2130.
47. Choe, G., et al., *Hydrogel Biomaterials for Stem Cell Microencapsulation*. *Polymers (Basel)*, 2018. **10**(9).
48. *Mathematical models of drug release*, in *Strategies to Modify the Drug Release from Pharmaceutical Systems*, M.L. Bruschi, Editor. 2015, Woodhead Publishing. p. 63-86.
49. Costa, P. and J.M. Sousa Lobo, *Modeling and comparison of dissolution profiles*. *European Journal of Pharmaceutical Sciences*, 2001. **13**(2): p. 123-133.
50. Lozano, R., et al., *3D printing of layered brain-like structures using peptide modified gellan gum substrates*. *Biomaterials*, 2015. **67**: p. 264-273.
51. Soto, A.M., et al., *Optical Projection Tomography Technique for Image Texture and Mass Transport Studies in Hydrogels Based on Gellan Gum*. *Langmuir*, 2016. **32**(20): p. 5173-82.

52. Desai, T.A. and Q. Tang, *Islet encapsulation therapy – racing towards the finish line?* Nature Reviews Endocrinology, 2018. **14**(11): p. 630-632.
53. Janeway, C., *Immunobiology Five*. 2001: Garland Pub.
54. Berghaus, L.J., et al., *Innate immune responses of primary murine macrophage-lineage cells and RAW 264.7 cells to ligands of Toll-like receptors 2, 3, and 4*. Comparative Immunology, Microbiology and Infectious Diseases, 2010. **33**(5): p. 443-54.
55. Ji, K.Y., et al., *The enhancing immune response and anti-inflammatory effects of Anemarrhena asphodeloides extract in RAW 264.7 cells*. Phytomedicine, 2019. **59**: p. 152789.
56. Bosshart, H. and M. Heinzemann, *THP-1 cells as a model for human monocytes*. Ann Transl Med, 2016. **4**(21): p. 438.
57. Chanput, W., J.J. Mes, and H.J. Wichers, *THP-1 cell line: an in vitro cell model for immune modulation approach*. International Immunopharmacology, 2014. **23**(1): p. 37-45.
58. Arango Duque, G. and A. Descoteaux, *Macrophage cytokines: involvement in immunity and infectious diseases*. Frontiers in Immunology, 2014. **5**: p. 491.
59. Lock, A., J. Cornish, and D.S. Musson, *The Role of In Vitro Immune Response Assessment for Biomaterials*. Journal of Functional Biomaterials, 2019. **10**(3).
60. Berger, A., *Th1 and Th2 responses: what are they?* BMJ, 2000. **321**(7258): p. 424.
61. Vishwakarma, A., et al., *Engineering Immunomodulatory Biomaterials To Tune the Inflammatory Response*. Trends in Biotechnology, 2016. **34**(6): p. 470-482.
62. Park, J., M.H. Gerber, and J.E. Babensee, *Phenotype and polarization of autologous T cells by biomaterial-treated dendritic cells*. Journal of Biomedical Materials Research Part A, 2015. **103**(1): p. 170-84.
63. Chen, R., et al., *In Vitro Response of Human Peripheral Blood Mononuclear Cells (PBMC) to Collagen Films Treated with Cold Plasma*. Polymers (Basel), 2017. **9**(7).
64. Silva-Correia, J., et al., *Biocompatibility evaluation of ionic- and photo-crosslinked methacrylated gellan gum hydrogels: in vitro and in vivo study*. Advanced Healthcare Materials, 2013. **2**(4): p. 568-75.
65. Oliveira, J.T., et al., *Gellan gum: a new biomaterial for cartilage tissue engineering applications*. Journal of Biomedical Materials Research Part A. **93**(3): p. 852-63.
66. Strand, B.L., et al., *Poly-L-Lysine induces fibrosis on alginate microcapsules via the induction of cytokines*. Cell Transplantation, 2001. **10**(3): p. 263-75.
67. Li, W., J. Zhou, and Y. Xu, *Study of the in vitro cytotoxicity testing of medical devices*. Biomedical Reports, 2015. **3**(5): p. 617-620.

SECTION 4: Concluding Remarks

Chapter IX: General Conclusions and Future Perspectives

IX.1 General Conclusions

Tissue Engineering and Regenerative Medicine (TERM) have changed the paradigm in medicine. We are now living an extraordinary era where the boundaries of medical and scientific achievements are pushed a lot forward, and the hopes in the future of medicine are quite elevated. If it is true that TERM raised the bar on the expectations for the future of medical practice, it is no less evident that hydrogels are of paramount importance to such reality.

As discussed in the first chapters of this thesis, hydrogels have been extensively used by the scientific community. That fact is reflected in the plethora of different materials and processing methods currently being used for research and development purposes, as introduced in Chapter I. This chapter aimed to give an insight into natural-based polymers and the processing techniques that lead to their transition into hydrogels.

However, the material source and the used processing approach are only two pieces of a more intricate puzzle. Like a Tangram, the hydrogel properties can result from the combination of different factors, and if the pieces are changed, the final hydrogel will show different outcomes. The combinations are virtually infinite, which rendered hydrogels as an interesting tool to solve the most complex challenges on TERM. Drug delivery, cell protection, cell delivery, imaging, tissue regeneration, or organ fabrication are just a few of the fields where hydrogels have been studied and used with favorable results. With such a broad spectrum of necessities and opportunities, it is crucial to understand how to tackle each problem with specificity, and tailor the hydrogel to meet the exact needs of the approach. Thus, Chapter II discussed the influence of different hydrogel formulations on the final cell-biomaterial interactions, and the strategies used to tailor that interface.

Bearing this in mind, this thesis aimed to study the properties of gellan gum, particularly methacrylated gellan gum, when crosslinked by means of using different methods. The methacrylated gellan gum used on the scope of this thesis was previously developed by our group, and it is a grand promise for future TERM applications. Thus, it was particularly relevant to study its behavior and characteristics under different conditions.

Due to its intrinsic properties, gellan gum is typically crosslinked using ionic solutions, such as Ca^{2+} - or Mg^{2+} -based solutions. The same goes for methacrylated gellan gum, which retains the ionic-responsive properties of low-acyl gellan gum. The ionic-driven crosslink can be achieved by different means, including the addition of cell culture media, ionic-based buffers, or merely ionic solutions.

In Chapter IV, the affinity of methacrylated gellan gum to divalent ions was used to prepare calcium reservoirs, envisioning bone tissue engineering applications. For this work, hydrogel beads were crosslinked with a calcium solution, a procedure already described in the literature to prepare gellan gum-based hydrogels. Nevertheless, a relationship between the application of calcium ions on the fabrication of gellan gum hydrogels and calcification of such hydrogels was never reported. Without any further supplementation, the produced hydrogels prompted the formation of a mineralized layer on their surface. This phenomenon was observed *in vitro*, in the presence of simulated body fluid, and *in vivo*, after subcutaneous implantation. The presence of a calcium-enriched environment, and the anionic nature of the methacrylated gellan gum polymer, promoted the deposition of calcium phosphates along the incubation time. The mineral layer was visible with the naked eye, and different characterization techniques confirmed the formation of semi-crystalline hydroxyapatite on hydrogels' surface. The mild processing method used to prepare the beads allowed the encapsulation of different model molecules, including dextran of different molecular weights and dexamethasone, that were used to study the permeability of the produced hydrogel. It was shown that the diffusion of molecules through the hydrogel is mainly dependent on the molecule's size. However, all the encapsulated molecules were released on the first hours after incubation, before the build-up of the mineral layer. Thence, the proposed hydrogel can be used to promote a synergistic therapeutic, where the effect of drugs such as dexamethasone could be combined with the pro-osteogenic cues provided by the hydrogel's mineralization. The host immune response to the hydrogel beads was also considered, and it was shown that hydrogels' presence did not trigger the complement system's activation, the primary effector of the innate immune response. Possible cellular and humoral immune responses were also measured, showing that calcium-based hydrogel beads triggered a mild pro-inflammatory state, and also signs of inflammation control. The simultaneous

secretion of cytokines involved in pro-inflammatory and regenerative responses indicate that the developed hydrogels can elicit an appropriate immune response, needed for the regenerative process. More than showing the potential of methacrylated gellan gum hydrogels for bone tissue engineering approaches, this chapter unveiled how the crosslinking method affects the final material response to the physiological environment, and the importance of tailoring the right crosslinking solution to the final intended application.

The ionic crosslinking approach was also used in Chapter V, in order to prepare injectable traceable hydrogels. Minimally invasive approaches that rely on the injection of the material into the body may greatly benefit from traceable features, as they can confirm the correct delivery of the material, prevent material misplacement, and allow its follow-up over time. Bearing this in mind, methacrylated gellan gum was used as a reservoir of manganese, a divalent paramagnetic ion, traceable by magnetic resonance imaging (MRI). Using only the intrinsic properties of the methacrylated gellan gum polymer, it was possible to give a functional characteristic to the produced hydrogel. Different concentrations of manganese were incorporated within the gellan gum matrix, without affecting the rheological properties of the material. The hydrogel was thus easily extruded, forming a continuous fiber upon contact with ion-rich solutions. This work was mainly focused on the interaction and behavior of the hydrogel in conditions similar to those observed in the vicinities of the central nervous system, envisioning an application towards amyotrophic lateral sclerosis and stroke. Therefore, gellan gum was crosslinked with artificial cerebrospinal fluid to mimic the target environment. The developed hydrogel showed high stability along time, and the incorporation of a suitable concentration of manganese ions allowed their tracking by MRI. The MRI detection was feasible *in vitro* but also *in vivo*, after injection in the intrathecal and intracerebral space. Regardless, the signal intensity was dependent on the injection site. The material injected in the brain showed a more intense signal as compared to the material injected in the spinal cord. That can be attributed to the dynamic environment of the intrathecal space, where the cerebrospinal fluid continuously flows. Such results point out the importance of tailoring the manganese concentration to the injection site. Additionally, human adipose stem cells were encapsulated within the polymeric matrix to ascertain the possibility of using the traceable hydrogels as cell carriers. The results showed that cells remain viable on the developed hydrogels, paving the way for future studies on cell-based therapies targeting the central nervous system.

Although the results obtained in the previous Chapter V tackled the potential of methacrylated gellan gum hydrogels on cell-based therapies, the stability of the hydrogel once formed may hinder the success of

approaches that rely on the effective delivery of cells to the injured site. That is, strategies where cells must exit the hydrogel to proliferate and differentiate, instead of only releasing important therapeutic factors. With that goal in mind, Chapter VI explores hydrogel blends prepared from methacrylated gellan gum and hyaluronic acid. While gellan gum allows the incorporation of manganese ions and ionic crosslinking, the presence of hyaluronic acid decreases hydrogel stability and increases degradation over time. As a result, encapsulated cells can migrate from the hydrogel to the surrounding tissues, where they can exert their therapeutic role. The introduction of hyaluronic acid still allowed the recognition of the hydrogel by MRI techniques, and was also compatible with the injection protocol, meaning that gellan gum polymer chains were still available for the interaction with ions. Similar to the findings described in Chapter V, human adipose stem cells were successfully encapsulated within hydrogel fibers and remained viable for up to 14 days. As expected, the introduction of hyaluronic acid allowed the cell escape and migration from the fibers to the external environment. Thence, it was shown that traceable Mn-based methacrylated gellan gum and hyaluronic acid hydrogel blends could be prepared not only for cell encapsulation but also for tuning cell delivery.

Another approach used on the present thesis was based on the anionic nature of gellan gum and its effect when combined with a cationic polymer, via polyelectrolyte complexation. As a result, methacrylated gellan gum and poly-L-lysine were combined in defined concentrations, and the resulting composition patented for use in veterinary or human medicine, as described in Chapter VII. The proof-of-concept was performed using hydrogel beads, comprising a gellan gum core surrounded by a polyelectrolyte semipermeable membrane that results from the interaction between the polymers with the opposite charge. The resulting hydrogels showed distinct diffusion profiles when used as a depot for molecules of different sizes. Human adipose stem cells and androgen-sensitive human prostate adenocarcinoma (LNCaP) cells were successfully encapsulated inside the hydrogel beads and remained viable for up to 7 days of culture.

The developed technology was studied in greater detail on Chapter VIII, as a prospective substitute to the layer-by-layer methodology currently used on cell immunoisolation. This strategy requires the use of stable materials that do not compromise the desired immunoprotection. Additionally, the interface between the hydrogel and the physiologic environment must allow the passage of small nutrients but block the critical effectors of the immune system. Contrarily to what occurs on ionic-cross linked hydrogels, the beads prepared using polyelectrolyte complexation showed distinct permeability to molecules of different molecular weight, and substantially block the diffusion of molecules larger than 70 kDa. That can be

attributed to the formation of a fibrillar inter complex aggregation of the polyelectrolyte complex, resulting in a semipermeable membrane that surrounds a hydrogel core. This membrane is stable in a wide range of conditions, including the presence of enzymes or pH modifications, that occur in physiologic conditions. Besides stability and permeability, the immunocompatibility studies supported the application of this approach to cell-based therapies. *In vitro* assays, based on the activation of the complement system, macrophage proliferation, and cytokine release, showed that the developed beads do not elicit an exacerbate immune reaction.

Interestingly, the amount of free poly-L-lysine molecules present at the surface of the developed beads was lower than the values reported in the literature for other immunoprotective systems. Instead of covering previously formed beads with poly-L-lysine, the developed technology uses a one-step approach, where methacrylated gellan gum reacts with poly-L-lysine, forming the beads. The quick polyelectrolyte complexation that occurs between the two polymers cancels the positive groups of poly-L-lysine. Thus, a semipermeable membrane is formed not by masking poly-L-lysine in a layer-by-layer fashion, but instead by a direct interaction through polyelectrolyte complexation. The *in vivo* preliminary tests, performed by subcutaneous implantation of beads on CD-1 male mice, confirmed the low immune response to the developed beads. Altogether, these results show the potential of gellan gum-based hydrogels for immunoisolation purposes, strengthening a future application of the patented technology.

Overall, this work allows a better understanding of gellan gum hydrogels, mainly when prepared using different methods. Additionally, it also highlights the potential of gellan gum in a multitude of TERM applications.

IX.2 Future Perspectives

The high expectations of our society regarding tissue engineering and regenerative medicine have been clear since its appearance. Being the interface between engineering and medicine, this scientific area was always presented with great potential to society, being even considered the profession with the most potential in 2000, by Time magazine.

Now, 20 years later, the possibilities are almost endless, and every day, in each publication, new strategies are presented that bring us closer to find the treatment of various pathologies that plague our society. However, the vastness of possible combinations and the complexity of the human body, bring additional hurdles for tissue engineering. It is, therefore, necessary to thoroughly understand the needs

that are intended to be met, to find perfectly adequate solutions that trigger the minimum adverse reactions.

Among the various solutions presented in the context of tissue engineering, hydrogels assume a very relevant role due to their versatility and proximity to the extracellular matrix. In this regard, different materials have been explored, from synthetic to natural polymers giving origin to platforms with very distinctive behavior. Although the knowledge in the area of hydrogels is currently quite vast, the commercialization and application of these strategies are still far from their maximum potential. Poor vascularization, inadequate mechanical properties, or deleterious host immune response are some of the challenges that must be tackled before making hydrogel's use a common scenario in our medical care. Nevertheless, the scientific community is still working hard to overcome said bottlenecks and with promising results.

The main goal of this thesis was to study in greater detail the properties of methacrylated gellan gum. This polymer showed to be compatible with different crosslinking strategies and processing techniques, and therefore might be suitable for application in various tissue engineering strategies. Besides said versatility, gellan gum can be further modified to elicit other responses that can improve the overall strategy. As an example, the introduction of cell-responsive motifs, such as RGD, would improve the cell-material interaction, which might be useful for cell-based approaches. Also, the introduction of other light-sensitive motifs may empower gellan gum with rapid light-sensitive photo crosslinking, that might be helpful on a personalized 3D bioprinting design.

As mentioned in the general conclusion, the work developed on the scope of the present thesis allowed a better understanding of methacrylated gellan gum hydrogel's behavior when prepared with different conditions. Indeed, the results showed along this work revealed the potential of gellan gum to tackle different TERM challenges. Consequently, different research lines can continue from this work, pursuing more complex and intricate models, that in the end, might result in real TERM solutions.

One of the next steps would be to tackle the vascularization phenomena. Although this thesis presented different approaches, all are dependent on a proper vascularization to be successful. Indeed, Chapter IV mentioned the importance of blood vessel formation within the void space of the hydrogel beads, to supply the *de novo* tissue formation. Likewise, Chapter VIII also highlights the importance of vascularization and nutrient supply. However, in this case, it is crucial that the blood vessels grow near the surface of the polyelectrolyte complex beads, but never inside the hydrogel.

Another aspect that can be further explored based on the work developed in Chapters VII and VIII is the handling of the developed hydrogels. Due to their size, it would be hard to handle the hydrogels in a clinic scenario. Additionally, the implantation of individual beads has resulted in hydrogel accumulation due to gravity, compromising the permeability properties of the hydrogels. Therefore, it would be useful to integrate these beads in a larger support structure, finding a balance between permeability, proper vascularization and easy handling.

Regarding the work developed in Chapters V and VI, further advantages would be achieved if a longer MRI signal could be obtained. Following this rationale, manganese reservoirs as micro- or nanoparticles could be used to gradually release the ions to the external environment. Nevertheless, the possible release of manganese particles from the hydrogel must be taken into account, as it may lead to unreliable results. Thus, the challenge would be to strongly link the particles to the hydrogel matrix, without compromising hydrogel formation and the manganese release. At last, it would also be interesting to test the developed hydrogels in more significant 3D platforms, as well as animal models, to verify the functional aspect of the developed hydrogels. The different proof-of-concepts obtained along this thesis are just a small indication of what could be achieved with gellan gum hydrogels, and large-scale studies would give a more accurate understanding of this polymer. For example, the osteogenic potential of calcium-enriched gellan gum hydrogels could be tested using orthotopic models, such as sheep or pig, where the beads would be used to fill a bone defect. On the other hand, the effectiveness of manganese-based hydrogels on cell-based therapies focused on the central nervous system should also proceed to *in vivo* disease models, such as the already used shiverer mouse, pigs or dogs diagnosed with degenerative myelopathy, where the effectiveness of encapsulated cells as therapeutic agents would be confirmed. Last, the functionality of the polyelectrolyte complex beads could be determined using insulin-producing cells as a treatment of a diabetic condition in an appropriate animal model, previously induced with Type 1 diabetes by chemical treatment or genetic modification.

The beauty of science is that the quest for knowledge is a never-ending journey. And the work presented in this thesis is not a closed circle, but rather a line that can continue to be written in the future.

READER NOTES